TECHNISCHE UNIVERSITÄT MÜNCHEN
Lehrstuhl für Steuerungs- und Regelungstechnik

Bio-Inspired Motion Vision for Aerial Course Control

Johannes Alberto Plett

Vollständiger Abdruck der von der Fakultät für Elektrotechnik und Informationstechnik der Technischen Universität München zur Erlangung des akademischen Grades eines

Doktor-Ingenieurs (Dr.-Ing.)

genehmigten Dissertation.

Vorsitzender: Univ.-Prof. Dr.-Ing. W. Hemmert

Prüfer der Dissertation:

1. Univ.-Prof. Dr.-Ing.(Univ. Tokio) M. Buss
2. apl. Prof. Dr.rer.nat. A. Borst
   Ludwig-Maximilians-Universität München

Die Dissertation wurde am 11.10.2012 bei der Technischen Universität München eingereicht und durch die Fakultät für Elektrotechnik und Informationstechnik am 31.01.2013 angenommen.

Preface

This work has emerged from the collaborative work between the Max Planck Institute of Neurobiology and the Institute of Automatic Control Engineering, Technische Universität München which I have been involved in during the last years.

First and foremost I would like to thank my two "Doktorväter" Kolja Kühnlenz and Axel Borst for all their invaluable advice, encouragement and immense experience, as well as for providing an incredibly open, friendly and collaborative working environment. At the same time I would like to sincerely thank Martin Buss for taking over as my *official* "Doktorvater" on such short notice.

My deepest thanks to Maximilian Jösch for introducing me to neurobiology and being a great friend. Very special thanks also to Väinö Haikala, Dierk Reiff and Adrian Wertz for their friendship and invaluable help and advice. Many thanks to Hubert Eichner, Franz Weber and Armin Bahl for all their help and fruitful discussions. Many thanks also to my student Thi Bui-Ngoc for his efforts and contributions to this thesis. Thanks to my lab colleagues Anselm Geiger, Étienne Serbe, Matthias Meier, Thorben Kurz, Bettina Schnell, Jürgen "Bulle" Haag, Jonathan Mackinnon, Georg Ammer and all the others who contribute to such a pleasant and positive lab atmosphere. Thanks to Alfredo Brockmann, Christoph Scheffelt, Gabriel Thiermann, Klaus-Stefan Gerber, Verónica Gonzalez and Matthias Detjen for being the best of friends.

Most importantly I want to thank my parents and my brother for their unconditional love and support, as well as Kathrin for being my motivation.

München, 2012. Johannes Plett

For my parents

Abstract

When it comes to extracting motion information from visual cues and processing it for flight control there is arguably no better performing or more adapted system than the visual system of the common fly. It is capable of fast, precise and reliable performance, while remaining robust in the face of low signal-to-noise regimes or perturbations such as wind gusts and drafts. Also, its underpinning algorithmic structure is computationally inexpensive and has been extensively studied. These characteristics make the fly motion vision system a prime candidate for technical implementation. However, little is known about its performance in technical applications, especially when operating under closed loop conditions.

This highly interdisciplinary thesis focuses on the analysis of fly motion detection principles for deployment in technical systems. The approach taken here consists of three orthogonal aspects covering the neurobiological background, analytical and simulation studies, as well as real-world implementation and practical assessment. New techniques for neurobiological studies of the fly visual system are established, revealing amenable characteristics for technical deployment as well as providing further insight into the underlying neuronal processing stages. A novel fly-inspired rotation sensor is proposed and implemented. Extensive simulations and experimental visual control trials on-board autonomous aerial robots reveal that among its advantages figure substantial improvements of control performance in terms of stability and robustness against time delays compared to conventional approaches.

In this work the advantages of fly motion detection principles are comparatively assessed under closed loop conditions, thereby establishing this type of biologically inspired motion sensor as a superior alternative to conventional algorithms. On one hand the contributions significantly advance the state of the art of motion estimation and visual control, while on the other hand they serve as a guidepost example of positive synergies between neurobiology and engineering sciences.

Zusammenfassung

Das visuelle System der Fliege gehört wohl zu den am besten geeigneten und angepassten Systemen, um aus optischen Reizen Bewegungsinformation zu entnehmen und diese zur Flugkontrolle zu benutzen. Selbst bei widrigen Signal-zu-Rausch-Verhältnissen oder erheblichen Störungen, wie z.B. Windstöße oder Zugluft, arbeitet es schnell, präzise und verlässlich. Des Weiteren ist seine grundlegende algorithmische Struktur rechnerisch effizient und zu großen Teilen gut erforscht. Diese Eigenschaften machen das Bewegungssehsystem der Fliege zu einem geeigneten Modell für die technische Umsetzung. Dennoch ist über sein Verhalten in technischen Implementierungen, vor allem im geschlossenen Regelkreis, wenig bekannt.

Diese interdisziplinäre Dissertation befasst sich mit der Analyse der Bewegungswahrnehmung der Fliege und ihrer Prinzipien für den Einsatz in praxis-orientierten technischen Anwendungen. Der Ansatz besteht aus drei orthogonalen Aspekten von der Untersuchung neurobiologischer Grundlagen, über analytische Studien und Simulationen, bis hin zur praktischen Implementierung und anwendungsnahen Bewertung. Neue Techniken und Hilfsmittel zur neurobiologischen Untersuchung des visuellen Systems der Fliege werden etabliert, welche zu neuen Erkenntnissen bezüglich der grundlegenden neuronalen Verschaltungen führen. Ein neuartiger Fliegen-inspirierter Rotationssensor wird konzipiert und implementiert. Anschließend werden die vorgeschlagenen Ansätze durch ausführliche Simulationen und praktische Experimente zur bordeigenen Sichtsteuerung von autonomen Flugrobotern validiert. Diese experimentellen Ergebnisse zeigen eine signifikante Verbesserung der Regelperformanz im Hinblick auf Stabilität und Robustheit bei Laufzeitverzögerungen gegenüber klassischen Systemen.

In dieser Arbeit werden die Vorteile des Bewegungsdetektionsapparates der Fliege im geschlossenen Regelkreis vergleichend untersucht. Hierbei erweist sich diese Art eines biologisch inspirierten Bewegungssensors als überlegen gegenüber klassischen Ansätzen. Einerseits erweitern die Beiträge den Stand der Technik der Bewegungsschätzung und bildbasierten Regelung und andererseits liefern sie ein wegweisendes Beispiel für positive Synergien zwischen der Neurobiologie und den Ingenieurswissenschaften.

Contents

Notations

Abbreviations

1D	One Dimensional
2D	Two Dimensional
2PLSM	Two-Photon Laser-Scanning Microscopy
3D	Three Dimensional
A/D	Analog to Digital
ACK	Acknowledge
AF	Action Field
amc	Amacrine Cell
ARM	Advanced RISC Machine
ASIC	Application Specific Integrated Circuit
aVLSI	Analog Very Large Scale Integration
Ca^{2+}	Calcium
CAN	Controller Area Network
CCD	Charged Coupled Device
CF	CompactFlash
CFP	Cyan Fluorescent Protein
CMOS	Complementary Metal-Oxide Semiconductor
CRT	Cathode Ray Tube
DMA	Direct Memory Access
DNOVS	Descending Neuron of the Ocellar and Vertical System
EMD	Elementary Motion Detector
EMI	Electromagnetic Interference
FIFO	First In First Out
FN-NMN	Frontal Nerve-Neck Motor Neuron
FOV	Field Of View
FPAA	Field Programmable Analog Array
FPGA	Field Programmable Gate Array
fps	Frames per second
GUI	Graphical User Interface
H1	Horizontally Sensitive Neuron 1
HRM	Hassenstein-Reichardt Model
HS	Horizontal System
HSE	Horizontal System Equatorial
HSN	Horizontal System Northern
HSS	Horizontal System Southern
I^2C	Inter-Integrated Circuit
IC	Integrated Circuit
IIR	Infinite Impulse Response

L1-5	Lamina Neurons
LCD	Liquid Crystal Display
LED	Light Emitting Diode
LPTC	Lobula Plate Tangential Cell
LUT	Look-Up Table
MAC/PHY	Media Access Control / Physical layer chip
MAD	Mean Absolute Deviation
MAV	Micro Aerial Vehicle
MCU	Microcontroller Unit
MMC	Multi Media Card
NACK	Negative Acknowledge
PC	Personal Computer
PCB	Printed Circuit Board
PCI	Peripheral Component Interconnect
PID	Proportional-Integral-Derivative
PMT	Photomultiplier Tube
PWM	Pulse Width Modulation
R1-8	Photoreceptor Cells
RAM	Random Access Memory
RAPS	Radially Averaged Power Spectrum
RISC	Reduced Instruction Set Computer
RMS	Root Mean Square
RMSD	Root Mean Square Deviation
SD	Secure Digital
SEM	Standard Error of the Mean
SDRAM	Synchronous Dynamic Random Access Memory
SNR	Signal-to-Noise Ratio
SPI	Serial Peripheral Interface
TTL	Transistor-Transistor Logic
TTX	Tetrodotoxin
TWI	Two Wire Interface
UAV	Unmanned Aerial Vehicle
USART	Universal Synchronous/Asynchronous Receiver/Transmitter
USB	Universal Serial Bus
UV	Ultra Violet
V1, V2	Vertically Sensitive Neurons
VHDL	Very High Speed Integrated Circuit Hardware Description Language
VS	Vertical System
WLAN	Wireless Local Area Network
YFP	Yellow Fluorescent Protein

Conventions

Scalars, Vectors, and Matrices

x, X	Scalar
$\boldsymbol{x}$	Vector
$\boldsymbol{X}$	Matrix, Scalar field
$\mathfrak{X}$	Vector field
$f(\cdot)$	Function
$\dot{x}$, $\ddot{\boldsymbol{x}}$	Equivalent to $\frac{\mathrm{d}}{\mathrm{d}t}x$, $\frac{d^2}{dt^2}\boldsymbol{x}$
$\langle x \rangle_\varphi$	Spatial average of x over angle φ
$\langle x, y \rangle$	Inner product of x and y
$\lvert x \rvert$	Absolute value of x
$(\cdot)^T$	Transpose

Symbols

Aspects of Insect Motion Vision

$\Delta\varphi$	Inter-ommatidial angle, angular resolution
λ	Spatial wavelength
λ_D	Dominant wavelength
$\Delta\lambda_{1/2}$	Spectral half-width
ν	Angular velocity
n	Number of samples
f_t	Temporal frequency
Δz	z axis image stack increment
τ	Time constant
Δt	Inter-stimulus interval
w	Tuning width
p	Statistical p-value

Insect-Inspired Rotation Sensing

C_{MAD}	Mean absolute deviation contrast
C_{RAPS}	Radially averaged power spectrum contrast
C_{RMS}	RMS contrast
I	Pixel intensity
L	Luminance
R	Reflectance
$\Delta\varphi$	Inter-ommatidial angle, angular resolution
ΔI	Pattern contrast
ω	Angular frequency
θ_{est}	Rotation axis sensor estimate
θ_{ref}	Reference rotation axis
n	Number of samples

λ	Spatial wavelength
$\langle R_i \rangle_\varphi$	Spatial EMD response average
τ_g	Gain adaptation low-pass filter time constant
τ_{HP}	High-pass filter time constant
τ_{LP}	Low-pass filter time constant

Fly-Inspired Motion Estimation for Flight Control

$(\cdot)^x$	Along / around x axis
$(\cdot)^y$	Along / around y axis
$(\cdot)^z$	Along / around z axis
$(\cdot)_A$	Receptive field
$(\cdot)_B$	Optic flow field field
$(\cdot)^{rot}$, $(\cdot)_{rot}$	Rotation
$(\cdot)^{tra}$, $(\cdot)_{tra}$	Translation
${}_i()$	Inertial frame
${}_b()$	Body frame
$(\cdot)_\phi$	Roll
$(\cdot)_\omega$	Pitch
$(\cdot)_\psi$	Yaw
$(\cdot)_{max}$	Maximum
$\boldsymbol{q}_i$	Feature point
$\boldsymbol{d}_i$	Feature point projection
μ_i	Nearness
$\boldsymbol{t}$	Translation vector
$\boldsymbol{r}$	Rotation vector
t	Time
$\boldsymbol{p}_i$	Optic flow point
$\boldsymbol{B}$	Projection matrix
θ, ϕ	Azimuth angle, elevation angle
$\boldsymbol{f}(\cdot)$	Optic flow
μ	Homogeneous nearness, dynamic viscosity of air at 20°
$\boldsymbol{S}_{AF}$	Action field
$\mathfrak{A}$	Receptive field
$\mathfrak{B}$	Optic flow field
D	Integration domain
D^*	Partial integration domain
Δ	Difference
n	Number of elements
a, b, c, ξ	Factor
m	Mass
$\boldsymbol{v}$	Velocity
$\boldsymbol{\omega}$	Angular velocity
$\boldsymbol{f}^n$	Net force
$\boldsymbol{f}$	Propulsion force
$\boldsymbol{f}^D$	Friction drag force
ρ	Mass density of air

C_D	Drag coefficient
A	Reference area
r_{th}	thoracic half-width
S	Wing surface
β	Stroke plane
u, v, w	Velocity scalar
p, q, r	Angular velocity scalar
f	Scalar force
$\boldsymbol{l}$	Angular momentum
$\boldsymbol{\tau}$	Torque vector
C	Frictional damping coefficient
$\boldsymbol{J}$	Inertia tensor
τ	Torque
J	Inertia
C_{body}	Frictional damping coefficient of the body
C_{wing}	Frictional damping coefficient of the wings
$\bar{D}_{dif}$	Differential wing profile drag
$\hat{r}_{CP}$	Distance to center of pressure
R	Wing length
$\bar{\omega}$	Mean saccadic turning rate
τ_{LP}	Low pass filter time constant
g	Gain
Δt	Delay
H	Minimum torque change criterion
t_1, t_2	Start and end time point

1 Introduction

The common household fly is arguably the most maneuverable flyer in the whole animal kingdom—and far superior to any man-made aircraft in that regard. It is capable of accurately controlling flight at linear velocities far exceeding 200 body lengths per second (which in comparison with an average 15 m long aircraft would correspond to airspeeds topping Mach 8), executing precise turns at angular velocities above $3000\,^\circ\,\mathrm{s}^{-1}$ and all this while navigating through complicated terrain and avoiding obstacles at these velocities. The key to such levels of performance is its highly adapted visual system as a result of over 300 million years of evolution.

As opposed to e.g. brains of vertebrates with their high degrees of plasticity and adaptability, the optic lobe of fly brains is highly stereotyped and hardwired. This means that for different tasks there exist hardwired dedicated circuits that are exceedingly optimized for their particular function. This stereotypy allows for systematic analysis of individual neurons or neuronal populations within one species as they remain largely identical both in function and morphology from one individual to the next. At the same time, a fly brain consists of only a few 100 000 neurons. Approximately half of these cells constitute the fly's optic lobes. Together with the optic lobes' stereotypy this has led to the fly visual system being one of the best characterized brain structures of all organisms, both anatomically and functionally.

In contrast to conventional artificial flight control systems that perform complex sequential computations using only a few sensor measurements, the fly visual system receives input from many thousands of sensors and computes them in a massively parallel fashion. This motion information computation can be described as a *divide and conquer* approach. In a highly parallel way for each sampled location in visual space local motion is computed. From all these individual local motion estimates global motion is inferred and appropriate motion commands are sent via descending neurons towards the motorneurons innervating the flight muscles.

The first algorithmic description of elementary insect local motion detection was outlined in the groundbreaking work of Hassenstein and Reichardt in 1956 [1]. To the present day their model is considered to be the most fitting algorithmic description of the basic principle of how local motion information is extracted from arrays of light intensity sensors such as the photoreceptors and ommatidia of the fly (Figure 1.1a).

The approach of integrating local motion into global motion estimates leads directly to the concept of *optic flow*. Flies navigate using *optic flow*, which by definition corresponds to the apparent motion of a visual scene caused by the relative motion of the observer within this scene. Nevertheless, flies are not the only complex systems that can directly benefit from this way of computing motion. Unmanned aerial vehicles (UAVs) and micro aerial vehicles (MAVs) in particular are becoming a continuously increasing area of active research. Due to their airborne nature they can greatly profit from new high-speed, lightweight and efficient ways of estimating motion and particularly ego-motion.

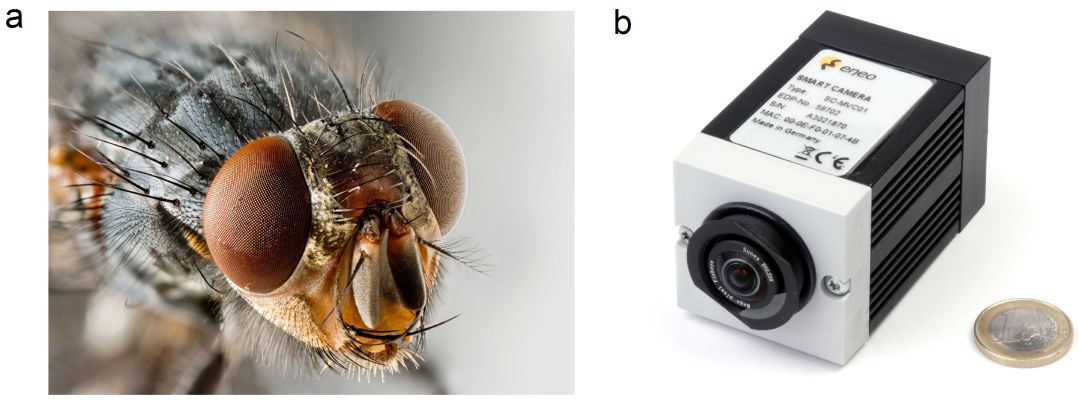

Figure 1.1: (**a**) Macro portrait of the fleshfly (*Sarcophagidae*) [2] (**b**) Fly-inspired artificial ego-rotation sensor system [3].

Traditionally, aerial robots are being equipped with complex sensors and high power computation devices allowing stabilization and navigation. Whereas this approach in the past has yielded satisfactory results in aerial vehicles of large payloads and energy resources it is still an open question whether this is the ideal solution for use on-board small and light-weight vehicles where efficiency is of utmost import. Yet, relatively little attention has been given to bio-inspired approaches of estimating (ego-)motion and using this knowledge for efficient control and navigation. Nevertheless, with the advent of new neurobiological tools, such as advancements in genetic engineering, new recording techniques and advances in stimulation devices continuously more insight is gained into how insects and particularly flies achieve such astounding feats of aerial flight control.

Therefore, by enabling transfer of knowledge between two relatively unrelated fields of research such as biology and applied engineering new solutions to open issues like robust and efficient visual flight control could arise. Arising from the current state of knowledge about the fly visual system and the current state of the art in aerial robot research novel flight sensing and control systems such as the one shown in Figure 1.1b can effectively introduce large degrees of autonomy and self-sufficiency into small aerial vehicles. The added benefit is not only autonomy in course and stabilization control but also autonomy in terms of energy efficiency since these bio-inspired algorithms represent an inherently different and more energy efficient way of computation when compared to conventional techniques. Moreover, these bio-inspired approaches often possess additional intrinsic features and advantages, which can have decisively positive effects on the performance of the aerial robot.

The work presented in this thesis focuses on first investigating several key properties of the fly visual system, then on transferring this knowledge from biology to the implementation of an artificial vision sensor and finally on assessing the performance of this type of processing and particular implementation in this new technical application scenario.

The main challenges exacerbating the analysis of the fly motion vision circuitry, design and implementation of the artificial vision system and performance assessment are summarized in the following.

1.1 Challenges

During neurophysiological analysis, algorithmic transfer and implementation assessment plenty of different challenges arise. Due to being a very interdisciplinary work presented here, this broad spectrum of challenges ranges from neurophysiological aspects of stimulation protocols, genetic tool development, information theoretic analysis and recording techniques to more applied engineering aspects such as hardware, firmware and software development as well as control performance assessment. Some of the key aspects addressed in this thesis are summarized as follows:

Neurophysiology Issues

Analysis of the insect visual system is a field of neurobiology, which has continuously received a lot of attention and important contributions for more than a century. It has therefore been provided with a rather strong theoretical foundation and good insight into many different aspects as to how vision—and motion vision in particular—is processed in the insect brain. However, this knowledge is by no means complete and an astounding number of open questions still remain.

Electrophysiology, as opposed to e.g. behavioral studies, is a tool which enables direct insight into activation patterns at single cell level at great temporal and spatial resolution. Yet, these two positive assets when recording can easily become a drawback at input level. Since electrophysiology enables real-time recordings of fast neuronal activity, any temporal artifacts introduced during stimulation that fall below flicker fusion frequency of the organism in question also cause unwanted artifacts during recording. This makes it hard, if not impossible to differentiate neuronal properties from artificially introduced artifacts. The same challenges have to be faced in terms of spatial resolution of the stimulus and the optical resolution of the organism under analysis. Here, aliasing effects and apparent motion issues need to be addressed. The mentioned drawbacks can be overcome by designing an appropriate stimulus device, which takes into consideration all the relevant properties of the biological systems that are to be investigated as well as all key aspects of the envisioned experimental steps.

Other challenges faced during neurophysiological research include developing well-suited stimulation protocols, appropriate choices of genetic tools, qualified recording devices and protocols, as well as conducive animal preparation techniques.

Therefore, a main challenge this thesis focuses on is the design of a visual stimulation device and protocols appropriate for both electrophysiology and behavioral studies. This work also addresses key aspects of preparation, recording and analysis of the fly visual system.

Technology Transfer Issues

When transferring solution approaches for a particular problem from biological systems to a technical system several challenges arise. The fly visual system has evolved to a state of massively parallel computing, where also many cells play major roles in seemingly different pathways and tasks. There may often be cases of e.g. a population of neurons actively involved in computing visual input, while at the same time playing a pivotal role in processing olfactory information. These same neurons can also additionally be key players

in many other information processing cascades. It is therefore a great challenge to assess which neurons or networks of neurons take on key roles for one specific behavior or task.

Another major challenge is the massively parallel way in which neuronal circuits process information. This is in stark contrast to traditional computation in computers and microcontrollers, which inherently process information sequentially. Despite major advances in computing power and speed, the rate of information which can be processed in such a parallel way even in such a small brain as the fly's is still not matched. Nevertheless, taking advantage of specific hardware allowing for certain degrees of parallel and pipelined computing, these parallel computing approaches can be transferred from biological systems to technical systems to a large degree.

Another challenge faced while mimicking biological solutions in technical applications is the traditionally large difference in size, weight and power density footprint. Whereas in nature astounding amounts of computations can be robustly carried out by a few densely packed neuronal cells that require little equivalents of electrical energy and power, state-of-the-art technology is at present still a long way from being able to achieve similar levels of computation, compactness and efficiency. Yet, by careful choices of appropriate components and ways of computation these challenges can be overcome to suit the needs for a particular application.

The main challenges addressed are the design and implementation of a system transferring the algorithmic approach of the fly visual system to motion and rotation detection to a technical equivalent sensor system, while keeping within the tight boundaries imposed by the intended deployment in miniature aerial robots.

Control Issues

The fly visual system is highly non-linear and adaptable to many different stimulus conditions. Due to these non-linearities it is able to cope well with low signal-to-noise ratio (SNR) environments [4, 5] or varying statistical stimulus properties [6]. Several of these beneficial properties of the fly visual system are preserved down to its individual atomic motion detection circuits. Nevertheless, other properties such as global motion detection or or rotation estimation arise only due to intricate networked connections between groups of these elements and their postsynaptic cells, thereby hindering linear analysis of these properties.

The main challenge here focuses on investigating beneficial dynamic properties of the algorithmic representation of the fly visual system when compared to conventional algorithms. This is specifically investigated in closed-loop conditions.

1.2 Main Contributions and Outline of the Thesis

The work presented in this thesis focuses on the fly visual system and its application to visual motion sensing. In comparison to conventional artificial motion vision algorithms the fly visual system estimates global motion by computing many local motion cues and integrating them over large fields of view using specialized integrating cells. This highly parallel approach enables high throughput, fast computation, robustness and several other advantages.

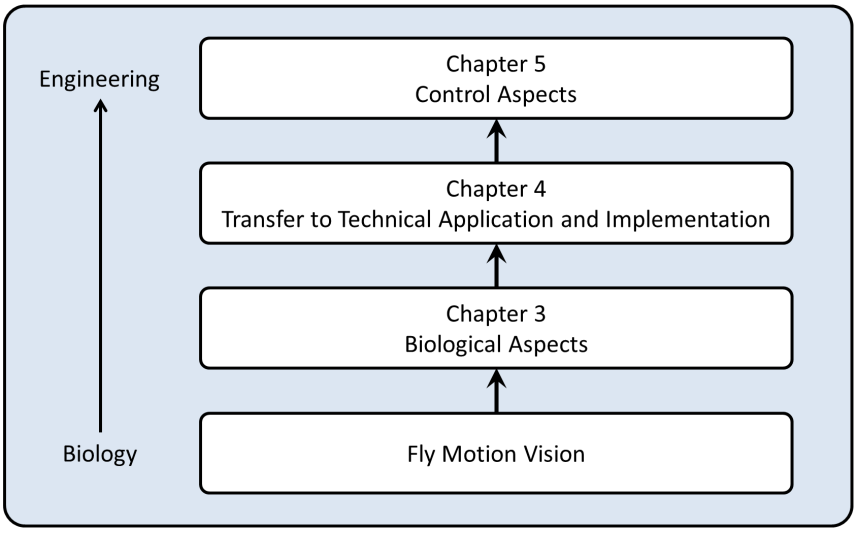

Figure 1.2: Outline of the thesis.

Therefore, the main aim of this thesis is to analyze basic properties of the fly visual system, then transfer these algorithms to a technical solution, assess this implementation's performance and finally establish this type of processing as a sensor outperforming conventional solutions. The driving idea behind this work is the transfer of knowledge from biology to applied engineering. In order to do so, fundamental aspects of the type of processing the fly visual system performs are investigated. To exploit the advantages of this type of computation a complete visual motion sensor is designed and implemented, fully retaining the fly's visual motion estimation algorithm structure. Capabilities and advantages of this type of sensing are assessed in open- and closed-loop control situations.

As outlined in figure 1.2, this thesis comprises three separate research topics, which successively build up on each other, thereby going from chiefly neurobiological aspects to applied engineering and thus bridging the gap between these two distinct fields. The main contributions of this work are presented in the following.

Neurobiological Aspects

When analyzing the visual systems of insects it is critical to be able to stimulate the desired processing elements with appropriate stimuli. However, thus far no appropriate visual stimulation device exists for electrophysiological analysis of the exceedingly fast vision system of the fly. This greatly restricts the analysis and investigation of key aspects and open questions as to how motion is computed in the fly at cellular level. Traditionally, cylinder shaped patterned drums were rotated around the fixed animal, thereby producing flicker- and glitch free stimuli, but greatly restricting the patterns that could be shown. Other solutions consisted of using computer screens or oscilloscope displays for visual stimulation. Yet, these devices introduced artifacts into the cellular responses due to inherently low frame and refresh rates or narrow fields of view. Therefore, in Chapter 3 a system is proposed that eliminates the shortcomings of traditional stimulation devices and enables research of vision in biological systems previously unfeasible. Using this system and a novel patch-clamp recording technique a pivotal neuronal subpopulation is investigated, establishing the fruitfly *Drosophila melanogaster* as a model organism for this particular

type of research. Furthermore, by incorporating the proposed stimulation device into a two-photon laser-scanning microscope (2PLSM), separation of light variations into distinct input pathways towards the fly motion vision system is found and one pathway is thoroughly described. Lastly, the role of two descending neurons directly projecting towards motor-neurons that constitute the output stage of the visual system is assessed. Taken together, these solutions and findings not only decisively further knowledge of biological motion vision but also pave the way for future investigation in this area.

Technical Motion Vision Implementation

While Chapter 3 focuses on the biological aspects of biological motion vision systems, in Chapter 4 this knowledge is transferred to a technical solution. Traditional visual sensor designs rely on complex calculations in a sequential manner, thereby often limiting performance in terms of speed and robustness to noise or mechanical failure. Biological systems, however, have developed in a very distinct manner. By adapting massively parallel and robust algorithms that only use few computing elements per pathway biological systems do not have the aforementioned drawbacks, making them ideal sources of inspiration for technical solutions. Therefore, in this work a visual motion and rotation sensor is developed, which processes visual motion cues using the same fundamental algorithms as the fly visual system does. As the envisioned application scenario of this sensor is on-board micro aerial vehicles (MAVs) very tight constraints in terms of size, weight and power are adhered to. The main contribution of this work is the proposal of a novel type of sensing rotation from visual motion cues and the development of a fully functional sensor compliant with this principle, which can be deployed autonomously on-board small MAVs.

Closed-Loop Control Analysis

Chapter 5 focuses on assessing the motion and rotation estimation techniques proposed in Chapter 3 and Chapter 4. In control systems aspects such as stability, noise and delays play pivotal roles. Here, the proposed sensing strategy is analyzed in closed-loop conditions in order to assess their applicability for control systems. Therefore, both extensive model simulations as well as practical trials in real life conditions are performed, revealing superior characteristics of the proposed solutions compared to conventional sensors.

The aspects addressed in this thesis substantially contribute to the understanding of biological motion vision and its applicability to technical deployment. The neurophysiological observations and tools presented here not only enhance the current state of knowledge but also provide a framework for future studies on biological motion vision as well as establishing biological vision principles as ideally suited for use in technical solutions. The aim of this highly interdisciplinary work is to integrate biology and engineering and emphasizing this positive synergy by introducing a high performance bio-inspired sensor, thereby providing a basis for future studies in this interface between two otherwise largely unrelated fields of research.

2 Neurobiological Foundations and Related Work

The study of fly motion vision has been an active and productive field of research for well over a century [7–10]. It is mainly driven by the question as to how these insects with strikingly small numbers of neurons and synapses can achieve such formidable flight maneuvers by largely relying on visual cues. The key to this performance lies in the fly's highly evolved and efficient neuronal network, which is perfectly adapted to this type of processing. There has been a multitude of studies contributing to the understanding of the underlying principles and constituting neuronal elements of the fly visual system. As a result, the neuronal connective of the fly visual system has been subject to a wide variety of different experimental approaches. While the earliest studies mainly draw from behavioral and anatomical observations [7–11], subsequent studies start involving also computational and system theoretical aspects [1, 12–14]. The more recent works additionally draw from a vast pool of genetic techniques, which allow precise manipulation of specific neurons or neuronal populations [15–18]. As a result of these studies significant insight has been gained in the past decades as to how flies achieve such skilled visual course control.

Attaining such levels of performance is also the ultimate goal of the control systems of technical aerial applications such as UAVs and MAVs. But despite considerable research in this field, as of yet the flight performance of a fly remains elusive for man-made flying platforms. Therefore research has begun to look at biologically inspired techniques for addressing many of the unsolved issues in flight control and motion sensing in general. Survey articles on these topics can be found in [19–21].

The aim of this chapter is to present an outline of the neurobiological fundamentals of fly motion vision as well as to provide a brief survey of the relevant state of the art.

2.1 Fly Visual System

A large portion of the fly brain is dedicated to processing visual information. This so called *optic lobe* consists of a series of consecutive neuronal layers. As depicted in Figure 2.1 visual information is first sampled in the retina of the fly compound eye. Depending on the species, this compound eye consists of several hundreds to several thousands of facet eyes called *ommatidia*. Each *ommatidium* contains a lenslet and a set of 8 photoreceptor cells numbered R1 through R8. From there visual information is conveyed in a retinotopic fashion onto the *visual ganglia*. Here, *retinotopy* means that information from adjacent regions in space are also processed in adjacent neuronal processing columns in the fly brain. The *visual ganglia* are a sequential set of neuronal layers or *neuropils* called *lamina*, *medulla* and *lobula complex*, which itself is composed of the *lobula* and *lobula plate*.

The first accounts of these neuronal structures were provided by Ramón y Cajal and Sánchez in the early 20th century [9, 22] by using a technique called *Golgi staining*, in which arbitrary neurons are stained in their entirety [23] and, thus, made visible by stand-

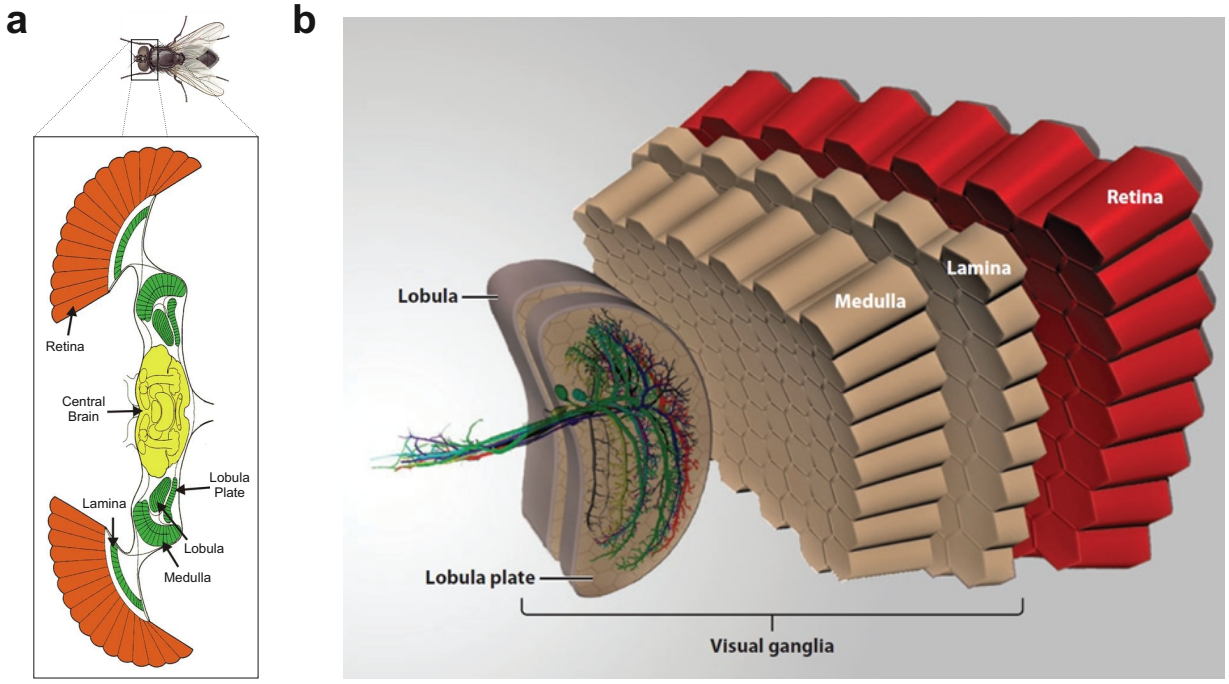

Figure 2.1: (**a**) Schematic horizontal cross-section through the head of the fly, adapted from [31]. (**b**) Schematic of the fly optic lobe, including LPTCs [32].

ing out against their surrounding tissue. Using this technique the exhaustive studies by Strausfeld [24] and Fischbach and Dittrich [25] on the common housefly *Musca domestica* and the fruitfly *Drosophila melanogaster*, respectively, have identified many neurons along the pathways involved in establishing visual course control.

The minimal circuitry presumed to be involved in this pathway commences with sampling visual information in the six photoreceptors R1 to R6, which project into the lamina onto the large monopolar cells L1 and L2. These further relay their information into the medulla towards the Mi1 and Tm1 cells, respectively [26, 27]. Mi1 is believed to project within the medulla onto T4, whereas Tm1 cells synapse onto T5 cells in the lobula [28]. These two separate pathways converge again when synpsing onto a prominent group of large neurons in the lobula plate called the lobula plate tangential cells (LPTCs) [25, 29, 30]. A brief outline of this candidate pathway is depicted in Figure 2.2a.

In the blowfly there exist about 60 LPTCs per hemisphere, which are individually identifiable through their anatomy and response properties depending on the visual input. These cells have first been shown to be involved in visual course control based on the strong effect in optomotor response when these cells are being ablated [15, 30, 33]. LPTCs sample information computed by many hundreds of adjacent columnar elements, thereby performing a wide-field integration of local motion computations. The individual type of LPTC defines which elements in which region are sampled. Two prominent groups of LPTCs sample vertical and horizontal information in specific dendritic integration regions. The group integrating vertical input is called the *Vertical System* (VS) cells and, accordingly, the horizontal group is called the *Horizontal System* (HS) cells.

A particular trait of both VS and HS cell types is their direction selectivity. If a stimulus such as a grating moves in a particular direction, the cell responds with a distinct signal depending on its response type. The response types of these neurons can be separated

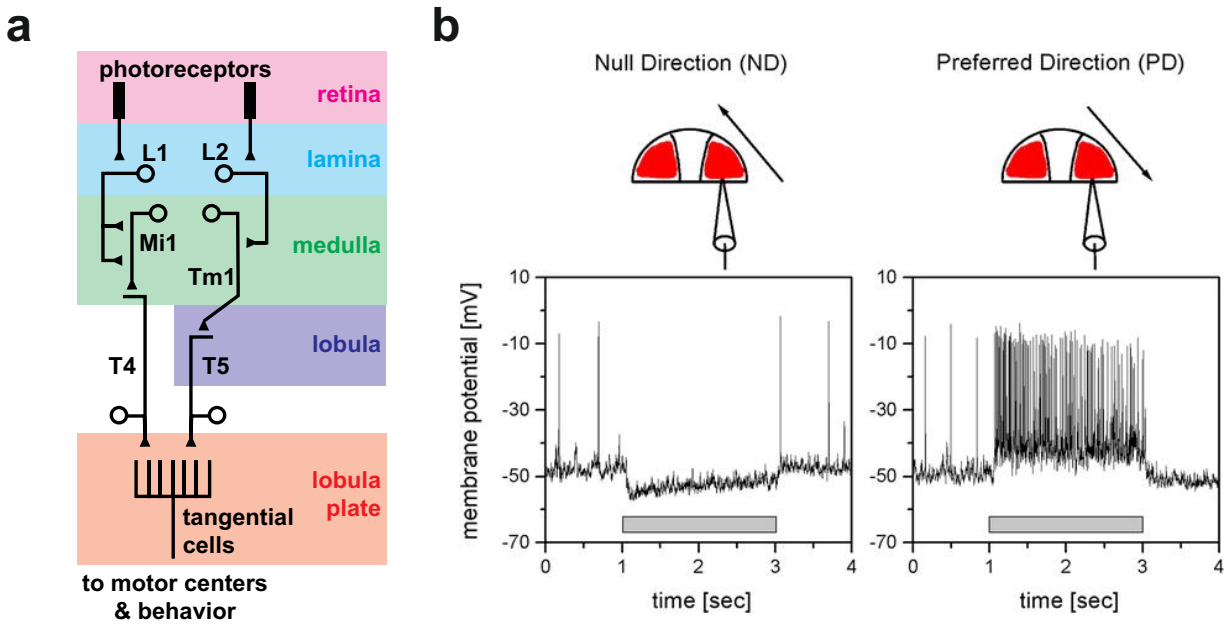

Figure 2.2: (**a**) Minimal circuitry candidates for implementing the course control pathway through the visual ganglia [28]. (**b**) Direction selectivity of LPTCs. Intracellular recordings of an HSE cell show hyperpolarization during motion in the null direction and depolarization with overlaid action potentials during motion in the preferred direction [31].

into graded, spiking and mixed response neurons. Graded response neurons depolarize upon excitation and hyperpolarize during inhibition. Spiking neurons increase their firing rates during excitation and decrease or fully suppress their firing rates during inhibition. Mixed types, consequently, respond with mixtures of both respective activities. Hence, if a grating moves in a VS or HS cell's preferred direction (PD) the cell responds by depolarizing and fires a train of action potentials [31, 34, 35], as is depicted on the right hand side of Figure 2.2b. If, on the other hand, the grating motion is towards the cell's null direction it hyperpolarizes and ceases to fire action potentials [31, 34, 35], as can be seen on the left hand side of Figure 2.2b. Some other LPTCs, such as e.g. H1, H2, H3, H4 or V1 are of the spiking kind and respond by producing regular action potentials [32].

Two interesting phenomena present themselves when analyzing the VS cells in terms of their receptive fields. By definition, a receptive field is the region of visual space in which a certain stimulus elicits a certain level of response in that particular neuron. As a first phenomenon it turns out that VS cells are most strongly tuned to the visual stimuli arising from rotations around particular body axes [36, 37]. As depicted in the lower three panels of Figure 2.3a the receptive fields of VS cells resemble rotations around axes on the equatorial plane sequentially arranged along the equator, as illustrated by the upper right hand sketch in Figure 2.3a.

A second striking phenomenon arises when observing the width of the measured receptive fields. Based on anatomical data VS cells receive dendritic input from retinotopic columnar elements corresponding to receptive field widths between 30° and 40° of horizontal visual space [38]. However, their axonal output corresponds to much broader receptive fields than their anatomy could allow [36]. This seeming contradiction was resolved by revealing gap junctions in the VS cell axon terminal regions, i.e. electrical connections individual VS cell

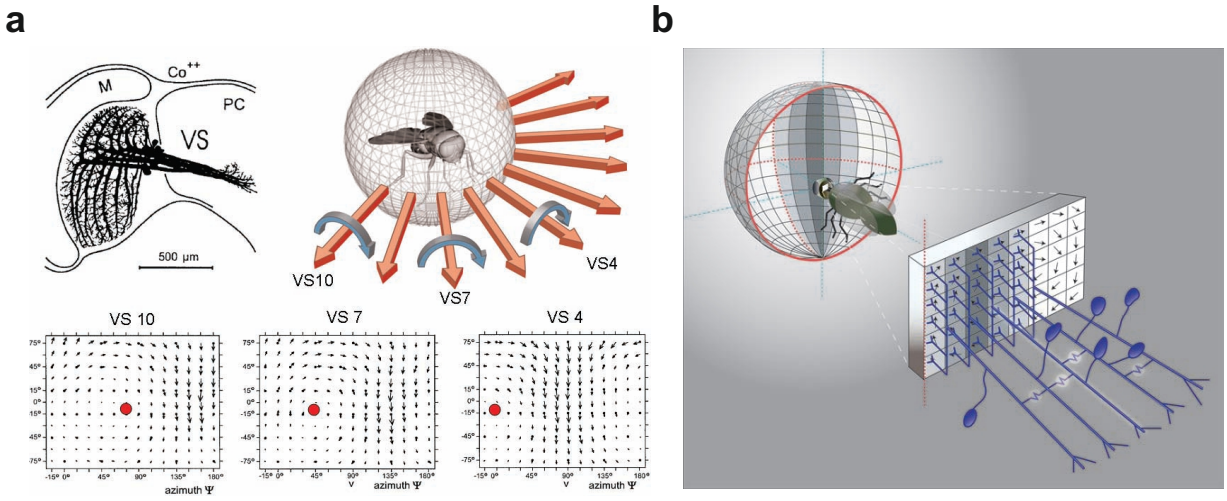

Figure 2.3: (**a**) VS cell receptive fields [42]. (**b**) VS cell network schematic [42].

axon terminals [39, 40]. As a result, VS cells "share" their direct dendritic input with their immediate VS cell neighbors [40], thereby resulting in a VS cell network. A schematic of this network and its connections is presented in Figure 2.3b.

For further details about fly motion computation the interested reader is referred to more extensive review articles, e.g. [31, 32, 41].

2.2 Reichardt Detector

Photoreceptor cells are strictly speaking pure light intensity sensors and therefore do not exhibit any direction selectivity. However, just a few synapses downstream of the photoreceptors, LPTCs—and VS cells in particular—in fact do show direction selectivity and respond in the aforementioned distinct ways when stimuli move in one or the other direction. Moreover, VS cells show a strong dependency on the relative stimulus velocity, making them a type of velocity gauge. Whereas the exact neuronal elements involved in computing this direction selectivity and velocity dependency between photoreceptors and VS cells are unknown and the pathway can only tentatively be outlined (see Figure 2.2a), its algorithmic nature can be explained with surprising detail by the correlation-type elementary motion detector (EMD) model, also known as the *Reichardt Detector*. Being put forth in the mid-1950s following research performed on the beetle *Chlorophanus viridis* [1], it yields direction-selective and velocity-dependent results by correlating the luminance levels of two spatially adjacent image points. As outlined in Figure 2.4a the Reichardt Detector consists of two mirror-symmetric subunits, each multiplying one input with a low pass filtered—and thusly time-delayed—version of the other input. The output of these two mirror-symmetric subunits is then subtracted, yielding a fully direction-selective output signal.

It is evident from this scheme that the Reichardt Detector is not a perfect linear velocity estimator but in fact yields a non-linear bell shaped velocity or temporal frequency steady state response curve. This behavior can be observed exemplarily in Figure 2.4b, where the EMD response displays an approximately linearly increasing relationship with increasing temporal frequency until reaching a plateau, after which the response will in fact decrease

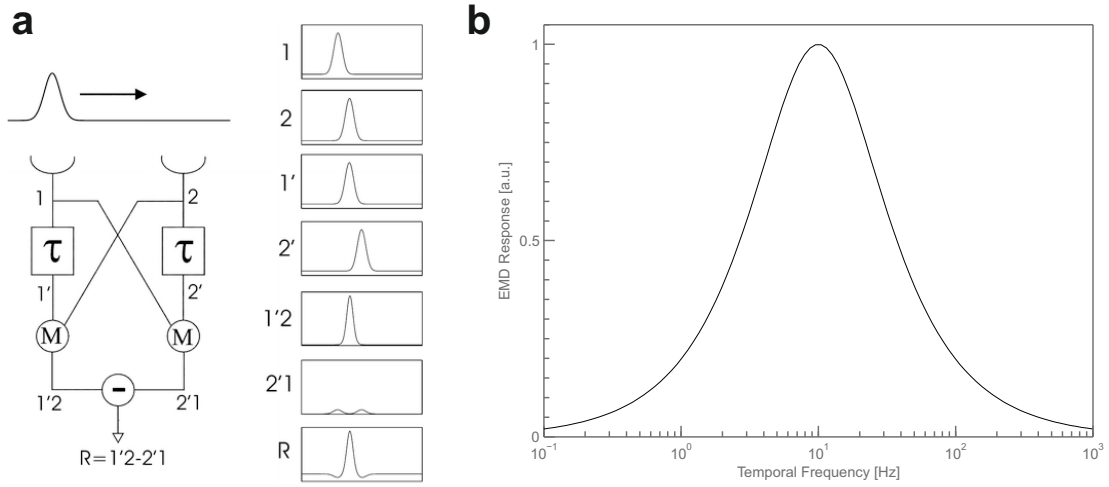

Figure 2.4: (**a**) The correlation-type elementary motion detector (EMD) model or Reichardt Detector, adapted from [31]. (**b**) Reichardt Detector steady state temporal frequency dependency.

again with increasing temporal frequency. This in fact corresponds rather accurately to measurements performed in flies and other insects. Note, the temporal frequency is defined here as the ratio of velocity and spatial wavelength of the pattern, e.g. a moving sine grating.

2.3 Neurobiological Concepts and Techniques

In the remainder of this work several neurobiological concepts and techniques will be referred to. The principal aspects of these shall be briefly outlined in the following.

Neuron The *neuron* constitutes the structural and functional elementary unit of the nervous system. This type of cell is typically comprised of a *cell body*, also called *soma*, the *dendrites* and the *axon*. The dendrites, which often branch out in a tree-like manner, receive information from other cells and constitute the input region of a neuron. The axon, on the other hand, can be viewed as the output channel of a neuron, which conveys information towards other cells. In terms of a neuronal control loop, neurons can be generally classified into three groups. As the first category, *sensory neurons* collect information from the environment, e.g. light, sound or pressure. As the second category, *motor neurons* directly innervate effector cells, such as muscles or glands, thereby eliciting a direct action upon the environment. The third category in this classification scheme is the *interneuron*. These neurons for the interconnections between all classes of neurons.

Synaptic Connections Information can be passed from neuron to neuron in mainly two ways. The most common way is via *chemical synapses*, in which the *presynaptic* cell in its axon terminal releases chemical *neurotransmitter* molecules that bind to receptors in the membrane of the *postsynaptic* cell. This in turn triggers a direct potential change or release of further chemical messengers in the postsynaptic cell. The second way of transmitting

information between neurons is via *electrical synapses* using *gap junctions*. These electrical coupling sites enable fast and bi-directional signaling.

Electrophysiology The study of electrical properties of biological tissue is called *electrophysiology*. There are basically three approaches to study the electrical signals of a neuron. The first technique is *intracellular recording* and involves direct measurement of voltages and currents across the membrane of a cell. Therefore, using a sharp glass micropipette electrode the cell is punctured and its membrane potential is measured. This voltage is then compared to a reference wire electrode measuring the potential of the extracellular fluid around the cell. The second technique is called *extracellular recording* and involves an electrode that records the activity of a neuron directly adjacent to its tip or the field potentials generated by a group of cells. A third and relatively new technique is called *patch-clamp recording*. With a glass micropipette a small patch of the membrane is sucked in, effectively pressing the electrode to the surface of the cell. This creates a high impedance seal that enables recording of currents flowing solely across the small patch of membrane and, concurrently, largely eliminates outside noise influences.

Green Fluorescent Protein The *green fluorescent protein* (GFP) is a protein that exhibits green fluorescence when excited by blue to ultraviolet light. It was discovered in the 1960ies in the jellyfish *Aequorea victoria* [43] and has recently begun to play a major role in molecular biology. Its fluorescent properties make it a prime tool as a biological marker. By e.g. expressing it in specific cells or cell populations these can be made visible and stand out against their surroundings when applying light of the appropriate excitatory wavelengths.

Genetically Encoded Calcium Indicators During neuronal activity, calcium (Ca^{2+}) concentrations change abruptly within a neuron. This in turn enables calcium fluctuations to be used as a measure of neuronal activity. In order to measure these fluctuations *calcium indicators* can be used. They fall into two categories, *synthetic reporters* and *genetically encoded calcium indicators* (GECIs). Synthetic reporters are dyes that can be delivered via electrodes into the cell, where they fluorescently color the cell upon specific Ca^{2+} changes. Here, the intensity of the fluorescence depends on both the concentration of Ca^{2+} and of the indicator present in the cell. An advantage of GECIs, on the other hand, is that they can be genetically targeted to specific cells or cell populations. Thus, they are expressed by these same cells, thereby eliminating the need for invasive dye delivery. They constitute a further development of GFP molecules and rely on Ca^{2+} ions to modulate their fluorescence levels. A particular sub-group of GECIs are based on *fluorescence resonance energy transfer* (FRET) [44]. This basic operational principle relies on a conformational change between two chromophores upon variations of Ca^{2+} concentrations to alter the ratio of absorbed and emitted wavelengths of light. By calculating this ratio very precise measurements of Ca^{2+} dynamics are possible irrespective of indicator concentrations.

Microscopy In microscopy there exists a manifold of different imaging techniques. The most classic of examples is *optical microscopy*, which uses light at visible wavelengths guided through a system of lenses in order to magnify the image of tissue samples. However, in this work two special types of fluorescence microscopes are also used. *Confocal*

microscopy is used for obtaining serial image stacks at high resolution. This technique detects fluorescence in a sample only in a small region close to the focal plane by tightly focusing the light source using point illumination. The resulting fluorescence then passes through a pin-hole, thereby enabling the recording of light from a precise location within the tissue. As a drawback of the pin-hole light intensities reaching the imaging device are rather dim, therefore requiring long exposure times for imaging. However, with this spatially precise technique it is possible to generate well-aligned three-dimensional (3D) image stacks in high quality. Another technique used in this work is *two-photon laser scanning microscopy* (2PLSM) [45]. It takes advantage of the effect of *two-photon absorption*, in which two low-energy photons are sufficient to excite a molecule into releasing a higher energy photon in one quantum event. In order to achieve the rare event of two photons simultaneously reaching the molecule in question, pulsed lasers yielding a high energy flux are employed for focusing a photon beam onto the sample through a lens system. The emitted high-energy photons are then detected using *photomultiplier tubes* (PMTs). This technique allows imaging from precise locations at high tissue depths, while presenting higher light detection efficiencies and less tissue damage than confocal microscopes.

GAL4/UAS System In *Drosophila* genetics a classic tool for controlled gene expression is called the *GAL4/UAS system*. Being proposed in 1993 [46] it is a genetic technique functionally separating *what* is expressed in cells from *where* it is expressed. Therefore, the system consists of two parts: the yeast protein *GAL4* and the *Upstream Activation Sequence* (UAS) enhancer. GAL4 specifically binds to UAS in order to start gene expression. GAL4 has no significant effect on cells as long as UAS is absent and *vice versa*. A wide variety of fly lines has been created with GAL4 being expressed only in very specific neurons or populations of neurons. On the other hand fly lines have been created in which all cells have reporter genes attached to the UAS region, such as e.g. for GFP. Thus, when one fly line expressing GAL4 is crossed with a fly line that has the information for GFP next to its UAS region, the offspring will express GFP only in the specific cells where GAL4 is present, making only these cells fluorescent and easily detectable.

Further information on biological concepts and techniques can be found in reference literature such as [47].

2.4 Visual Stimulation

When investigating the visual system of animals one of the most crucial experimental aspects is controlling the visual stimulus in a precise and repeatable way, i.e. controlling exactly *what* the animal sees exactly *when*. Depending on the desired experiments and the animal under examination the requirements for the visual stimulation device vary widely. Thus, stimuli can range from simple light on / light off conditions to showing complicated flight scenes at high spatial and temporal resolutions over large fields of view. Although there have been many different designs using a wide range of techniques from mechanically moving parts to intricate optic-fiber based approaches, the current state of the art designs mostly involve LEDs for visual stimulation. This is mainly due to the LED's exceedingly fast switching rates and high luminous intensities. Therefore a brief review of LED-based designs is outlined in this section.

LED Designs

There have been several LED based designs of visual stimulus devices due to their amenable characteristics. In [48] a visual stimulus apparatus is described that consists of 720 LEDs arranged in a cylindrical fashion around the preparation. It is able to display moving vertical stripes of 30°, yet frame rates, refresh rates or other details of its capabilities are not given.

In [49] a system is presented consisting of 180×32 LEDs in a cylindrically shaped arena. It features a maximum luminance of $60\,\mathrm{cd\,m^{-2}}$, an optical resolution of $2^\circ \times 2^\circ$ and a frame rate stated to be 1000 fps. This system however is described as tailored specifically to closed loop experiments while displaying rotating landscapes and objects. Therefore, displaying arbitrary stimulus sequences not corresponding to moving visual scenarios seems to be out of the scope of this system.

The visual stimulus device presented in [50] differs from the two previously mentioned approaches as it resembles a spherical arena. This is achieved using 14 out of 20 triangles of an icosahedron with an inscribed sphere of 22.4 cm radius. Its resolution is about 2.3° and it operates at frame rates up to 175 Hz at 8 intensity levels.

A more recent description of an LED based stimulus device is given in [51]. Here, a modular system is presented that allows individual 8×8 LED dot matrix display panels to be interconnected in arbitrary geometrical configurations. Thus, depending on the configuration and settings, either high refresh rates or a good optical resolution could be achieved [52]. Nevertheless, both are not possible at the same time. When prototypes of this system were built exploratively as part of the present study, several major shortcomings were found. Among these were low frame rates, large size, frequent instabilities, etc. However, due to its potential and open source nature this system is further detailed in the following.

Modular LED Arena Design

The focus of the arena design described in [51] is mainly on modularity, versatility and ease of use. Its envisaged primary application is behavioral studies. As depicted in Fig. 2.5a it consists of three main parts:

$$\boxed{\text{Control PC}} \longrightarrow \boxed{\text{Display Controller}} \longrightarrow \boxed{\text{Individual LED Panels}}$$

The control PC is connected to the display controller via a serial interface for direct control of pattern start, stop, velocities, etc. Actual patterns are generated using MATLAB (MathWorks Inc.) and transferred onto a CompactFlash (CF) card, which in turn is inserted into the display controller. This display controller is housed on a Printed Circuit board (PCB) containing two microcontroller units (MCUs). The flash MCU is dedicated to reading out the patterns from the CF card and transmitting them towards the main MCU. The main MCU takes this pattern information and sends it via an Inter-Integrated Circuit (I^2C) bus, also called Two Wire Interface (TWI) as seen in Fig. 2.5, towards the individual panel controllers. On each panel controller a dedicated MCU receives this pattern data and refreshes an 8×8 LED dot matrix display accordingly.

The individual panel controllers are connected via I^2C directly to the display controller board and are powered either directly by this board or by an external power supply. Each panel controller features a 3.2 mm × 3.2 mm LED dot matrix display harboring 8×8

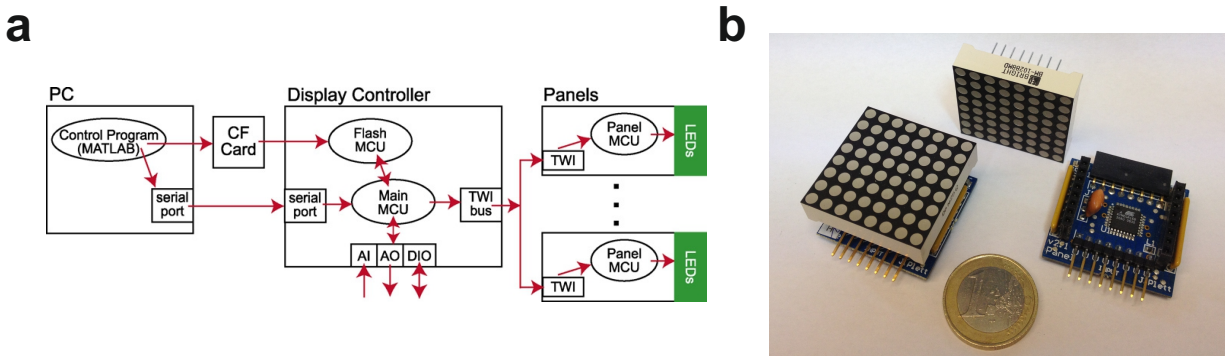

Figure 2.5: (**a**) Principal components of the modular arena design [52]. (**b**) Panel controller boards similar to the design presented in [51], including $3.2\,\mathrm{cm} \times 3.2\,\mathrm{cm}$ 8×8 LED dot matrix display, next to a €1 coin for size comparison.

green LEDs (BM-10288MD, American Bright Optoelectronics Corp.) and an ATmega8 MCU (Atmel Corp.) similar to Fig. 2.5b. Communication with external devices, such as digital to analog (D/A) or analog to digital (A/D) converters is accomplished using the analog input (AI), analog output (AO) and digital input/output (DIO) ports of the display controller.

In order to make the system modular the individual panel controllers possess 8-pin connectors making them stackable in a column-wise fashion. In terms of temporal control, the system possesses two distinct rates, one being the refresh rate of a frame and the other the actual frame rate. The rate at which an individual frame is refreshed, i.e. the internal refresh rate of each panel controller is fixed at 372 Hz for an eight-level greenscale pattern, which coincidentally is the maximum number of intensity levels attainable [52]. The actual frame rate, i.e. how many different frames can be shown per time interval, depends on the total number of panels used. For an arena consisting of 11 individually addressable 8×8 panels the frame rate is approximately 68 fps [52]. Nevertheless, even if signal transmission degradation and associated dropped frames were duly being taken care of, up-scaling of the system would linearly reduce the effective frame rate. Thus, an increase to 120 individually addressable panels would yield a maximum frame rate of only around 6.2 fps.

Despite its drawbacks such as its relatively low frame rates for large fields of view this LED arena design represents the current state of the art in visual stimulus devices. This is mainly due to its modularity, ease of use and open source nature.

2.5 Fly-Inspired Sensor Implementations

Due to its many beneficial features the fly visual system has been a source of inspiration for several works proposing direct technical implementations of its computational aspects.

In [53] a fly-inspired sensing scheme is applied to the course control of a blimp. Additionally, this EMD-based scheme also doubles as a type of visual odometer. Images are acquired at a constant 10 fps and sent to an off-board computing platform, where 90×30 EMD estimates are computed and used for course control of the aerial vehicle. Albeit only operating at low frame rates, this system proved sufficient for controlling a stable and slow vehicle such as a blimp.

Similar results are achieved in [54], where a blimp is controlled using EMD estimates computed off-board and converted to control signals to be sent back to the aircraft. Additionally, the system is augmented to also include biologically inspired collision avoidance based on a model of the *Lobula Giant Movement Detector* neuron found in the locust.

The work presented in [55] describes autonomous indoor flight of a quadrocopter achieved by using a wide-field implementation scheme similar to fly LPTCs, albeit based on local motion estimates computed using conventional gradient based methods.

In [56] a helicopter testbed is proposed for off-board computation and testing of EMD-based control strategies. A camera is used capable of capturing images at 60 fps while being tethered via an IEEE 1394 cable to an image capturing PC, thus limiting the application radius of this setup.

An EMD-inspired sensor capable of one-dimensional optic flow estimates is presented in [57]. This design consists of a single EMD with two inputs from photodiodes. Two computation architectures are compared, one consisting of a Field Programmable Analog Array (FPAA) and one using a microcontroller unit (MCU). The MCU-based implementation is found to yield promising results while being smaller and lighter than the FPAA solution.

A one-dimensional sensor array comprised of 37 EMDs is presented in [58]. The sensor is built upon a custom aVLSI implementation using 1.3 µm CMOS technology. The output of this implementation yields responses similar to an HS cell and features adjustable time constants. Using this system on-board a robot optomotor response and fixation similar to flies could be achieved.

Using both digital and analog circuitry a VLSI implementation of a visual ego-motion detector is presented in [59]. Motion is estimated using 4 EMD arrays oriented at 0°, 90°, 180° and 270°, respectively. Using several corresponding global motion templates ego-motion is roughly estimated. Promising results were achieved for particular types of pure motion, but not combinations of them.

The work presented in [60] features a Field Programmable Gate Array (FPGA) for implementing a testbed for EMD parameter optimization. Using the advantages of re-programmable FPGAs this testbed system is capable of computing estimates at 29 fps and a spatial resolution of 88×88. However, results are stored on an on-board memory, thus forfeiting real-time output and its use as a sensor for control.

Another EMD implementation using an FPGA is described in [61]. Here, a linear array of 245 EMDs is implemented on an FPGA evaluation board. Its envisaged primary application is linear terrain following.

A more versatile sensor also using an FPGA is put forth in [62]. At a spatial resolution of 127×100 at typically 100 fps in laboratory conditions this system is capable of computing reasonable global motion estimates while using high-contrast artificial stimuli. With more naturalistic stimuli, however, no conclusive estimates were possible.

In [63] a superior FPGA-based implementation is presented, which is capable of 256×256 EMD estimates at 350 fps. However, a major drawback of this sensor is its size and power requirements since it is implemented on a PCI-FPGA card within a host computer, while using an external high-speed camera connected via Camera Link. Albeit providing superior performance in comparison to prior sensor implementations it forfeits use on-board small aerial vehicles and real-world control situations.

2.6 Summary

In the past century the visual system of the fly has been studied in remarkable detail. Much information about its structure and connectivity has been gathered using anatomical microscopy and histological studies. Most knowledge about its function and behavioral properties has thus far been obtained by behavioral assays and electrophysiological recordings. However, many open questions still remain due to the inaccessibility of certain essential neuronal structures to conventional electrophysiology and the lack of appropriate visual stimulation devices.

In many past studies the fly visual system has also been revealed to exhibit numerous advantages over conventional technical approaches of motion detection. To date, there have been several attempts at implementing the basic algorithmic features of the fly visual system into a technical sensor application as to draw from said advantages of this biological sensing scheme. Barring some noteworthy exceptions, most of these advances have been made by using small linear arrays of input elements and subsequent processing according to the elementary motion detector model of insect vision. However, almost all these studies present certain drawbacks for deployment in autonomous control of aerial systems. As such, none have so far simultaneously achieved the temporal *and* spatial resolution of the fly visual system as well as small size and low weight for deployment on-board small aerial platforms. Moreover, these works consider only the sensory aspect of the fly motion vision system. Its performance as part of a closed loop sensorimotor system has received little attention.

Therefore, in this thesis a novel stimulation device is presented, which together with novel recording approaches enables stimulation and electrophysiological recordings of previously inaccessible neurons, thereby gaining significant insight into how flies perceive and process visual motion cues. Also, a custom high performance and small size implementation of a novel fly-inspired rotation sensor scheme is presented. Moreover, in the present work a comparative assessment of the principles underlying fly motion vision is conducted in analytical studies and numerical simulations in closed loop. Subsequently, these findings are validated in experimental trials using the newly developed sensor implementation.

The contributions of the presented work advance the state of the art in functional neurobiology, computational neurobiology, vision-based control and visual guidance of aerial robots.

3 Aspects of Insect Motion Vision

In neurobiology, a large and fruitful field of research is the study of how animals, including humans, perceive and process motion. A great wealth of insight has been gained in the last century by analyzing the visual system of insects and inferring its properties from specific experiments. Thus, in the middle of the 20th century much progress in this area has been made as the basic principle of operation of insect motion detection was proposed [1]. This Hassenstein-Reichardt model (HRM) continues to be the accepted explanation of how insects—and probably many other animals, too—perceive motion. At the same time, despite intense research, it has not yet been possible to completely elucidate whether this model truly underlies fly motion vision and which neuronal elements constitute it.

For answering many open questions of how these particular neuronal systems work, the key elements are manifold. However, amongst these the correct visual stimulus preparation is of utmost import. Only when being able to stimulate the *right* sensory organs at the *right* time with the *right* stimuli one can reliably infer properties of a system as complex as the visual system of animals. Yet, for investigating many aspects of insect motion vision there is a clear lack of adequate visual stimulation devices and techniques.

In this chapter three key aspects of fly motion vision are addressed by proposing an advanced visual stimulus device together with new preparation and stimulation techniques, which together enable investigation of aspects of the visual system previously not accessible and enriching the toolkit for analyzing it. A light emitting diode (LED) based visual stimulation system is devised and implemented. With this apparatus three key questions are addressed. The first question is whether the vast collection of knowledge on the blowfly visual system and especially its vertical system (VS) cell network is substantially preserved across dipteran fly species. The second question addressed here is to what extent the fly visual system processes light increments and decrements in separate pathways. The last question analyzed here is what possible role and function the descending neurons of the visual system towards the neck-motorneurons of the fly may have.

The remainder of this chapter is organized as follows: The proposed stimulus device and its properties are described in Section 3.1. In section 3.2 the response properties of the *Drosophila* VS cell network are analyzed. The separation into light increment and light decrement channels and its associated half-wave rectification are investigated in Section 3.3. Two specific descending neurons of the fly visual system and their role in the visual information processing pathway are described in Section 3.4. Finally, some concluding remarks towards the role of the fly VS cell network and possible technical applications are given in Section 3.5.

3.1 Visual Stimulation

Dating back as far as the late 19th century and earlier [7,8] insect vision has been a fruitful and intense field of research. A great wealth of studies employ direct visual stimulation in order to infer properties of these systems. For generating those stimuli there has been a multitude of different approaches and mechanisms, ranging from simple light on – light off conditions using incandescent light bulbs (e.g. [1,12,64]) to sophisticated virtual arenas using light emitting diode (LED) matrices or PC screens (e.g. [49–51]).

All these approaches have their advantages and disadvantages, whether that be cost, size, temporal resolution, optical resolution, ease of use, etc. When working with very fast vision systems as the fly's it is imperative to use stimulus devices with high temporal resolution. Therefore, display technologies such as cathode ray tubes (CRT), conventional liquid crystal displays (LCD), plasma screens or electrophoretic ink (E ink) are not suited for visual stimulation of insects due to their frame rates being inherently lower than flicker fusion rates of insect visual systems [65].

For the design of a stimulus device custom built to be used in conjunction with electrophysiological recordings of the fly visual system the two obvious choices are new LCD PC monitors or LED displays. LCD PC monitors nowadays offer the advantage of operating at refresh rates up to 120 Hz while offering exceptionally high optical resolution. As a benefit they are relatively easily controlled using PC based graphics cards and drivers. Nevertheless, as of yet they still have the fundamental shortcoming of being large and rigid, thus making it impossible to be bent into the arena-like shapes as required for most behavioral or electrophysiology setups. Moreover, a refresh rate of 120 Hz is still beneath flicker fusion frequency of the fly visual system.

Using LED displays on the other hand offers temporal resolutions many times better than PC monitors or commercial television sets. They do bear the disadvantage, though, of making it difficult to obtain large spatial resolutions. This, however, is usually not of great import when analyzing the visual system of flies since these generally possess poor optical resolutions themselves. Additionally, LED based approaches are substantially easier to arrange in an arena shaped fashion that is required for the envisioned type of use. Due to all these reasons an LED based approach is chosen for this work as the most promising solution.

As outlined in Section 2.4 there are numerous designs of visual stimulation devices. However, none of those are suitable for the stringent requirements of the electropysiological recordings needed to elucidate the Reichardt Detector at cellular level. The most promising design was put forth by Reiser and colleagues [51] (see also Section 2.4). This system was designed bearing in mind behavioral studies and focuses mainly on modularity, versatility and ease of use. Albeit not complying with i.e. temporal resolution requirements by several orders of magnitude along with several other major shortcomings, its open source nature makes it a good starting point for a stimulus device design. Nevertheless, for use in electrophysiology of the fly visual system it therefore needs to be completely re-designed and -engineered.

The steps involved and the final outcome of this redesign is outlined in the following sections.

3.1.1 Performance Requirements

The primary application environments for the visual stimulation device described here are electrophysiological and behavioral studies in the fruitfly *Drosophila melanogaster*. Since during electrophysiological recording all neuronal activity is measured at cellular level with high precision, even small artifacts at stimulation time tend to introduce large and usually non-linear unwanted effects at recording time. Therefore, measures have to be taken to ensure stimulus integrity. Among the numerous requirements to be met figure the following:

- Flicker fusion frequency of diptera lies in the range between 300 Hz to 500 Hz [66,67]. In order not to introduce any flicker artifacts the flicker frequency of the visual stimulation device should be raised above 500 Hz.
- Hence, in order not to introduce any artifacts due to frame changes the frame rates also have to be above 500 fps.
- Spatial resolution of *Drosophila melanogaster* amounts to inter-ommatidial angles of $\Delta\varphi = 5°$ [68]. As to rule out aliasing effects the spatial resolution of the visual stimulation arena therefore ought to be better than 2.5°.
- Since motion is approximated by apparent motion stimuli for smooth transitions there need to be least 16 distinct intensity levels.
- An ideal configuration for the stimulus arena would be a spherical one. To avoid spherical tessellation problems, however, a cylindrical shape is preferable. Hence, the stimulation device is to be designed in cylindrical shape.
- The compound eye of diptera extends about 190° in the horizontal and 198° in the vertical plane [11]. However, the spatial acuity of flies is highest in the frontal hemisphere. Therefore the stimulation device needs coverage of about 180° of frontal azimuth. To keep its size reasonable despite its cylindrical setup while at the same time maintaining a substantial part of the fly's visual field the stimulation arena is required to cover about 90° of frontal elevation.
- Existing setup tables are spatially restrictive due to microscope mountings or holes for incorporating stimulation and recording gear. Therefore the visual stimulation system has to comply with these space restrictions
- As the envisaged primary application scenario is electrophysiological recordings a critical aspect is electromagnetic interference (EMI). In order to minimize artifacts at recording time electromagnetic emissions from the stimulation device have to be significantly beneath recording thresholds.
- Other, equally important requirements include the need for precise timing between frames, ease of use, safety of operation, etc.

In order to devise a system that simultaneously complies with all these criteria a new approach to stimulus design has to be taken. The design approaches and resulting system are outlined in the following.

3.1.2 Design Approach

System Overview

The stimulus presentation system is split into five separate subsystems, each taking care of different aspects and, thus, partitioning tasks between each other. These five subsystems are itemized as follows in sequential processing chain order:

- Control PC
- Main Controller
- Power and Data Distribution System
- Panel Controllers
- Dot Matrix Displays

On the control PC stimuli are generated and stored on a CompactFlash (CF) card for later transfer towards the main controller board. During experiments the PC control software suite takes care of which stimulation sequences are to be shown when and at what frame rate, as well as recording and storing of electrophysiology data. It is connected via an RS232 serial connection to the main controller board. This board features two MCUs: a CF controller and a main controller. The former takes care of reading in pattern data from the CF card and purveying it to the latter. This main controller then takes care of general timing issues and sends this pattern data via a power and data distribution board using an I^2C bus towards the individual panel controllers. Each panel controller receives its individual pattern data and stores it on an on-board flash memory. During experiments they receive general call commands over the I^2C bus that indicate which frame of which pattern is to be shown. These outputs are then transferred directly via parallel ribbon cables towards the individual LED dot matrix displays with very precise timing. A connection schematic of the system is given in Figure 3.1. Here, the control PC components are shown in orange colors, dedicated printed circuit boards in light blue, individual MCUs in dark blue, interface logic in violet, power distribution in red and LED dot matrix displays in green.

The approach taken in order to fulfill all requirements outlined in Section 4.3.1 is presented in the following.

Spatial Extent and Resolution

The targeted visual extent of the cylindrical LED arena is roughly 180° in azimuth and 90° in elevation as viewed from its center. At the same time the angular resolution is required to be better than 2.5°. As the system is built around the I^2C bus which can handle up to 127 individual addresses, this would be the theoretical maximum number of individual displays, effectively limiting spatial extent and resolution. The chosen configuration therefore is a half-cylindrical arrangement of 8×15 dot matrix displays of 8×8 individual green LEDs each, yielding a total of 7680 LEDs. For incorporating this stimulus arena into existing electrophysiology setups and fitting them at acceptable heights under the microscope new 20 mm footprint dot matrix displays need to be used. The display of choice is a TA08-81GWA (Kingbright Corp., Taipei, Taiwan) 20 mm green common anode dot matrix display with dominant wavelength $\lambda_D = 568\,\text{nm}$ and spectral half-width $\Delta\lambda_{1/2} = 30\,\text{nm}$.

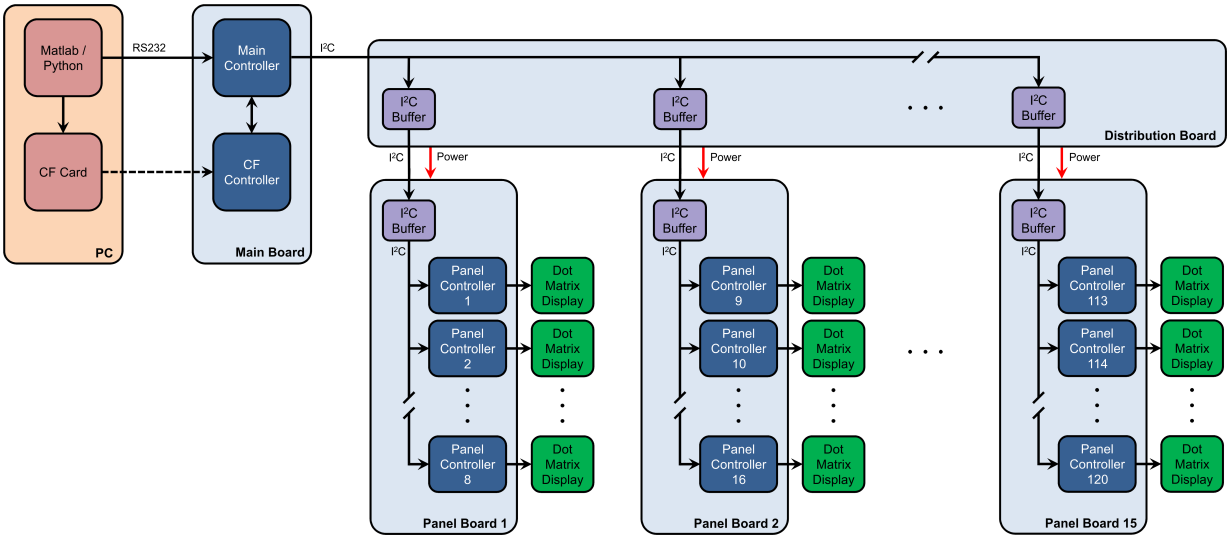

Figure 3.1: Schematic overview of the stimulus device design.

While successfully reducing overall height to 160 mm such small panels forfeit use of the original modular design due to lack of PCB real estate for components and routing. Therefore, modularity was reduced from individual displays with 8×8 LEDs to columns of 8 displays and, thus, $8 \times 8 \times 8$ LEDs per elementary display unit. New panel controller boards had to be designed in order to drive these smaller displays. The connection between each panel controller board and its associated display column is now established via two 64-pin AWG 26 ribbon cables.

This configuration yields a semi-cylindrical arena of 180° azimuth and 90° elevation with an angular resolution strictly equal or better than 1.5°. This fulfills the design requirements in full and even surpasses them.

Temporal Resolution

For electrophysiological recordings from interneurons of the fly visual system frame rate and especially flicker frequency of the stimulation device need to be strictly above flicker fusion frequency of the biological visual system in question. For flies these limits lie in the range of 300 Hz to 500 Hz [66, 67]. Therefore flicker frequency of the system needs to be elevated above these levels, including a safety margin as to not introduce any artifacts into neuronal recordings.

In order to raise the frame rate by roughly two orders of magnitude from the original 6.2 fps of the initial design several measures have to be taken. As a first step the overall processing speed is increased by using MCUs capable of operational frequencies of 20 MHz as opposed to the original 16 MHz. Secondly, the main and panel controller firmware was rewritten bearing processing speed in mind, thus, thoroughly optimizing overall performance and reliability.

The largest impact on performance, however, was brought upon by a paradigm shift in data transmission and handling. Analysis of the initial system revealed the data transmission to be by far the largest bottleneck for frame rate performance. The original design implied sending all packet data to be shown to each panel controller during ongoing stim-

ulation. This is the decisively limiting factor, since between these kinds of MCUs the I²C bus is capable of transfer rates of maximally 400 kbit s^{-1}.

To this end the *general call* broadcast capability of the I²C bus is taken advantage of. Now, prior to the experiment all image data is sent to the panel controllers and stored locally on-board AT45DB321D 32 Mbit 2.7 V serial flash memories (Atmel Corp., San Jose, USA) connected via Serial Peripheral Interface (SPI) bus. This way each panel controller already holds all display data it needs at stimulation time. During experiments the main controller then only broadcasts *general calls* to all panel controllers, indicating exact frame number and pattern number to be shown presently. Each panel controller then fetches said frame from its attached flash memory and displays it on the connected dot matrix display. Hence, during experiments this results in a transmission data reduction and associated increase in attainable frame rates of several orders of magnitude.

All this code streamlining, optimization, component improvements and preloading of stimulus data onto on-board memory yields system flicker rates of 600 Hz and achievable frame rates of 600 fps, thus fulfilling and surpassing design requirements.

Intensity Resolution

An LED stimulus device is by definition not capable of displaying true motion but rather employs apparent motion. Thus, individual LEDs do not move in time but are sequentially lit or turned off suggesting motion to the beholder. In order to mask this apparent motion nature of the stimulus device several resolution aspects need to be taken care of. The first two critical aspects, namely spatial and temporal resolution have been addressed in the two preceding sections. However, apart from these two a third critical aspect is intensity resolution. The more different shades of green can be shown the closer the resemblance between true and apparent motion becomes. Smoothly moving edges are a classical example of this effect. To improve this the 3 bit greenscale value encoding of the initial design that leads to a maximum of 8 different intensity levels was raised to 4 bit pixel value encoding at full frequency and frame rate. This effectively doubles the attainable intensity levels to 16 linearly increasing steps, thus fully complying with design restrictions.

Bus Reliability and Power Buffering

A sizable drawback of the I²C bus is its susceptibility to high bus capacitance that effectively limits both bus length and maximum node number. The bus topography of this system is comprised of 121 nodes, with the main controller acting as bus master and the 120 individual panel controllers constituting slaves. This number of devices and the implied length between them surpasses the maximum tolerable bus capacitance of 400 pF by a margin. Since for this system high throughput is paramount the simple solution of lowering bus frequency is not a viable option.

The solution chosen here is the use of LTC4303 bidirectional I²C bus buffers (Linear Technology Corp., Milpitas, USA). These devices have the benefit of not only buffering clock and data lines, but also featuring a *stuck bus recovery* system. In case the bus gets stuck low for more than 30 ms this IC automatically breaks the data and clock bus connection, while generating up to 16 clock pulses on the output clock line attempting to free the bus. This solution vastly increases fanout and, thus, enables the use of as many

as 121 spatially highly scattered nodes. It has also been found to fundamentally improve bus reliability.

Another aspect not properly addressed in the original design is the lack of a current source for driving the LED dot matrix displays. Although sinking current through ULN2804A Darlington arrays (Toshiba Corp., Tokyo, Japan) the panel MCUs are left to directly source current for the displays. This forces the MCUs to operate at their absolute performance limit, which causes sizeable excess heat generation, high thermal stress and increased failure rate. In order to overcome this problem 74HCT241 high-speed tri-state Si-gate CMOS octal buffers (NXP Semiconductors, Eindhoven, Netherlands) are used for current sourcing. These line drivers effectively reduce excess heat generation in the MCUs and aid in overall stability and reliability.

3.1.3 System Modules

As outlined in Section 3.1.2 the whole visual stimulation system is comprised of five subsystems. In this section a brief summary and description of each one is given.

PC Control System

The control software suite serves two basic purposes. On one hand it allows for pattern generation and storage on the CF card, while on the other hand it serves as an operator control station during experiments. Two largely identical versions of the software suite were written, one in MATLAB (MathWorks Inc., USA) for use on Windows-based (Microsoft, Redmond, USA) PCs and one in Python for use on Unix-based machines.

A single stimulus pattern consists of a sequence of still frames the size of the arena, i.e. 120×64 pixels. For obtaining 16 greenscale levels these frames feature 4 bit intensity encoding for each pixel. After conversion to a one-dimensional (1D) array the patterns of choice are written to a CF card along with an information header pertaining number, size, storage address, etc. of these patterns. A FAT16 system was implemented on the CF card controller MCU and the CF card itself for rapid and standardized transfer and retrieval of pattern data.

During visual stimulation time the PC software controls what patterns are to be shown when and at what frame rates, as well as other runtime parameters. These commands are sent via a serial RS232 interface towards the main controller board. For this purpose there exist both a graphical user interface (GUI) and a scripting interface. Whereas the GUI is used mainly for manual testing and debugging purposes the scripting interface is used during experiments for timing reasons and synchronous electrophysiology data acquisition using a PCI-DAS6025 data acquisition board (Measurement Computing Corp., Norton, USA).

Main Controller Board

The main controller board handles the tasks of sending frame data to individual panels, timekeeping, issuing frame updates as well as executing commands sent from the PC. Once the pattern data is written to a CF card on the PC side, this CF card is inserted into the main controller board. Using its dedicated ATmega128 (Atmel Corp., San Jose, USA) MCU acting as a CF card controller this data is read in and sent towards the main

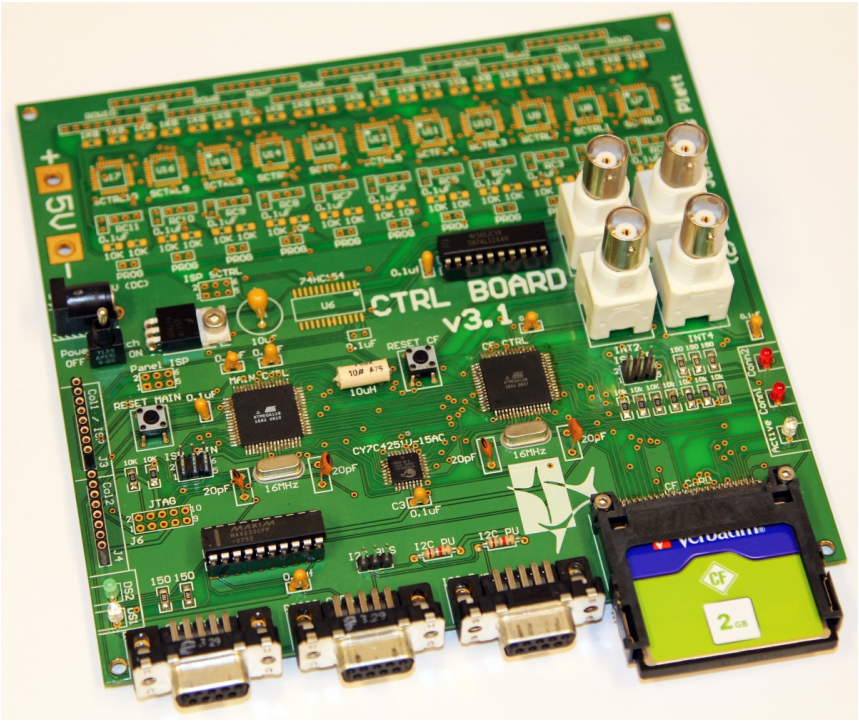

Figure 3.2: Main Controller Board

ATmega128 MCU via a synchronous CY7C4251V First In First Out (FIFO) memory (Cypress Semiconductor Corp., San Jose, USA). Previous to the experiment this main MCU sends all pattern data towards the individual panel controllers for local data storage.

During experiments the board receives commands from the control PC via its serial RS232 interface. With these commands the pattern number, the initial frame number within that pattern, the direction, the frame rate, etc. are set. Once a *start* command is issued the main controller sends an I^2C *general call* broadcast to all panels, indicating pattern number and frame number to be shown. A precise internal timer keeps track of the elapsed time as to when a new frame is due. Once the time pre-set in accordance to the desired frame rate has elapsed a new *frame update* command is sent on the I^2C bus. This way very precise frame rate timing can be achieved.

At the same time the first *update frame* command is sent on the I^2C bus, i.e. when the pattern starts, a TTL-compatible signal is set *high* on a BNC type output port for data acquisition. Accordingly, simultaneously with a *stop* command, i.e. when the pattern stops, this output signal is set to *low*. This *high*/*low* signal indicating stimulus *on*/*off* is useful in later data analysis for precise timing with electrophysiological response signals. This exact timing is only feasible due to the high timing precision of the main MCU, which is far superior to the timing accuracy of non-real-time Windows and Linux operating systems used here.

A second output port for timing aspects was implemented for frame changes. Each time a new frame command is issued towards the individual panel controllers, a TTL-compliant output signal is toggled. Thus, the edges of this signal can be used for precise frame timing during off-line data analysis. Figure 3.2 illustrates the main controller board with its two MCUs, FIFO, interface logic and CF card slot.

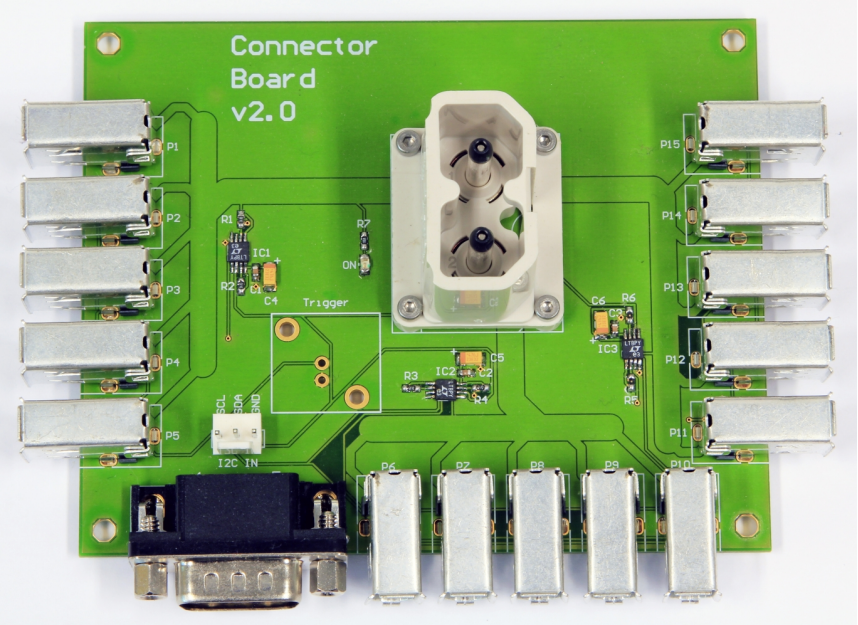

Figure 3.3: Power and Distribution Board

Power and Data Distribution Board

Performance of the I^2C bus is greatly influenced by bus capacitance. The limit for proper operation is 400 µF, since over this limit the rise- and fall times of the system would be too long to achieve 400 kHz *Fast Mode* performance without data corruption. Since the envisioned 120 individual LED dot matrix panel controllers and their added bus lengths would be substantially over this limit, a solution is found by incorporating bidirectional I^2C bus buffers. Therefore, the power and distribution board receives direct I^2C input from the main board and conveys it over LTC4303 I^2C buffers (Linear Technology Corp., Milpitas, USA) towards the panel controller boards. The distribution board features a total of three such buffers, each handling communications to and from 5 panel controller boards and, thus, a total of 40 individual panels, i.e. a third of the whole arena.

Power consumption of the LED dot matrix displays can sum up to considerable levels due to the large number of LEDs comprising the stimulus arena. Per panel controller board maximum consumption is found to lie in the range of 1 A to 1.5 A. Hence, in order to increase mechanical and electrical stability the distribution board and the panel controller boards are interconnected via mechanically rugged FireWire cables and connectors. This provides data and power integrity, as well as reverse polarity protection and ruggedness. For proper current sourcing a ES150-5 power supply (Deutronic Electronik GmbH, Adlkofen, Germany) capable of 5 V output at 30 A is used in conjunction with appropriate connectors and large PCB traces. The resulting distribution board design can be seen in Figure 3.3.

Panel Controller Board

In order to control all 120 LED dot matrix displays the stimulus arena employs 15 panel controller boards. Each of these boards harbors 8 individual panel controllers along with data transmission and power conversion circuitries. Each board features one bidirectional

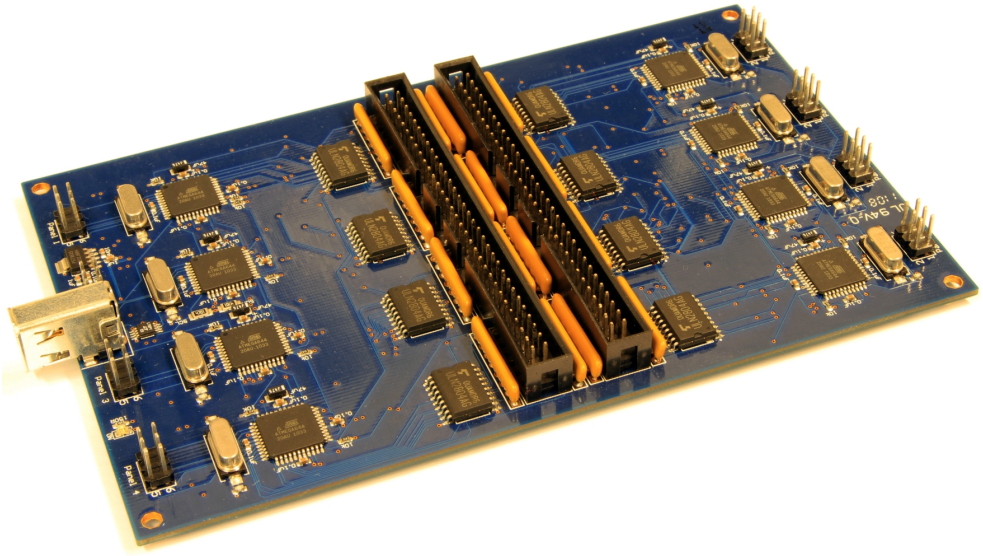

Figure 3.4: Panel controller board design featuring an ATmega664 MCU and AT45DB321 flash memory for each of the 8 individual controllers.

LT4303 I^2C bus buffer (Linear Technology Corp., Milpitas, USA) to filter input to its 8 panel controller circuits. These 8 panel controller circuits consist of an ATmega644 MCU (Atmel, San Jose, USA), a ULN2804A octal Darlington array (Toshiba Corp., Tokyo, Japan), a 74HCT241 high-speed CMOS octal buffer (NXP Semiconductors, Eindhoven, Netherlands) and an AT45DB321D 32 Mbit serial flash memory (Atmel Corp., San Jose, USA), along with glue logic and tantalum filters. For proper operation of all 2.7 V serial flash memories a TPS73633 low dropout linear voltage regulator (Texas Instruments, Dallas, USA) provides the required operational voltage.

Each panel controller is given an individual I^2C address ranging from 1 to 120. Over the I^2C bus it receives its pattern information to be stored on-board its non-volatile serial flash memory. Depending on the amount and size of stimuli this can take up to around 30 min. However, due to the large capacity of the non-volatile flash memories many patterns can be programmed and used should the need arise. Practice and operation for several years has shown that new patterns usually need to be programmed only once or twice per year, thereby rescinding long programming times as a drawback.

During operation, each panel controller fetches the frame from its serial flash memory that is indicated by the *general call* broadcast sent from the main controller board to all panel controllers. This frame is then displayed on the connected 8×8 LED dot matrix. Due to the pulse width modulation (PWM) operational principle of dot matrix displays only one column of LEDs is lit at a time. These displays therefore need to be cyclically refreshed, which translates to a fully lit LED being effectively on for only $1/8^{\text{th}}$ of the time. Furthermore, for achieving 16 greenscale levels, the "full" $1/8^{\text{th}}$ of a complete refresh cycle is further subdivided into 15 basic time-slots. For this reason a complete refresh cycle is comprised of $8 \times 15 = 120$ elementary cycles. Thereby, a fully lit LED is on for 15 elementary cycles and a fully switched-off LED is off for all 120 elementary cycles. A dimly lit LED that is on e.g. for just 3 out of the total 120 elementary cycles corresponds to intensity level 3 on the scale from 0 (minimum) to 15 (maximum).

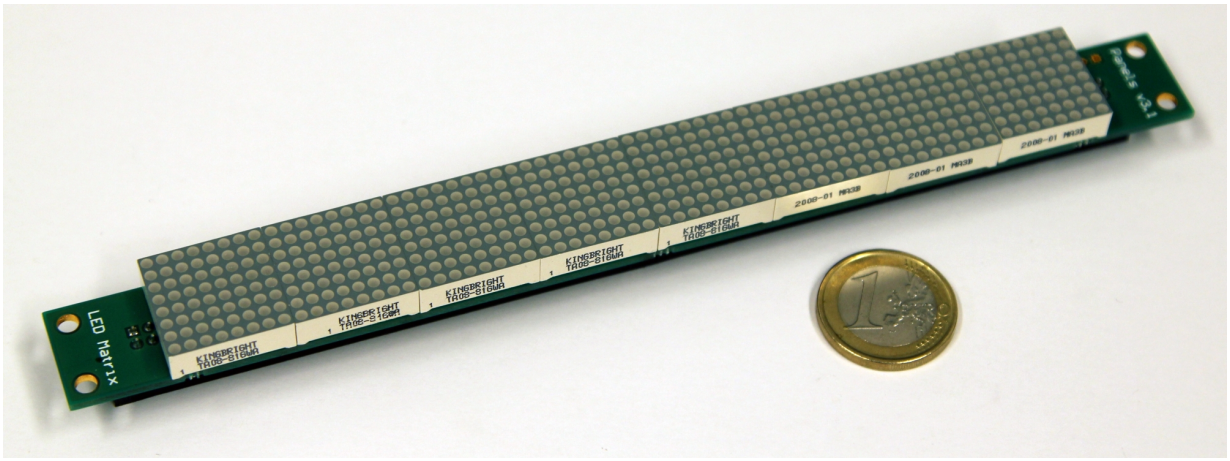

Figure 3.5: LED dot matrix display board featuring $2.0\,\mathrm{cm} \times 2.0\,\mathrm{cm}$ dot matrix displays, next to a €1 coin for size comparison.

By extensive optimization, code streamlining and optimized hardware the complete refresh cycle rate was raised beyond 600 Hz, thereby far surpassing the fly visual system's flicker fusion rate and, thus, preventing flicker artifacts.

Due to the reduction of modularity and concentration of 8 individual panel controllers on one 160 mm×100 mm Eurocard format 4-layer PCB direct mounting of the LED dot matrix displays would not be practical. Therefore, two 64-way AWG 26 ribbon cables connect each of the 15 panel controller boards with their respective LED dot matrix display boards. The two 64-pin connectors used for this can be seen in the middle portion of the panel controller PCB depicted in Figure 3.4. Current is sourced from the 74HCT241 octal buffers on the bottom plane and sent via current limiting resistors over the ribbon cables to the dot matrix displays. The ULN2804A Darlington line drivers are used for current sinking.

LED Dot Matrix Display Board

For displaying the final stimulus patterns green TA08-81GWA 20 mm common anode dot matrix displays are chosen for their small footprint and well suited wave length characteristics, i.e. dominant wavelength $\lambda_D = 568\,\mathrm{nm}$ and spectral half-width $\Delta\lambda_{1/2} = 30\,\mathrm{nm}$. For proper alignment and cylindrical arrangement as a 180° visual stimulus arena all 120 displays are mounted in columns of 8 displays each on dedicated PCBs. These LED dot matrix display boards are connected via 64-way AWG 26 ribbon cables to their respective panel controller boards. As shown in Figure 3.5 the displays face forward, while the two 64-pin connectors are mounted on the back side facing out of the arena. The display boards are held in place using half-ring shaped acrylic glass holders.

In order to fully comply with EMI restrictions for electrophysiological recordings the inner surface of the display arena is covered with a thin grounded wire mesh, which effectively shields electromagnetic influences of the displays on the recording and reference electrodes while not interfering with the fly's visual perception of the arena. Also, the ribbon cables and all cables to and from the recording stage are properly grounded using thick sheets of aluminium foil.

3.1.4 Specialized Versions

In order to cater for different sets of experiments with different requirements in terms of spatial extent or timing parameters several versions of the arena were designed and implemented. In the following these versions are presented and detailed.

Large Field Stimulation

Many neurons in the fly visual system receive input not just from the ipsilateral but also from the contralateral compound eye. Examples of these include i.e. the DNOVS2 cells, which exhibit interesting characteristics. Hence, in order to properly investigate these cells the existing arena with its 180° extent does not suffice for whole field stimulation and analysis of the contralateral input.

The simplest and most obvious solution would be to use the 120 displays in a different spatial configuration, extending over a larger field of view (FOV) in azimuth and in exchange lower the spatial resolution. This, however, is precluded by the fact of this type of experiments being conducted with the blowfly *Calliphora vicina* due to its more amenably sized neurons. In comparison to *Drosophila melanogaster* this fly species possesses a much higher spatial resolution. Further increase of the worst case angular separation of $\Delta\varphi = 1.5°$ between adjacent LEDs could introduce artifacts into recording results due to low spatial resolution. In fact, *Calliphora vicina* possesses an angular resolution $\Delta\varphi$ between 1.07° and 1.28° [69], prompting for a further reduction of angular separation between LEDs of the arena as to not introduce stimulus artifacts when using this fly species for experiments.

In order to overcome this a new arena design is put forth by fusing the components of four of the arenas presented in the previous sections into one large one. While addressing the problem of spatial resolution and extent, this approach also brings along several complications and challenges. One major issue is the total number of resulting I^2C devices. Per bus specification the I^2C bus allows up to 127 individually addressable devices on the bus. In the four arena configuration, however, there are 480 such devices, i.e. 480 panel controllers. In order to solve this problem, apart from the panel addresses also arena addresses are introduced. This way each panel is addressable by both arena and device number. Thus, four devices share a common device address but distinct arena addresses, making them individually addressable.

At pattern programming time, nevertheless, each sub-arena now needs to be individually programmed as to not introduce any I^2C bus problems due to duplicate device addresses, such as corrupted acknowledge (ACK) or negative acknowledge (NACK) signals. At stimulus presentation time, however, this plays no role due to the *general call* nature of I^2C commands used there and, thus, validates the approach taken.

In order to accommodate the four arenas the PC software for pattern creation and programming onto CF card needed to be re-written and adjusted. Also the main controller and panel controller firmware had to be re-written do drive all four sub-arenas as a whole.

The resulting *Calliphora* arena consists of a total of 480 8×8 panels arranged in a 240×128 LED fashion, spanning 240° in equatorial azimuth and 95° in frontal elevation, while operating at the full 600 fps frame rate and 600 Hz refresh frequency. With this approach both critical requirements of this design could be met: Angular extent and spatial resolution. The angular extent of the arena in this configuration covers 240°,

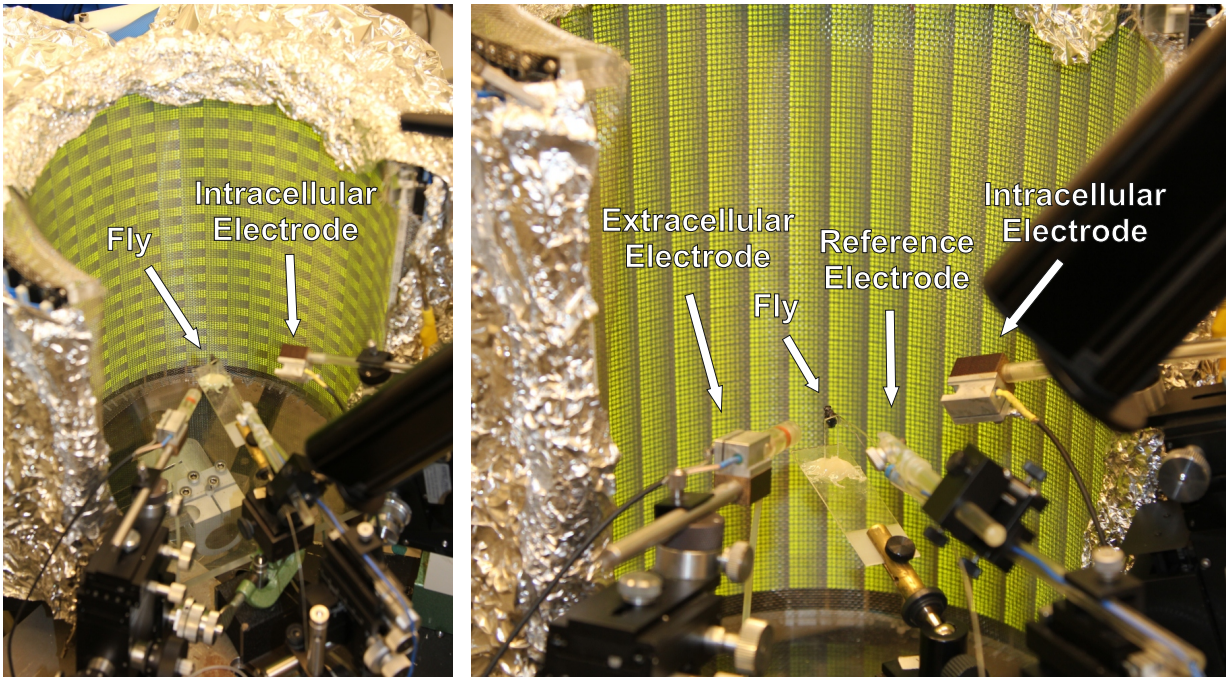

Figure 3.6: Large field visual stimulation arena. In this preparation the fly is looking straight into the center of the arena. For different types of recordings intra- and extracellular electrodes are placed to the right and the left of the fly preparation, respectively. The reference electrode is located dorsally from the fly. Note the grounded aluminium foil electromagnetic shielding around the arena.

hereby enabling stimulation of both ipsilateral and contralateral sides of the neurons being analyzed. While at the same time using 240 LEDs in azimuth, this yields a worst case resolution of $\Delta\varphi = 1.0°$ in azimuth. In elevation this is even better at 128 LEDs over 95° yielding $\Delta\varphi = 0.74°$. In Figure 3.6 frontal views into the resulting large field *Calliphora* arena are shown.

Gated Stimulation

The visual stimulation device presented in the preceding sections employs a type of PWM. On one hand this means that per dot matrix display only elements of one column of LEDs are lit at a time. On the other hand—barring the case of a whole field *off stimulus*—it also means that at all times at least some LEDs are lit and, thus, emitting photons stimulating photoreceptors in the fly visual system. Evidently, these photons do not distort electrical recordings during electrophysiology or adulterate analysis of behavioral studies. However, they can substantially perturb optical recordings. This can to some extent limit the use of this type of stimulation when using optogenetics.

A fairly new and highly advantageous technique for optical recording is two photon laser scanning microscopy (2PLSM), which requires two photomultiplier tubes (PMTs) for recording and amplification of the very few photons emitted by the fluorophore that is being excited. PMTs are highly sensitive devices, capable of sensing and greatly amplifying even single photons. The amplification involved can reach values over eight orders of magnitude.

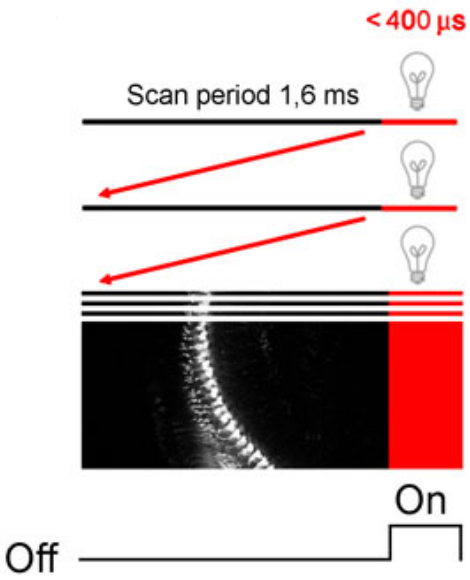

Figure 3.7: Temporal separation of visual stimulation and 2PLSM active line scan [71].

Considering the fact that when measuring fast single-cell activity in neurons very few photons are released by the fluorescent dye, this type of sensing is highly appropriate.

However, due to the high PMT amplification values necessary for proper recording of neuronal signals every other light source irradiating photons onto the PMT surface would not only substantially distort the recordings, but potentially destroy the PMTs through over-excitation. This is why in such experimental situations great care needs to be taken to completely seal the preparation from any outside light sources. This is feasible in large animals such as mice, rats and even in large fly species. In *Drosophila* however, this is not possible since the small size of the fly head makes it virtually transparent to light irradiated from the LED arena through the eyes and neural tissue into the 2PLSM light path. This fact forecloses use of the present arena design in 2PLSM studies.

One way of blocking photons emitted from the LED arena entering the PMTs is spectral separation. PMTs in 2PLSM are tuned to photons of a very specific wavelength using filters, depending on the fluorophores used in the specimen. Yet, in the case of *Drosophila* experiments involving fluorophores in the green part of the visible spectrum such as TN-XXL [70] this is not feasible due to the LED arena's dominant wavelength $\lambda_D = 568\,\text{nm}$ and spectral half-width $\Delta\lambda_{1/2} = 30\,\text{nm}$, which lies too close to these fluorophores' spectral characteristics.

Therefore, a novel temporal separation technique is presented here. By gating excitation and recording in mutually exclusive time slots temporal separation can be achieved, therefore enabling use of this type of visual stimulation in 2PLSM in *Drosophila*.

Close observation of the basic function principles of 2PLSM reveal that the scanning process is carried out in line-scanning fashion using small scanning mirrors. Thus, these scanning mirrors possess scanning periods comprised of two parts: an active scanning period and a flyback time in which the mirror is oriented back to the beginning of the line. Typically the active period of the line scan lasts about 1.6 ms per line and the flyback time around 400 µs, yielding a total time of roughly 2 ms per line. Since data is recorded only during active scanning time the *dead time* of the flyback period can be used for active

stimulation without perturbation of the optically recorded data. This scheme is outlined in Figure 3.7.

In order to implement this scheme many modifications in both hardware and firmware were necessary. A key element as to temporally gate the stimulus arena is exact knowledge of the present state within the scanning period. Therefore a TTL-compatible output signal from the 2PLSM setup is used, which elicits a short rectangular positive pulse each time a line scan is initiated. This signal is used as a trigger signal and fed through a coaxial cable onto the data and power distribution board, from where on it is transmitted via Firewire cable and dedicated PCB traces to all 120 panel controllers on all 15 panel controller boards.

Displaying the present pattern on the LED panel is now closely linked to this trigger signal for each panel controller. Once a pulse is detected on this line the 1.6 ms active scanning period is waited for with all LEDs strictly switched off. Once this time has elapsed another 35 µs are allowed to pass as a safe margin before displaying the present frame on the LED displays for about 330 µs, yielding another 35 µs safe margin before the onset of the next line scan. These times were chosen as conservative margins as to keep the possibility of PMT over-excitation negligible.

Still adhering to the PWM principle during the 330 µs stimulation period exactly 3 elementary time slots are allotted, allowing for a total of 4 different intensity levels. Hence, a maximally lit LED means being on for only 330 µs of the complete 2 ms cycle and results in a reduction in luminous intensity in the *light on* state. However in the dark adapted state of the animal the relative contrast between *light on* and *light off* is maintained by the almost complete absence of photons in the *light off* state. Another point worth noting is the introduction of a 500 Hz flicker due to the 2 ms cycle. Nevertheless, this lies beyond the flicker fusion frequency of flies and therefore does not have a major impact on the animal.

3.1.5 Discussion

In this section a visual stimulation device has been presented, which enables new types of experiments that have thus far been elusive due to lack of appropriate stimulus delivery. An LED based arena design has been put forth whose implementation complies with all tight restrictions imposed by the stringent requirements of electrophysiological, behavioral or optogenetic studies in living flies. The resulting complete stimulation arena is shown in Figure 3.8.

Among its main characteristics it features temporal resolution and frame rates far above flicker fusion frequency of any fly species in order not to introduce any flicker artifacts into recording data. It was designed in a modular fashion as to allow for a large variety of arrangements. In its current basic arrangement it possesses a half cylindrical shape consisting of 120×64 individual LEDs over 180° in azimuth and 90° in elevation as viewed from the center. It was built for presenting arbitrary visual stimulus patterns that are easily created by the user on either Windows or Linux based PCs. Furthermore it is capable of 16 linearly scaled intensity levels at maximum temporal resolution. However, it is possible to increment this intensity resolution to 32, 64 or more levels by sacrificing temporal resolution.

Also, several additional modifications of the arena for special applications have been presented. For one specific set of experiments large field stimulation at simultaneous high temporal and spatial resolution has been achieved using an extension in I^2C bus addressing

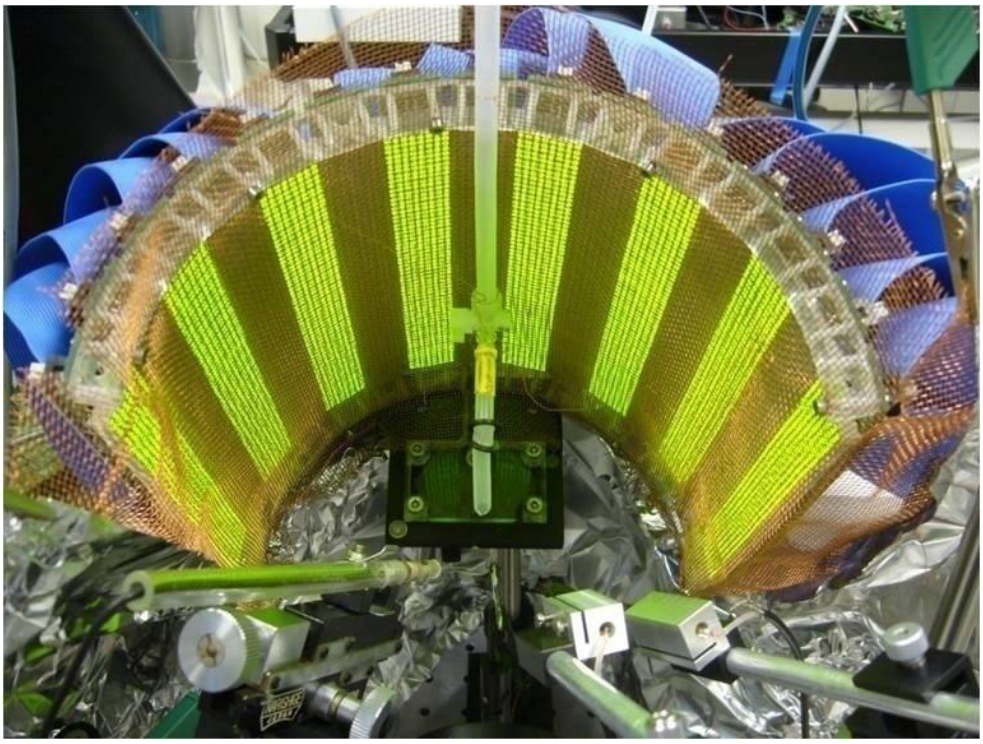

Figure 3.8: The small field visual stimulation arena. Note the grounded wire mesh and aluminium electromagnetic shielding in front of and beneath the arena.

scheme and firmware reconditioning. In order to be able to use the present stimulation system in 2PLSM a novel type of temporal gating was proposed and implemented, indicating large potential of this type of visual stimulus generation.

The design has been intensively tested and tried in long term studies, where it has been found to perform reliably and satisfactorily in all aspects. Three such experimental setups and their outcome are detailed in the following.

3.2 LPTC Response Properties in Drosophila

The crystalline-like structure of the optic lobes of the fruit fly *Drosophila melanogaster* has made them a model system to study neuronal cell fate determination, axonal path finding and target selection. For functional studies, however, the small size of the constituting visual interneurons has presented a formidable barrier so far.

In this section it will be shown how to overcome this problem by establishing in vivo whole cell recordings [16] from genetically targeted visual interneurons of *Drosophila* using the advanced stimulus device introduced in the previous section. With this it is now possible to describe the response properties of six motion-sensitive large-field neurons in the lobula plate that form a network consisting of individually identifiable, directionally-selective cells most sensitive to vertical image motion (VS cells [72, 73]). Individual VS cell responses to visual motion stimuli exhibit all the characteristics that are indicative for presynaptic input from elementary motion detectors of the correlation-type [74, 75]. Different VS cells possess distinct receptive fields that are arranged sequentially along the eye's azimuth, corresponding to their characteristic cellular morphology and position

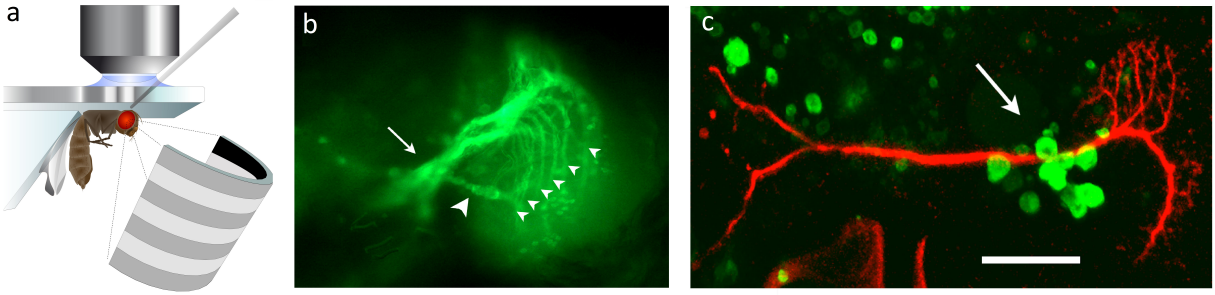

Figure 3.9: Whole cell patch clamp recordings from genetically labeled visual interneurons in the lobula plate. (**a**) Schematic drawing of the fly preparation including recording electrode and stimulus arena in the fly's ventral field of view. (**b**) Six labeled VS cells (VS 1–VS 6) with their dendrites (white arrowheads) and axons (white arrow). HSS dendrite also visible (large white arrowhead). (**c**) View of a lobula plate directly after recording from VS 1. LPTC somata are labeled in green (white arrow), VS 1 perfused with Alexa-568 is labeled red. The VS 1 soma was removed during withdrawal of the patch pipette. Scale bar: 25 µm [76].

within the retinotopically organized lobula plate. In addition, lateral connections between individual VS cells cause strongly overlapping receptive fields that are wider than expected from their dendritic input.

3.2.1 Drosophila Overview

Motion vision in the *Drosophila* visual system is considered an ideal model system to address the fundamental rules of information processing in neural networks. This notion is based on genetic amenability that meets a crystalline-like organization of the neural lattice. Moreover, experiments can be guided by a conceptually much advanced theoretical background: precisely defined visual stimuli are being used in experiments [12] that can be fed into a well established computational model [74]. Following this idea, cellular responses of giant motion-sensitive cells within the lobula plate of large flies have been extensively analyzed [31]. However, these experiments were at some point limited by the lack of elaborated genetic tools in large flies, whereas in *Drosophila* similar experiments were so far hampered by difficulties in stimulating and recording from identified neurons in the intact animal.

Inspired by the detailed findings in large flies, the present work focuses on experiments suitable to address recent as well as classical aspects of visual motion detection such as direction-selectivity and orientation tuning, recently described receptive field organization and computations within the VS cell network [39, 40, 77] and various hallmarks of the correlation-type model of motion detection. This work reproduces these findings in *Drosophila* and demonstrates that it is now possible to combine functional cellular approaches with the rich repertoire of genetic techniques as established in many other studies. This combination promises important insights into the neural circuitry underlying elementary motion detection in columnar neurons of the second visual ganglion, the medulla, as well as information processing within the VS cell network of the lobula plate.

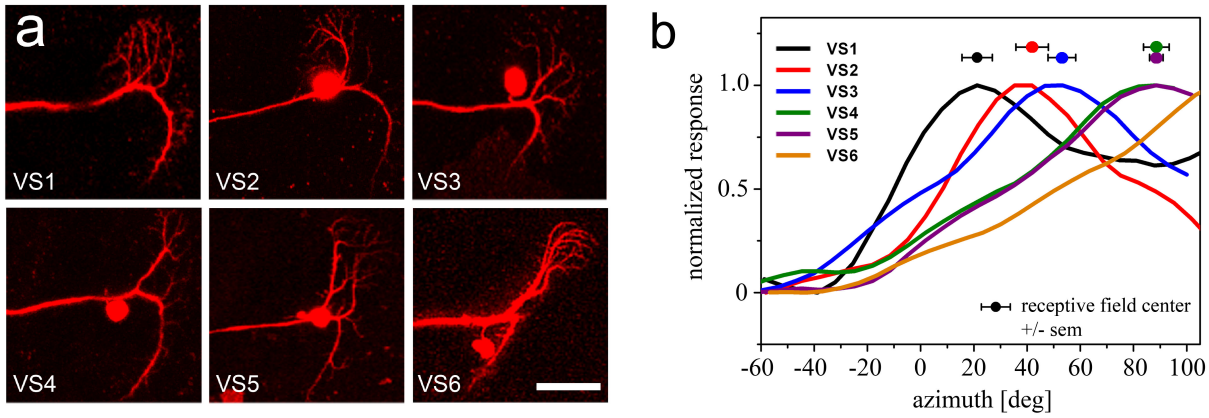

Figure 3.10: Receptive fields of *Drosophila* VS 1 to VS 6 cells (**a**) Alexa 568, loaded via the patch pipette, enabled reliable identification of the recorded VS cell type (VS 1 to VS 6; collapsed confocal image stacks, scale bar: 25 µm). (**b**) Average receptive fields of VS 1 to VS 6 (mean ± SEM). Note that for VS 6 the center is located outside (posterior) of the stimulated area [76].

3.2.2 Whole Cell Patch Recordings

Recently it has been shown that individual neurons in *Drosophila* are accessible to whole cell patch-clamp recording [16]. Following this approach it is now possible to report the first single unit recordings of motion sensitive, individually identified *Drosophila* visual interneurons (Figure 3.9a, for methods see Appendix A). Since the preparation prevents the use of high contrast providing optics (like differential interference contrast), it was necessary to use the Gal4-UAS system [46] and water immersion optics to fluorescently target a small population of tangential cells within the third visual ganglion of the optic lobe, the lobula plate (DB331-Gal4→UAS-YC3.3; Figure 3.9b).

Based on their morphological similarities to the corresponding lobula plate tangential cells in *Calliphora* [31,38,78] these neurons have previously been characterized in fruit flies as three HS cells (HSS-cell: large white arrowhead in Figure 3.9b) and six more posterior VS cells (small white arrowheads in Figure 3.9b) [15,25,72,73]. *Drosophila* VS cells extend their closely intermingled axonal projections (Figure 3.9b, white arrow) to the central brain and possess large dendrites that span large parts of the lobula plate tangentially. The six VS cell dendrites tile the lobula plate sequentially (Figure 3.9b, white arrowheads; see also Figs. 3.9c, 3.10b) with partially overlapping dendritic fields.

In a first set of experiments the direction selectivity and orientation tuning in the six anatomically described *Drosophila* VS cells was investigated. A red fluorescent dye was added to the intracellular solution and the electrode was directed towards green fluorescent cells. Stable whole cell patch-clamp recordings were only feasible from cell bodies. However, since these cell bodies were not clearly visible in neurons that expressed cytosolic YC3.3 (Figure 3.9b), visually guided patch-clamp recordings were facilitated by expression of a green fluorescent marker (DB331-Gal4→UAS-mCD8-TN-XL-8aa; details in Appendix A) that predominantly highlights somata (Figure 3.9c).

Using this marker, recordings were obtained from more than 100 VS cells all individually identified from dye fills subsequent to the recording. As an example Figure 3.9c exhibits a collapsed confocal image stack view of the lobula plate of an experimental animal im-

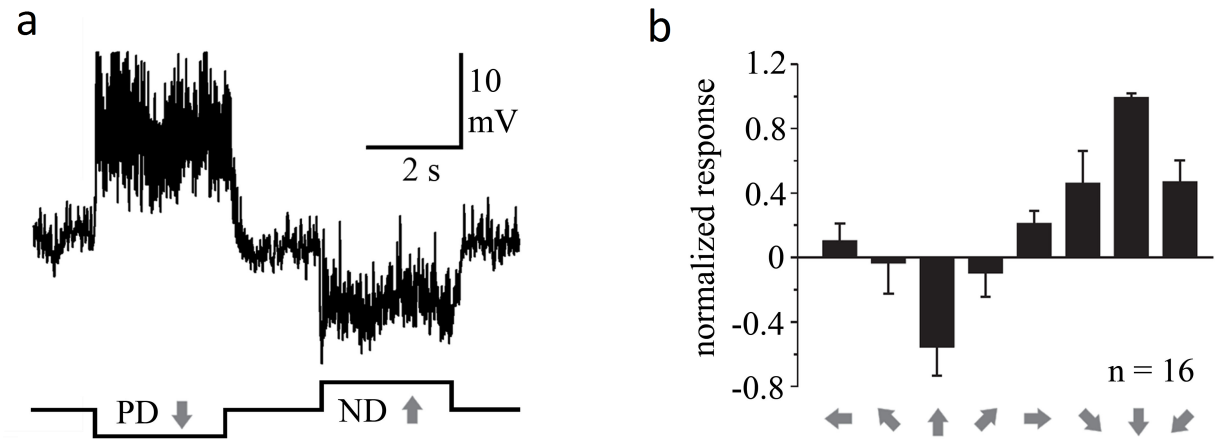

Figure 3.11: Direction selectivity and orientation tuning. (**a**) Direction selectivity of the recorded membrane potential of the VS 1 cell shown in Figure 3.9c. Grating motion is indicated by the bottom black line (large field sinusoidal horizontal grating, $\lambda = 44°$ and $\nu = 50\,°\mathrm{s}^{-1}$; (**b**) Orientation tuning of *Drosophila* VS cells. Directions are indicated by the grey arrows. Data and error bars represent mean ± SEM, $n = 16$ [76].

mediately after recording of a VS 1 cell. The expression of the green fluorescent marker (DB331-Gal4→UAS-mcD8-TN-XL-8aa, see Appendix A) highlights mostly the somata of LPTCs (white arrow) and a few other cells. The recorded cell was perfused with Alexa 568 (red). The VS 1 soma was removed during withdrawal of the patch pipette (see methods in Appendix A). VS cells revealed an input resistance of 20 MΩ to 40 MΩ, a resting potential of about −45 mV (−55 mV when corrected for the liquid junction potential) and showed spontaneous fast membrane fluctuations even in the absence of moving visual stimuli.

During the presentation of vertically moving periodic gratings (velocity $\nu = 50\,°\mathrm{s}^{-1}$, spatial wavelength $\lambda = 44°$, as seen by the fly) all VS cells exhibited directionally selective responses, such as shown for a VS 1 cell (Figure 3.11a, Figure 3.12). Upward motion (ND = null direction) and downward motion (PD = preferred direction) of a periodic horizontal grating elicited a graded hyperpolarization and depolarization of the membrane potential, respectively, superimposed by small action potentials of irregular amplitude that can likely be attributed to Tetrodotoxin (TTX) sensitive fast voltage-activated sodium currents as their main source (Figure 3.13). These fast events were reduced in frequency and amplitude during upward motion and increased during downward motion (Figure 3.11a, Figure 3.12).

There were observable differences from cell to cell in the rate at which fast membrane fluctuations of irregular amplitude occur. As indicated in Figure 3.12 in one type of cells (cell 1) spike-like events are basically absent if a still grating is presented (no motion) and during PD-motion fast membrane fluctuations are easily detectable that are superimposed on the steady-state depolarization (see close-ups to the right in Figure 3.12). The other type of cells is represented by cell 2. Spike-like events are highly abundant even in the absence of grating motion. During PD-motion a more pronounced steady-state membrane potential depolarization is exhibited during which individual spike-like potential deflections are not easily detectable (see close-ups to the right in Figure 3.12). During ND-motion fast membrane potential fluctuations were almost completely suppressed in both types of cells. Both types were observed at similar abundance and did not correlate with the specific VS cell type. Grating motion is indicated by the black line underneath the recording traces to

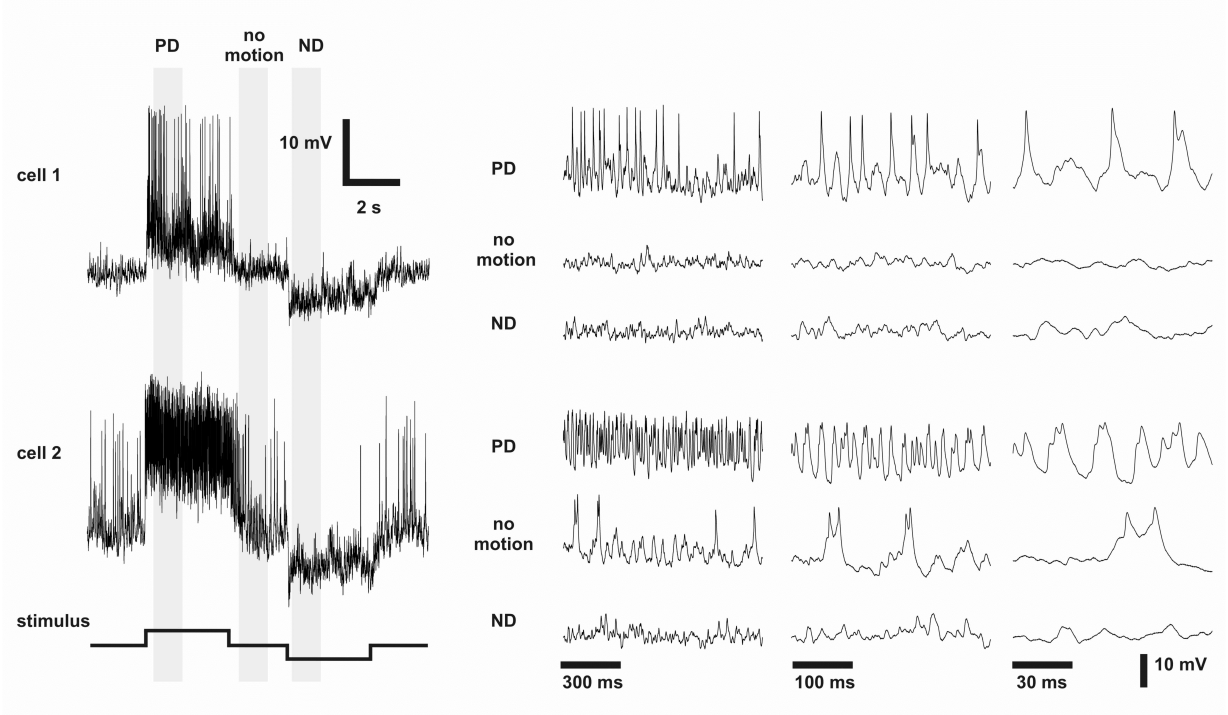

Figure 3.12: Recording traces of two VS cells during presentation of a periodic sinusoidal grating ($2\,\mathrm{cd\,m^{-2}}$ to $80\,\mathrm{cd\,m^{-2}}$) [76].

the right. Sections of the recording traces at the time marked by the grey stripes are shown at increasingly finer time-scale in the panels to the right. It has to be mentioned that in big flies membrane potential fluctuations have been shown to be dependent on the mean brightness [46]. However, in the present experiments this parameter was not changed.

Presentation of large field grating motion in eight different directions and four different orientations separated by 45° (Figure 3.11b) revealed that all six VS cell types were indistinguishably sensitive to large field stimuli moving along the vertical axis of the animal, thus the responses of VS cell types from VS 1 to VS 4 were pooled ($n = 16$, $\nu = 25\,^\circ\mathrm{s}^{-1}$, $\lambda = 25^\circ$).

To investigate if TTX-sensitive fast voltage-activated sodium currents are among the ionic repertoire of *Drosophila* VS cells, −1 nA current was injected for two seconds (indicated by the black bar) turning the membrane potential more negative by additional 30 mV (Figure 3.13). Then, the neuron was released from hyperpolarization. All this was done without visual stimulation. The black recording trace shows that the fast membrane potential fluctuations are reduced during hyperpolarization. Immediately after being released from negative current, the neuron generated a series of high frequency rebound spikes that can be considered intrinsic in origin and that were blocked by application of TTX onto the lobula plate (grey recording trace).

Thus, TTX-sensitive fast voltage-activated sodium currents are likely to be a main source of the irregular amplitude high-frequency events. This interpretation would further corroborate the idea of common mechanisms and pathways of visual motion detection in Dipteran flies [14, 79, 80]. Nonetheless it is necessary to consider that the complete block of all fast membrane potential fluctuations by TTX might include blocking of action potentials in columnar elements that provide input to VS cells

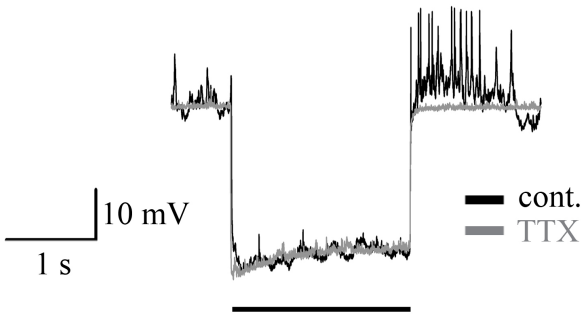

Figure 3.13: Active membrane properties in *Drosophila* VS cells involve TTX-sensitive fast voltage-activated sodium currents. (TTX: $500\,\mathrm{nM}$ on the lobula plate, grey trace, $n = 6$; $10\,\mu\mathrm{l}$ of a $25\,\mu\mathrm{M}$ TTX-ringer solution were added to $0.5\,\mathrm{ml}$ ringer in the bath) [76].

3.2.3 Receptive Field Organization and Drosophila VS Cell Network

Because the fly visual system is organized retinotopically, the visual surround is mapped onto the individual VS cell dendrites by their connections to presynaptic columnar elements [25]. Six VS cells (VS 1 to VS 6) have consistently been described in *Drosophila* [[15,25,72, 73] and each compound eye looks at approximately 180° elevation and 180° azimuth [81]. Estimating a dendritic overlap of 50% between adjacent cells, each cell is supposed to sample local motion detectors from maximally about 60° along the azimuth and almost 180° elevation. However, the architecture of the receptive fields might be more complex as shown in *Calliphora* where the visual surround is indeed mapped onto the ten VS cell dendrites in precisely this way, yet the extent of the VS cell receptive fields along the azimuth is much broader [36, 39, 82].

The present work sets out to analyze how vertical motion in different areas of the visual surround of the fly is represented by the six *Drosophila* VS cells. A small bar of 6° width was moved up- and downwards in the ventral field of view from 0° to 50° ventrally at 28 different positions along the azimuth from −60° on the contralateral side to 105° on the ipsilateral side (0° = frontal). As can be seen in Figure 3.14, during the experiment increasingly depolarizing and hyperpolarizing responses are elicited during PD- and ND-motion, respectively, as the bar moves into the center of the receptive field (upper trace). These potential deflections disappear again as the bar reaches more frontal positions (see close ups, left trace: receptive field center; right trace: off-center). The mean normalized response (PD minus ND) of each cell at each position of the moving bar was averaged for VS cells of the same cell type (n = 4, 6, 9, 5, 5 and 2 cells for VS 1 to VS 6, respectively). Dye fills allowed unequivocal identification of different VS cells (Figure 3.10a) based on their distinct dendritic branching pattern [72, 73]. Plotting the normalized responses for each cell type (Figure 3.10b) as a function of the azimuth shows that

(i) each *Drosophila* VS cell type possesses its distinct receptive field,

(ii) the receptive field centers of the different VS cells are sequentially arranged along the azimuth with VS 1 being most frontal and VS 6 most lateral (Figure 3.10b). Note, however, that it was not possible to characterize the receptive field in the dorsal part of the eye due to the arrangement of the fly in the recording setup (Figure 3.9a).

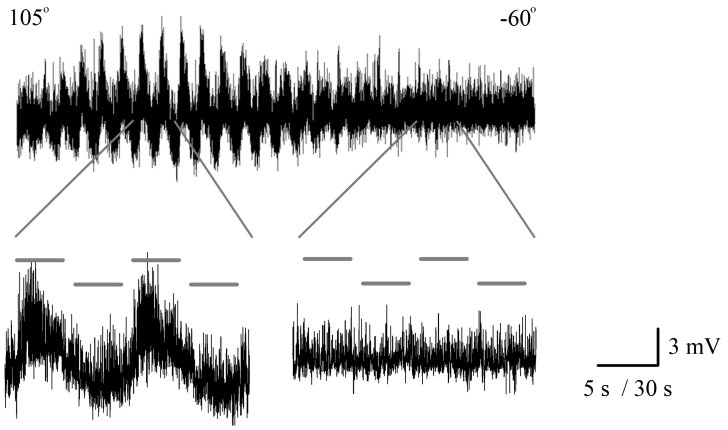

Figure 3.14: Analysis of receptive field width. Five minutes of a recording of a VS 3 cell are shown. A horizontal bar of 6° width was moved up- (ND) and downwards (PD) from vertically 0° to −50° at successive horizontal positions within the ventral field of view. The horizontal positions ranged from ipsilateral 105° posterior to contralateral −60° [76].

(iii) The receptive fields of VS cells cover more than 100° of visual space along the azimuth (half-width of about 80°) which is much wider than expected (see above). Only the position of the receptive field center is determined by the position of the dendrite while the width of their receptive fields seems to be affected by other factors, too.

The width and overlap of VS cell receptive fields as described in *Calliphora* [36,39,40,82] might represent a common organization principle for dipteran VS cells. According to this view, VS cells partially inherit their receptive fields from their immediate VS cell neighbors. The emerging VS cell network is endowed with intricate computational properties [77, 83] where electrical synapses to neighboring VS cells play a key role. In the present work possible electric coupling in *Drosophila* VS cells was investigated indirectly by perfusion of an individual VS cell with a mixture of two different dyes, Alexa 568 and Neurobiotin, loaded via the same patch pipette (Figure 3.15). As in all other experiments Alexa 568 never spread to other cells but remained restricted to the recorded one. This allowed the immediate identification of the patched neuron. After fixation and labeling of Neurobiotin via Streptavidin-Alexa 568, the diffusion of Neurobiotin to other neurons within the lobula plate or the lateral protocerebrum was detected in all trials ($n = 15$, all types of VS cells analyzed). Typically, Neurobiotin labeled the immediate neighbors of the perfused VS cell, usually at least four neighboring VS cells revealing an intensity gradient with distant cells being stained more faintly. In Figure 3.15 the axons and basal dendrites of four VS cells neighboring the patched VS 6 neuron are strongly labeled (white arrow) and additional labeling was observed in cell bodies within the cortex of the lobula plate (white arrowheads). Thus, VS cells in *Drosophila* show dye coupling providing indirect evidence for electric coupling between neighboring VS cells as the basis for their large receptive fields [84].

3.2.4 Computational Structure of the Motion Detection Circuitry

Directionally selective responses in insects are computed locally and in parallel from the changing retinal brightness distribution [1, 74, 75] by correlating, at each image location,

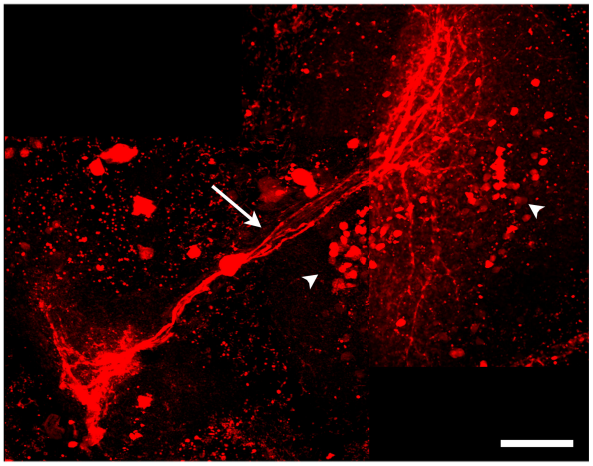

Figure 3.15: Dye coupling of neighboring VS cells. A single, genetically labeled (DB331-Gal4→UAS-mCD8-TN-XL-8aa) VS 6 cell was perfused with a mixture of Alexa-568 (red) and Neurobiotin via the patch pipette. Four to five VS cell axons (white arrow) and two clusters of small cell bodies from unidentified columnar neurons (white arrowheads) are stained (scale bar $50\,\mu m$). Comparable results were obtained from all types of VS cells in 15 independent experiments [76].

the brightness values as derived from neighboring photoreceptor signals after asymmetric temporal filtering. Doing this twice in a mirror-symmetrical fashion and subtracting the output signals of both subunits leads to a fully directional output signal. As a hallmark of such a computation, the response of the animal to a drifting sine grating is expected to show a velocity optimum, which is a linear function of the pattern wavelength resulting in a constant temporal frequency optimum. This has been found to hold true in behavioral experiments on the beetle *Chlorophanus* [1], the honeybee *Apis* [85], the housefly *Musca* [86, 87] as well as in *Drosophila* [12, 14, 88]. Subsequent work in the blowfly *Phaenicia* and *Calliphora* confirmed that, amongst other predictions of the Reichardt model [79, 80], this response feature is fully retained, too, in large-field motion-sensitive neurons in the lobula plate [5, 89]. Thus, in order to see if this holds true in the present setup the velocity dependence was measured at different spatial wavelengths presenting sine gratings at spatial wavelength $\lambda = 44°$ and $22°$, respectively, that drifted downward for three seconds at various speeds. Plotting the normalized mean response as a function of pattern velocity revealed a response optimum at $44\,°\,s^{-1}$ for the large and at $22\,°\,s^{-1}$ for the small wavelength pattern (Figure 3.16a). When plotted as a function of the temporal frequency (Figure 3.16b), both curves coincide with the same response optimum at 1 Hz. This finding makes a strong argument for elementary motion detectors of the correlation-type providing input to VS cells in *Drosophila*.

Characteristic step-response transients elicited by the abrupt onset of motion represent another key feature of the presynaptic motion detection circuitry [90,91]. In *Calliphora* this step-response consists of initial transient oscillations followed by a plateau-like steady state response. The initial oscillations are imposed by the frequency of brightness changes of the pattern and do not reflect intrinsic oscillatory dynamics of the neural circuitry. However, both components depend on features of the visual stimulus itself and precisely match model calculations based on a correlation-type detector model [92]. In the following experiments

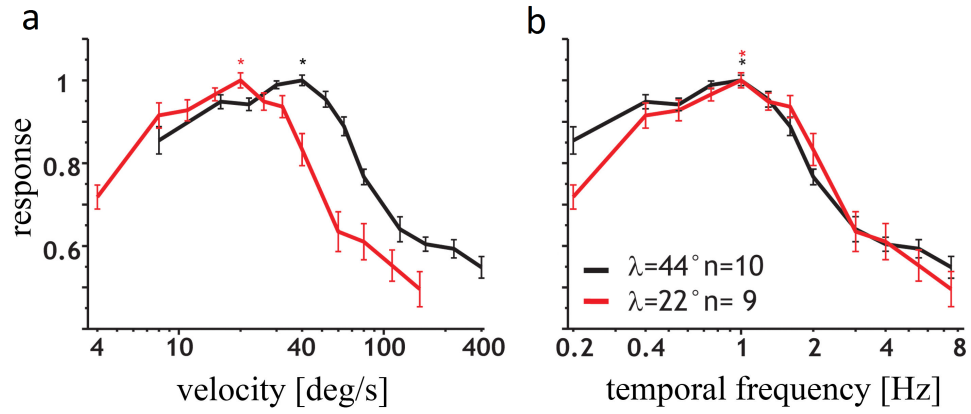

Figure 3.16: Velocity tuning of *Drosophila* VS cells. (**a**) Normalized responses of VS cells to PD-motion are plotted against the velocity of the stimulus using two different sine wave stimuli (red: $\lambda = 22°$, black: $\lambda = 44°$). At each stimulus velocity the first 500 ms of the recording trace after motion-onset were normalized to the maximum response. Each cell was measured at least four times for each stimulus condition, asterisks indicate the maximum of the mean response. Data of VS 1 to VS 4 cells are averaged, $n = 9$ and 10 cells, respectively, mean ± SEM. (**b**) Same data as in (a), but plotted as a function of the temporal frequency (velocity divided by the pattern wavelength) [76].

step-responses were analyzed in VS cells of *Drosophila* (Figure 3.17a). Prior to the onset of grating motion, either an identical stationary grating ($\lambda = 50°$, Figure 3.17a) or an isoluminant homogeneous screen (Figure 3.17b) was presented to the flies. After four seconds the grating started moving abruptly at a velocity of $150\,° \mathrm{s}^{-1}$ corresponding to a temporal frequency of 3 Hz which allowed detection of several oscillation cycles. With both types of pre-stimulus conditions experiments were performed at 85 %, 28 % and 14 % pattern contrast (black, red and blue recording traces, respectively, in Figure 3.17a and 3.17b). When starting from a stationary grating, the response oscillated at 3 Hz (Figure 3.17a). The oscillations lasted for several seconds and their amplitude depended on the pattern contrast: with increasing contrast the oscillations were damped more quickly and gave way to the underlying steady-state response. When a homogeneous green screen was presented before the onset of grating movement (Figure 3.17b), the oscillations tended to have much smaller amplitudes. Small remaining oscillations can most likely be attributed to the limited spatial resolution of the LED arena. As expected, under these conditions the steady-state component showed a similar positive dependence on pattern contrast. The responses of all experiments were used to calculate the power spectra of the recordings taken at both pre-stimulus conditions (Figure 3.17c and 3.17d). With the grating presented prior to motion VS cell responses oscillated with three-fold higher power at the fundamental frequency of the moving grating (3 Hz) compared to the homogeneous screen as starting condition (indicated by black arrows). These results are in line with the step-responses measured in *Calliphora* tangential cells [91] and can be precisely simulated in a correlation-type model of elementary motion detection that includes two temporal filters [92]. Adaptation of the time-constant of a high-pass filter in the cross-arms of the detector can fully reproduce these results whereas other models or versions of motion detectors fail.

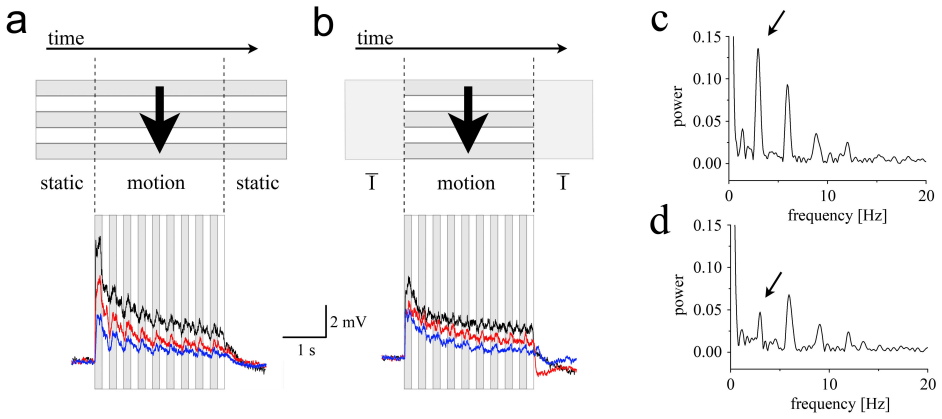

Figure 3.17: Step-responses of *Drosophila* VS cells. (**a**) Still grating present before motion onset ($\lambda = 50°$, 3 Hz, indicated by the grey stripes in the background). A periodic square-wave grating was presented, after four seconds the grating started to move abruptly at a constant velocity of $150\,°\,s^{-1}$ ($f_t = 3\,Hz$). Experiments were performed at constant mean luminance with 85% (black), 28% (red) and 14% (blue) pattern contrast. (**b**) Equal conditions as in (a), but showing an equiluminant homogeneous screen prior to motion onset. (**c**,**d**) Power spectrum analysis of the mean response of all experiments in (a) and (b), respectively. Cell types VS 1 to VS 4 averaged, $n = 8$ cells; 8 to 20 sweeps per cell [76].

One prerequisite of a directionally selective neuron is its capability to encode the direction of image motion independent of the sign of contrast. This property was investigated by presenting either a dark bar moving on a bright background or a bright bar moving on a dark background (Figure 3.18a). In the different VS cell types upward and downward motion of the bar was always reported by hyperpolarization and depolarization of the membrane potential, respectively, independent of the sign of contrast. As a further test for the Reichardt-model, the contrast dependence of the VS cell response was studied. Due to the multiplication of luminance values, a quadratic contrast dependence of individual correlation-type motion detectors is expected in principle [79]. However, as analyzed in all species so far, such a quadratic contrast dependence is found for small contrasts only (contrast less than 10%); for higher contrast levels, the response strongly saturates [12,93]. Here a similar saturation nonlinearity could be observed in *Drosophila* VS cells when flies were stimulated with a periodic grating drifting at 1 Hz temporal frequency at four different contrast levels (10 %, 40 %, 75 % and 100 %). The response increased with increasing pattern contrast and showed clear signs of saturation at high luminance contrast (Figure 3.18b). In agreement with behavioral studies on the optomotor response in *Drosophila* [12], the half-maximum response was reached at about 24% luminance contrast.

The final experiments described in this section elucidated the final step in local motion detection, i.e. the subtraction of local motion detectors with opposite preferred direction. If this subtraction stage was presynaptic to the dendrites of VS cells (alternative 1), a single type of fully directional input would be expected. The synaptic transmitter release of this input would be up- and down-regulated according to preferred or null direction motion. If the subtraction stage was realized on the dendrites of VS cells themselves (alternative 2), two types of inputs with opposite preferred direction should provide in-

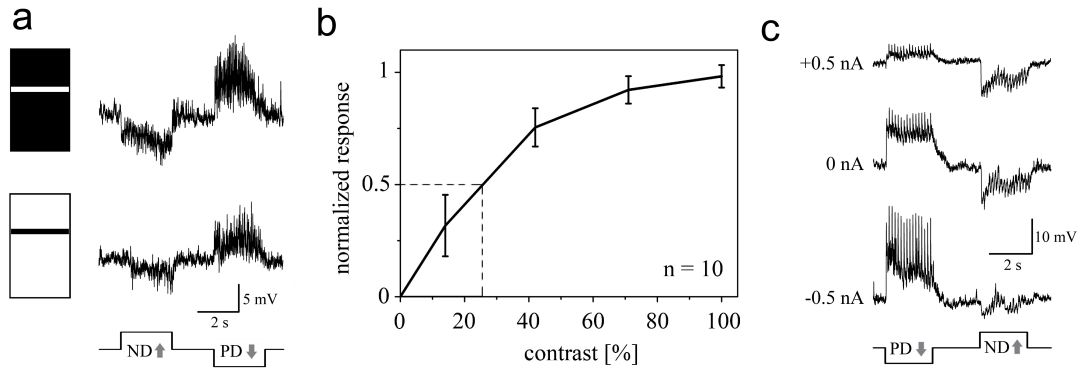

Figure 3.18: Further response characteristics of VS cells. (**a**) VS cell contrast sign invariance. A white bar in front of a black background (upper trace) and a black bar in front of a white background (lower trace) moving up- and downwards are reported by similar membrane potentials ($n = 14$). (**b**) A periodic grating ($\lambda = 25°$) moving at constant speed and a temporal frequency of 1 Hz. The normalized response of VS cells increases with increasing pattern contrast and exhibits a saturation characteristic with a half-maximum response at 24% pattern contrast ($n = 10$, mean $\pm$ SEM). (**c**) Recording traces of a VS cell in current clamp during PD- and ND-motion reveal that responses evoked by grating motion depend on the magnitude and polarity of the injected current. Current was injected permanently ($0.5\,\mathrm{nA}$, $0\,\mathrm{nA}$ and $-0.5\,\mathrm{nA}$) while the pattern moved up- or downwards. Grating motion indicated by black line underneath traces ($n = 10$). In all panels data was pooled from VS 1 to VS 4 [76].

hibitory and excitatory input to the VS cell dendrites, respectively. These two alternatives can be investigated in various ways, all of which have been done in tangential cells of *Calliphora*, and all of which provide evidence for the latter situation [94–96]. Here it was set out to record from VS cells in current clamp mode and inject constant current while presenting periodic grating motion in preferred and null direction (Figure 3.18c). If alternative 1 holds true, injection of constant current should affect both preferred and null direction response similarly by shifting the membrane potential away from the synaptic reversal potential. If, however, alternative 2 is realized, hyperpolarizing the postsynaptic cell should decrease the null direction response by reducing the driving force and, at the same time, increase the preferred direction response by increasing the driving force. Injection of depolarizing current would cause the opposite. Injection of $-0.5\,\mathrm{nA}$ eliminated the hyperpolarization during null direction motion completely while the preferred direction response became larger. Depolarizing current injection of $0.5\,\mathrm{nA}$ increased the amplitude of the null direction motion response whereas the amplitude of the graded depolarization and the small action potentials during preferred direction motion was decreased. These findings provide evidence that VS cells in *Drosophila* receive input from two types of local, motion-sensitive elements: an excitatory one tuned to downward motion and an inhibitory one tuned to upward motion. Thus, in terms of the computational structure described above, the subtraction stage of the correlation-type motion detector is implemented as a push-pull mechanism between excitatory and inhibitory inputs on the dendrites of VS cells in *Drosophila*.

3.2.5 Conclusions

In summary, in the work presented in this section, *Drosophila melanogaster* was established as a model system for the cellular analysis of visual motion detection and the first account on *Drosophila* VS cell response properties was provided. By comparing properties of *Drosophila* VS cells with previous knowledge about VS cells of large flies like *Calliphora* it is suggested that

(i) uniform neural mechanisms of visual motion processing exist across different dipteran species,

(ii) *Drosophila* qualifies for the analysis of population coding within the VS cell network,

(iii) *Drosophila* allows to unravel the neural implementation of elementary motion detection in columnar neurons of the medulla.

This can be achieved by combining the expression of genetic tools allowing to activate or inactivate neural function [97,98] in genetically targeted columnar neurons while recording from VS cells during visual stimulation with the stimulus device presented in section 3.1.

3.3 Half-Wave Input Rectification of Motion Detection Circuitry

In the visual system of *Drosophila*, photoreceptors R1 to R6 relay achromatic brightness information to five parallel pathways. Two of them, the lamina monopolar cells L1 and L2, represent the major input lines to the motion detection circuitry. The present work sets out to elucidate the role of L2 neurons in the motion detection pathway by optical recording of visually highlighted changes in intracellular calcium (Ca^{2+}) in neurons using targeted expression of a genetically encoded Ca^{2+} indicator in combination with the stimulus device presented in Section 3.1.

3.3.1 Background

The fly visual system continuously provides information about the motion of objects, conspecifics, predators and the three-dimensional structure of the environment. This information underlies the execution of notable visually driven behaviors [99–102]. However, the manner in which small-scale neural networks accomplish such computational efficacy remains an open question and the complete motion detection circuitry has not yet been determined in any animal [31, 103]. In the present work this question is examined in *Drosophila* by analyzing how brightness changes become encoded in changes in the concentration of presynaptic Ca^{2+} in the axon terminals of L2 neurons, a major input channel to the motion detection circuitry [104–107].

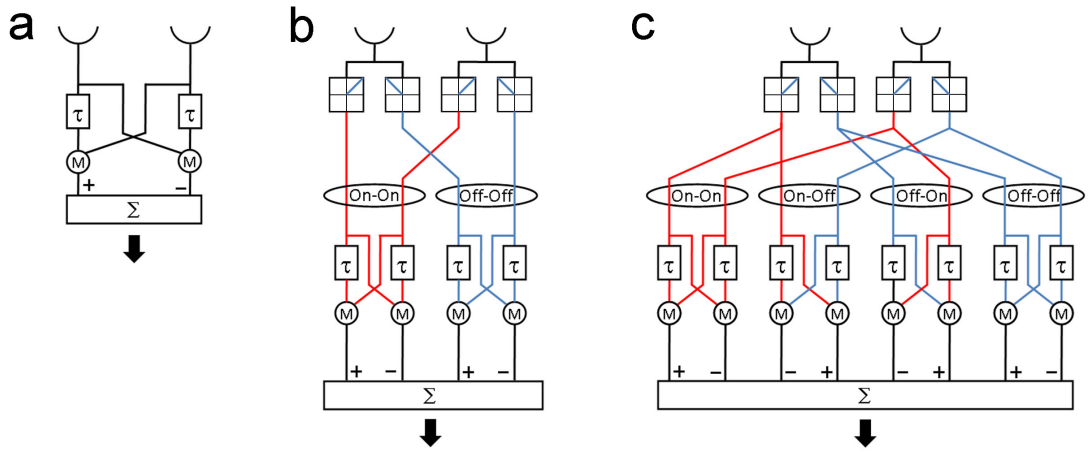

Figure 3.19: Different Hassenstein-Reichardt Models (HRMs) (**a**) Basic Hassenstein-Reichardt Model [1]. (**b**) HRM variant as suggested in [113, 114] with separate channels for the processing of positive and negative input signals. (**c**) HRM variant inspired by the "Four Quadrant Multiplier" [1].

The processing of brightness changes underlies the detection of visual motion. On the basis of a detailed input-output analysis of the optomotor response in tethered beetles, the well-known Hassenstein-Reichardt model (HRM) of visual motion detection was derived [1, 108]. The HRM (Figure 3.19a) essentially performs a spatio-temporal cross-correlation of two luminance input signals by multiplying the signals derived from two neighboring image points after one of them has been temporally delayed. This operation is executed in each of two mirror-symmetrical half-detectors that operate with opposite sign. Summing the output of both half-detectors results in a directionally selective response of the full detector. Notably, the HRM precisely describes the observed optomotor behavior of walking beetles and walking or flying flies in algorithmic terms [1,12]. Furthermore, the fundamental computations of the HRM can explain motion detection in different vertebrate species, including humans [109–112]. In flies, directionally selective responses that closely match the predictions of the model were observed in the large tangential neurons of both (reviewed in [32]) large fly species (reviewed in [31]) and *Drosophila* [17,76]. These cellular responses carry distinct signatures that derive from the correlative processing in the HRM [1] (reviewed in [31, 32, 103]).

Because of the purely algorithmic nature of the HRM, no immediate conclusions about the underlying neuronal hardware can be drawn; different implementations of the model can result in similar output. To gain insight into the cellular implementation of the model [113–115], extracellular responses of the directionally selective H1 neuron were recorded while presenting apparent motion stimuli [116]. Sequential stimulation of individual photoreceptor pairs (R1 and R6) [114] of the same ommatidium led to the proposal that each input signal is split into an ON and an OFF channel that then feed into separate multipliers for the processing of brightness increments and decrements, respectively [113, 114] (Figure 3.19b).

However, interactions among brightness increments and decrements are inherent in the original HRM (Figure 3.19a) and have repeatedly been observed in behavioral optomotor responses [1] and in the cellular responses of the H1 neuron [115]. Apparent motion stimuli with opposite polarity induce responses that report a reversal of the true direction of the

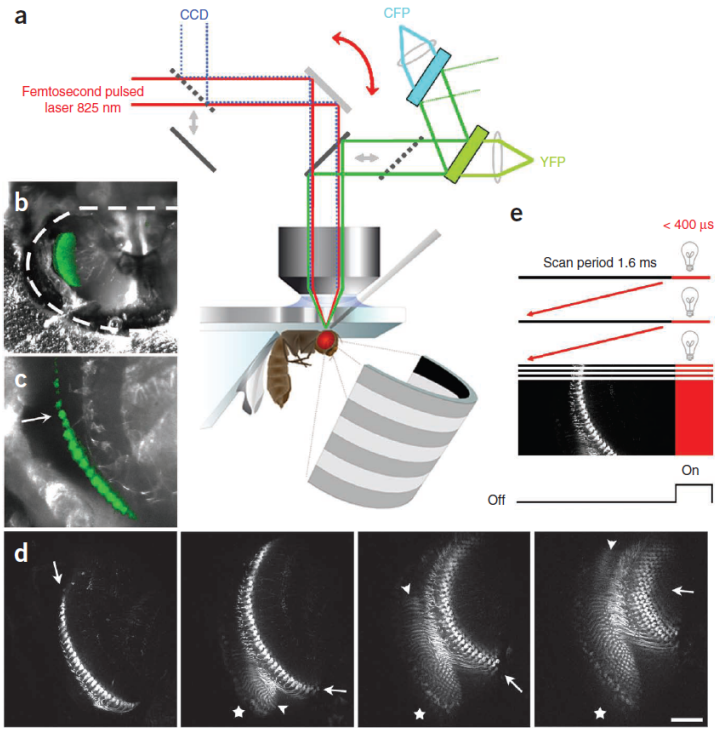

Figure 3.20: Experimental approach (**a**) 2PLSM setup (**b**) CCD camera top-view of the preparation. (**c**) Close-up at the position of the outer medulla (CCD images as in (b)); the arrow indicates an individual L2 axon terminal. (**d**) In vivo two-photon imaging of L2. Scale bar represents 30 µm for panels (b) to (d). (**e**) Temporal separation of optical recording and visual stimulus presentation. CFP, cyan fluorescent protein; YFP, yellow fluorescent protein [71].

stimulus [115], a phenomenon that is known in psychophysics as reverse-phi [117]. If a neuron is assumed to perform a multiplication in a sign-correct manner, then this neuron's output signal should increase in a supra-linear way when both inputs increase as well as when both inputs decrease. To the best of the author's knowledge, no biologically plausible mechanism is known that could accomplish such a computation.

A circuit was proposed [1] (Figure 3.19c) that was inspired by the "four-quadrant multiplier" used in analog signal processing: bipolar (both positive and negative signal components) input signals are half-wave rectified, resulting in only positive signals. These signals are subsequently processed in four separate multipliers accounting for all possible interactions (ON-ON, ON-OFF, OFF-ON and OFF-OFF). The output of the individual multipliers is then summed by a postsynaptic integrator in a sign-correct manner. From the perspective of this integrator, the models in Figure 3.19a and Figure 3.19c are mathematically identical. Thus, in contrast with a previous account [115], separate input channels for the processing of brightness increments and decrements cannot be excluded on the basis of responses of the integrating neuron to mixed input signals.

In flies, the lamina monopolar neurons L1 and L2 are the largest and best-investigated second-order visual interneurons postsynaptic to the photoreceptors R1 to R6 [24–27]. L1 to L3 and one amacrine cell (amc) all express a chloride channel encoded by the *ort* gene [118], which is gated by the photoreceptor transmitter histamine [119, 120]. The

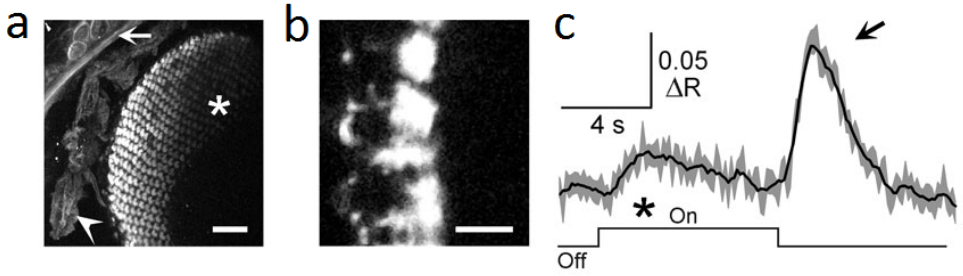

Figure 3.21: Visually evoked changes in Ca^{2+} in L2 axon terminals. (**a**) Retinotopic map, scale bar represents $20\,\mu m$ (**b**) Typical recording situation of L2 axon terminals, scale bar represents $10\,\mu m$ (**c**) Light-OFF induced uniform increase in presynaptic Ca^{2+} [71].

processes of amacrine cells stay in the lamina where they synapse onto L5 and where L4 receives input from L2 (and feeds back onto two more lateral L2 neurons) [26]. L4 and L5, as well as L1 to L3 project to distinct layers in the medulla [27]. Thus, five possible parallel processing streams (three direct channels, L1 to L3; two indirect channels, L4 and L5) transmit information about brightness changes from the lamina [26] to the medulla [27]. Behavioral and genetic experiments suggest that L3 is involved in processing of ultraviolet light and in phototaxis [106]. In contrast, L1 and L2 provide the major input to the motion detection circuitry in the medulla [104–107]. Recordings of their dendritic membrane potential revealed nondirectional, strongly adapting responses in large fly species [121]. Dendritic voltage changes in L1 and L2 to a transient light pulse correspond to an inverted, high passfiltered biphasic version of the voltage change recorded in photoreceptors [121–124] that depolarize in response to light. The reported inhibitory current through histamine-gated chloride channels [120] explains the hyperpolarizing ON response [125]; however, it does not explain the excitatory OFF component at the end of a light pulse that has been observed in large flies [121–125]. Depolarizing voltage responses to light-OFF have not been observed in *Drosophila* [126].

Even though there have been electrophysiological studies on lamina monopolar cells and few other columnar neurons in Calliphora [127, 128], the signals that are transmitted by lamina monopolar cells to neurons of the motion detection circuitry in the medulla [129] could not be recorded so far for methodological reasons. Here, this problem is addressed in fly motion vision by investigating how L2 axon terminals in the medulla [27] encode brightness changes in presynaptic intracellular calcium. Visually evoked Ca^{2+} is measured by a new method that employs optical recording of the genetically encoded calcium indicator TN-XXL [70] targeted to L2 neurons and the interlaced visual stimulation technique presented in Section 3.1.

3.3.2 Functional Two-Photon Imaging

The expression of the dual chromophore calcium indicator TN-XXL [70] was targeted to the roughly 750 nonspiking L2 lamina monopolar cells of the visual system of *Drosophila* using the enhancer trap line 21D-Gal4 (Figure 3.20) [104]. L2 neurons were chosen on the basis of the availability of this specific Gal4-driver line and the supposed pivotal role of L2 in visual motion detection [103–107]. Visually evoked spatio-temporal changes in Ca^{2+} in the highly ordered [24, 26], retinotopically organized lattice of L2 axon terminals [104]

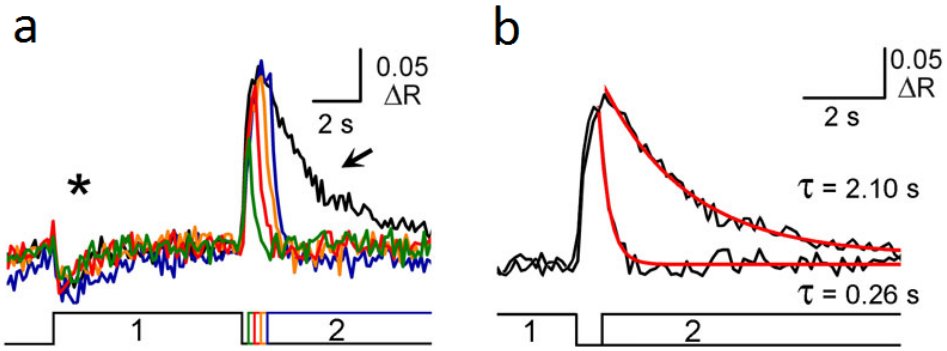

Figure 3.22: (**a**) Mean Ca^{2+} response in the presence of a second light pulse. (**b**) Eightfold time constant decrease for the decay of Ca^{2+} in the presence of subsequent light-ON [71].

(Figure 3.20bd) were monitored using 2PLSM [45] (Figure 3.20a). Two-photon excitation of photoreceptors was prevented as two-photon excitation is confined [45, 130] to a small volume in the focal plane of the objective that was kept distant from the photoreceptor layer. Furthermore, one-photon excitation of Drosophilas photoreceptors by laser light ($\lambda = 825\,\mathrm{nm}$) was prevented by reducing the laser power to a maximum of 10 mW. As a typical value, 5 mW was measured at the specimen.

The fly was placed under a water-immersion objective [76] attached to a custom-built 2PLSM, while looking at the LED arena. A piece of cuticle of about $0.3\,\mathrm{mm}^2$ was removed from the backside of the fly's head (outline indicated by the dashed line in Figure 3.20b). The superposition of a wide-field image of the exposed brain with TN-XXL fluorescence revealed expression of TN-XXL in the lateral posterior optic lobe (CCD camera images in 3.20b,c). Figure 3.20d depicts in vivo two-photon imaging of the retinotopic arrangement of L2 axon terminals in layer 2 of the medulla [27]. In the fly optic lobe, the calcium indicator was almost exclusively [104] expressed in L2 neurons (21D-Gal4 [104] / UAS-TN-XXL [70]). Each visual sampling unit was innervated by one L2 axon terminal as indicated by the arrow in each frame. L2 cell bodies (indicated by the asterisk) were in the lamina cortex. The dendrites (indicated by the arrow head) of L2 cells spanned the entire lamina. Individual frames were chosen from an image stack (Δz per image = 1 µm) and are separated along the z axis by about 20 µm.

As outlined in section 3.1, another technical problem of calcium imaging during visual stimulation of the fly's eye is protecting the photomultiplier tubes from light originating from the visual stimulus (Figure 3.20e). This was achieved by fast switching of the LED arena synchronized to the movement of the horizontal scanning mirror of the 2PLSM (Figure 3.20a,e). This design allowed to separate the recording of TN-XXL fluorescence and the presentation of visual stimuli in time. Scan time was 2 ms per line, of which 400 µs were spent on the fly-back period of the horizontal scanning mirror. 330 µs of this fly-back time was used to gate the LEDs. This resulted in a visual stimulus flickering at 500 Hz, which is far beyond the temporal resolution of Drosophila photoreceptors [131] and thus should be perceived as continuous light ($60\,\mathrm{cd\,m^{-2}}$ during light ON).

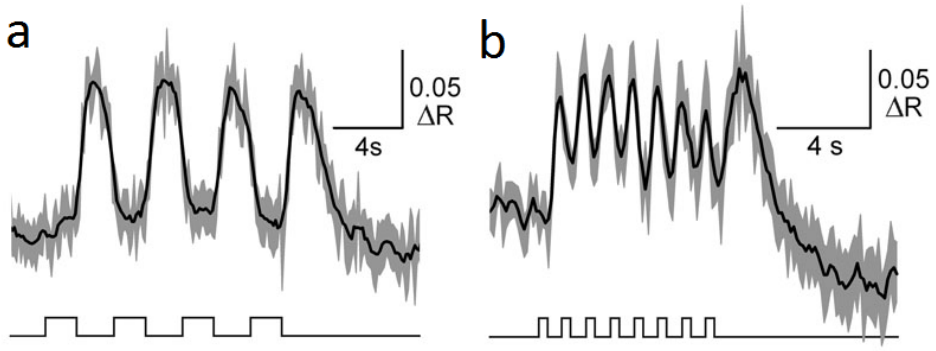

Figure 3.23: (**a**) Response to $0.25\,\mathrm{Hz}$ flicker ($n = 4$ flies, 50 image sequences). (**b**) Decreasing modulation depth of Ca^{2+} at a flicker frequency of $1\,\mathrm{Hz}$ and appearance of a tonic signal component ($n = 3$ flies, 53 image sequences) [71].

3.3.3 ON-OFF Processing in the L2 Pathway

Encoding of whole-field increments and decrements in brightness in L2 axon terminal Ca^{2+} in the medulla was investigated by recording TN-XXL fluorescence changes in small arrays of up to six individually identifiable L2 axon terminals (Fig. 3.21a,b) per image sequence. Figure 3.21a depicts TN-XXL-expressing L2 axon terminals forming a retinotopic map (asterisk) in layer 2 of the medulla (the arrow indicates ommatidial lenses and cuticle, the arrow head indicates air sacs). A typical recording situation with four individually identifiable neighboring L2 terminals and their axons is shown in Figure 3.21b. Small non-uniform changes in Ca^{2+} induced by light-ON were observable. In one set of experiments (Fig. 3.21c) a single, spatially uniform pulse of light (8 s duration, dark-adapted eye, recordings interspersed by 60 s of darkness) elicited a small, slow increase in Ca^{2+} at the onset of the light pulse (5 flies, $n = 88$). In other experiments, however, a small negative change in Ca^{2+} induced by light-ON (Figure 3.22 a) could be observed. In contrast, brightness decrements induced a uniform, strong and long-lasting increase in Ca^{2+}. This calcium signal, induced by light-OFF, could be fitted by single exponential functions with a time constant of $\tau = 0.22\,\mathrm{s}$ to $0.26\,\mathrm{s}$ for the rise and $2.10\,\mathrm{s}$ for the decay (Figure 3.22b). The strong increase in Ca^{2+} in response to light-OFF suggests an inversion and half-wave rectification of the input signal in L2 axon terminals.

Changes in Ca^{2+} induced by individual light-OFF stimuli might superimpose in a linear way during periodic flicker. Alternatively, light-ON might affect the observed increase in calcium induced by light-OFF. It was found that increased Ca^{2+} in response to brightness decrements was effectively reduced to baseline following brightness increments (Figure 3.22a). Here, Ca^{2+} induced by the end of the first light pulse (1) was quickly reduced (black arrow) to baseline by the onset of a subsequent light pulse (2). The colored traces show the mean calcium response in the presence of a second pulse of light (interstimulus interval Δt: blue, 1.16 s; orange, 0.86 s; red, 0.56 s; green, 0.26 s; black, only first pulse; four flies, $n = 33$, 29, 41, 34 and 33 image sequences). The variability in the response was comparable to the results shown in Figure 3.21c and Figure 3.23. This finding is reflected in a much shorter time constant of the decay of this truncated calcium signal ($\tau = 0.26\,\mathrm{s}$ compared with 2.10 s; Figure 3.22b) that was the same for all of the interpulse intervals that were tested (0.26 s to 1.16 s; Figure 3.22a,b). Furthermore, brightness increments

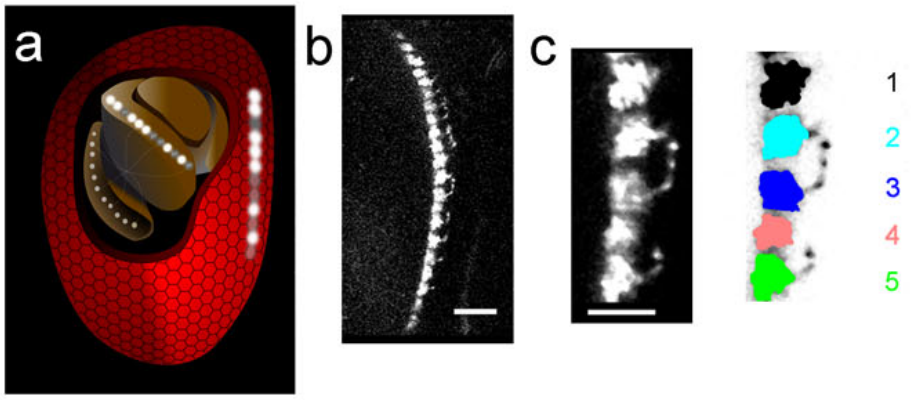

Figure 3.24: (**a**) Schematic drawing of the fly head and optic lobe during recording. (**b**) Two-photon image of a row of L2 axon terminals in layer 2 of the medulla. Scale bar represents 20 µm. (**c**) Five individually identifiable neighboring L2 terminals with different colors assigned to each throughout an image sequence. Scale bar represents 10 µm [71].

presented before the response to the preceding brightness decrement reached its maximum reduced the amplitude of the Ca^{2+} signal (Figure 3.22a). Thus, L2-terminals are sensitive to brightness increments. There was a small, non-uniform calcium signal induced by light-ON in the dark-adapted state, as well as a rapid reduction in Ca^{2+} if presynaptic Ca^{2+} was elevated from a preceding decrement in brightness.

Furthermore, the encoding of subsequent brightness increments and decrements in Ca^{2+} was tested by stimulating the eye of the fly with light flickering at 0.25 Hz (Figure 3.23a) and 1 Hz (Figure 3.23b). As expected, the L2 terminal Ca^{2+} rose in response to brightness decrements and was rapidly reduced to baseline by subsequent brightness increments. A full modulation of Ca^{2+} with maximum increase and full return to baseline was exhibited at 0.25 Hz (Figure 3.23a), whereas switching between brightness increments and decrements every 500 ms (1 Hz stimulus) led to a smaller modulation of Ca^{2+} superimposed on an ongoing positive component (Figure 3.23b). These results suggest that light-OFF induced Ca^{2+} and its rapid reduction by light-ON represent the main signal transmitted by L2. However, these results cannot reveal the frequency range that is transmitted by L2 axon terminals, as binding to and unbinding of calcium from TN-XXL results in substantial low-pass filtering of the unperturbed calcium signal [70] (Figure 3.22b).

3.3.4 Moving Visual Stimuli

Drifting visual gratings elicit modulations of the photoreceptor potential independent of the direction of motion. In contrast, tangential cells in the third neuropile of the optic lobe, the lobula plate, exhibit directionally selective responses (reviewed in [31,32]). These directionally selective cells are supposedly important for the control of visually driven optomotor behavior. In recent behavioral experiments [106], flies lacking the lamina neurons L1 and L2 were found to be motion blind [104, 105] and flies with L4 cells specifically blocked were also reported to be motion blind. Furthermore, anatomical connections in the lamina [26, 104] suggest that L2 and L4 are involved in a direction-selective pathway with higher sensitivity for the detection of front-to-back motion [104]. However, the output signals of L1 and L2 cells in the medulla during the presentation of moving visual stimuli

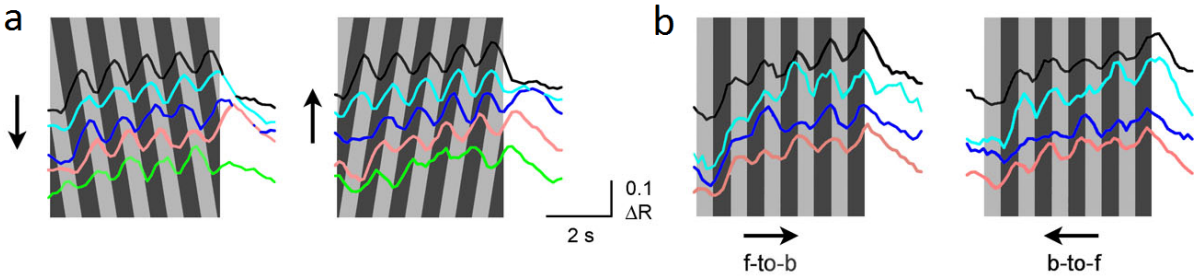

Figure 3.25: (**a**) Mean Ca^{2+} changes in individual terminals during down- and upward grating motion ($\lambda = 30°$, $\nu = 30\,°\,s^{-1}$, $f = 1\,Hz$, motion period $= 5\,s$). (**b**) Mean Ca^{2+} changes during front-to-back and back-to-front motion. Colors correspond to Figure 3.24c [71].

to the eye have not been analyzed so far. In the present work it was therefore set out to elucidate whether the calcium signals in L2 axon terminals in the medulla carry any sign of motion, orientation or direction selectivity, or whether they transmit signals that purely encode local luminance changes.

Visual gratings of 30° spatial wavelength moving at $30\,°\,s^{-1}$ were presented, resulting in 1 Hz temporal frequency, in four orthogonal directions (Figs. 3.24, 3.25 and 3.26). Time-locked to the visual stimuli, calcium-induced fluorescence changes were recorded from groups of individually identifiable L2 terminals in the same depth of the medulla (Figs. 3.20 and 3.24a). The L2 terminals were oriented along the dorso-ventral axis (Figs. 3.24 and 3.26). Grating motion elicited fluorescence modulations in the individual L2 terminals at a frequency of 1 Hz for all directions of motion. When motion was along the dorso-ventral axis, modulations in neighboring terminals were phase-shifted by $\pi/3$ (Figure 3.25a), corresponding nicely to the relationship between the interommatidial angle of about 5° in *Drosophila* [109] and the 30° spatial wavelength of the stimulus (that is, one-sixth). In contrast, motion along the horizontal axis elicited synchronous oscillations in neighboring L2 terminals of the same vertical row (Figure 3.25b), as was expected from their vertically aligned receptive fields (Figure 3.24a).

Front-to-back and back-to-front motion at a temporal frequency of 1 Hz elicited changes in Ca^{2+} that could not be distinguished from changes in Ca^{2+} induced by spatially homogeneous flicker at the same frequency (Figure 3.26). For the traces shown in Figure 3.25a,b and Figure 3.26, the plotted mean fluorescence signals were calculated from 23, 20 and 20 image sequences, respectively, that were recorded at the same position and animal. Similar experiments were performed in $n = 6$, 5 and 6 flies and 150, 130 and 250 image sequences.

Taken together, these results suggest that Ca^{2+} in L2 terminals predominantly encodes decrements in local brightness, irrespective of the direction of motion. This information is transmitted to postsynaptic neurons in the medulla while retaining the original resolution of the *Drosophila* compound eye [12].

3.3.5 Exclusive Photoreceptor Transmission to L2

In the lamina, photoreceptor signals from R1 to R6 are transmitted to four different cell types (Figure 3.27a). Achromatic brightness information perceived by these outer photoreceptors R1 to R6 is transmitted to three direct pathways to the medulla (L1 to L3) and to two indirect pathways (amc→L5 and L2→L4; in Figure 3.27a only amc is shown). L1

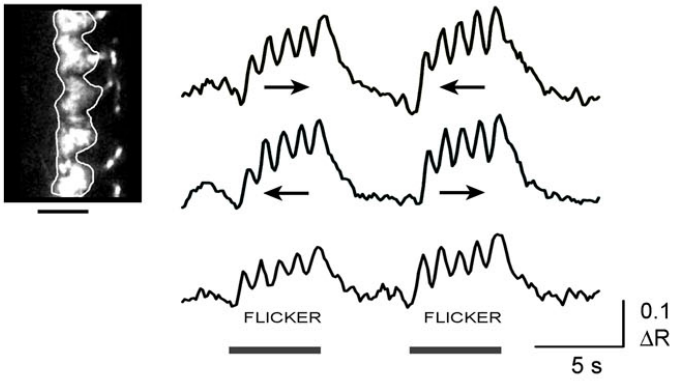

Figure 3.26: Fluorescence modulations in L2 terminals. Top trace: front-to-back motion was followed by back-to-front motion. Middle trace: reverse sequence. Bottom trace: 1 Hz flicker. Scale bar represents 10 µm [71].

to L3 and amc express the histamine-gated chloride channel encoded by the gene *ort* [118] and sense the photoreceptor transmitter histamine.

To test whether interactions between the different lamina cell types contribute to the observed calcium signals in L2, flies were investigated in which L2 neurons were the only interneurons to receive direct input from the photoreceptors [104]. In these L2 rescue flies, TN-XXL and the wild-type histamine receptor were specifically expressed in L2 neurons in a histamine receptor null mutant [104] (ort^1/ort^{US2515}; *21D-Gal4*; *UAS-ort*). As a control, ort^1/ort^{US2515} flies without L2 rescue did not show any transients in the electroretinogram (such transients at the begin and at the end of a light pulse reflect L1 and L2 activity [132]), were motion blind and their tangential cells in the lobula plate did not respond to large field motion stimuli, suggesting that photoreceptor-to-lamina transmission was completely blocked [104, 132].

In L2 rescue flies, a brightness decrement induced a strong and long-lasting increase in Ca^{2+} that was immediately reduced by a subsequent brightness increment (Figure 3.27b). Compared with wild-type flies, however, the time course of the recorded Ca^{2+} signal in L2 axon terminals was slowed. The time constants of the rise and the decay of Ca^{2+} were 0.80 s and 6.36 s, respectively (compared to around 0.26 s and 2.1 s; Figure 3.22). The time constant for the decay in the presence of a subsequent brightness increment was reduced to 0.34 s (Figure 3.27c). These results suggest that photoreceptor-to-L2 signaling and processing in L2 neurons was sufficient to qualitatively generate the observed changes in Ca^{2+}. However, the possibility cannot be excluded that L2 elicits activity in the surrounding medulla or neighboring lamina cells. Such feedback network activity could contribute to the observed characteristics of Ca^{2+}. Notably, the increased time constants for the rise and decay in the L2 rescue flies suggest that photoreceptor-to-lamina signaling in parallel channels is required for fast and temporally precise signaling.

3.3.6 Discussion

L2 cells have been implicated as major input elements to the motion detection circuitry in flies [104–107]. The data on L2 terminal Ca^{2+} presented here corroborate the previously reported inversion and high pass filtering [121–124] and complete the processing by adding

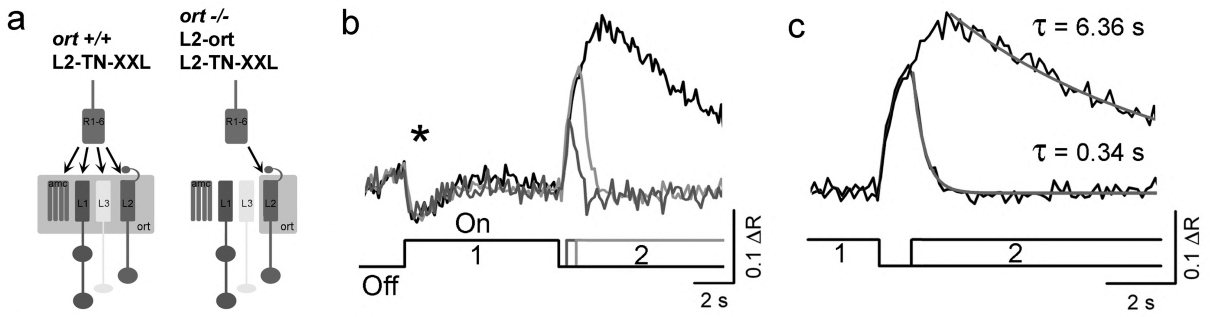

Figure 3.27: (**a**) Motion pathway connection schematic. Left: TN-XXL was specifically expressed in L2 cells. Right, mutations in the *ort* gene render amc and L1 to L3 insensitive to histamine [104]. Photoreceptor-to-L2 signaling is rescued exclusively in L2 cells. (**b**) Ca^{2+} changes in L2 rescue flies to successive light pulses (inter stimulus interval $\Delta t = 0.86\,\mathrm{s}$ (light gray) and $0.26\,\mathrm{s}$ (dark gray); $n = 3$ flies, 103 image sequences). (**c**) Decay of the OFF Ca^{2+} response in the reconstituted L2 pathway: $\tau = 6.36\,\mathrm{s}$ for the simple OFF Ca^{2+} and $\tau = 0.34\,\mathrm{s}$ when truncated by a consecutive light-ON stimulus (single exponential data fit, $R = 0.97$ and 0.94, respectively) [71].

half-wave rectification (Figure 3.21c and Figure 3.22a) of the brightness signal. Taking into account the role of Ca^{2+} in presynaptic vesicle release, it is proposed here that L2 primarily transmits the information about brightness decrements to the motion detection circuit in the medulla.

Dendritic recordings of L2 membrane potential in large flies show at least small depolarizing responses induced by light-OFF [121–125], suggesting that the underlying processing likely involves an amplification of the positive dendritic membrane potential and opening of voltage-activated Ca^{2+} channels in L2 terminals induced by light-OFF. Light-ON hyperpolarizes the L2 membrane potential [121–125], which might rapidly inactivate the calcium channels. Efficient calcium extrusion then likely mediates the observed rapid return of the calcium signal to baseline that is induced by light-ON [121].

Nonlinear processing steps represent an important feature of second-order visual interneurons in flies [121–124] and in the vertebrate retina; vertebrate ON- and OFF- bipolar cells preferentially relay either increments or decrements in brightness [133]. However, half-wave rectification in bipolar cells is not complete and partly results from inhibitory interactions among ON and OFF channels [134, 135]. The increase of the time constant observed in L2 rescue flies (Figure 3.27b,c) suggests that interactions between different lamina cell types are involved in the generation of imperfectly half-wave rectified light-OFF calcium responses in L2 axon terminals. Such interactions are also suggested by the rich anatomical connections at the level of the dendrites in the lamina [26] and at the level of the axon terminals in the medulla [24, 27]. Furthermore, given that L2 terminals transmit their main signal at light-OFF, other channels must exist for the signaling of brightness increments [113, 114]. Such ON and OFF signaling is a common motif in different animals and sensory modalities [136].

Although not necessary for Hassenstein-Reichardt-type computations [115] (Figure 3.19), half-wave rectifying the input signals into parallel ON and OFF channels and multiplying each pair separately allows the outputs to be treated in a sign-correct manner [1] (Fig-

ure 3.19). The devised stimulation and imaging approach should pave the way for future studies that ultimately reveal the cellular implementation of the HRM of visual motion detection.

3.4 Ego-Motion Coding in Descending Neurons

In many species, motion sensitive neurons responding to optic flow at higher processing stages are well characterized. However, less is known how this representation of ego-motion is further transformed into an appropriate motor response. The work described in this section sets out to analyze the visuomotor transformation from motion-sensitive neurons in the lobula plate (V2 and VS cells) onto premotor descending neurons (DNOVS cells) feeding into the motor circuit of the fly thoracic ganglion. The complete analysis is carried out in the large blowfly *Calliphora vicina* due to its amenable size for electrical recordings.

3.4.1 DNOVS cells

Optic flow is an important source of information for an animal about its ego-motion [137]. Accordingly, it is used to control walking [138], or to trigger landing [139] and to estimate travel distance [140]. Motion sensitive neurons analyzing this optic flow often have large receptive fields and are selective for particular flow fields. Well known examples are neurons in the lobula plate, the third optic lobe of flies [76, 141, 142].

In blowflies, a set of about 60 large-field motion-sensitive neurons in the lobula plate are involved in the processing of optic flow. These lobula plate tangential cells can be identified due to their invariant anatomy and characteristic visual response properties [31,38,78,143]. As one subgroup, the ten VS cells have large and complex receptive fields matching the optic flow that occurs during rotations of the fly around different body axes [36]. The directionally selective input from an array of local motion detectors [80, 144] together with the coupling amongst VS cells and other lobula plate tangential cells [39, 145, 146], are responsible for the VS cells' tuning to specific flowfields [40, 147].

The ten VS cells are major output elements of the brain and synapse onto premotor descending neurons feeding into the motor circuit of the fly thoracic ganglion [148]. The physiology and connectivity of two Descending Neurons of the Ocellar and Vertical System (DNOVS1 and DNOVS2) were described recently [146, 149]. Whereas DNOVS1 responds with a graded membrane potential shift, DNOVS2 responds with action potentials to motion stimuli. Both DNOVS cells are electrically coupled to different subsets of VS cells. DNOVS1 is most strongly coupled to VS 6 and VS 7 and DNOVS2 to VS 5 and VS 6. Neighboring VS cells are coupled more weakly to the descending neurons. DNOVS2 integrates additional motion information from the contralateral eye, probably via the V2 cell [149]. Although the specific wiring is already described, it is not yet clear why DNOVS cells integrate motion information from more than one VS cell.

In the present work the consequences of this connectivity pattern are elucidated by a precise comparison of the ego-motion representation in pre- (VS and V2 cells) and post-synaptic elements (DNOVS1 and DNOVS2). Stimulating the cells by large-field motion patterns presented on the stimulus device of Section 3.1, subtending 240° by 95° of the

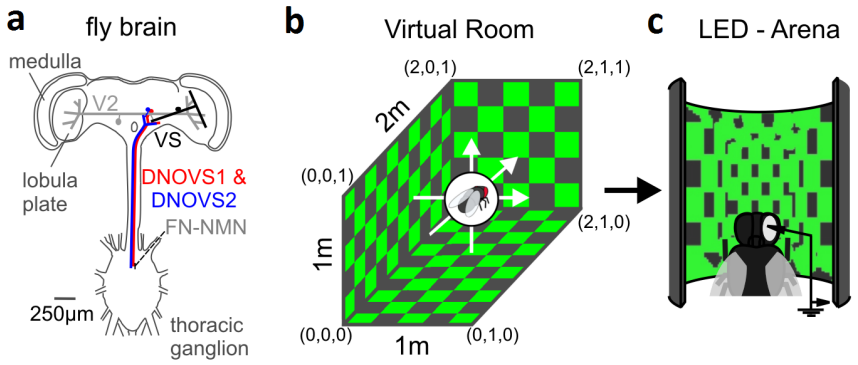

Figure 3.28: (**a**) Schematic drawing of the investigated neural network. (**b**) Stimulus movies are generated by moving a virtual fly along or around the x, y or z axes in a virtual room exhibiting a checkerboard pattern. (**c**) Movies are presented on the LED arena to a real fly while cells are recorded [150].

visual field of a fly, first the preferred axis of rotation of a cell is determined. Secondly, two major questions are addressed:

(i) Are DNOVS cells tuned to an axis of rotation more specifically than their presynaptic cells?

(ii) In what other respect does the representation of ego-motion in DNOVS cells differ from the one in lobula plate tangential cells?

3.4.2 Ego-Motion Preferences

In order to determine the preferred type of ego-motion of DNOVS cells and their presynaptic cells (Figure 3.28a), a virtual room with regularly tiled checkerboard walls, ceiling and floor is programmed such that a virtual fly can be translated along and rotated around the x, y and z axes (Figure 3.28b). This stimulus is denominated "checkerboard room" (see Appendix C). At every point in time, the environment is projected onto the virtual fly's eye and resulting movies are subsequently used as stimuli displayed to a real fly in the LED arena (Figure 3.28c).

All movies are shown consecutively, with motion first in one direction (black arrows, Figure 3.29a) followed by the opposite direction (red arrows), while recording from the neuron of interest. In the following, all responses are shown as if the fly was performing the motion in question. To all three translational and rotational movements, DNOVS1 depolarized in one direction and hyperpolarized in the opposite (Figure 3.29a). On average, the three rotational movements elicited a stronger response in DNOVS1 than translational motion (Figure 3.29b). DNOVS1 responded maximally to nose-down pitch, while counterclockwise roll movements or leftward yaw elicited weaker responses. Interestingly, a transient response of DNOVS1 was only observed for yaw movements. Whereas DNOVS1 responds with a graded shift of the membrane potential, DNOVS2 responds with action potentials to motion stimuli.

Peristimulus time histograms of one DNOVS2 cell (Figure 3.30a) and mean responses to all kinds of motion (Figure 3.30b) show that spike frequency in DNOVS2 was maximally increased for counterclockwise roll motion. Nose-up pitch and yaw elicited weaker

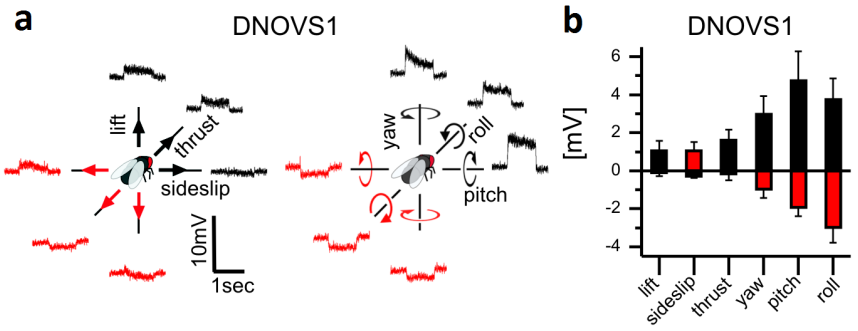

Figure 3.29: (**a**) DNOVS1 example responses to the three translations (lift, sideslip and thrust) and to the three rotations (yaw, pitch, and roll). The movies were shown for- and backwards, corresponding to opposite movement directions of the fly, indicated by the black and red color. (**b**) Mean responses ± SEM of DNOVS1 from $n = 6$ flies [150].

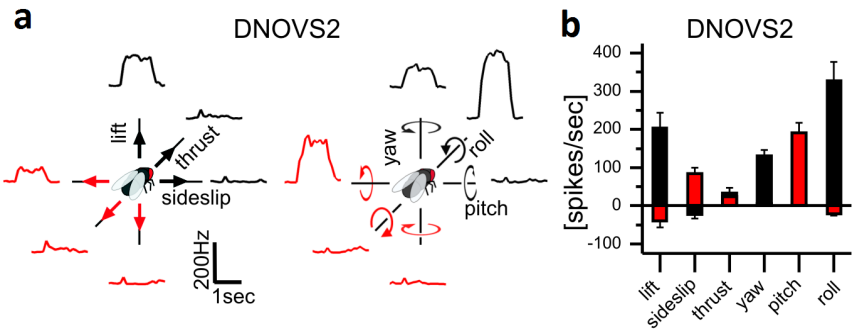

Figure 3.30: (**a**) Average peristimulus time histogram of the firing frequency of a DNOVS2 cell to the different movements (10 trials, bin size: 100 ms). (**b**) Mean response ± SEM of DNOVS2 from $n = 5$ flies [150].

responses. Whereas DNOVS2 responded only with slight increase to sideslip and thrust, it responded strongly to an upward lift.

To exactly determine the preferred axis of rotation of DNOVS1 and DNOVS2, the virtual fly was rotated around 36 different axes of rotation within the horizontal plane. Figure 3.31a depicts an example response of DNOVS1 to 12 rotations in the horizontal plane, separated by 30°. Again, the cell depolarized for rotation in one direction and hyperpolarized in the opposite. As the tuning curve of DNOVS1 to different axes of rotation showed sinusoidal response characteristics, a sine function was fitted to the tuning curve. For DNOVS2 a truncated sine function was fitted to the tuning curve as the hyperpolarization of the cell is limited by the non-negative firing frequency. These functions allowed for determining the response maxima which represent the preferred axis of rotation. Mean responses of DNOVS1 and DNOVS2 to all 36 rotations together with corresponding maxima are shown in color code in Figure 3.31b. Red represents depolarization of DNOVS1 or increase of the firing rate of DNOVS2, blue a hyperpolarization of DNOVS1. Maxima are marked by black stripes. Counterclockwise roll movement around the longitudinal body axis is defined as a rotation with a pole at 0°, nose down pitch with a pole at 90° and nose-up pitch with a pole at −90°. DNOVS1 depolarized to counterclockwise rotations around poles from 100° to −200°. The opposite movements elicited a hyperpolarization in

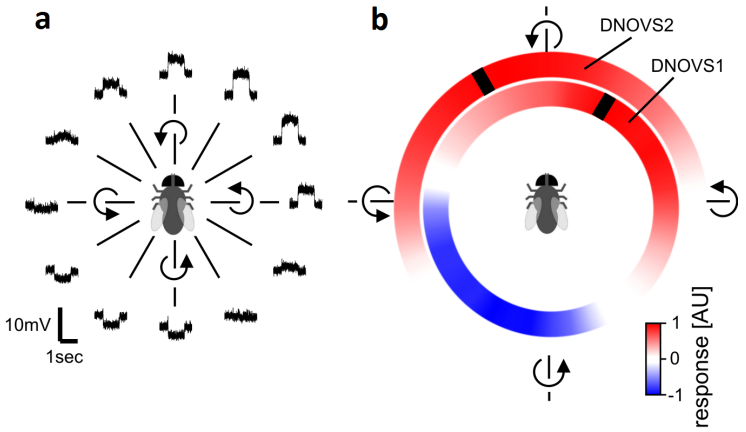

Figure 3.31: (**a**) Example responses of DNOVS1 to 12 different axes of rotation. (**b**) Mean responses to 36 axes of rotation of DNOVS1 ($n = 4$ flies) and DNOVS2 ($n = 3$ flies), shown in color-code. Red represents depolarization of DNOVS1 or increase in firing rate of DNOVS2, blue hyperpolarization. Black bar indicates preferred axis of rotation [150].

DNOVS1. DNOVS1 responded maximally to a counterclockwise rotation around an axis at an azimuth position of $32° \pm 3°$. DNOVS2 increased its firing rate for counterclockwise roll movements around poles from $-90°$ to $50°$ and its preferred axis of rotation was at an azimuth position of $-30° \pm 3°$.

3.4.3 Specific Rotation Axis Tuning

The question arises whether DNOVS cells are more specifically tuned to an axis of rotation than VS cells. To compare the global motion preferences of DNOVS cells with those of VS cells measurements were performed to analyze the response of VS cells to movements along (translation) and around (rotation) the x, y and z axes (Figure 3.32). As expected from their receptive fields [36] and previous global motion stimulations [151], rotations in the horizontal plane elicited the strongest response in VS cells.

To determine the preferred axes of rotation, responses of all VS cells to 36 rotations within the horizontal plane were measured as described above for DNOVS cells. In Figure 3.33a the mean response of all 10 VS cells to the 36 rotations is shown beginning with VS 1 plotted in the innermost circle and VS 10 in the outermost. Again, red represents a depolarization and blue a hyperpolarization of a given cell. From VS 1 to VS 10 the preferred axes of rotation leading to maximum depolarization shifted along the azimuth from $-93°$ to $75°$. Compared to DNOVS1, VS cells responded with larger graded potential changes up to 20 mV. VS 1 depolarized to nose-up pitch and nearby axes of rotation. VS 6 on the other hand responded with a depolarization to counterclockwise rotation around the longitudinal body axis with a pole of rotation approximately at $0°$ (roll motion of the fly). VS 10 was found to be most sensitive to rotations approximating nose-down pitch.

With the same set of stimuli V2 responses to different rotations were recorded (Figure 3.33b). Here, red represents an increase of the spike frequency. V2 responded to rotations from nose-down pitch to nose-up pitch with the strongest response approximately for counterclockwise roll. The preferred axis of rotation at $-7°$ is indicated by a black bar and was calculated by fitting a truncated sine function to the tuning curve of V2.

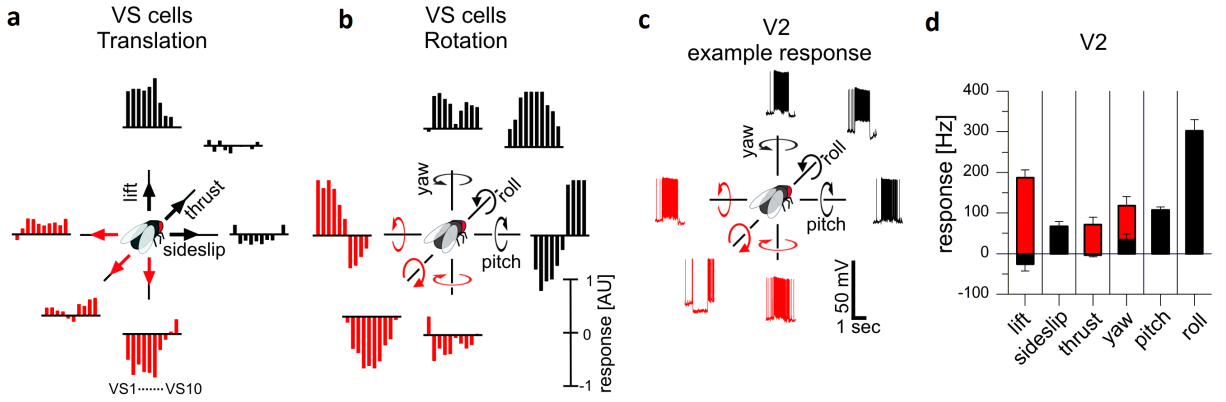

Figure 3.32: Responses of VS cells and V2 to translation and rotation (**a**,**b**) Mean normalized responses of 10 VS cells to translation (lift, sideslip, thrust) and rotations (yaw, pitch, roll). Bars represent mean of VS 1 ($n = 6$), VS 2 ($n = 2$), VS 3 ($n = 4$), VS 4 ($n = 6$), VS 5 ($n = 3$), VS 6 ($n = 5$), VS 7 ($n = 7$), VS 8 ($n = 5$), VS 9 ($n = 2$), VS 10 ($n = 1$). (**c**) Example response of V2 to three rotations. (**d**) Mean responses of V2 cells ($n = 4$) to the same global motion stimuli used in (a) and (b) [150].

To investigate whether DNOVS cells are more specifically tuned to their preferred axis of rotation than their presynaptic cells, tuning widths of VS, V2 and DNOVS cells were calculated. Tuning width was defined as the part of the response curve where over 50 % of the maximum response was elicited (Figure 3.33c). DNOVS1 was found to be coupled most strongly to VS 6 and VS 7 [82] and its tuning width proved similar to VS 7 (Figure 3.33d). The tuning width of VS cells decreased slightly from VS 1 to VS 10. For DNOVS2, the tuning width was similar to VS 5 and VS 6, while also being coupled most strongly to these two cells [149]. In addition, tuning widths of V2 and DNOVS2 were nearly identical. Thus, DNOVS cells are neither broader nor more specifically tuned to an axis of rotation than their presynaptic VS or V2 cells.

3.4.4 Robust Coding in DNOVS1

Modeling studies [77, 83] have suggested that electrical coupling between VS cell axon terminals should smooth out response fluctuations during rotation that arise from spatial inhomogeneities of the visual surround. Thus, at the output of VS cells, the representation of the axis of rotation should be robust even in presence of textureless patches of the visual surround. To investigate whether this robust coding can be observed also in DNOVS cells postsynaptic to VS cells, responses of DNOVS1 were recorded for comparison with VS 6 and VS 7 in the dendrite as well as in the axon (Figure 3.34a).

For the first experiments the “artificial room” stimulus was used (Figure 3.34b, see Appendix C). The stimulus sequence corresponded to the fly rotating around an axis of 30° in azimuth which approximately equates to the preferred axis of rotation of DNOVS1. The movie was presented for- and backwards representing clock- and counterclockwise rotations. To quantify response fluctuations over time the membrane potential distributions of the responses recorded in a VS 6 dendrite, a VS 6 axon and the DNOVS1 cell were quantified (Figure 3.34c-e). Blue and red histograms represent membrane distributions occurring during clock- and counterclockwise rotation, respectively. The black histogram represents

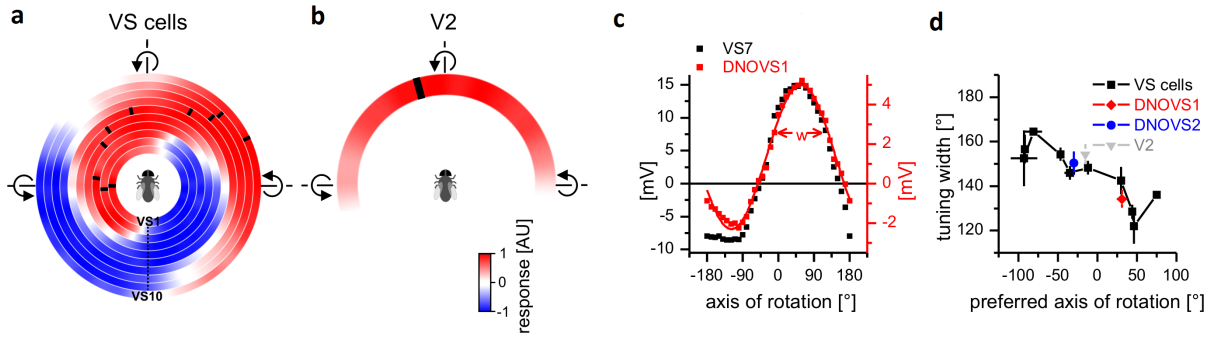

Figure 3.33: Preferred axis of rotation and tuning width of LPTCs and DNOVS cells. (**a**) Mean responses to 36 axes of rotation for 10 VS cells. Preferred axis of rotation (black ticks) shifts along the azimuth with increasing VS cell number. Data represents mean response of VS 1 ($n = 5$), VS 2 ($n = 3$), VS 3 ($n = 4$), VS 4 ($n = 6$), VS 5 ($n = 3$), VS 6 ($n = 5$), VS 7 ($n = 5$), VS 8 ($n = 4$), VS 9 ($n = 2$) and VS 10 ($n = 1$). (**b**) Mean responses to 36 axes of rotation of V2 cells ($n = 3$). (**c**) Tuning curve measured in DNOVS1 and VS7. Line drawn through DNOVS1 data points indicates fitted sinusoidal function (w denotes tuning width). (**d**) Tuning widths of DNOVS, VS and V2 [150].

membrane potential distribution when no stimulus was applied. The potential distribution indicates time-dependent membrane potential fluctuations. The more narrow the distribution is, the less fluctuation is found in the membrane potential, and, accordingly, the more robust the stimulus representation turns out to be. It was found that the fluctuations of the membrane potential were strongest in the VS 6 dendrite and decreased continuously via the VS 6 axon to the DNOVS cell (compare responses in Figure 3.34c-e). The same phenomenon was observed in potential distributions of VS 7 dendrite (Figure 3.34f) and VS 7 axon (Figure 3.34g). Here, the focus lay on VS 6 and VS 7 which are most strongly coupled to DNOVS1 [82], but similar results were found in neighboring VS cells (Figure 3.36).

In order to parameterize potential distributions from different recording sites the Fano factor was obtained by dividing the variance by the mean for both stimulus situations (Figure 3.34h). For VS axon and VS dendrite data VS 6 and VS 7 were pooled. Fano factors of DNOVS1 for both stimulus situations differed significantly from Fano factors of VS axon or VS dendrite. Thus, less variation in the response to these stimuli was found in DNOVS1. In other words, the axis of rotation is represented more robustly in the time-dependent membrane potential of DNOVS1 than in VS cells.

As a further test to this robustness the "natural room" stimulus was presented (see Appendix C), which contained a more naturalistic scene characterized by its irregular texture and inhomogeneous contrast distribution (Figure 3.34i). Yet again, the Fano factor of DNOVS1 was found to differ significant from the Fano factors of VS axon and VS dendrite adding further evidence to the robust representation of axis of rotation in DNOVS1. As a control the "checkerboard room" stimulus was used as described before (Figure 3.28b,c). Compared to the "artificial room" the "checkerboard room" had about the same mean luminance but a four times lower motion variance. For this stimulus, no significant difference of Fano factors between DNOVS1, VS axon and VS dendrite could be found. Thus, DNOVS1 responses are more invariant to the spatial structure of the environment than are

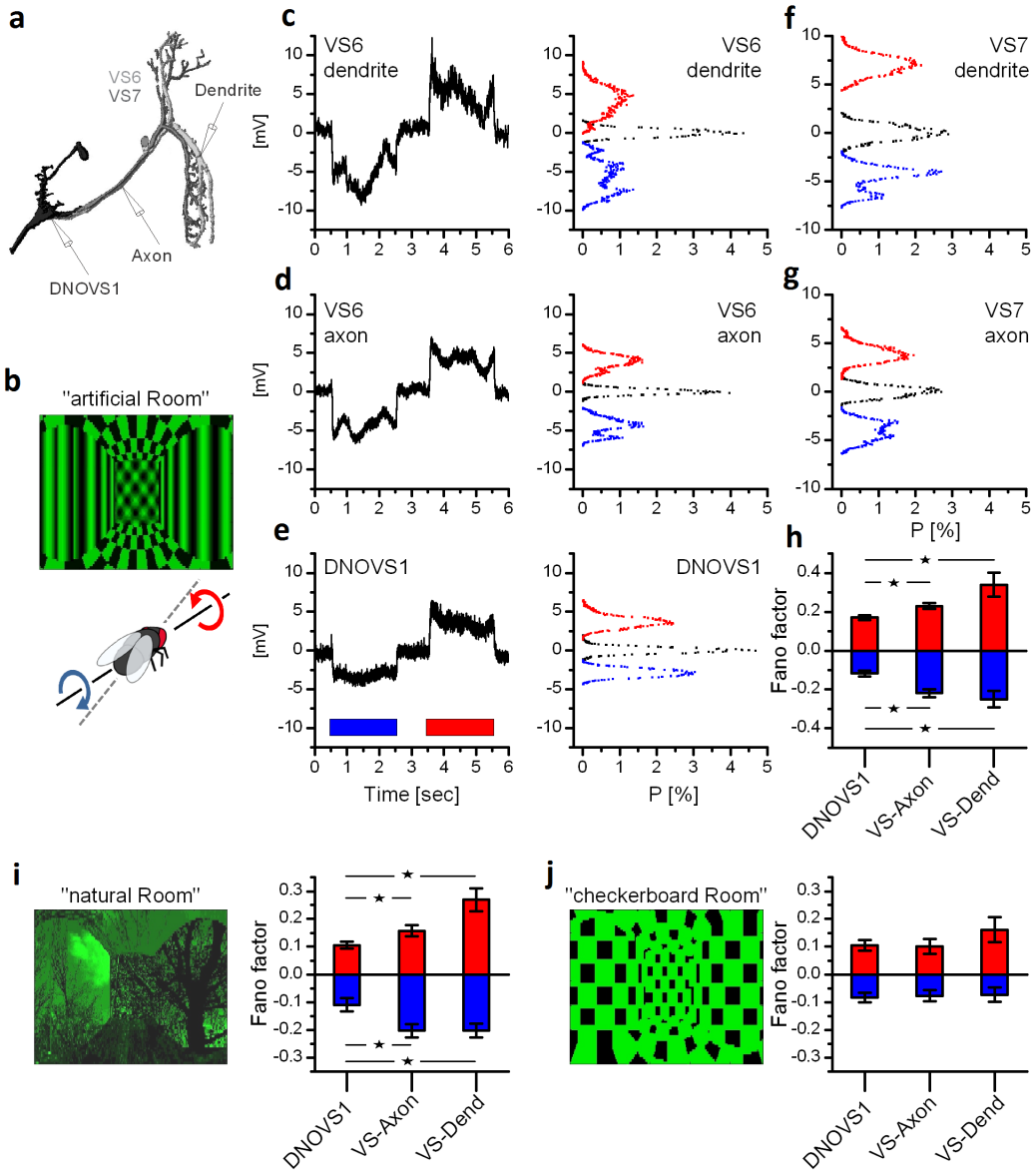

Figure 3.34: Robust coding of axis of rotation in DNOVS1. (**a**) Schematic drawing of the intracellular recording sites. VS 6 and VS 7 were recorded in the dendrite as well as in the axon, DNOVS1 in the dendrite. (**b**) "Artificial room" stimulus. (**c-e**) Average responses and membrane potential distributions of a VS 6 dendrite, VS 6 axon and DNOVS1 to clockwise (blue) and counterclockwise rotation (red). Black distributions represent variation of resting membrane potential. (**f**, **g**) Example membrane potential distributions of VS 7 dendrite and VS 7 axon. (**h**) Mean Fano factors of DNOVS1, VS axon and VS dendrite (pooled data from VS 6 and VS 7) for clockwise (blue) and counterclockwise rotation (red). Data shown from DNOVS1 ($n = 7$), VS axon ($n = 7$) and VS dendrite ($n = 12$). (**i**) "Natural room" stimulus. Data shown from DNOVS1 ($n = 8$), VS axon ($n = 5$) and VS dendrite ($n = 9$). (**j**) "Checkerboard room". Data shown from DNOVS1 ($n = 5$), VS axon ($n = 3$) and VS dendrite ($n = 8$). (*$p < 0.05$, Wilcoxon rank sum test) [150].

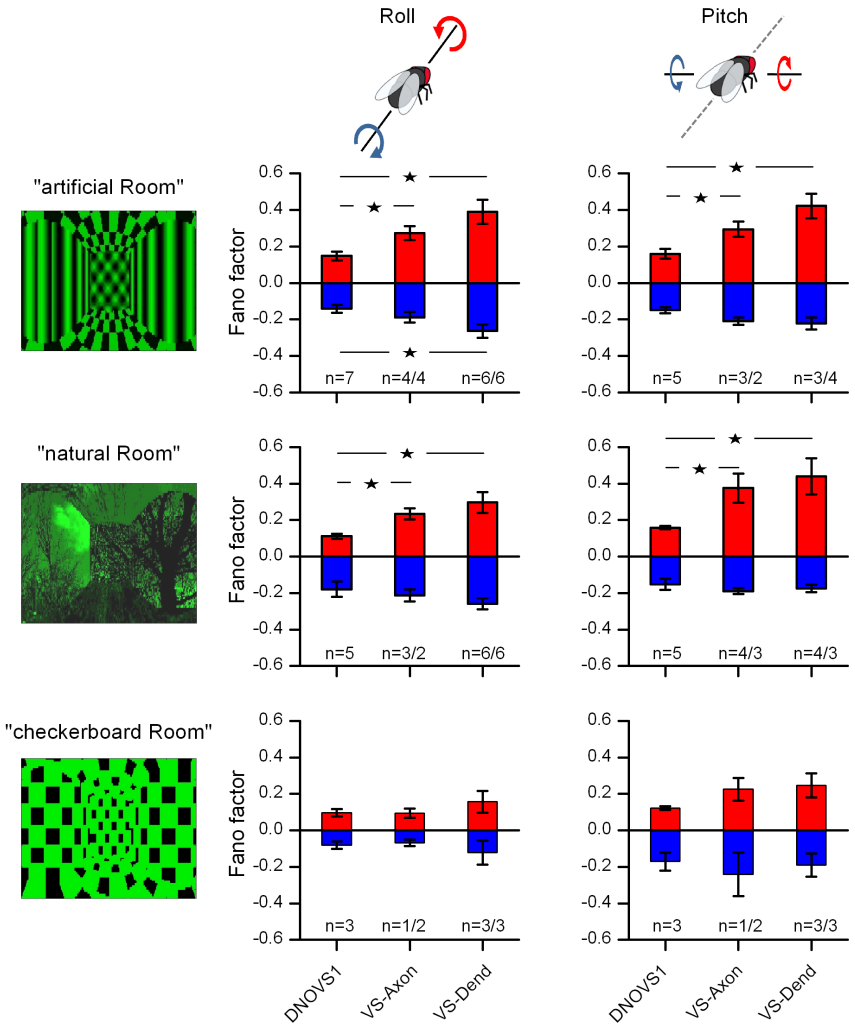

Figure 3.35: Robust representation of roll and pitch axis. Mean Fano factors of DNOVS1, VS axon and VS dendrite (pooled data from VS 6 and VS 7) for clockwise (blue) and counterclockwise rotation (red) around roll and pitch axis. Cell number counts are indicated in plots as $n = n_{\mathrm{VS\,6}}/n_{\mathrm{VS\,7}}$ (*$p < 0.05$, Wilcoxon rank sum test) [150].

VS cell responses. Similar results were found for pitch and roll movements (Figure 3.35) adding even further evidence to a robust coding of ego-motion parameters in DNOVS1.

3.4.5 Discussion

In this study, ego-motion tuning has been characterized in two descending neurons in the fly called DNOVS1 and DNOVS2, as well as in their presynaptic cells in the lobula plate. Both DNOVS cells are found to be tuned to rotations around different body axes (Figure 3.31). DNOVS cells are tuned neither more broadly nor more selectively to an axis of rotation than their presynaptic cells (Figure 3.33). However, DNOVS1 responses are found to fluctuate less during rotation of spatially inhomogeneous patterns than presynaptic VS cells (Figure 3.34 and 3.35). It can therefore be concluded that at the level of DNOVS cells a robust representation of ego-motion is obtained.

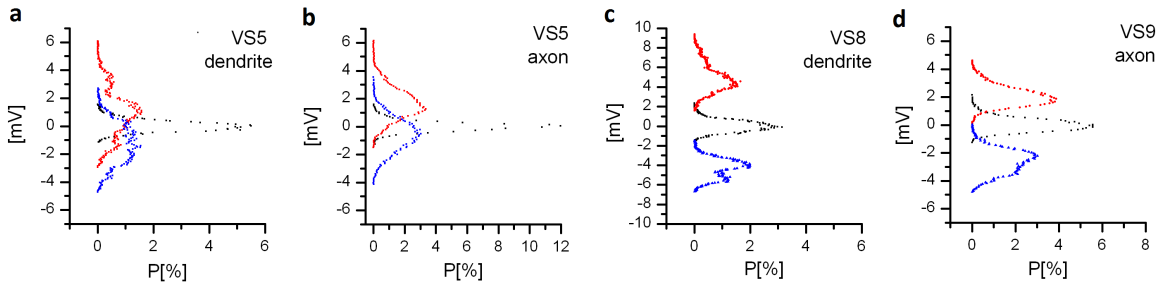

Figure 3.36: Membrane potential distributions from neighboring VS cells. Average membrane potential distributions recorded from VS 5 in the dendrite (**a**) and in the axon (**b**), from VS 8 in the dendrite (**c**) and from VS 9 in the axon (**d**). Also in VS cells next to VS 6 and VS 7, variation of the membrane potential decreased from dendrite to axon [150].

Given the linear integration found in DNOVS1 [82], no increase in response selectivity at this level in comparison to the presynaptic neurons would be expected. Nevertheless, as shown in Figure 3.33, this in fact is precisely what was found: the tuning width of DNOVS1 lies in the range of VS cells. However, responses of VS cells and DNOVS1 differed when using artificial or naturalistic stimuli with irregular contrast distributions as opposed to homogeneous contrast distributions (Figure 3.34). Compared to axonal or dendritic recordings of VS 6, VS 7 or neighboring VS cells (Figure 3.36), DNOVS1 responded in a more invariant way to these stimuli. This suggests that linear interpolation of VS cell output leads to a robust representation of the axis of rotation. Electrical coupling between VS cells [39] as well as electrical coupling between DNOVS1 and VS cells [82] is the most likely explanation for this robust coding. In a simulation study [77] it has been shown that a robust coding can be achieved through electrical axo-axonal coupling between VS cells. This finding was confirmed recently by calcium-imaging experiments revealing that axon terminal responses of VS cells are linear interpolations of dendritic responses of neighboring VS cells [147]. Since due to technical reasons measurements of the membrane potential in the axonal terminal of VS cells were not feasible, it is hard to determine whether this linear interpolation occurs exclusively in VS cells. However, DNOVS1 is electrically coupled at least to VS 6 and VS 7, suggesting that they form a functional syncytium which collectively is responsible for this robust coding. To avoid comparison of graded potential responses with action potential responses of DNOVS2, the present analysis focussed on DNOVS1. However, as DNOVS2 is electrically coupled to VS 5 and VS 6 [149], similar results are to be expected for DNOVS2. Thus, at the level of descending neurons not the selectivity but the robustness is increased when compared to VS cells.

DNOVS1 and DNOVS2 cells receive synaptic input from lobula plate tangential cells as well as from the ocelli via ocellar interneurons [82, 149]. The three ocelli are light sensitive organs and form a triangle on the dorsal surface of the head (for an overview see [152]). Stimulating the ocelli with an LED elicited short ON and OFF responses in DNOVS1 [82] as well as in DNOVS2 [149]. Directionally selective responses to UV-gratings have recently been described in ocellar interneurons of dragonflies [153]. In dragonflies [154] as well as in locusts [155], the ocelli are effective rotation detectors, crucial to proper gaze and flight stabilization. In blowflies it has recently been found that the ocellar component of V1's response appears to be tuned to rotation [156]. Whether these rotation-specific ocellar signals are transmitted to DNOVS cells or the ocellar component of DNOVS responses

itself is tuned to rotation is not yet clear. In addition to visual motion and stimulation of the ocelli, DNOVS cells also respond to air currents delivered to the antennae [157]. Thus, at the level of descending neurons like DNOVS cells, at least three sensory modalities are integrated. How the different modalities are integrated and whether they lead to a higher selectivity in DNOVS cells are still open questions and require systematical analysis of combinations of these modalities.

Functional Relevance

DNOVS1 and DNOVS2 project to the thoracic ganglion and there *inter alia* onto frontal nerve-neck motor neurons (FN-NMN) [148, 157]. 21 pairs of neck motor neurons have been identified, which are organized on each side as four neck muscle nerves innervating 21 neck muscles [158] involved in the fly gaze stabilization system. FN-NMNs innervate a variety of different neck muscles, which based on their anatomy [158] could potentially be involved in nose-up pitch, nose-down pitch, yaw and roll of the head. In addition, FN-NMNs are motion sensitive [159] and have receptive fields reminiscent of specific optic flow fields generated during pitch, a combination of pitch and roll and almost pure roll rotation [160]. DNOVS1 is tuned to a combination of pitch and roll, while DNOVS2 is tuned to an almost pure roll rotation. Thus, the synaptic connection between lobula plate tangential cells and descending neurons might be regarded as a coordinate transformation where, from the full set of preferred axes of rotation represented within the lobula plate, only those become transmitted towards the motor centers that are most appropriate for the muscles they finally innervate.

In contrast to the primary receptive fields of lobula plate tangential cells, most neck motor neurons have binocular receptive fields and are therefore more selective to rotation over translation than lobula plate tangential cells [160]. Although DNOVS2 is sensitive to contralateral motion in the presence of ipsilateral downward motion [149], contralateral motion alone elicited no response, neither in DNOVS2 [149] nor in DNOVS1 [82]. Thus, to achieve binocular receptive fields found in FN-NMNs [160], different descending neurons should converge onto FN-NMNs. The integration of binocular visual motion information at the level of descending neurons, such as was found for DNOVS2 [149] or at the level of neck motor neurons, are at least two possibilities to achieve a higher binocularity and thus a higher selectivity in FN-NMNs.

In addition, VS cells encode multiple preferred axes of rotation (Figure 3.33a and [36]). It has recently been shown that joint responses of different subpopulations of VS cells can provide unambiguous information about lift, roll or pitch components of an animal's ego-motion [161]. In that study it was proposed that the specificity to self-rotation is enhanced by subtracting the responses of two sets of VS cells from opposite sides of the visual sphere having the same preferred axes of rotation but with opposite directions. Whether postsynaptic descending neurons make use of this population code is not yet clear, as DNOVS1 integrates only ipsilateral motion. However, DNOVS2 increases its selectivity for roll movements by integrating motion information from the contralateral eye and could be the key player for encoding the roll axis. Therefore, to understand the transformation of the population code from lobula plate tangential cells onto descending neurons, further descending neurons like e.g. DNOVS3 or DNColHS [148, 162] need to be analyzed.

Flies rely heavily on optic flow in order to initiate landing when collisions are impending [163, 164] and to control course stability during flight [102, 165, 166]. Therefore, head rotations of blowflies effectively compensate part of the thorax rotations, resulting in improved conditions for vision [167, 168]. Between saccades the head is kept stable to maximize information of translational optic flow about the three-dimensional structure of the visual environment. During saccades, the head compensates most of the thorax rotation [168]. By minimizing head rotation duration, rotational optic flow is kept to a minimum and optic flow due to translation will then dominate. To achieve this, the fly gaze stabilization system consists of at least two visuomotor transformations:

(i) Integration of binocular visual motion information, increasing rotation selectivity of neck motor neurons [160].

(ii) Interpolation of VS cell output signals, leading to a robust coding of ego-motion parameters in DNOVS cells.

Both mechanisms are necessary to achieve an appropriate motor response.

3.5 Summary

The fly visual system is very well suited for research in how visual information is processed in neuronal pathways. This is mainly due to neuronal populations being preserved over individuals of one species and in general principle also across species. Therefore the same neuronal subpopulations may be observed and analyzed over many individuals. The main drawbacks, however, are small scale, relative inaccessibility and very fast response times of these neurons, thus complicating stimulation and recording of these cells.

In this chapter a visual stimulation apparatus and technique have been proposed. This stimulus solution consisted of an LED arena of high frame rates and high update frequencies, while maintaining a large field of view and sufficient optical resolution. Using this device three key aspects of fly motion vision were investigated. First, the general response properties of *Drosophila melanogaster* were analyzed and compared with those of bigger fly species, such as *Calliphora vicina*. Then, the fundamental motion detection scheme of *Drosophila* was assessed in regard to whether light increments and decrements are processed in separate pathways. Finally, the role of two descending neurons of *Calliphora vicina* were investigated.

The contributions of this chapter are manifold. Firstly, the proposed stimulus device enables electrophysiological and behavioral studies on the insect visual system that were previously not feasible. Owing to its high temporal and spatial resolution now basic problems in biology and information theory can be addressed, which have thus far remained elusive. Secondly, key aspects of the fly visual system have been elucidated. On one hand the response properties of *Drosophila* reveal fundamental similarities between fly species, suggesting uniform neural mechanisms across different dipteran species and most importantly the feasibility of using *Drosophila* for unraveling the neural implementation of elementary motion detection. On the other hand, it has been shown in this chapter that the *Drosophila* visual system in fact processes light increments and decrements in separate pathways. The L2 neuron was identified as a key player in processing light decrements. Finally, it has been shown in this chapter that in *Calliphora* the descending neurons

DNOVS1 and DNOVS2 show similar receptive fields when compared to their presynaptic VS cells, but in fact the robustness to noise is significantly augmented.

Taken together, the outcome of this chapter decisively enriches the toolkit for examining the insect visual system and provides meaningful insight into how the fly brain computes visual motion input. Substantial parts of this chapter have been published in [76], [71] and [150].

4 Insect-Inspired Rotation Sensing

In the preceding chapter key functional aspects of the fly visual system have been investigated. This chapter focuses on transferring and applying that knowledge to a technical system. Following the reported involvement of the VS cell network in visual rotation sensing in flies [36, 77], here, a visual rotation sensor is developed by recreating this VS cell network in hardware, oriented towards use on-board unmanned micro aerial vehicles (MAVs).

MAVs are inherently fast and highly unstable dynamic systems. For visual on-board rotation sensing it is therefore imperative to maintain sufficient temporal resolution as well as a large field of view (FOV) while keeping a certain level of optical resolution. Due to the complexity of achieving these feats simultaneously, there have been but few attempts of technical implementations of visual rotation sensing. Conventional approaches such as block-matching algorithms infer the pose of objects in the visual scene relative to the observer in time, thereby estimating relative rotation. Nevertheless, this is computationally expensive and not suited for use on MAVs. Biologically inspired algorithms, such as the VS cell network on the other hand offer a promising alternative well suited to this application. However, to the author's best knowledge there are no known works describing successful implementations using this VS cell approach for on-board calculation of rotations while maintaining similar spatial and temporal resolution over a similar field of view when compared to the biological original.

The innovation of this chapter lies in a pipelined parallel Field Programmable Gate Array (FPGA) based computing approach using dedicated hardware components with small footprints in terms of size, weight and power requirements. The main goal is keeping algorithmically as close as possible to the biological model and, thus, inheriting its characteristics and capabilities. Contributions are substantially higher performance in terms of frame rate, optical resolution, small size, low weight and low power requirements when compared to previous solutions, while performing all tasks strictly on-board the host MAV in real-time.

The remainder of this chapter is organized as follows: Motivation, background and previous solution strategies are outlined in Sections 4.1 and 4.2. The proposed design including implemented algorithms as well as hardware, firmware and software solutions is introduced in Section 4.3. In Section 4.4 the real-time performance of the elaborated system is assessed both in comparison to the biological model system as well as evaluating its sensor capabilities.

4.1 Motivation and Previous Work

Perception of visual motion has been an intense and fruitful field of research over many decades. Especially studies of insects—and flies in particular—have revealed astoundingly simple, yet robust and elegant solutions of extracting motion information from noisy and complex environments. Flies are able to autonomously navigate at very high speeds through highly unstructured settings, by and large relying only on visual cues. Despite having only a few 100 000 neurons, they are able to achieve these feats because of the highly optimized way these neurons are interconnected and the ideally suited basic operation principles of motion vision. Flies extract cues about motion relative to the environment from the *optic flow* at remarkably high temporal resolution. The true optic flow is the velocity field of the projection of the relative motion between observer and visual surroundings onto the retina [137]. Given that this true optic flow is not directly measurable it is estimated from spatiotemporal luminance patterns on the retina by dedicated neuronal circuits. Since these dedicated circuits are very effective, robust and efficient in terms of implementation they lend themselves well for technical applications.

4.1.1 State of the Art

In recent years unmanned aerial vehicles (UAVs) and micro aerial vehicles (MAVs) have become more and more common in tasks such as aerial reconnaissance, surveillance and exploration. To cope with the rising complexity of these challenges increasing levels of automation are needed. This usually leads to larger and computationally more intense solutions which require large on-board processing units (e.g. [169]) somewhat limiting their use on board small flying vehicles. One solution to this problem is "out-sourcing" of computational load to off-board computing platforms (e.g. [54, 63, 170]). This, however, is often not possible due to inadequacies of wireless transmission, such as low throughput, large delays, jitter, temporary loss of signal, etc. A promising way of solving these issues is the on-board use of highly efficient algorithms, such as those found in biological vision systems. In fact, over the past decades the insect visual system has inspired many studies towards visually guided autonomous vehicles. Much emphasis has been put on the implementation of collision avoidance strategies (e.g. [54, 171]) and local navigation (e.g. [20, 21, 55, 172–174]). Moreover, considerable work has been put forth on autonomous height control (e.g. [175, 176]).

Rotation Sensing

One aspect of fly motion vision that has received relatively little attention in technical implementations is rotation sensing. There have been studies on basic motion detection circuits for rotation detection [61, 177], but despite considerable advances in understanding of the fly neuronal rotation sensing circuitry [32, 36, 77] there have been few biologically realistic practical applications involving these findings. In [177] a rotation sensor using a custom aVLSI chip has been put forth that relies on basic motion detection circuitry for a one-dimensional circular array of 40 input photodiodes. The work in [61] uses a Field Programmable Gate Array (FPGA) based solution with a linear 12-photodiode array, theoretically capable of handling up to 245 input elements. In [62] a solution is proposed of higher spatial resolution at 120×100 input pixels over a 40° horizontal field of view and

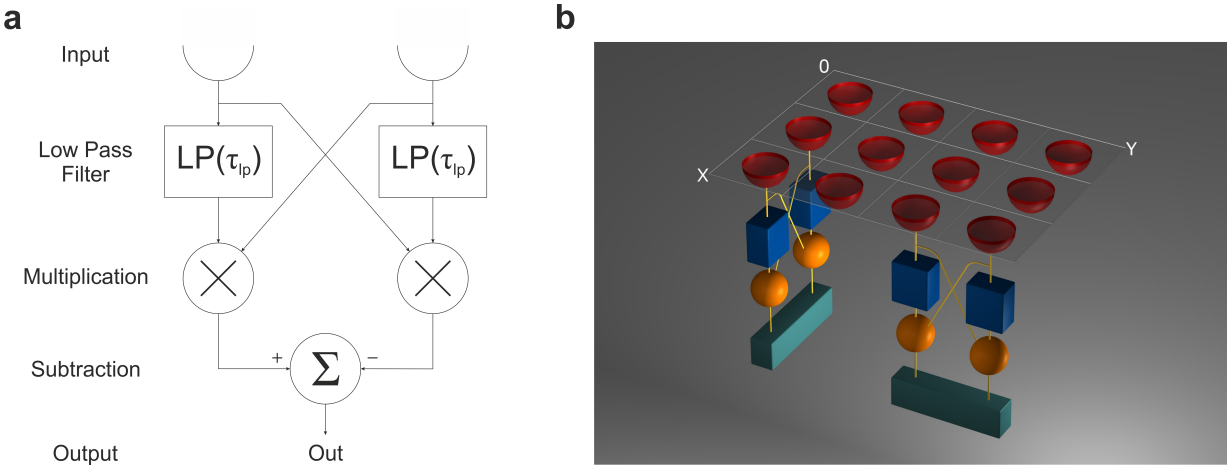

Figure 4.1: (**a**) Basic Reichardt Detector consisting of two mirror-symmetric units, each correlating one input with a low-pass filtered version of the other. Final subtraction of both sub-unit outputs yields a directionally selective signal depending on stimulus velocity and direction. (**b**) Two-dimensional arrangement of Reichardt Detectors giving rise to 2D local motion estimates by estimating vertical and horizontal components of local motion [3].

a temporal resolution of 100 frames per second (fps), expandable up to 200 fps in bright outdoor conditions. But despite promising results in artificially structured environments, the system did not work in naturalistic settings. A similarly oriented approach was used in [63]. They successfully implemented 256×256 motion detection circuits operating at 350 fps and six motion templates for template matching based motion detection. However, their system architecture residing on a PCI-FPGA card in a host PC forfeits use on board small aerial vehicles. Also, to the author's best knowledge there is currently no commercially available visual ego-rotation sensor for this specific purpose.

Therefore, main aim of the present work is the implementation of a small and lightweight fly-inspired visual rotation sensor for MAVs, keeping algorithmically as close as possible to the biological model while maintaining similar spatial and temporal resolution over a similar field of view.

4.2 Fly Visuomotor Loop

As outlined in Setion 2.1, the fly motion vision system can be segmented into several distinct functional and anatomical units. The input layer is the compound eye, which consists of a hexagonal array of several hundreds to thousands of *ommatidia*, each harboring a lenslet and a set of photoreceptor cells. This stage constitutes the retina, from where information is passed retinotopically on to three successive neuropiles, the lamina, medulla and lobula complex. In the medulla local motion estimates are computed according to the detector model put forward in [1], commonly known as the *Reichardt Detector* or elementary motion detector (EMD). As depicted in Figure 4.1a, the simplest form of the Reichardt Detector consists of two mirror-symmetric subunits, each correlating two spatially adjacent input signals with each other by multiplying one input signal with a temporally low-pass filtered version of the other (see Section 2.2). The output of both subunits is then subtracted, yielding a direction-selective output while suppressing non-

motion artifacts. This way of estimating motion is particularly well suited for applications in presence of noise, i.e. with poor signal to noise ratio [4, 178]. However, it is not a perfect velocity estimator as it depends not only on velocity but also on local texture and contrast [79,179]. Furthermore, individual local motion estimators suffer from the *aperture problem* due to their limited field of view [180].

To circumvent these problems flies spatially integrate local motion estimates over larger areas, thus to a large extent averaging out the aforementioned effects [80]. This is done in the lobula plate by large interneurons called lobula plate tangential cells (LPTCs). These neurons form an ensemble of roughly 60 uniquely identifiable cells, out of which two prominent groups—the vertical system (VS) and horizontal system (HS) cells—are preferentially sensitive to vertical and horizontal motion, respectively. Per hemisphere, the blowfly *Calliphora erythrocephala* possesses ten VS cells VS 1 through VS 10, whose dendritic receptive fields sequentially cover narrow but overlapping vertical stripes of the visual field, going around the dorso-ventral axis from frontal (VS 1) to caudal (VS 10). Each VS cell integrates the responses from local vertical motion detectors within its own specific receptive field. Strikingly, the response of VS cells in their axon terminal regions suggest much broader receptive fields [147]. This broadening of the axon terminal response has been shown to be caused by gap junctions interconnecting the VS cells [39, 40, 84]. Furthermore, VS 1 and VS 10 cells mutually inhibit each other [39, 146]. This gives rise to the VS cell network illustrated in Figure 4.2a with its associated connection strength matrix given in Figure 4.2b. The reason for this network scheme is thought to be strengthening of robustness to inhomogeneities of pattern contrast, i.e. making this system more suitable for use in naturalistic environments [77, 147, 150]. Note that the model analyzed here additionally includes the effect of the HSN cell on the dendritic compartment of VS 10, thereby accounting for reported responses to dorsal horizontal motion [36, 145, 146].

The responses of the VS cell network in its axonally coupled form can be used to robustly infer the approximate center of rotation for rotations around axes lying on the equatorial plane [77]. Due to their vertical directional sensitivity, the VS cells on one side of the center of rotation will respond by hyperpolarizing, while to the other side they will depolarize. The location where VS cell responses change signs, i.e. the *zero-crossing* location, indicates the approximate location of the center of rotation.

Finally, this motion information is projected directly onto neck motorneurons or via descending neurons onto motor neurons in the thoracic ganglion [82, 148–150]. These motor neurons act upon the neck-, wing- and leg muscles that determine the animal's course, thereby constituting the last step of the fly visuomotor loop.

4.3 System Design

4.3.1 Requirements and Restrictions

The goal of this study is the construction of an optic flow based sensor system that is algorithmically as close as possible to the biological original of the fly visual system, in particular the VS cell network. Therefore the design requirements include similar spatiotemporal resolution and field of view (FOV) when compared to a fly, as well as reasonable light weight, low power consumption and compact size [181].

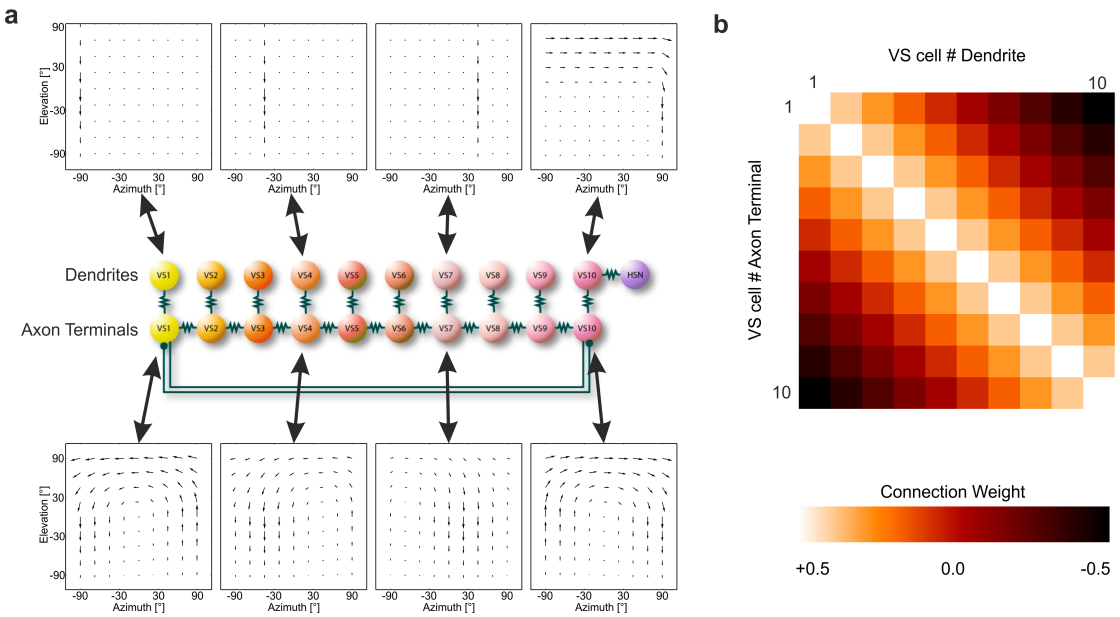

Figure 4.2: (**a**) VS cell network showing coupling between adjacent cells in their axon terminal regions, including bi-directional mutual inhibition between VS 1 and VS 10. HSN and VS 10 are connected directly in the dendritic regions. Ideal receptive fields of individual cells are shown for both the dendritic and the axon terminal regions. (**b**) Connection strength matrix for network coupling. The axon terminal output of a cell is exited strongly by its own dendritic input, slightly less by its immediate neighbors, little by more distal cells and even inhibited by most distal cells [3].

The blowfly *Calliphora* is able to detect flicker up to rates between 200 Hz and 300 Hz [66] or even higher [67]. Thus, the design goal is set to achieve frame rates well above 300 fps, exceeding cutoff frequencies of 150 Hz. Each compound eye of *Calliphora* extends about 190° in the horizontal and 198° in the vertical plane [11]. To achieve a large FOV the camera system is equipped with a fisheye lens covering a solid angle of approximately 2π sr, i.e. half of the unit sphere. The highest spatial resolution found in *Calliphora* amounts to inter-ommatidial angles of $\Delta\varphi = 1.07°$ [69] and is reached in the frontal visual field [182]. Thus, to obtain a spatial resolution better than 1° per pixel in the frontal part while using a 185° fisheye lens the sensor system needs to have a resolution of at least 185×185 pixels. Commonly found MAVs are able to carry payloads only up to a few hundred grams. The envisaged primary test platform for this sensor system is the AscTec Hummingbird quadrocopter (Ascending Technologies, Krailling, Germany), which features a payload of up to 200 g. Hence, the weight restrictions of the sensor system are fixed to an upper limit of 200 g. Due to these weight restrictions also battery power on board is limited. Power consumption restrictions are thus limited to a permissible maximum of 4 W. In terms of size the system is required to be able to be mounted on such an MAV without interfering much with its aerodynamics.

4.3.2 Computations

The computation of rotational axis and velocity estimates is divided into the following five pipelined sequential steps:

(i) **Image acquisition** is done by the image sensor in a row-wise fashion pixel by pixel at full frame rate.

(ii) **Pre-processing** suppresses illumination artifacts by automatic gain adaptation and homomorphic filtering.

(iii) **Local motion detection** is performed using a Reichardt Detector correlation model.

(iv) **Global motion integration** is achieved by wide-field integration of local motion estimates.

(v) **Rotation estimation** is accomplished by calculating location and slope of the VS cell network zero-crossing.

The individual processing steps are described in more detail in the following sections.

Pre-Processing

At the core of this sensor design lies the aforementioned Reichardt Detector, also known as Elementary Motion Detector (EMD). An EMD inherently displays a quadratic dependence on image contrast which makes it also sensitive to changes in overall lighting. To improve robustness against lighting changes a homomorphic filtering approach [183] was applied as a pre-processing stage to the EMD. In a visual scene, illumination and reflectance combine multiplicatively and are therefore not linearly separable. Nevertheless, they usually occupy distinct regions in the frequency domain since illumination tends to vary slowly in time and space while reflectance provides mostly high temporal frequency components due to reflections from objects. For a given pixel in an image its value is given by

$$I(x, y, t) = L(x, y, t) \cdot R(x, y, t) \tag{4.1}$$

where $I(x, y, t)$ represents the value of the pixel at location (x, y) at time point t, while $L(x, y, t)$ and $R(x, y, t)$ represent illumination and reflectance for that location and time point. By taking the logarithm of the pixel value these two components become additive (Eq. 4.2) and the low frequency illumination components can be filtered out using a high-pass filter, leaving only reflectance (Eq. 4.3).

$$\log\big(I(x, y, t)\big) = \log\big(L(x, y, t)\big) + \log\big(R(x, y, t)\big) \tag{4.2}$$

$$\mathrm{HP}\Big(\log\big(I(x, y, t)\big)\Big) \approx \log\big(R(x, y, t)\big) \tag{4.3}$$

Using this homomorphic filtering technique the elaborated Reichardt Detector used for final implementation effectively included a logarithmic stage via lookup table and a first order temporal high-pass filter acting together as an input stage to a basic EMD (Figure 4.3a).

To further optimize the dynamic range of the image sensor pixel values over a large illumination range an automatic camera gain adaptation control was implemented. The temporally low-pass filtered mean pixel values of each frame ($\tau_g = 1\,\mathrm{s}$) were utilized as a crude measure for overall illumination. A simple proportional controller was used to adjust the internal camera gain as to keep the mean pixel values reasonably centered within the sensor coding range.

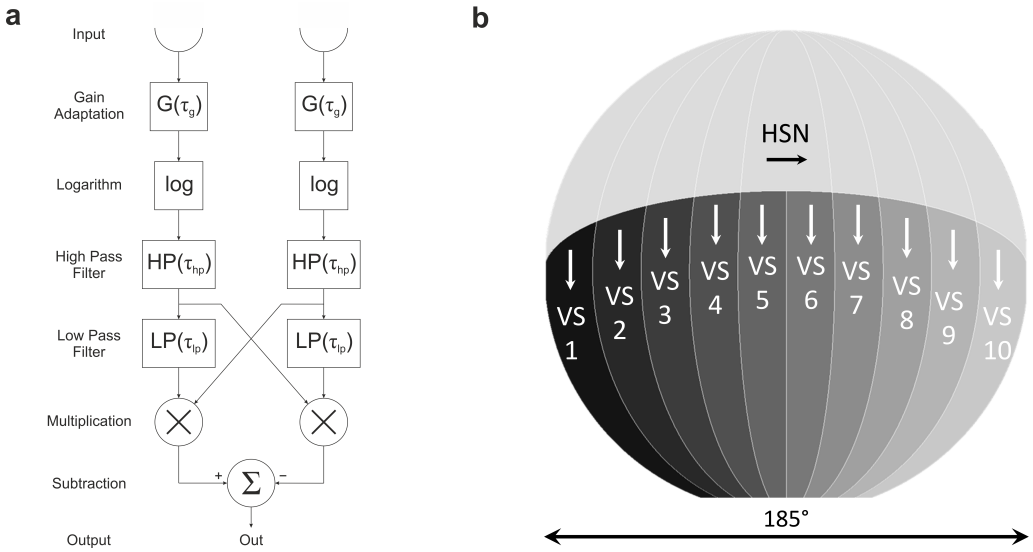

Figure 4.3: (**a**) Elaborated Reichardt Detector including automatic gain adaptation and a homomorphic filtering stage sequentially connected giving input to a basic Reichardt Detector. (**b**) VS and HSN cell dendritic field distribution over the half sphere captured by the $185°$ fisheye lens showing direction of motion sensitivity of each cell [3].

Local & Global Motion Detection

For local motion detection of each pixel the elementary Reichardt Detector of Figure 4.1a was used in conjunction with a homomorphic pre-processing stage, constituting the elaborated EMD (Figure 4.3a). Each incoming pixel value is thusly correlated with its immediate horizontal and vertical neighbor, giving rise to a two-dimensional (2D) local motion estimate (Figure 4.1b).

For wide field integration of these local motion estimates a network akin to the Calliphora VS cell network was established. For all ten VS cell homologues the vertical components of local motion estimates within their respective receptive fields are linearly summed up. For the three HS cell homologues this was done for the respective horizontal components. The ten VS cells' receptive fields are linearly spaced along the equator, each covering a tenth of the fisheye lens projection on the image plane, ranging from VS 1 on the far left up to VS 10 on the far right (Figure 4.3b). Similarly, the HSN receptive field covers the upper third of the lens projection (Figure 4.3b), the HSE receptive field the middle third and the HSS receptive field the lower third. The HSE and HSS cells, however, were not used for rotation sensing and therefore included for future extensions only.

To improve robustness as in the biological original [77] the cells in the network were interconnected as outlined in Figure 4.2. In this wiring scheme adjacent cells are strongly coupled while most distant cells are mutually inhibitory, as indicated by the connection matrix of Figure 4.2b. This yielded a robust and symmetrical response pattern of the network.

Rotation Estimation

Estimation of the axis of rotation based on the VS cell output relies on the fact that VS cells' receptive fields resemble matched filters for rotations around rotations sequentially

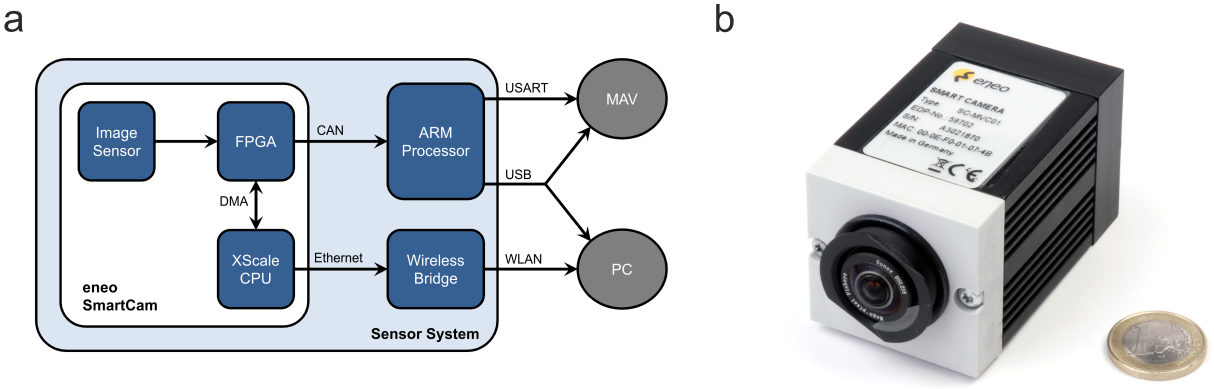

Figure 4.4: (**a**) General system architecture. At the system core lies an eneo SmartCam with its embedded FPGA and XScale processor, weighing 148 g including the fisheye lens and consuming 1.69 W. Further processing and communication with the MAV and an optional real-time data acquisition PC is carried out using an ARM processor hosted on a custom PCB weighing 30 g and consuming 0.51 W. For wireless transmission of live images and processed data towards the PC ground station the eneo SmartCam Ethernet port is used via a wireless bridge weighing 15 g and consuming 1.47 W. Total system weight was 193 g while consuming a total of 3.67 W. (**b**) eneo SmartCam including 185° fisheye lens in size comparison with a €1 coin [3].

arranged around the dorso-ventral axis on the equatorial plane [36]. As introduced in Section 4.2, by calculating the zero-crossing location of the VS cell network responses the center of rotation can be inferred. Furthermore, at that location the slope of the curve is strongly correlated with the rate and direction of rotation. If the curve has a positive slope going from a negative VS 1 response to a positive VS 10 response the rotation of the visual scene is clockwise. Accordingly, a negative slope indicates a counter-clockwise rotation. Also, a fast rotation would produce a steep slope, whereas slower rotations would yield a more shallow slope. Hence, this slope magnitude correlates directly with the rate of rotation, albeit in a non-linear bell-shaped fashion.

4.3.3 Implementation

Components Overview

The key challenges of the implementation of this sensor system were the high computation rate and small footprint required. For the computing platform the typical choices were off-board computation on a PC or on-board computation using microcontrollers, microprocessors, programmable logic or fully custom designed chips. For the off-board computation the images would have to be first sent from the MAV to the PC, which with the current wireless transmission standards such as WLAN, ZigBee or Bluetooth is not yet possible at frame rates much higher than around 100 frames per second. Therefore the choices were limited to on-board solutions, of which due to the high throughput requirements and size / weight constraints microcontrollers and sequential general purpose microprocessors were ruled out. Fully custom designed Application Specific Integrated Circuits (ASICs) were not an option due to their high cost and time consuming design cycles. Since optic

flow calculations are highly parallel FPGAs were the ideal choice owing to their inherently parallel and pipelineable nature, thus permitting high throughputs.

As the core image capture and processing unit an eneo SmartCam SC-MVC01 module (Videor, Rödermark, Germany) was chosen, being able to provide a spatial resolution of 640×240 pixels at 390 fps at 8 bit resolution in row interlaced mode. It features a 1/2 inch Micron MT9V403 CMOS image sensor, an Intel XScale PXA255 processor running at 400 MHz, a Xilinx Spartan-3 series XC3S1000 FPGA and an Infineon HYB25L256160AF 256 Mbit Mobile-RAM module accessible freely from the FPGA. Using a 185° DSL215B-NIR miniature fisheye lens (Sunex, Carlsbad, USA) and a custom built light weight camera backplane the camera possessed a $72\,\text{mm} \times 45\,\text{mm} \times 45\,\text{mm}$ footprint weighing 148 g. Additional processing was carried out on an Atmel AT91SAM7A3 ARM processor (Atmel, San Jose, USA) on a custom designed printed circuit board (PCB) also housing power conversion circuitry and communication interfaces. Overall hardware costs amounted to approximately EUR 2 000.

In order to monitor the outcome of the optic flow calculation, ego motion estimation and the captured camera images, a wireless communication system was used to communicate with an external laptop PC (Dell, Round Rock, USA) hosting a control and monitoring interface. A general schematic of the system hardware architecture is given in Figure 4.4.

FPGA Design

Pre-processing, computation of the local motion estimates and subsequent spatial integration was implemented on board the Xilinx Spartan-3 FPGA using VHDL. The internal design was broken down into several modules dealing with specific tasks, such as image data acquisition from the image sensor, local motion estimation, external SDRAM communication and management, large field integration of local motion estimates, internal timing management, communication with the off-board ARM processor and monitoring PC, etc.

The fisheye lens projects a centered circular image onto the imager's row interlaced 640×240 pixels, but only the central 240×240 pixels were used. To estimate local motion, each pixel was correlated with the adjacent left and upper pixel, using the elaborated EMD, resulting in a two-dimensional local motion vector for each pixel. The distance between EMD input arms $\Delta\varphi$—equivalent to the fly's inter-ommatidial angle—is thus equal to 1 pixel, which in the frontal part of the the FOV equates to $\Delta\varphi = \frac{185°}{240} = 0.77°$.

Taking advantage of an FPGAs inherent parallel capabilities, the local motion estimate computation was implemented in a pipelined fashion, thus, reducing the elaborated EMD to 15 atomic instructions (such as memory fetch, table look up, multiplication, sum and subtraction operations), each being executed in strictly less than 20 ns (Figure 4.5). For multiplication, dedicated hardware multipliers of the Spartan-3 series were used. EMD computations were carried out at 18 bit Q10.7 fixed point precision, thereby accounting for fractional results ensuring minimal loss of precision through truncation.

The elaborated EMD incorporates temporal low-pass and high-pass filters whose immediate results need to be stored between image cycles, yielding an amount of data of over four times the total internal Block RAM storage capacity of the Spartan-3 XC3S1000. Therefore, the external SDRAM attached to the FPGA needed to be used to store and retrieve inter-frame filter data. An SDRAM controller module loosely based on application notes [184, 185] was implemented, operating in half-duplex mode at 100 MHz and a 16 bit data bus width.

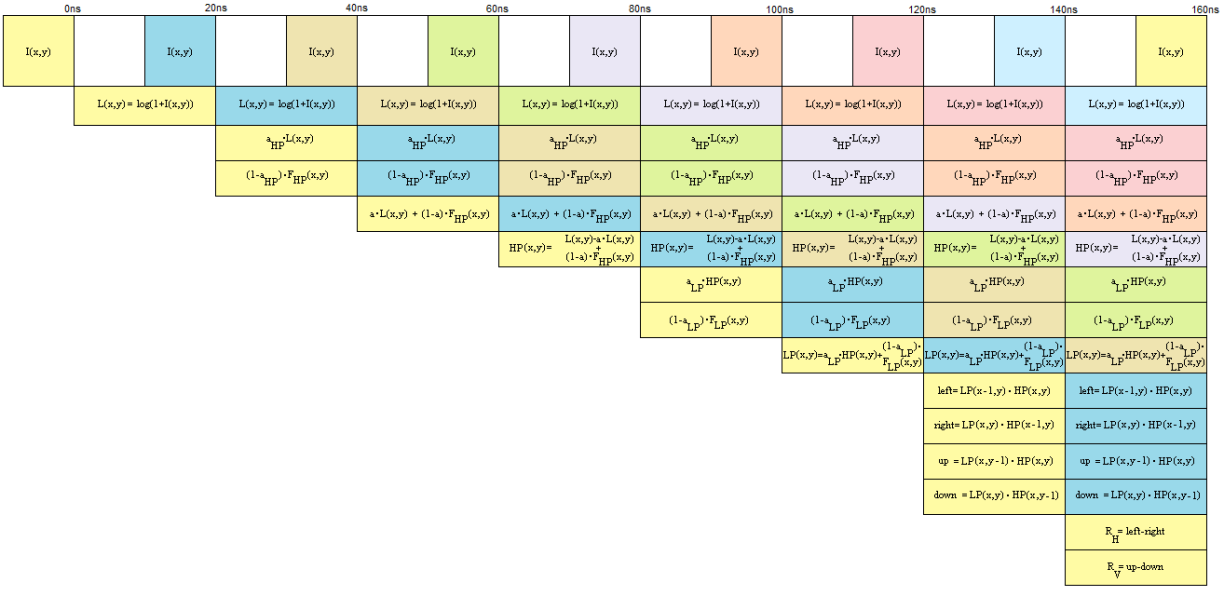

Figure 4.5: Pipeline timing diagram. In this schematic $I(x, y)$ is the 8 bit pixel value at location (x, y). a_{HP} and a_{LP} represent high- and low pass filter coefficients, respectively. Final outcome of the pipeline is the horizonal (R_H) and vertical (R_V) Reichardt Detector outputs, representing x and y components of a 2D vector. Same colors indicate data processing of the same pixel through the pipeline. Elementary time step is 20 ns [3].

A wide field integration module was written to calculate the dendritic part of the VS cell network output from the local motion estimates via Boolean map lookup, yielding one scalar value for each VS and HS cell.

Also a communication module was implemented for relaying the resulting wide field integration data at full frame rate towards the external ARM processor. The SmartCam hardware was modified in a way that its High Speed CAN bus output could be used directly by the FPGA. For establishing the communication with the ARM processor a custom CAN bus controller FPGA core operating at 1 Mbit/s was written. The communications module also handles data transfers from and towards the SmartCam internal Intel XScale processor via the shared 64 MByte SDRAM memory between FPGA and XScale processor using Direct Memory Access (DMA).

Using a speed optimized XST synthesizer the complete design occupied 47% of available slice flip flops, 69% of all 4-input look up tables (LUTs) and 83% of available block RAM of the Spartan-3 XC3S1000.

XScale Firmware

The internal Intel XScale processor of the SmartCam module controls several variables and parameters of the image sensor, such as operation modes, buffer sizes and frame rate. These parameters along with incoming image data are transferred via DMA through the shared SDRAM memory. For communication towards an external PC the SmartCam features a 10/100 Mbit/s Ethernet MAC/PHY directly connected to the processor. Its operating system is an embedded Linux Kernel 2.6.6 for which a resident camera daemon application was written in C++ that takes care of initialization routines, handshaking protocols and

communication between XScale processor and FPGA as well as between XScale processor and the ground station PC. To communicate wirelessly between camera system and ground station PC the internal PCB of an Asus WL-330gE wireless bridge (Asus, Taipeh, Taiwan) was used. One transmitted data frame consists of an image, local motion estimates and the associated wide field integration results.

ARM Firmware

For further processing of the raw wide field integration data computed on board of the FPGA the XScale processor was unsuitable because of the lack of interfaces towards the MAV and the difficulty of allotting well-defined time slots for real-time processing. Therefore, a custom 60 mm × 60 mm PCB featuring an AT91SAM7A3 ARM processor and interface logic has been developed. Its primary objective is the extraction of axis of rotation and rotation rate from the raw wide field integration data, calculated on the FPGA and transmitted towards the ARM processor via CAN bus at full frame rate in simplex mode. As shown in [77] during rotations the fly's VS cell network and its lateral axo-axonal gap junction couplings provide a robust way of encoding the axis of rotation. This *zero-crossing* strategy was implemented on the ARM processor. The axon terminal output of each VS cell was calculated as the weighted sum of the incoming dendritic VS cell data according to the matrix and connection diagram given in Figure 4.2. As dendritic VS 10 input into the network the simple sum of pure dendritic VS 10 and HSN values was used. Subsequently the axis of rotation is obtained by determining the zero-crossing location of the resulting ten axon terminal VS cell values. For a crude estimate of the rate and direction of rotation the slope at the zero-crossing location is calculated. Both rotation axis and rate are then further transmitted at full frame rate towards the MAVs flight controller via USART. A USB 2.0 link was also implemented for data transmission towards the MAV or an external PC, e.g. for data logging.

Thus, the interface array on board the PCB consists of two CAN bus ports for accepting incoming data from two independent SmartCam modules, a USART port for communication with the MAV and a microUSB port for MAV communication or optional data logging. An MMC/SD card slot is also provided for future on board data logging, e.g. during flight. For power conversion to the SmartCam's voltage requirements of 24 V a Traco Power THB 3-1215 converter (Traco Electronic AG, Zürich, Switzerland) has been included, which additionally strengthens robustness against voltage irregularities owing to motor noise and battery depletion. Total weight of the PCB was 30 g.

PC Monitoring Software

In order to display and monitor in real time the captured image data along with the estimated local motion and wide field integration data a Linux monitoring interface was written in C++ using the QT framework. For proper visualization in the Graphical User Interface (GUI) the optic flow vectors are scaled and overlaid onto the camera video stream while VS cell homologue data is shown in a corresponding plot (Figure 4.6). Data is acquired via an IEEE 802.11g wireless link between the laptop and the sensor system. Due to the limited bandwidth of the wireless connection on average between 10 and 15 frames could be transmitted per second, which nevertheless is sufficient for a human observer to monitor the live image stream and the corresponding optic flow output of the system. For

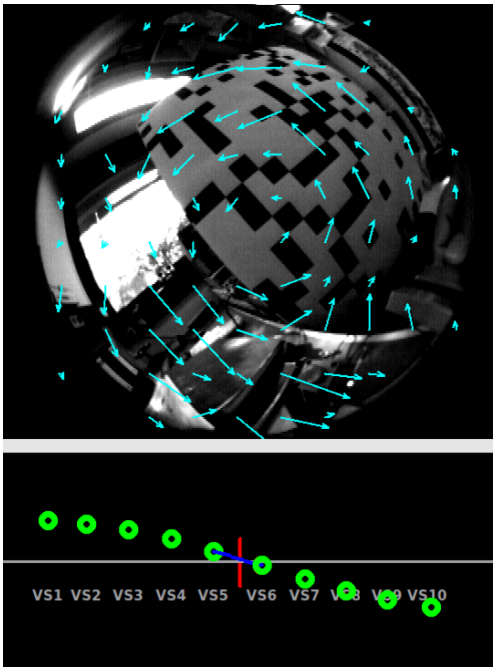

Figure 4.6: Screenshot of the GUI on the ground station PC during a rotation around an axis close to zero. The upper graph shows the local motion estimates overlaid on top of the live video stream, while the corresponding VS cell network axon terminal responses are displayed in the lower graph [3].

recording wide field integration data at full frame rate the USB connection between the ARM PCB and the monitoring laptop could be used.

4.3.4 Design Outcome

The final sensor system was able to compute 350 ego-motion estimates per second for transmission towards the MAV flight controller and / or data logging PC, while weighing a total of 193 g and consuming less than 4 W off a standard three cell 12 V LiPo RC model battery. At the same time, real time images, flow fields and ego-motion estimates were sent to a control ground station PC at a reduced frame rate of roughly 12 frames per second. Using automatic gain adaptation the 8 bit image sensor produced pixel values roughly centered in its 0 to 255 coding range. In dim indoor lighting conditions between 10 cd m^{-2} and 30 cd m^{-2} with an exposure time of 2.85 ms per frame temporal noise caused a typical standard deviation of 2.2% of this range.

4.4 Performance Evaluation

To test the functionality and reveal the characteristics of the sensor system two kinds of trials were conducted. On one hand, experiments were carried out to ascertain the resemblance with the biological original. On the other hand, essays to elucidate the actual sensor characteristics and accuracy of measurement were performed.

4.4.1 EMD Output Characteristics

A distinct feature of correlation type motion detectors is the existence of a velocity optimum in response to moving sine grating stimuli [13,64]. As shown in [92] for a Reichardt Detector configuration with a temporal high-pass filter in its input lines the velocity response curve for sinusoidal gratings is given by

$$\langle R_i \rangle_\varphi = \Delta I^2 \frac{\tau_{\mathrm{lp}} \tau_{\mathrm{hp}}^2 \omega^3}{(1+\tau_{\mathrm{lp}}^2\omega^2)(1+\tau_{\mathrm{hp}}^2\omega^2)} \sin(2\pi\Delta\varphi/\lambda), \tag{4.4}$$

where ΔI is the pattern contrast, ω the angular frequency, $\Delta\varphi$ the inter-ommatidial angle, λ the wavelenth and τ_{lp} and τ_{hp} are the low-pass and high-pass time constants, respectively. The velocity optimum is a linear function of the spatial pattern wavelength leading to a constant temporal frequency optimum. This has been observed in behavioral and electrophysiological studies in resting, walking and flying animals across various fly species. These studies have revealed frequency optima around 1 Hz for stationary *Drosophila*, *Phaenicia* and *Calliphora* (see [76], [89] and [5], respectively). For walking *Drosophila* optima from 2 Hz to 3 Hz have been shown [186, 187]. In flying animals, optima have been reported between 3 Hz and 10 Hz for *Drosophila* [188, 189], 1 Hz to 10 Hz for *Musca* [190] and 5 Hz to 7 Hz for *Calliphora* [191, 192].

Here, filter time constants were adjusted to values yielding a theoretical frequency optimum similar to *Calliphora* during flight, i.e. at 7.3 Hz ($\tau_{\mathrm{lp}} = 45\,\mathrm{ms}$ and $\tau_{\mathrm{hp}} = 33\,\mathrm{ms}$). For confirming the existence and location of the velocity optimum of the sensor system the next step consisted of measuring the sensor output for vertically moving sine gratings at spatial wavelengths $\lambda = 12°$, 24° and 48° at different velocities using a cylinder shaped LED arena [193]. The normalized mean response of VS 7 cells over $n = 23$ trials revealed velocity optima at $85\,°\,\mathrm{s}^{-1}$, $175\,°\,\mathrm{s}^{-1}$ and $350\,°\,\mathrm{s}^{-1}$ for $\lambda = 12°$, 24° and 48°, respectively (Figure 4.7a). Dividing the velocity optima by the corresponding spatial wavelength, the frequency optima coincide around 7.3 Hz as predicted by the model calculations in Eq. 4.4 (Figure 4.7b).

4.4.2 Receptive Fields

To measure the sensor's receptive fields, a custom built arena consisting of three 120 Hz SyncMaster 2233RZ monitors (Samsung, South Korea) in combination with NVIDIA GeForce GTX 480/580 graphics cards (NVIDIA Corp., California, USA) using NVIDIA 3D Vision Surround technology was used. The monitors were perpendicularly placed in front, left and right of the sensor, covering the visual space from −135° to 135° in equatorial azimuth and from −58° to 58° in frontal elevation. Monitor radiance inhomogeneities were largely compensated by using diffusing filter paper. Stimuli were written in Python and rendered using the open source graphics engine Panda3D [194]. They consisted of a small 5.7° × 5.7° white square moving at $120\,°\,\mathrm{s}^{-1}$ on a dark background (92% Michelson contrast) sweeping the extent of the arena in the frontal hemisphere up and down to reveal the vertical components and left and right to reveal the horizontal components of the receptive fields. For $n = 21$ complete trials the response data was spatially divided into 36 × 36 equisolid angle bins covering the frontal hemisphere. Both dendritic and axon terminal responses from all implemented VS and HS cells were recorded at the camera frame rate of 350 measurements per second. As expected, the dendritic compartments

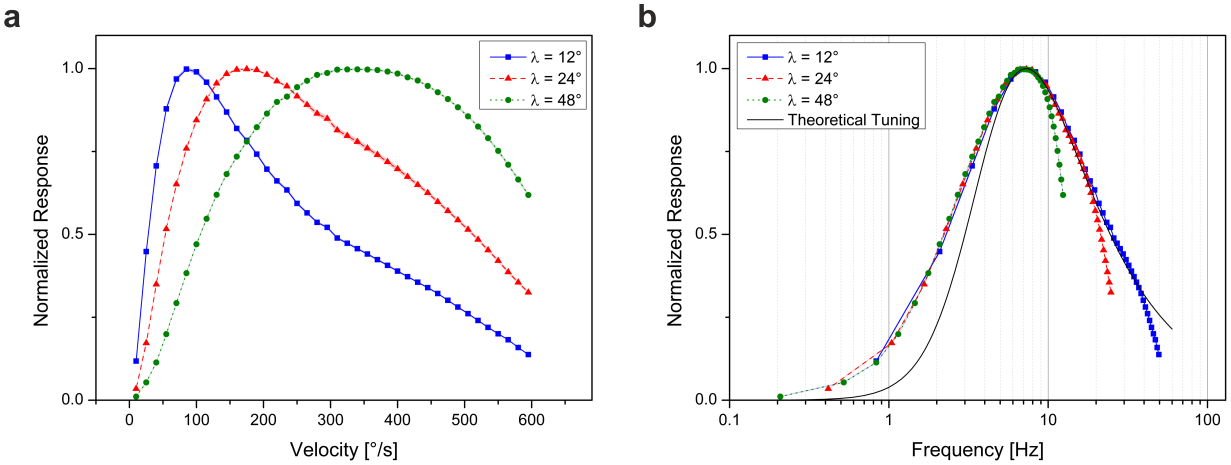

Figure 4.7: VS cell velocity tuning. (**a**) Normalized VS cell response curves for sinusoidal gratings of spatial wavelengths $\lambda = 12°$, $24°$ and $48°$ of visual angle as seen by the fly over a wide range of velocities, displaying optima at $85\,°\,\mathrm{s}^{-1}$, $175\,°\,\mathrm{s}^{-1}$ and $350\,°\,\mathrm{s}^{-1}$, respectively. Representative data from VS 7 cells over $n = 23$ trials are shown. Standard Deviation is within symbol size. **b** VS cell frequency tuning. Data from **a** are plotted as a function of temporal frequency by dividing velocity by the respective pattern wavelength. Frequency optima for all three wavelengths lie around 7.3 Hz. Standard Deviation is within symbol size [3].

respond to vertical motion in rather narrow stretches of the visual field (Figure 4.8a and Figure 4.9a), while in the axon terminals the cells exhibit responses over a much broader area (Figure 4.8b and Figure 4.9b) owing to the lateral connections with their neighboring cells, as depicted in Figure 4.2. Thus, the axon terminal output receptive fields resembled matched filters for optic flow generated by rotations around axes sequentially arranged along the equator (see [36, 37]).

4.4.3 Rotation Axis Estimation

The main objective of this sensor system is the estimation of the axis of rotation during ego-motion. In order to examine the measurement accuracy of the sensor system it was tested both in a simulation environment and in a real world scenario. The experimental setup used for the simulation environment was the same as for the receptive field analysis described in Section 4.4.2. For spatially correct stimulus presentation *cube mapping* was used [195]. The sensor system was mounted in the focal spot and the simulated environment was rotated around axes ranging from $\theta_{ref} = -60°$ to $60°$ along the equator in $15°$ steps at angular velocities from $30\,°\,\mathrm{s}^{-1}$ to $100\,°\,\mathrm{s}^{-1}$ in $5\,°\,\mathrm{s}^{-1}$ steps for each axis. For performance evaluation the Root Mean Square Deviation (RMSD) between sensor axis estimate and reference angle was defined as

$$\mathrm{RMSD}(\theta_{est}, \theta_{ref}) = \sqrt{\frac{\sum_{i=1}^{n} \big(\theta_{est}(i) - \theta_{ref}(i)\big)^2}{n}}, \tag{4.5}$$

where θ_{est} is the sensor axis estimate and θ_{ref} the reference angle.

Three contrast metrics were defined for the presented images. RMS contrast (C_{RMS}) was defined as the standard deviation of pixel values divided by their mean. As a second

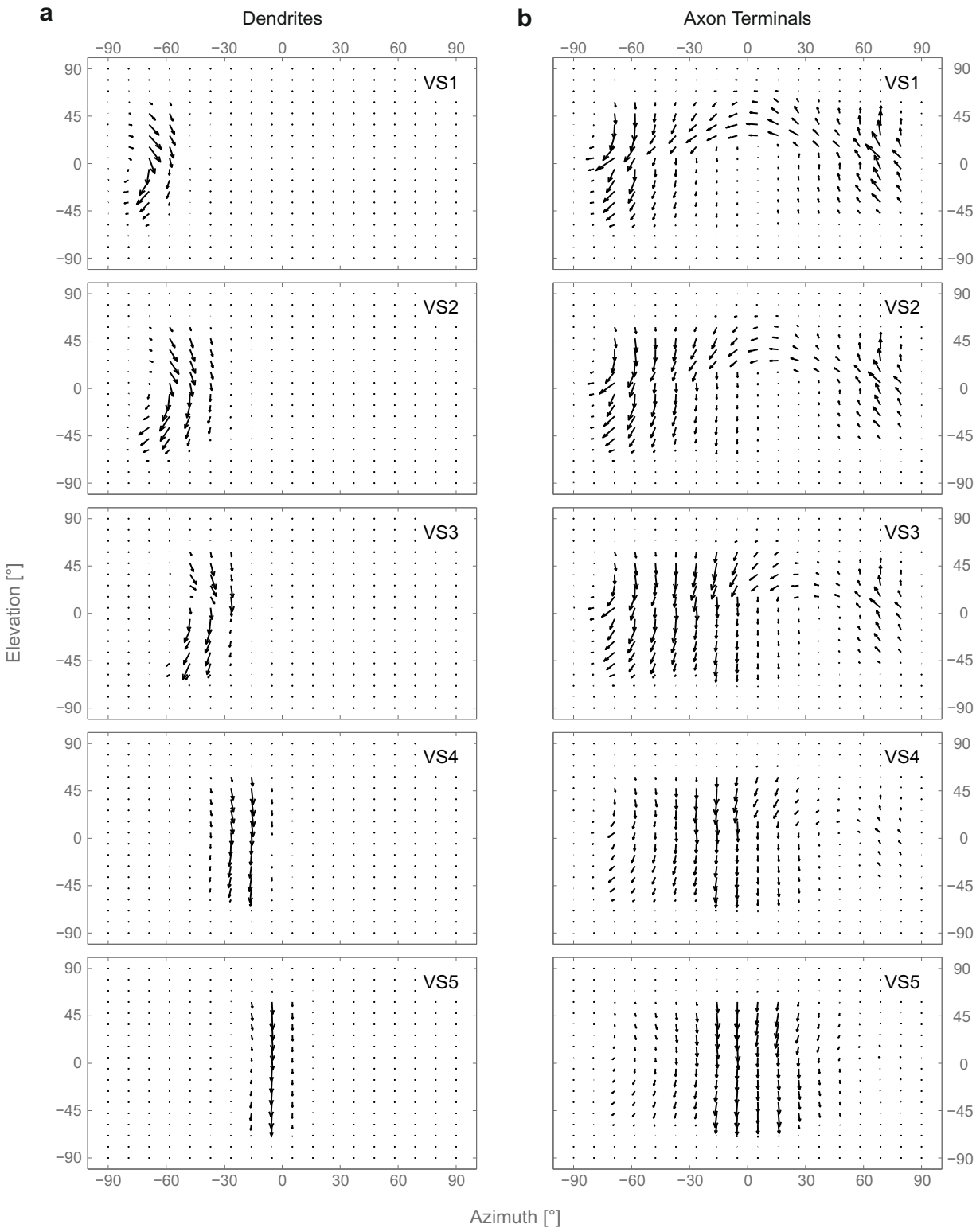

Figure 4.8: Receptive fields of VS 1 to VS 5 for (**a**) dendritic and (**b**) axon terminal regions. Average data from $n = 21$ trials are shown. Note the resemblance between axon terminal receptive fields and rotations around axes sequentially arranged on the equator [3].

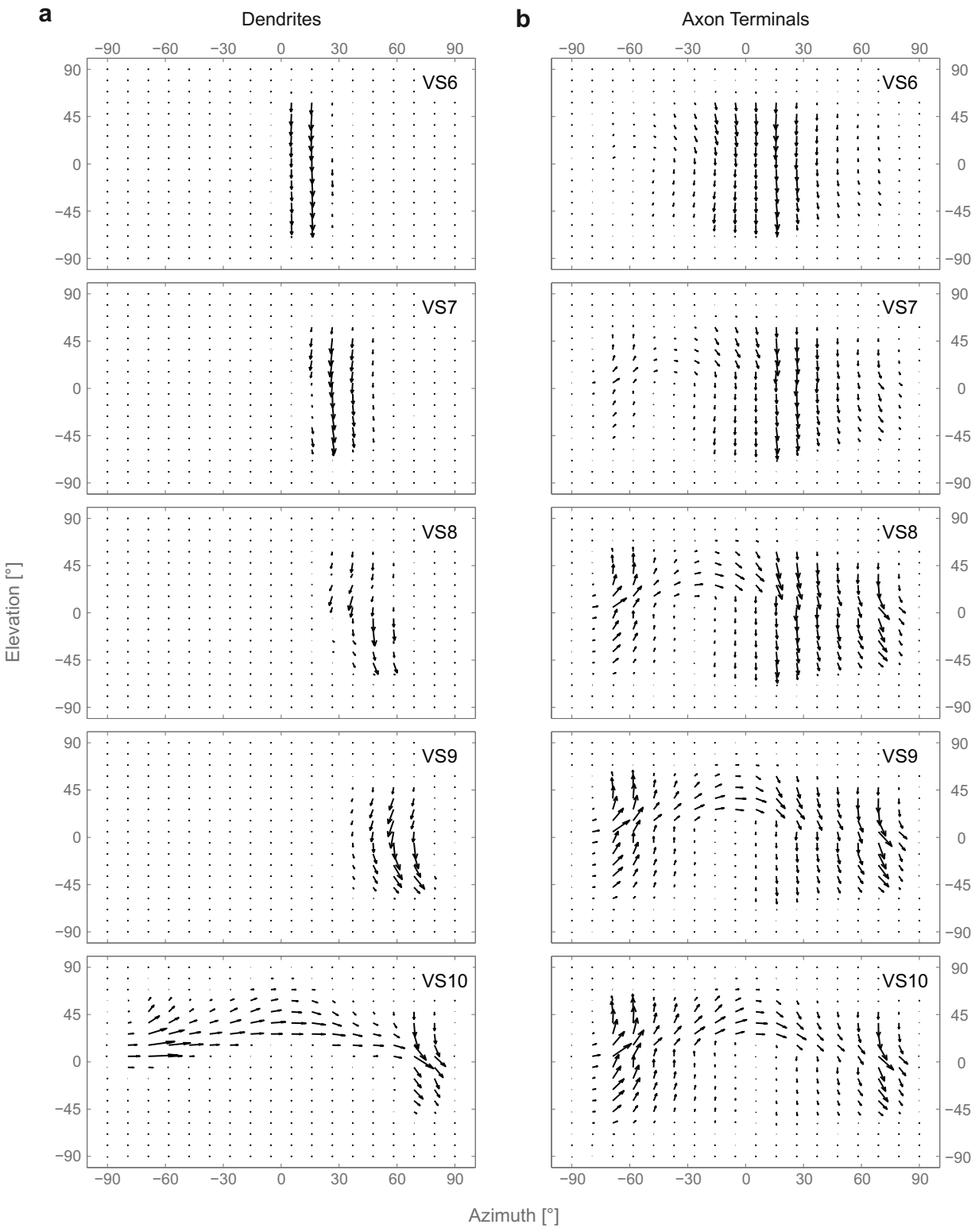

Figure 4.9: Receptive fields of VS 6 to VS 10 for (**a**) dendritic and (**b**) axon terminal regions. Average data from $n = 21$ trials are shown. Note the resemblance between axon terminal receptive fields and rotations around axes sequentially arranged on the equator [3].

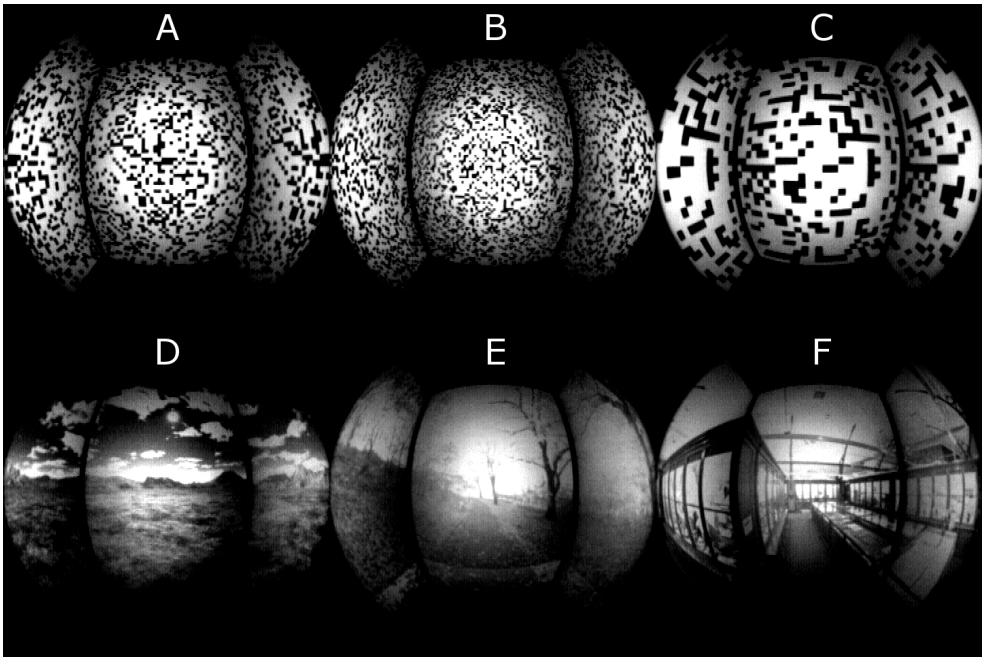

Figure 4.10: Screenshots of visual scenarios used in the simulation environment for rotation estimation. Scenes A, B and C were artificially generated using random probability distributions while scenes D, E and F are cube mapping projections of photographic scenes [3].

metric MAD contrast (C_{MAD}) was defined as the Mean Absolute Deviation (MAD) of pixel values. These two metrics are global measures and therefore do not depend on the spatial frequency content or the spatial brightness distribution. Hence, radially averaged power spectrum contrast (C_{RAPS}) was defined as the square root of the mean of the radially averaged power spectra between 0.0649 cycles per degree and 0.6486 cycles per degree, thereby covering the spatial coding range of the sensor system up to its Nyquist limit.

Three artificial and three naturalistic scenarios were presented in the simulation environment (Figure 4.10). Owing to their high contrast ratios the artificial scenarios yielded very robust and exact estimation of the rotational axes, on average deviating by less than 5° from the actual axis of rotation (see Table 4.1). Natural images displayed larger RMS deviations between 9° and 18° due to their lower contrast and the relatively low mean luminance values of available scenes in the experimental setup. In line with the motion de-

Table 4.1: Contrast and RMSD for simulated scenes

		Contrast			Result
Scene	Type	C_{RMS}	C_{MAD}	C_{RAPS}	RMSD
A	Artificial	1.39	0.28	0.19	3.00°
B	Artificial	1.36	0.26	0.17	3.65°
C	Artificial	1.38	0.31	0.16	4.59°
D	Natural	1.70	0.17	0.06	9.01°
E	Natural	1.39	0.20	0.04	14.44°
F	Natural	1.42	0.20	0.07	18.42°

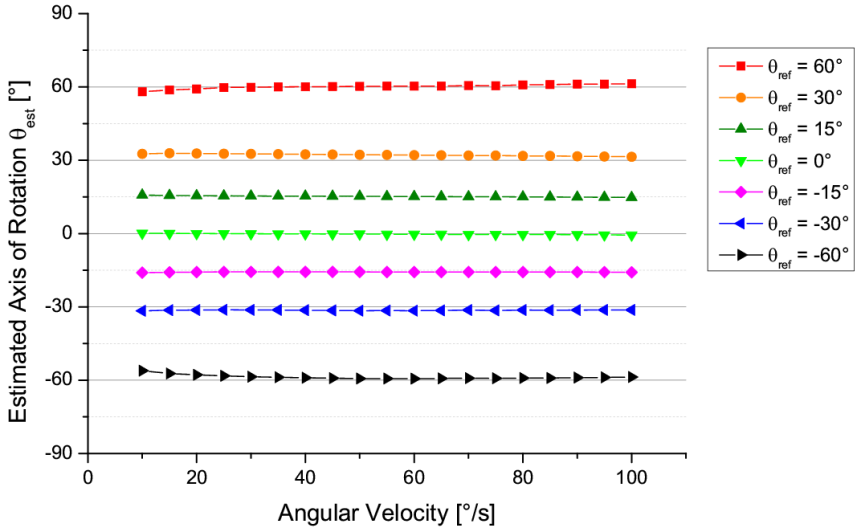

Figure 4.11: Axis estimation during real world trials. The sensor system was rotated in a wide range of angular velocities around different reference axes, yielding highly accurate rotation axis estimates virtually regardless of angular velocity [3].

tection model, the higher the contrast the better the sensor system performed. To test an extreme case and an exception to this rule a scene with high rotational asymmetries (Table 4.1, row F) was included. In this case the sensor generated the highest RMS deviations in the test set despite not having the lowest contrast. Remarkably, this worst case RMSD of 18.42° is almost identical to the 18.5° spacing between VS cell dendritic receptive fields. This means that the worst case sensor inaccuracy tends to be at most one cell to the left or to the right of the true center of rotation.

For recording data in a real world environment the sensor system was mounted axially on a PLE40 planetary gear with a 100:1 gear reduction ratio (Neugart, Kippenheim, Germany) and rotated using a PANdrive PD1-140-42-SE-232 motor with an integrated control unit (Trinamic, Hamburg, Germany). Situated in an indoor environment with both high and low visual contrast areas the sensor system was rotated around the axes $\theta_{ref} = -60°$, $-30°$, $-15°$, $0°$, $15°$, $30°$ and $60°$ along the equator at angular velocities ranging from $10\,°\,s^{-1}$ to $100\,°\,s^{-1}$ in $5\,°\,s^{-1}$ steps. The actual angular velocity was monitored utilizing the integrated encoders. As can be observed in Figure 4.11 rotation axis estimation by the sensor system accurately reflects the actual axis of rotation, basically regardless of rotational velocity. There tends to be, however, slightly higher accuracy towards higher velocities, as can also be seen in Figure 4.11.

4.4.4 Rotation Rate Estimation

Concurrently with the rotation axis estimation, the sensor system also computes an estimate of the rate of rotation around that particular axis by calculating the slope at the zero-crossing location. To analyze the properties of these estimates, the camera system was subjected to $n = 22$ trials with rotations around the rostro-caudal axis at angular velocities ranging from $10\,°\,s^{-1}$ to $1000\,°\,s^{-1}$ using the same scenes as for the axis estimation trials in Section 4.4.3. Figure 4.12 presents the typical bell shaped response curves of the system. Peak responses were found between $100\,°\,s^{-1}$ and $251\,°\,s^{-1}$.

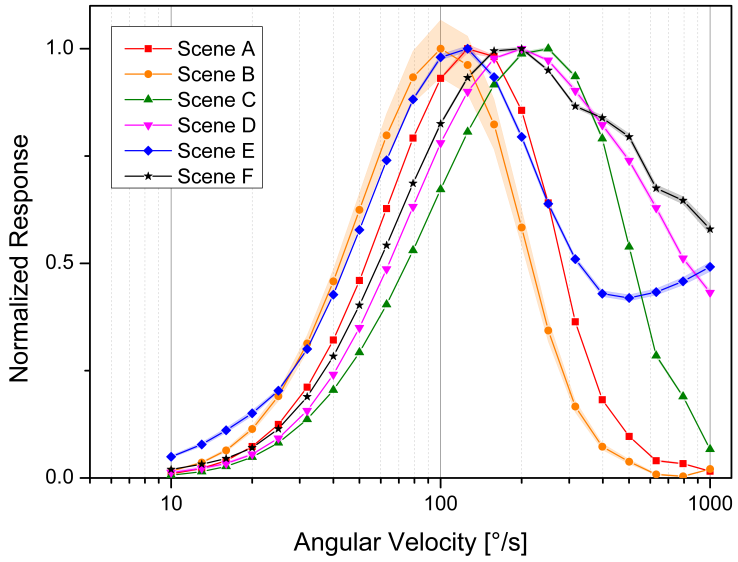

Figure 4.12: Rotation rate estimation for naturalistic and artificial scenes. Traces show mean estimates while shaded areas indicate Standard Deviation between $n = 22$ trials. Velocity optima lie between $100\,^\circ\,\mathrm{s}^{-1}$ and $251\,^\circ\,\mathrm{s}^{-1}$ [3].

4.5 Discussion

Bio-inspired visual motion and rotation sensors traditionally suffer from low frame rates, poor spatial resolution and narrow fields of view. Due to the complexity of achieving all these features at once the only comparable solutions are large and PC based, therefore forfeiting their use on-board small aerial vehicles such as MAVs. Sending image data via wireless transmission and subsequent off-board processing is also not a viable option due to low achievable frame rates and inherent transmission delays and interruptions.

In this chapter a fly-inspired visual rotation sensor has been put put forth, capable of accurate measurements in a variety of visual scenes, while maintaining the tight restrictions necessary for use on-board MAVs, while operating at very high frame rates. The outcome of all experiments substantiated on one hand the close resemblance of this implementation with the biological original. On the other hand, the results demonstrated the good performance over a wide range of different visual environments. This implementation was specifically designed to be used on-board MAVs and therefore features only a small footprint in terms of size, weight and power consumption while maintaining mechanical robustness.

One possible source of performance degradation is the inherent barrel distortion of fisheye lenses. Various correction algorithms have therefore been tested on board the FPGA with slight, albeit not substantial performance improvements. This suggests that fisheye lens distortion does not decisively perturb sensor performance.

A particularly useful property of the proposed FPGA and ARM based implementation was the versatility and ease of adding other functionalities. By adding different templates for global motion integration, new uses of this sensor system could arise. The simple sum of all VS cell templates for instance, could be used as a measure of global vertical motion for lift control. The sum of HS cells might be used for indication of global horizontal motion for yaw control. Using specialized horizontal templates, *tunnel centering* behavior [19]

could be implemented for autonomous robot navigation. Along these same lines, collision detection can be envisioned by using templates for radial expansion. The advantage of this system lies in the fact that there are sufficient free resources for all these computations to be implemented simultaneously, at full frame rate and resolution.

The system has been designed to be used with either one or two cameras, potentially covering the complete 4π sr unit sphere of visual space for true global motion integration and consequently added robustness of ego-motion estimates. Also multi-modal integration of other sensors, such as rate gyroscopes, accelerometers, etc. is supported. This is particularly useful for future studies on sensor fusion with inertial data, akin to integration of vision and inertial haltere measurements in the fly brain. The system presented here might therefore prove useful when employed complementarily to inertial measurement units.

The contribution of this chapter is a new type of visual ego-rotation sensing based on the fly visual system and its subsequent successful implementation keeping within tight space, weight and performance restriction boundaries. A novel measurement device is proposed that enriches the tool set of measuring ego-rotations with great accuracy, speed and robustness. On the other hand this chapter demonstrates the usefulness of direct application of biological algorithms to solving specific technical problems. The work presented in this chapter has been published in [3].

5 Fly-Inspired Motion Estimation for Flight Control

In the previous chapters several key aspects of the fly visual system have been investigated and transferred to a technical sensor implementation. This solution's sensing characteristics were then analyzed as an open loop system. The present chapter focuses on the dynamic analysis of this novel type of sensor under closed loop conditions.

Biologically inspired correlation-type EMD motion processing possesses a number of advantages over other types of motion sensing. As such it has been shown to be ideally suited for use in low signal-to-noise regimes, thereby significantly outperforming gradient-based methods [4, 5]. Under closed loop conditions it has been found to cope well with high gains, outperforming perfect linear velocity detectors in terms of residual slip speed and overall stability [196]. Another notable feature of this type of processing is its inherent dynamic gain adaptation to the prevailing stimulus statistics [6].

Provided with these amenable intrinsic static and dynamic properties, the HRM- or EMD-type motion detection scheme poses a promising solution for motion detection in feedback control systems. However, few studies exist that investigate feedback control loop properties of the HRM [196, 197]. Furthermore, to the author's best knowledge as of yet there are no conclusive studies on closed loop behavior of EMD-based visual rotation sensors and their underpinning wide field integration network scheme. Yet, the combination of these two principles of operation might prove beneficial under conditions the original biological system, i.e. the fly, faces during typical flight situations.

As such, during flight a fly usually experiences simultaneous rotation and translation. However, most previous art concentrates on motion along just one degree of freedom (DOF) [175, 196] or restricted to a 2 DOF stable plane of motion [174, 198]. Nevertheless, considering translation superimposed onto rotations and the implied mixed flow-fields is vital for construction of sensors for use on-board real-world technical applications such as UAVs or MAVs. The present work therefore sets out to analyze this type of sensor in regard to separability of translation and rotation, both analytically and experimentally.

The nature of the fly phototransduction cascade imposes inherent and variable delays between photon absorption and photoreceptor output. This in turn poses a considerable source of instability in the fly sensorimotor loop, especially at high gains. However, this issue is completely effaced by the fly visual system, suggesting a high resilience against temporal delays already in the early stages of the fly motion detection system. The rationale behind this work is therefore to investigate the performance of a EMD-based sensor in closed loop conditions when facing delays compared to an ideal linear sensor.

The primary goal of this chapter is the performance analysis of insect-inspired visual rotation sensing in closed loop conditions. Key concerns addressed here are overall stability, influence of superimposed translation and effects of large delays. Contributions are improved stability, immunity against a large variety of translatory motions and substantial performance improvements when facing delays. Key challenges are system modeling and

formulation, stability analysis as well as design and assembly of a real-time experimental evaluation setup.

The remainder of this chapter is organized as follows: First, in Section 5.1 the theoretical separability of rotation and translation for this type of sensor is analyzed. Then in Section 5.2 the task framework for analysis of the proposed EMD-type sensor is outlined and the dynamic equations used throughout this chapter are derived. Subsequently closed loop stability and performance are assessed in a simulation environment. Analogously, in Section 5.3 the closed loop stability and performance analyses are presented in real-time experimental evaluation. Finally, the chapter is concluded with a summary and discussion in Section 5.4.

5.1 Effects of Translation Superposition

As discussed at length in the previous two chapters the fly VS cell network and its derived technical implementation are sensors for pure rotations around axes lying on the horizontal plane. However, in typical flight conditions, pure rotations in a hovering state lacking translations are more exceptions than the general rule. Usually, flight patterns include translations on top of rotations [199]. Hence, resulting optic flow fields tend to be mixed and complex, thus, exacerbating extraction of pure rotational or pure translational velocities.

Neuronal responses of the fly visual system do not only depend on the flow fields generated by flight through the present visual scene but also on the receptive fields of the involved neurons. In fact, these receptive fields act as matched filters on the flow field input [37, 200]. The relationship between receptive field, induced optic flow and neuronal output was analyzed in [201]. In this study the concept of the action field was put forth, enabling an analytical approach for relating any given motion to the output of neurons or groups of neurons with specific receptive field properties. However, in this study only pure rotations and pure translations were considered over either a complete 4π sr FOV or a limited symmetrically reduced FOV. Also, only perfect continuous integration was considered. However, both biological and technical systems feature only discrete input systems such as faceted compound eyes or pixel-based CMOS or CCD arrays. The rationale behind the present study therefore is to analyze asymmetric integration domains, such as found in realistic applications, and assess the separability of translation and rotation. Additionally, the effects of a discrete approach as opposed to continuous integration is to be evaluated in terms of performance and introduced distortion.

5.1.1 Continuous Action Fields

Optic Flow Fields

As outlined in [201, 202] the fly eyes can be modeled as a sphere of unitary radius centered at the vantage point $\mathbf{0}$. A point $\boldsymbol{q}_i$ in the surrounding visual environment will then be projected onto the point $\boldsymbol{d}_i$ on the surface of the sphere, where $\boldsymbol{d}_i = \boldsymbol{q}_i \mu_i$ with $\mu_i = |\boldsymbol{q}_i|^{-1}$ describing the nearness to point $\boldsymbol{q}_i$. For every movement of the fly this projection $\boldsymbol{d}_i$ changes accordingly. At the same time, according to Chasles' theorem [203] any motion of the vantage point, i.e. the fly center, can be unambiguously characterized by a translation along a vector $\boldsymbol{t}$ and a rotation around vector $\boldsymbol{r}$. For a forward translation of the fly in an

incremental time Δt the displacement of $\boldsymbol{q}_i$ relative to the vantage point $\mathbf{0}$ becomes

$$\Delta \boldsymbol{q}_i = -\boldsymbol{t}\Delta t, \tag{5.1}$$

whereas a clockwise rotation of the fly yields

$$\Delta \boldsymbol{q}_i = -\left(\boldsymbol{r} \times \boldsymbol{q}_i\right)\Delta t. \tag{5.2}$$

therefore, an arbitrary motion can be described as

$$\Delta \boldsymbol{q}_i = -\left(\boldsymbol{t} + \boldsymbol{r} \times \boldsymbol{q}_i\right)\Delta t. \tag{5.3}$$

This relative motion of $\boldsymbol{q}_i$ also induces a change in its projection $\boldsymbol{d}_i$ onto the fly eye. However, only transverse motion induces a change in the projection. Motion in the radial direction does not influence the projection. Hence, the translation needs to be adjusted accordingly by subtracting its radial part $\left(\boldsymbol{t} \cdot \boldsymbol{d}_i\right)\boldsymbol{d}_i$, thus yielding

$$\Delta \boldsymbol{d}_i = -\mu_i\left(\boldsymbol{t} - \left(\boldsymbol{t} \cdot \boldsymbol{d}_i\right)\boldsymbol{d}_i + \boldsymbol{r} \times \boldsymbol{q}_i\right)\Delta t. \tag{5.4}$$

The optic flow $\boldsymbol{p}_i$ can be defined as the time derivative of this direction, which then becomes

$$\boldsymbol{p}_i = \frac{\partial \boldsymbol{d}_i}{\partial t} = -\mu_i\left(\boldsymbol{t} - \left(\boldsymbol{t} \cdot \boldsymbol{d}_i\right)\boldsymbol{d}_i\right) - \boldsymbol{r} \times \boldsymbol{d}_i. \tag{5.5}$$

By subtracting $\left(\boldsymbol{t} \cdot \boldsymbol{d}_i\right)\boldsymbol{d}_i$ from $\boldsymbol{t}$ this part of the equation was effectively orthogonalized with respect to $\boldsymbol{d}_i$. Furthermore, $\boldsymbol{r} \times \boldsymbol{d}_i$ is evidently orthogonal to $\boldsymbol{d}_i$, thereby rendering $\boldsymbol{p}_i$ orthogonal to $\boldsymbol{d}_i$. Hence, albeit being three-dimensional, $\boldsymbol{p}_i$ possesses just two degrees of freedom and can therefore be unambiguously represented by a two-dimensional vector tangent to $\boldsymbol{d}_i$. Following the rationale of [201], $\boldsymbol{p}_i$ can be projected onto a two-dimensional vector by multiplication by a 2×3 orthonormal matrix $\boldsymbol{B}$. In line with [201], the most convenient choice is

$$\boldsymbol{B} = \begin{bmatrix} -\sin\theta & \cos\theta & 0 \\ -\sin\phi\cos\theta & -\sin\phi\sin\theta & \cos\phi \end{bmatrix}, \tag{5.6}$$

whose rows represent a local coordinate system positioned at (θ, ϕ) on the surface of the sphere with its axes pointing towards longitude and latitude. This facilitates a change of indexing from the sub-index i to a location on the sphere with azimuth angle $\theta \in [-\pi, \pi]$ and elevation angle $\phi \in [-\frac{\pi}{2}, \frac{\pi}{2}]$. The resulting two-dimensional optic flow at location (θ, ϕ) induced by a translation along $\boldsymbol{t}$ and rotation around $\boldsymbol{r}$ can therefore be expressed as

$$\boldsymbol{f}(\boldsymbol{r}, \boldsymbol{t}, \theta, \phi) = \boldsymbol{B}\,\boldsymbol{p}(\boldsymbol{r}, \boldsymbol{t}, \theta, \phi), \tag{5.7}$$

where $\boldsymbol{r}$ and $\boldsymbol{t}$ can be expressed in spherical coordinates as

$$\boldsymbol{r} = v_{rot}\begin{bmatrix} \cos\theta_{rot}\cos\phi_{rot} \\ \sin\theta_{rot}\cos\phi_{rot} \\ \sin\phi_{rot} \end{bmatrix} \tag{5.8}$$

and

$$\boldsymbol{t} = v_{tra}\begin{bmatrix} \cos\theta_{tra}\cos\phi_{tra} \\ \sin\theta_{tra}\cos\phi_{tra} \\ \sin\phi_{tra} \end{bmatrix}, \tag{5.9}$$

with v_{rot} and v_{tra} representing the velocities and $\theta_{rot}, \phi_{rot}, \theta_{tra}$ and ϕ_{tra} the angles of the respective rotation and translation vectors [201]. The optic flow $\boldsymbol{f}$ can now be decomposed in its rotational and translational components

$$\boldsymbol{f}(\boldsymbol{r}, \boldsymbol{t}, \theta, \phi) = \boldsymbol{f}(\boldsymbol{r}, 0, \theta, \phi) + \boldsymbol{f}(0, \boldsymbol{t}, \theta, \phi), \tag{5.10}$$

yielding

$$\boldsymbol{f}(\boldsymbol{r}, 0, \theta, \phi) = v_{rot} \begin{bmatrix} \mathrm{c}\phi\mathrm{s}\phi_{rot} - \mathrm{s}\theta\mathrm{s}\phi\mathrm{c}\phi_{rot}\mathrm{s}\theta_{rot} - \mathrm{c}\theta\mathrm{s}\phi\mathrm{c}\phi_{rot}\mathrm{c}\theta_{rot} \\ \mathrm{c}\phi_{rot}(\mathrm{s}\theta\mathrm{c}\theta_{rot} - \mathrm{c}\theta\mathrm{s}\theta_{rot}) \end{bmatrix} \tag{5.11}$$

and

$$\boldsymbol{f}(0, \boldsymbol{t}, \theta, \phi) = \mu v_{tra} \begin{bmatrix} \mathrm{c}\phi_{tra}(\mathrm{s}\theta\mathrm{c}\theta_{tra} - \mathrm{c}\theta\mathrm{s}\theta_{tra}) \\ -\mathrm{c}\phi\mathrm{s}\phi_{tra} + \mathrm{s}\theta\mathrm{s}\phi\mathrm{c}\phi_{tra}\mathrm{s}\theta_{tra} + \mathrm{c}\theta\mathrm{s}\phi\mathrm{c}\phi_{tra}\mathrm{c}\theta_{tra} \end{bmatrix}, \tag{5.12}$$

where $\mathrm{c}(\cdot)$ and $\mathrm{s}(\cdot)$ denote $\cos(\cdot)$ and $\sin(\cdot)$, respectively. Note the general assumption of homogeneous distances to the vantage point, i.e. fly eye, by assuming $\mu(\theta, \phi) = \mu$ for all points (θ, ϕ) [201].

Action Fields

Using Eqs. 5.10 to 5.12 it is now possible to analytically calculate the theoretical optic flow field produced by any arbitrary motion. However, the output of the fly visual system does not only depend on the perceived optic flow field but also on the receptive fields of the individual neurons. The output of these individual neurons can be interpreted as an inner product of its receptive field and the perceived optic flow.

In order to quantify this, the action field $\boldsymbol{S}_{AF}$ is defined as the inner product of the receptive field $\mathfrak{A}$ and the flow field $\mathfrak{B}$ [201]. Note that $\mathfrak{A}$ and $\mathfrak{B}$ are vector fields whereas $\boldsymbol{S}_{AF}$ is a scalar field. Over the complete unitary sphere with the domain D with $\theta \in [-\pi, \pi]$ and $\phi \in [-\frac{\pi}{2}, \frac{\pi}{2}]$ it can be shown that

$$\begin{aligned} \boldsymbol{S}_{AF}(\mathfrak{A}, \mathfrak{B}) = \langle \mathfrak{A}, \mathfrak{B} \rangle &= \iint_D \boldsymbol{p}\left(\boldsymbol{r}_A, \boldsymbol{t}_A, \theta, \phi\right) \cdot \boldsymbol{p}\left(\boldsymbol{r}_B, \boldsymbol{t}_B, \theta, \phi\right) \cos\phi \, \mathrm{d}\theta \, \mathrm{d}\phi \\ &= \frac{8}{3} \pi \left(\boldsymbol{r}_A \cdot \boldsymbol{r}_B + \mu^2 \, \boldsymbol{t}_A \cdot \boldsymbol{t}_B\right), \end{aligned} \tag{5.13}$$

which implies a linear behavior of the action field with simultaneous rotation and translation. Therefore translation and rotational components are linearly separable by using the corresponding receptive fields as filters. If e.g. rotations are to be detected, the receptive field $\mathfrak{A}$ could be designed possessing no translational components, i.e. $\boldsymbol{t}_A = \boldsymbol{0}$. If the presented rotational optic flow field $\boldsymbol{r}_B$ now matches the rotational part of the receptive $\boldsymbol{r}_A$ the action field $\boldsymbol{S}_{AF}$ will be maximal and independent of the optic flow's translational component $\boldsymbol{t}_B$.

Partial Field Integration

According to Eq. 5.13 by integrating over the complete domain D with $\theta \in [-\pi, \pi]$ and $\phi \in [-\frac{\pi}{2}, \frac{\pi}{2}]$ as well as careful selection of the receptive field $\mathfrak{A}$ pure rotational or translational components of the induced optic flow $\mathfrak{B}$ can be reconstructed. This, however, changes substantially when limiting the field of view of the sensor, i.e. reducing the domain D over which to integrate. It has been shown that for the special case of a strictly

symmetric reduction of the integrating domain around the axis of rotation of the receptive field still yields separability of rotation and translation [201]. Nevertheless, to the best of the author's knowledge as of yet there are no studies regarding the general case of non-symmetric reduction.

A single compound eye of the fly is a prime example of such a non-symmetric reduction of the FOV, i.e. integrating domain, for the case of e.g. a roll movement of the fly around its longitudinal body axis. In this case, by integrating over half the sphere, i.e. D^* with $\theta \in [-\pi, 0]$ and $\phi \in [-\frac{\pi}{2}, \frac{\pi}{2}]$ it can be shown that

$$\begin{aligned} \boldsymbol{S}_{AF}(\mathfrak{A}, \mathfrak{B}) &= \iint_{D^*} \boldsymbol{p}\left(\boldsymbol{r}_A, \boldsymbol{t}_A, \theta, \phi\right) \cdot \boldsymbol{p}\left(\boldsymbol{r}_B, \boldsymbol{t}_B, \theta, \phi\right) \cos\phi \, \mathrm{d}\theta \, \mathrm{d}\phi \\ &= \frac{4}{3}\pi \left(\boldsymbol{r}_A \cdot \boldsymbol{r}_B + \mu^2 \, \boldsymbol{t}_A \cdot \boldsymbol{t}_B\right) + \mu \, v_A^{rot} \, v_B^{tra} \left(r_A^y \, t_B^z - r_A^z \, t_B^y\right) \\ &\quad + \mu \, v_A^{tra} \, v_B^{rot} \left(t_A^z \, r_B^y - t_A^y \, r_B^z\right). \end{aligned} \tag{5.14}$$

This means that when considering only a limited field of view the action field does not maintain its additivity and thus it is generally not possible to linearly separate rotation and translation components.

However, when closely observing the receptive fields of the VS cell network it can readily be seen that they resemble a set of almost purely rotational flow fields around axes lying on the equatorial plane [36]. This means that for the functional analytic equivalent of these receptive fields the translational component $\boldsymbol{t}_A$ is null, leaving only $\boldsymbol{r}_A$ and, thus, yielding a pure rotation. In fact, by integrating over the hemisphere fixing the receptive field to a rotation around the y axis the action field yields

$$\begin{aligned} \boldsymbol{S}_{AF}(\mathfrak{A}_{rot}^y, \mathfrak{B}) &= \iint_{D^*} \boldsymbol{p}\left(\left[0 \; r_A^y \; 0\right]^T, \boldsymbol{0}, \theta, \phi\right) \cdot \boldsymbol{p}\left(\boldsymbol{r}_B, \boldsymbol{t}_B, \theta, \phi\right) \cos\phi \, \mathrm{d}\theta \, \mathrm{d}\phi \\ &= \frac{4}{3}\pi \, v_A^{rot} \, v_B^{rot} \left(r_A^y \, r_B^y\right), \end{aligned} \tag{5.15}$$

which depends only on the rotational components of the receptive field and the optic flow field. This clear separability is due to the strictly symmetric FOV reduction around the axis of rotation.

A substantially different picture presents itself if the axis of rotation is chosen in an asymmetrical way with respect to the integrating domain, e.g. a rotation around the x axis. In this case the integration yields

$$\begin{aligned} \boldsymbol{S}_{AF}(\mathfrak{A}_{rot}^x, \mathfrak{B}) &= \iint_{D^*} \boldsymbol{p}\left(\left[r_A^x \; 0 \; 0\right]^T, \boldsymbol{0}, \theta, \phi\right) \cdot \boldsymbol{p}\left(\boldsymbol{r}_B, \boldsymbol{t}_B, \theta, \phi\right) \cos\phi \, \mathrm{d}\theta \, \mathrm{d}\phi \\ &= \frac{4}{3}\pi \, v_A^{rot} \, v_B^{rot} \left(r_A^x \, r_B^x\right) + \pi\mu \, v_A^{rot} \, v_B^{tra} \, r_A^x \, t_B^z, \end{aligned} \tag{5.16}$$

which depends strongly on the vertical lift component of the induced optic flow field. Hence, the rotational component is not linearly separable from translational influences. The same applies to the case of arbitrary axes of rotation lying on the xy plane, where

integration yields the action field

$$\begin{aligned}\boldsymbol{S}_{AF}(\mathfrak{A}_{rot}^{xy}, \mathfrak{B}) &= \iint_{D^*} \boldsymbol{p}\left(\left[r_A^x \; r_A^y \; 0\right]^T, \mathbf{0}, \theta, \phi\right) \cdot \boldsymbol{p}\left(\boldsymbol{r}_B, \boldsymbol{t}_B, \theta, \phi\right) \cos\phi \, \mathrm{d}\theta \, \mathrm{d}\phi \\ &= \frac{4}{3}\pi \, v_A^{rot} \, v_B^{rot} \left(r_A^x \, r_B^x + r_A^y \, r_B^y\right) + \pi\mu \, v_A^{rot} \, v_B^{tra} \, r_A^x \, t_B^z, \end{aligned} \tag{5.17}$$

with

$$\boldsymbol{r}_{A_{rot}^{xy}} = \left[r_A^x \; r_A^y \; 0\right]^T. \tag{5.18}$$

Despite this obvious drawback flies are still capable of separating rotational and translational flow components. This fact can be explained by close inspection of common free flight statistics of flies. When observing the average flight patterns of blowflies it can be inferred that their translation tends to be mostly consistent of forward flight as opposed to lift [199]. In this flight pattern—similar to fixed-wing aerial vehicles—the translational lift component can be largely ignored, yielding $t_B^z \approx 0$. For the case of a rotation around the x axis this would therefore result in

$$\boldsymbol{S}_{AF}(\mathfrak{A}_{rot}^{x}, \mathfrak{B}) \approx \frac{4}{3}\pi \, v_A^{rot} \, v_B^{rot} \left(r_A^x \, r_B^x\right) \tag{5.19}$$

and therefore depend only on the rotational components. For the more general case of a receptive field resembling a rotation around an arbitrary axis lying on the xy plane this would yield

$$\boldsymbol{S}_{AF}(\mathfrak{A}_{rot}^{xy}, \mathfrak{B}) \approx \frac{4}{3}\pi \, v_A^{rot} \, v_B^{rot} \left(r_A^x \, r_B^x + r_A^y \, r_B^y\right), \tag{5.20}$$

thus being devoid of translatory influences. Therefore, as long as flight patterns are governed by rotations and translations in the xy plane, the rotational components with axes on the xy plane can be detected and estimated by simply adjusting the receptive fields accordingly.

5.1.2 Discrete Action Fields

The action fields of Eq. 5.15, Eq. 5.19 and Eq. 5.20 derived by integration over a continuous FOV show the separability of rotation and translation. However, when considering real life facet eyes as well as conventional imaging devices the action field becomes a discrete sum of inputs instead of a smooth integral over the unit sphere. This introduces artifacts whose influence depends directly on the inter-ommatidial angles $\Delta\theta$ and $\Delta\phi$, which act as a discretization step. It is assumed here that the inter-ommatidial angles are equal, i.e. $\Delta\theta = \Delta\phi$, which in fact generally holds true for flies. Also, the amount of photoreceptors n_θ and n_ϕ are assumed equal and uniformly distributed.

Rotation around the x axis When considering a receptive field of a rotation around the x axis the action field becomes

$$\begin{aligned}\boldsymbol{S}_{AF}(\mathfrak{A}_{rot}^{x}, \mathfrak{B}) &= \sum_{\theta}^{n_\theta} \sum_{\phi}^{n_\phi = n_\theta} \boldsymbol{p}\left(\left[r_A^x \; 0 \; 0\right]^T, \mathbf{0}, \theta, \phi\right) \cdot \boldsymbol{p}\left(\boldsymbol{r}_B, \boldsymbol{t}_B, \theta, \phi\right) \sin\left(\Delta\phi\right) \sin\left(\Delta\theta\right) \cos\left(\phi\right) \\ &= a\left(n_\theta\right) v_A^{rot} \, v_B^{rot} \, r_A^x \, r_B^x + b\left(n_\theta\right) \mu \, v_A^{rot} \, v_B^{tra} \, r_A^x \, t_B^z, \end{aligned} \tag{5.21}$$

where

$$a\left(n_\theta\right) = \xi\left(n_\theta\right)\left(2\cos\left(\frac{\pi}{n_\theta}\right) + 3\,n_\theta\cos\left(\frac{\pi}{n_\theta}\right) + n_\theta\right), \tag{5.22a}$$

$$b\left(n_\theta\right) = \xi\left(n_\theta\right)\left(2\,n_\theta\cos\left(\frac{\pi}{n_\theta}\right) + n_\theta\right), \tag{5.22b}$$

with

$$\xi\left(n_\theta\right) = \frac{\sin\left(\frac{\pi}{n_\theta}\right)\left(\cos\left(\frac{\pi}{n_\theta}\right)+1\right)}{2\left(1+2\cos\left(\frac{\pi}{n_\theta}\right)\right)}. \tag{5.23}$$

A simple test to see whether this approximation is applicable is the convergence of this sum towards the integral. This is in fact true since

$$\lim_{n_\theta\to\infty} a\left(n_\theta\right) = \frac{4}{3}\,\pi, \tag{5.24a}$$

$$\lim_{n_\theta\to\infty} b\left(n_\theta\right) = \pi. \tag{5.24b}$$

In flies the inter-ommatidial angle depends on the fly species, ranging from $\Delta\theta = 5°$ for *Drosophila* [68] to roughly $\Delta\theta = 1°$ for *Calliphora* [69]. It is therefore valid to assume $\Delta\theta = \Delta\phi = 1°$ in the frontal part, which means $n_\theta = n_\phi = 180$ when summing over 180° in both azimuth and elevation. For that approximation the coefficients become

$$a\left(180\right) = 4.1998, \tag{5.25a}$$

$$b\left(180\right) = 3.1412. \tag{5.25b}$$

The approximation of the integral by sums of 180 elements therefore induces an error of approximately 0.26% for $a\left(n_\theta\right)$ and -0.01% for $b\left(n_\theta\right)$. Therefore, this discrete approximation done by the fly eye is highly accurate and deviates only marginally from an ideal continuous integration scheme.

Rotation around the y axis When considering a receptive field of a rotation around the y axis the action field becomes

$$\begin{aligned}\boldsymbol{S}_{AF}(\mathfrak{A}^y_{rot},\mathfrak{B}) &= \sum_{\theta}^{n_\theta}\sum_{\phi}^{n_\theta}\boldsymbol{p}\left(\left[0\ r^y_A\ 0\right]^T,\mathbf{0},\theta,\phi\right)\cdot\boldsymbol{p}\left(\boldsymbol{r}_B,\boldsymbol{t}_B,\theta,\phi\right)\sin\left(\Delta\phi\right)\sin\left(\Delta\theta\right)\cos\left(\phi\right)\\ &= c\left(n_\theta\right)v^{rot}_A\,v^{rot}_B\,r^y_A\,r^y_B,\end{aligned} \tag{5.26}$$

where

$$c\left(n_\theta\right) = \xi\left(n_\theta\right)\left(4\cos\left(\frac{\pi}{n_\theta}\right) + 3\,n_\theta\cos\left(\frac{\pi}{n_\theta}\right) + n_\theta + 2\right), \tag{5.27}$$

with

$$\xi\left(n_\theta\right) = \frac{\sin\left(\frac{\pi}{n_\theta}\right)\left(\cos\left(\frac{\pi}{n_\theta}\right)+1\right)}{2\left(1+2\cos\left(\frac{\pi}{n_\theta}\right)\right)}. \tag{5.28}$$

Convergence of the sum towards the integral is fulfilled since

$$\lim_{n_\theta \to \infty} c\left(n_\theta\right) = \frac{4}{3}\,\pi, \tag{5.29}$$

confirming the validity of this approximation. For the fly-like approximation of the integral by sums of 180 elements the coefficient $c\left(n_\theta\right)$ becomes

$$c\left(180\right) = 4.2231. \tag{5.30}$$

Therefore, this approximation of the integral by sums of 180 elements as is done in the fly visual system induces an error of only approximately 0.82% for $c\left(n_\theta\right)$.

Rotations around axes on the xy plane The action field when considering a receptive field of a rotation around an arbitrary axis lying on the xy plane becomes

$$\begin{aligned}\boldsymbol{S}_{AF}(\mathfrak{A}_{rot}^{xy}, \mathfrak{B}) &= \sum_{\theta}\sum_{\phi} \boldsymbol{p}\left(\left[r_A^x \; r_A^y \; 0\right]^T, \mathbf{0}, \theta, \phi\right) \cdot \boldsymbol{p}\left(\boldsymbol{r}_B, \boldsymbol{t}_B, \theta, \phi\right) \sin\left(\Delta\phi\right) \sin\left(\Delta\theta\right) \cos\left(\phi\right) \\ &= a\left(n_\theta\right) v_A^{rot}\, v_B^{rot}\, r_A^x\, r_B^x + b\left(n_\theta\right) \mu\, v_A^{rot}\, v_B^{tra}\, r_A^x\, t_B^z + c\left(n_\theta\right) v_A^{rot}\, v_B^{rot}\, r_A^y\, r_B^y, \end{aligned} \tag{5.31}$$

where

$$a\left(n_\theta\right) = \xi\left(n_\theta\right)\left(3\, n_\theta \cos\left(\frac{\pi}{n_\theta}\right) + 2\cos\left(\frac{\pi}{n_\theta}\right) + n_\theta\right), \tag{5.32a}$$

$$b\left(n_\theta\right) = \xi\left(n_\theta\right)\left(2\, n_\theta \cos\left(\frac{\pi}{n_\theta}\right) + n_\theta\right), \tag{5.32b}$$

$$c\left(n_\theta\right) = \xi\left(n_\theta\right)\left(3\, n_\theta \cos\left(\frac{\pi}{n_\theta}\right) + 4\,\cos\left(\frac{\pi}{n_\theta}\right) + n_\theta + 2\right), \tag{5.32c}$$

with

$$\xi\left(n_\theta\right) = \frac{\sin\left(\frac{\pi}{n_\theta}\right)\left(\cos\left(\frac{\pi}{n_\theta}\right) + 1\right)}{2\left(1 + 2\cos\left(\frac{\pi}{n_\theta}\right)\right)}. \tag{5.33}$$

Again, a convergence of the sum towards the integral holds true since

$$\lim_{n_\theta \to \infty} a\left(n_\theta\right) = \frac{4}{3}\,\pi, \tag{5.34a}$$

$$\lim_{n_\theta \to \infty} b\left(n_\theta\right) = \pi, \tag{5.34b}$$

$$\lim_{n_\theta \to \infty} c\left(n_\theta\right) = \frac{4}{3}\,\pi, \tag{5.34c}$$

confirming the approach being valid. Also, for a quantitative assessment of the accuracy of this approximation done in the fly visual system, i.e. an approximation of the integral by sums of 180 elements these coefficients become

$$a\left(180\right) = 4.1998, \tag{5.35a}$$

$$b\left(180\right) = 3.1412, \tag{5.35b}$$

$$c\left(180\right) = 4.2231. \tag{5.35c}$$

The biologically realistic approximation of the integral by sums of 180 elements therefore induces an error of approximately 0.26% for $a\,(n_\theta)$, -0.01% for $b\,(n_\theta)$ and 0.82% for $c\,(n_\theta)$.

Taken together, the results presented here confirm the validity and well suited nature of the receptive field and optic flow based computation scheme used by the fly visual system. Analytically, the action fields turn out to be highly exact and robust rotation estimators even in the presence of arbitrary overlaid translations in the xy plane. This holds true for symmetric and under mild restrictions even asymmetric integration domains, such as the partial fields of view of individual fly compound eyes. Also, a more realistic summation of discrete photoreceptor inputs could be proven to be a valid approximation with only marginal added distortion of typically less than 1%.

5.2 Closed Loop Rotation Analysis

The function and performance of the fly visual system and the derived technical sensor have thus far in this work been analyzed in open loop conditions, i.e. as pure sensors. This results in a good insight into their respective static sensing capabilities. However, as in the biological original, the visual system is but one element embedded in a larger, more complex dynamical system. Hence, in order to fully appreciate the benefits and performance of the visual system it needs to be analyzed in closed loop conditions within a freely "behaving" dynamical system, which in turn maneuvers within a realistic environment.

In order to analyze the visual system—in this specific study the VS cell network and its rotation sensing—in a fully dynamic feedback environment a complete 6 DOF simulation environment is devised, which is based on a custom built physics engine that takes into account all relevant physical laws governing the kinematics and dynamics at scale. Using this environment the closed loop properties of a virtual fly such as overall stability, gain restrictions, delay immunity, robustness, etc. are assessed in full feedback conditions.

In the following, the physics engine and its governing equations and constants are derived. The resulting system is then analyzed with respect to overall closed loop stability. Subsequently, the influence of superposition of translation onto rotations is investigated. Finally, the system's robustness to added temporal delays is assessed.

5.2.1 Virtual Flight Environment

In order to build a numerical simulation environment a physics engine needs to be implemented, which in turn needs to incorporate accurate models of the rigid body dynamics of translational and rotational motion. Therefore, in the following, equations for translational and rotational motion are deduced, similar to [204] and [205], after which the corresponding constants and parameters are derived.

Translational Motion

In inertial reference frames mass, velocity and force can be related according to Newton's laws as

$$m\frac{d\,({}_i\boldsymbol{v})}{dt} = \boldsymbol{f}, \tag{5.36}$$

where m denotes mass, ${}_i\boldsymbol{v}$ is the velocity in the inertial frame and $\boldsymbol{f}$ represents force. With the Coriolis equation this can now be expressed in the body frame as

$$m\left(\frac{d\left({}_b\boldsymbol{v}\right)}{dt} + {}_b\boldsymbol{\omega} \times {}_b\boldsymbol{v}\right) = {}_b\boldsymbol{f}^n, \tag{5.37}$$

where ${}_b\boldsymbol{f}^n$ denotes net force in the body frame, which can be separated into propulsion force ${}_b\boldsymbol{f}$ and opposing friction drag force ${}_b\boldsymbol{f}^D$ as

$${}_b\boldsymbol{f}^n = {}_b\boldsymbol{f} - {}_b\boldsymbol{f}^D. \tag{5.38}$$

This friction drag force can be expressed as

$${}_b\boldsymbol{f}^D = \frac{1}{2}\,{}_b\boldsymbol{v}^2 \rho\, C_D A, \tag{5.39}$$

where ρ denotes the mass density of air, ${}_b\boldsymbol{v}$ is the velocity, C_D is the drag coefficient and A is the reference area, which in turn can be expressed as

$$A = \pi r_{th}^2 + 2S\sin(\beta), \tag{5.40}$$

with r_{th} being the thoracic half-width, S the wing surface area and β representing the stroke plane angle during straight forward flight. By now substituting Eq. 5.38 through Eq. 5.40 into Eq. 5.37 and expressing the velocity in body coordinates ${}_b\boldsymbol{v} = [u\ v\ w]^T$ and the angular velocity in the body frame ${}_b\boldsymbol{\omega} = [p\ q\ r]^T$ the following expression can be derived:

$$\begin{bmatrix} \dot{u} \\ \dot{v} \\ \dot{w} \end{bmatrix} = \begin{bmatrix} rv - qw \\ pw - ru \\ qu - pv \end{bmatrix} + \frac{1}{m}\begin{bmatrix} {}_bf_x \\ {}_bf_y \\ {}_bf_z \end{bmatrix} - \frac{\rho\, C_D\left(\pi r_{th}^2 + 2S\sin(\beta)\right)}{2m}\begin{bmatrix} u^2 \\ v^2 \\ w^2 \end{bmatrix}. \tag{5.41}$$

Rotational Motion

In an analogous fashion to translational motion, using the Coriolis equation for rotational motion the angular momentum ${}_b\boldsymbol{l}$ and torque ${}_b\boldsymbol{\tau}$ can be related as

$$\frac{d\left({}_b\boldsymbol{l}\right)}{dt} + {}_b\boldsymbol{\omega} \times {}_b\boldsymbol{l} + C\,{}_b\boldsymbol{\omega} = {}_b\boldsymbol{\tau}, \tag{5.42}$$

where C represents the frictional damping coefficient and the angular momentum depends on inertia and angular velocity as

$${}_b\boldsymbol{l} = \boldsymbol{J} \cdot {}_b\boldsymbol{\omega}, \tag{5.43}$$

with the $\boldsymbol{J}$ being the inertia matrix and ${}_b\boldsymbol{\omega}$ denoting angular velocity. Substituting Eq. 5.43 into Eq. 5.42 then yields

$$\frac{d\left(\boldsymbol{J} \cdot {}_b\boldsymbol{\omega}\right)}{dt} + {}_b\boldsymbol{\omega} \times \boldsymbol{J} \cdot {}_b\boldsymbol{\omega} + C_b\boldsymbol{\omega} = {}_b\boldsymbol{\tau}. \tag{5.44}$$

Considering that the angular velocity is comprised of three components as

$${}_b\boldsymbol{\omega} = \begin{bmatrix} p \\ q \\ r \end{bmatrix}, \tag{5.45}$$

while the torque is separable into

$$ {}_b\boldsymbol{\tau} = \begin{bmatrix} \tau_\phi \\ \tau_\theta \\ \tau_\psi \end{bmatrix} \tag{5.46} $$

and the inertia matrix can further be expressed as

$$ \boldsymbol{J} = \begin{bmatrix} J_x & 0 & 0 \\ 0 & J_y & 0 \\ 0 & 0 & J_z \end{bmatrix} \tag{5.47} $$

means that separating vectors and matrices in Eq. 5.44 into their constituting components finally results in

$$ \begin{bmatrix} \dot{p} \\ \dot{q} \\ \dot{r} \end{bmatrix} = \begin{bmatrix} \frac{J_y - J_z}{J_x} qr \\ \frac{J_z - J_x}{J_y} pr \\ \frac{J_x - J_y}{J_z} pq \end{bmatrix} + \begin{bmatrix} \frac{1}{J_x}\tau_\phi \\ \frac{1}{J_y}\tau_\theta \\ \frac{1}{J_z}\tau_\psi \end{bmatrix} - C \begin{bmatrix} \frac{1}{J_x}p \\ \frac{1}{J_y}q \\ \frac{1}{J_z}r \end{bmatrix}. \tag{5.48} $$

Now having obtained Eq. 5.41 for translational and Eq. 5.48 for rotational motion, the physics engine can be implemented using these dynamics equations and the corresponding constants. This is described in the following section.

Flight Parameter Selection

For simulating a virtual fly in the flight simulator the parameters of the governing equations need to be experimentally determined or taken from the established literature. In this work the large blowfly *Calliphora vicina* is chosen as a model organism due to the broad range of literature pertaining its morphological aspects, flight kinematics and flight dynamics. The parameters for obtaining the translational dynamics of Eq. 5.41 are summarized in Table 5.1.

Consequently, *Calliphora vicina* is also chosen as the model organism for the rotational dynamics described by Eq. 5.48. The moments of inertia are determined by approximating the fly body by a three dimensional solid ellipsoid of body mass $m = 62\,\mathrm{mg}$, length $L = 12\,\mathrm{mm}$ and diameter $D = 5\,\mathrm{mm}$, as illustrated in Figure 5.1. The semi-axes of this ellipsoid are thusly denoted $a = 6\,\mathrm{mm}$, $b = 2.5\,\mathrm{mm}$ and $c = 2.5\,\mathrm{mm}$. The inertia tensor $\boldsymbol{J}$ for

Table 5.1: Parameters of Translational Dynamics

Parameter	Description	Value	Reference
m	Mass	$62.0 \times 10^{-6}\,\mathrm{kg}$	[206]
ρ	Air density	$1.2\,\mathrm{kg\,m^{-3}}$	[207]
C_D	Drag coefficient	1.46	[208]
r_{th}	Thoracic half-width	$2.5 \times 10^{-3}\,\mathrm{m}$	This study
S	Wing surface	$57.8 \times 10^{-6}\,\mathrm{m^2}$	[206]
β	Stroke plane angle	$47.1°$	[206]

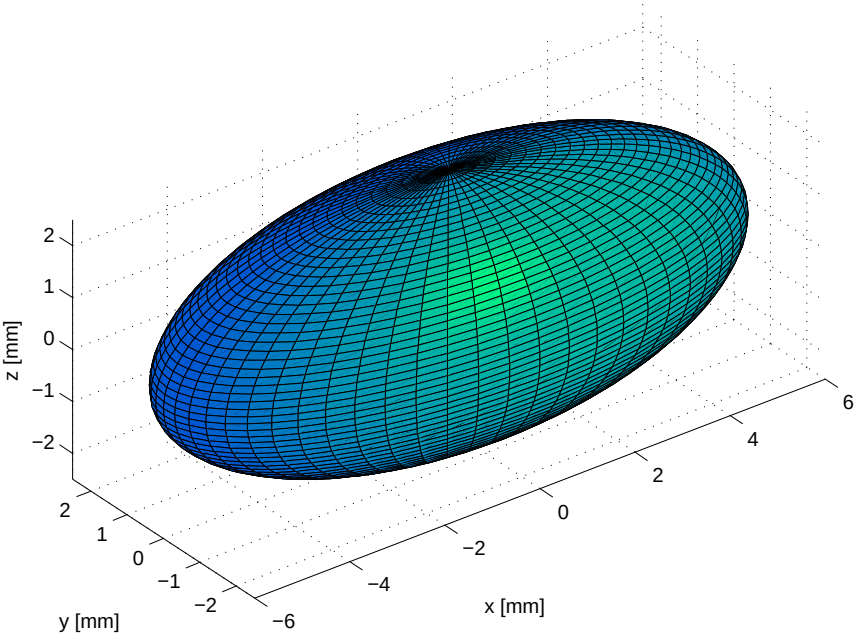

Figure 5.1: Approximation of the fly body by an ellipsoid of semi-axes $a = 6\,\mathrm{mm}$, $b = 2.5\,\mathrm{mm}$ and $c = 2.5\,\mathrm{mm}$.

rotations around the center of mass therefore yields

$$\boldsymbol{J} = \begin{bmatrix} J_x & 0 & 0 \\ 0 & Jy & 0 \\ 0 & 0 & J_z \end{bmatrix} = \begin{bmatrix} \frac{1}{5}m\left(b^2+c^2\right) & 0 & 0 \\ 0 & \frac{1}{5}m\left(a^2+c^2\right) & 0 \\ 0 & 0 & \frac{1}{5}m\left(a^2+b^2\right) \end{bmatrix}, \tag{5.49}$$

which substituting accordingly results in

$$J_x = 1.55 \times 10^{-10}\,\mathrm{N\,m\,s^2}, \tag{5.50a}$$
$$J_y = 5.24 \times 10^{-10}\,\mathrm{N\,m\,s^2}, \tag{5.50b}$$
$$J_z = 5.24 \times 10^{-10}\,\mathrm{N\,m\,s^2}. \tag{5.50c}$$

The frictional damping coefficient C is here defined as the sum of body and wing damping effects, i.e.

$$C = C_{body} + C_{wing}. \tag{5.51}$$

The body damping coefficient can be readily determined by an integration of Stokes' law [209], which results in

$$C_{body} = \frac{\pi\mu L^3}{3\ln\left(\frac{L}{2D}\right)} = 1.82 \times 10^{-10}\,\mathrm{N\,m\,s}, \tag{5.52}$$

with $\mu = 1.83 \times 10^{-5}\,\mathrm{kg\,m^{-1}\,s^{-1}}$ being the dynamic viscosity of air at 20 °C [209]. The wing damping coefficient on the other hand is calculated using a quasi-steady aerodynamics approach as

$$C_{wing} = \frac{\bar{D}_{dif}\hat{r}_{CP}\left(R + 0.5D\right)}{\bar{\omega}} = 1.69 \times 10^{-7}\,\mathrm{N\,m\,s}, \tag{5.53}$$

where $\bar{D}_{dif} = 5.78 \times 10^{-4}\,\mathrm{kg\,m\,s^{-2}}$ is the differential wing profile drag, $\hat{r}_{CP} = 0.7$ is the distance to the center of pressure [210], $R = 9.2\,\mathrm{mm}$ is the wing length [206] and $\bar{\omega} = 1600\,^\circ\,\mathrm{s}^{-1}$ [207] is the mean saccadic turning rate. Finally, the resulting frictional damping coefficient comes to be

$$C = 1.70 \times 10^{-7}\,\mathrm{N\,m\,s}. \tag{5.54}$$

It is now possible to estimate the time constants for rotations around the different body axes by dividing the respective moment of inertia by the frictional damping coefficient, thus resulting in

$$\tau_\phi = \frac{J_x}{C} = 0.91\,\mathrm{ms}, \tag{5.55a}$$

$$\tau_\theta = \frac{J_y}{C} = 3.09\,\mathrm{ms}, \tag{5.55b}$$

$$\tau_\psi = \frac{J_z}{C} = 3.09\,\mathrm{ms}, \tag{5.55c}$$

which means that for pitch and yaw the time constant is roughly equal to half a fly stroke cycle of about 6 ms, while for roll it is considerably shorter. Having obtained the damping coefficient $C = 1.70 \times 10^{-7}\,\mathrm{N\,m\,s}$ and supposing a maximum angular velocity of $\omega_{max} = 2000\,^\circ\,\mathrm{s}^{-1} = 34.91\,\mathrm{rad\,s}^{-1}$ [199] the maximum torque can be estimated by

$$T_{max} = C \cdot \omega_{max} = 5.92 \times 10^{-6}\,\mathrm{N\,m}. \tag{5.56}$$

This maximum torque of $5.92 \times 10^{-6}\,\mathrm{N\,m}$ is on roughly the same order of magnitude as previous estimates [199].

5.2.2 Closed Loop Performance

Once the complete numerical simulation framework with all the equations and parameters behind the visual and aerodynamic models are obtained, the model simulations can be performed as to assess the system's closed loop behavior. In order to do so a simulation environment is created in which a virtual fly can be moved in all its six degrees of freedom—namely thrust, lift, sideslip, roll, pitch and yaw—within virtually any kind of visual surround. By making use of the aforementioned physics engine dynamical physical properties of this fly, such as drag, inertia, etc. can be fully taken into account. For presentation of the visual panorama *cube mapping* is employed [195], in which the walls of a virtual room of cubic proportions with 2 m side length can be tapered with the six corresponding cubic projections of any one of a wide array of visual sceneries. All simulations are conducted in MATLAB (MathWorks Inc.) using an elementary time step of 1 ms.

In Figure 5.2 a schematic of the complete simulation environment is depicted. At its core in the *Fly Dynamics* block it features the physics engine computing current pose and motion parameters of the virtual fly, which then in the *Environment* block get translated to a corresponding resulting visual image on the vantage point, i.e. the virtual fly's retina. This input is then sampled akin to the fly's ommatidia in a discrete fashion—in this case as a homologue to the technical sensor implementation of Chapter 4 as a 240×240 quadratic polar grid array of inputs to the subsequent *Local Motion Detection* block. Here, these inputs are processed both horizontally and vertically according to a basic HRM scheme with a time constant of $\tau_{LP} = 33\,\mathrm{ms}$, thus resulting in 240×240 two-dimensional elementary

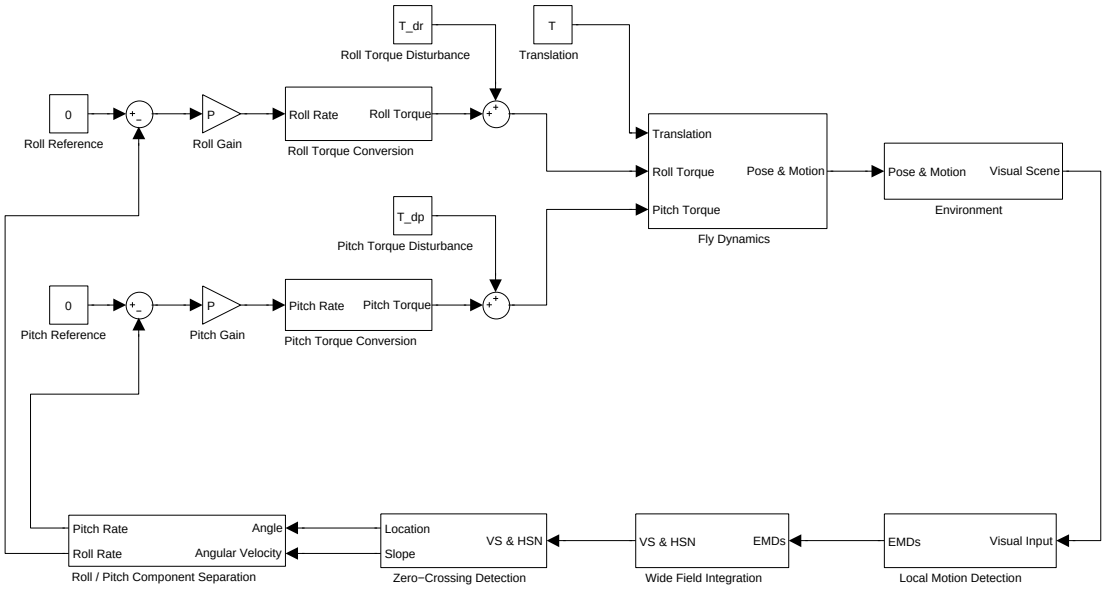

Figure 5.2: Schematic of the full 6 DOF simulation environment.

motion estimates. In the *Wide Field Integration* block these estimates are integrated into global motion estimates akin to the HS and VS cell network, which in turn serve as a basis for the rotation axis and angular velocity estimation using a *zero-crossing* scheme in the thusly named block. These estimates are then in the next block crudely separated into their roll and pitch components by weighting the angular velocity estimate by the projection of the 2D rotation axis estimate on the equatorial plane onto the 0° roll axis and the 90° pitch axis, respectively. These two signals are then used as the actual feedback inputs into the two control loops handling roll and pitch separately. In this case, albeit being physically linked into one multiple input multiple output (MIMO) system, these two parameters can be treated as two independent single input single output (SISO) systems due to the relatively weak linkage for this particular system and operational range.

The two control loops are devised as zero control systems with a proportional controller onto which a torque signal is imposed as disturbance [196]. This corresponds to realistic disturbances such as drafts or wind gusts a fly typically encounters in its natural surroundings, thus validating the control environment implemented here as a biologically relevant task the fly visual system indeed has to face and overcome on a regular basis.

The coordinate system is chosen coinciding with the fly brain's vantage point. As such, the virtual animal's rostrocaudal axis is defined as the 0° axis and the dextro-sinister axis as the 90° axis on the equatorial plane. In this scheme, as depicted in Figure 5.3, a roll movement would therefore result in a rotation around 0°, whereas a pure pitch motion would be around 90°. It is worth noting that in this study only one fly compound eye is simulated, i.e. the 240×240 input elements are distributed over the right 2π sr hemisphere, so that one complete HS and VS cell network can be analyzed. The additional left hemisphere is easily implementable so that in future studies both compound eyes can be interconnected, thereby sampling the complete visual surround and speculatively adding

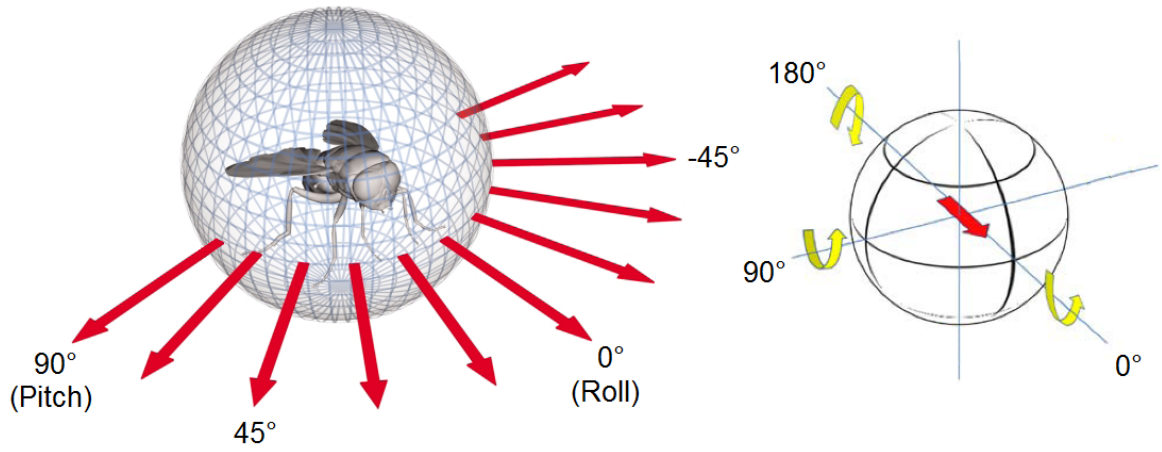

Figure 5.3: Coordinate system definition for simulations and axes definitions. As shown here for the right hemisphere, rotational velocities are defined as positive around an arbitrary axis following the right hand rule. Adapted from [211] and [201].

further robustness to estimations. Also, specific neural interconnections could thusly be analyzed.

Control Performance and Residual Slip Speed

Now with the complete control environment in place the first set of simulations can be performed assessing the control performance in terms of residual rotational velocity of the system. Following the pertinent literature the unitary gain was arbitrarily defined as the gain reducing rotational velocity to 70% of the open loop angular velocity [196], thus enabling direct comparison between different sensor modalities. In this first set of experiments a motion bias torque of $1.3032 \times 10^{-7}\,\mathrm{N\,m}$ is applied as a step disturbance to each control loop, which if applied to each loop alone would result in an open loop angular velocity of $44\,^{\circ}\,\mathrm{s}^{-1}$ around that particular axis. The chosen visual scene is the one previously shown in Figure 4.10f.

An exemplary disturbance combination is shown in Figure 5.4. Here, a disturbance torque is applied from $t = 0.2\,\mathrm{s}$ to $0.4\,\mathrm{s}$ on the pitch axis (blue shading), from $t = 0.6\,\mathrm{s}$ to $0.8\,\mathrm{s}$ on the roll axis (green shading), from $t = 1\,\mathrm{s}$ to $1.2\,\mathrm{s}$ again on the pitch axis (blue shading), from $t = 1.2\,\mathrm{s}$ to $1.6\,\mathrm{s}$ on both the pitch and roll axes (yellow shading) and finally from $t = 1.6\,\mathrm{s}$ to $1.8\,\mathrm{s}$ again only on the pitch axis (blue shading). The resulting open loop angular velocity of the virtual fly can be readily seen in the black trace of the upper graph in Figure 5.4. The green and red traces in the upper graph indicate the system's closed loop residual angular velocity using a theoretical ideal sensor and the proposed EMD sensor, respectively. In this scenario an ideal sensor is regarded as a sensor that reflects the true instantaneous velocity at the given point in time. Here, the same gain $g = 2.0$ is used for both pitch and roll control loop. As can be observed, both sensor modalities essentially yield the same residual rotational velocity for the system in question. The only notable difference is the latency of roughly 40 ms in the system's response when employing the EMD sensor variant. This is largely due to the EMD's inherent use of a low pass filter with its time constant of $\tau_{LP} = 33\,\mathrm{ms}$. Notably, for the segment of simultaneous disturbance torques on both pitch and roll axes from $t = 1.2\,\mathrm{s}$ to $1.6\,\mathrm{s}$ the system remains stable and,

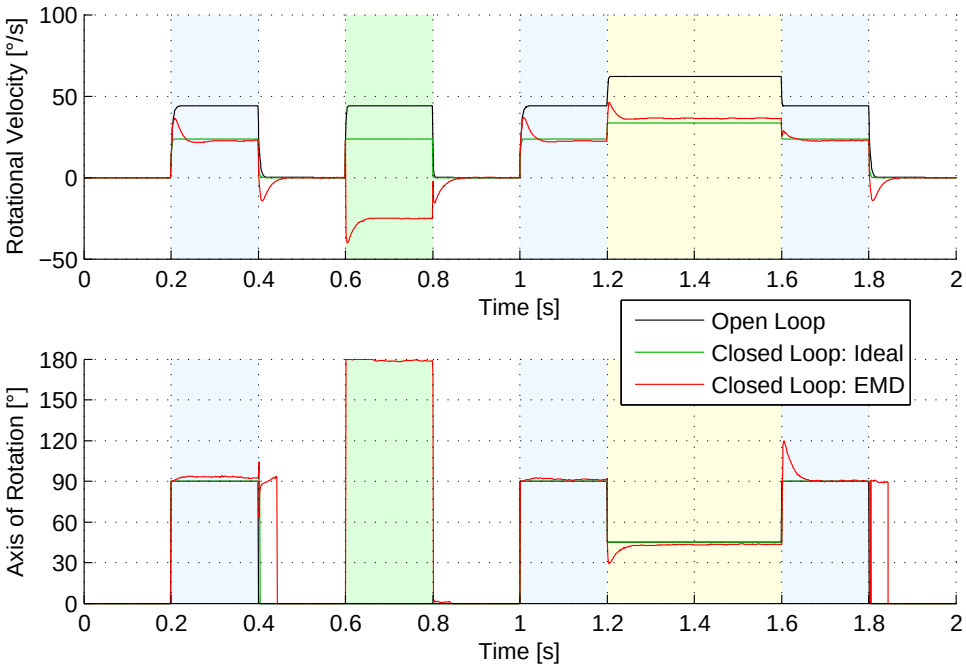

Figure 5.4: Closed loop trial with a combination of disturbances at gain $g = 2$. Blue shaded areas indicate applied pitch disturbance torque, green shading roll disturbance and yellow shading simultaneous pitch and roll disturbances. Non-shaded white areas indicate absence of disturbance torques.

thus, validates the initial assumption of separability of the full dynamical MIMO system into two SISO systems controlling pitch and roll independently.

The lower graph of Figure 5.4, indicating the axis of rotation, reveals the accuracy of the EMD sensor in this regard. While using this kind of sensor from $t = 0.2\,\mathrm{s}$ to $0.4\,\mathrm{s}$, i.e. during disturbance purely around the 90° pitch axis, the system rotates around axes closely following the 90° line (red trace). In fact, for this period the system's rotation is on average around 92.45° which translates to an average deviation of 2.45° for a pitch disturbance torque. On the other hand, for a pure roll disturbance torque, such as present from $t = 0.6\,\mathrm{s}$ to $0.8\,\mathrm{s}$ using the EMD sensor the system's rotation is on average around 178.35°, thereby deviating by 1.65° from a perfect rotation around 0° or equivalently 180°. Note, that following the right hand rule [212] shown in Figure 5.3 the system's velocity indeed becomes negative as the axis of rotation nears 180° in this segment from $t = 0.6\,\mathrm{s}$ to $0.8\,\mathrm{s}$. In other words, the right-eye mimicking EMD sensor correctly perceives a positive rotation around a frontal axis roughly equal to a negative rotation around a posterior axis.

As can be seen from $t = 1.2\,\mathrm{s}$ to $1.6\,\mathrm{s}$ the proposed EMD sensor also responds to combined rotations around axes resulting from torques in roll and pitch simultaneously. Since in this case both disturbance torques are equal in magnitude the resulting rotation results around 45° and is effectively $\sqrt{2}$ times as fast around that axis. Yet again, both ideal and EMD-based sensors stabilize the system while rotating around an axis close to 45° at a rotational velocity that depends on the applied gain.

It can be concluded from these experimental results, that the proposed EMD sensor can successfully stabilize the system in presence of torque disturbances on the pitch and roll

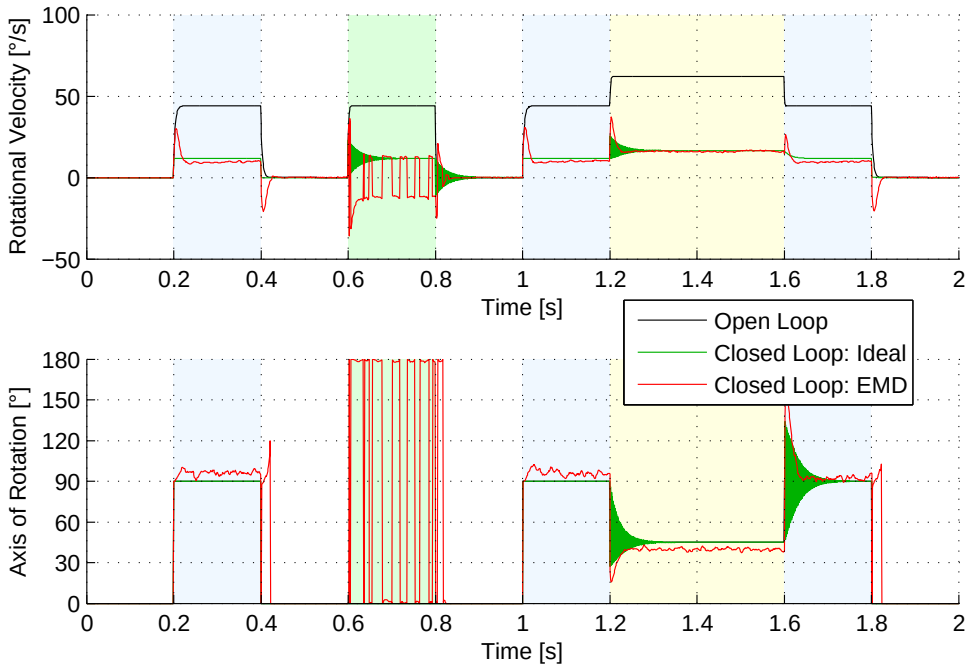

Figure 5.5: Closed loop trial with a combination of disturbances at gain $g = 6.5$. Blue shaded areas indicate applied pitch disturbance torque, green shading roll disturbance and yellow shading simultaneous pitch and roll disturbances. Non-shaded white areas indicate absence of disturbance torques. Note the positive angular velocity for roll around axes near $0°$ and negative velocities for roll around axes near $180°$, as observable e.g. from $t = 0.6\,\mathrm{s}$ to $0.8\,\mathrm{s}$.

axes. Also, simultaneous disturbances on both axes, resulting in arbitrary axes in between are handled satisfactorily. Moreover, the proposed sensor's performance in terms of residual rotational velocity is equal to—if not better than—the performance of a theoretical ideal linear sensor.

Gain and Overall Stability

The feedback gain is evidently the critical parameter largely responsible for the residual rotational velocity. Generally, the higher the gain is set the lower the resulting residual rotational velocity is to be expected. However, this usually holds true up to a certain critical gain, after which the system becomes unstable. When comparing the control performance at gain $g = 2$ of Figure 5.4 with the control performance using $g = 6.5$ as shown in Figure 5.5 it is evident that residual rotational velocity is lower for the higher gain scenario. However, at the same time in Figure 5.5 it can be observed, that this gain is already on the brink of instability for roll rotations.

Therefore, in order to assess the permissible gains and overall stability of the system a second set of experiments is carried out. In this scenario a unit step disturbance torque is applied on the pitch axis over a range of different gains, while the system is observed in terms of behavior and stability. For better quantification of the behavior the residual slip speed is defined as the ratio of residual rotational velocity and open loop velocity [196]. This dimensionless relative slip speed is used as performance metric here onwards, indicating a better performance the lower it is.

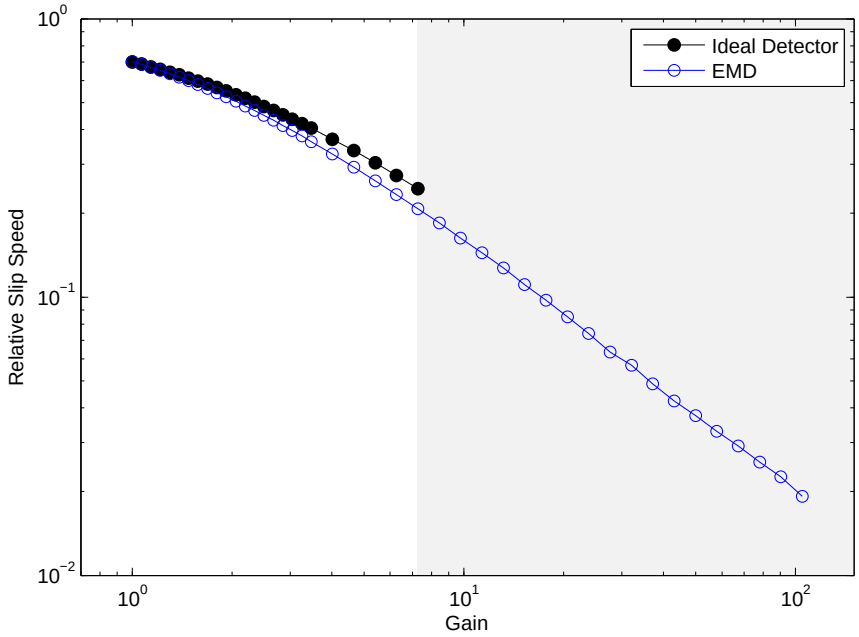

Figure 5.6: Residual slip speed as a function of the overall system gain under closed loop conditions for unitary step disturbance torques around the pitch axis.

When performing this analysis for ideal and EMD sensors over step disturbances in the pitch control loop the relative slip speed depends on the gain as illustrated in Figure 5.6. Notably, when employing the ideal sensor the system becomes unstable for gain values above 7.25, whereas it continues to stay stable when using the EMD-based sensor at these gain values. Moreover, the system not only remains stable but also slip speed performance continues to increase with larger gains. For this scenario the proposed EMD-based sensor in fact at all gain values yields superior performance when compared to the theoretically ideal linear sensor while maintaining better overall stability. This means that by utilizing this sensor the feedback gain may be adjusted to higher values, thus achieving lower residual rotational velocity and therefore better disturbance rejection.

A highly beneficial attribute of EMDs is their high resilience against visual input noise [4, 5]. It is therefore of practical interest to see whether this also holds true for noise fluctuations in the system's torque disturbances. In order to assess the system's noise rejection the same experimental conditions as in the previous simulations are used, but on top of the step disturbances a normally distributed noise torque with a standard deviation of 10% of the step size is added. The resulting traces for gain $g = 2.0$ can be observed in Figure 5.7a. Similar to the previous simulations without noise (Figure 5.4), after a disturbance the system stabilizes quickly around a given residual slip speed, fluctuating around it depending on the imposed noise. When assessing permissible gain values with respect to overall stability it is revealed in Figure 5.7b that the stability margins for the ideal sensor are reduced, while the EMD sensor continues to remain stable throughout all gain settings. This asserts the higher noise rejection of the EMD sensor in comparison to a theoretically ideal linear sensor.

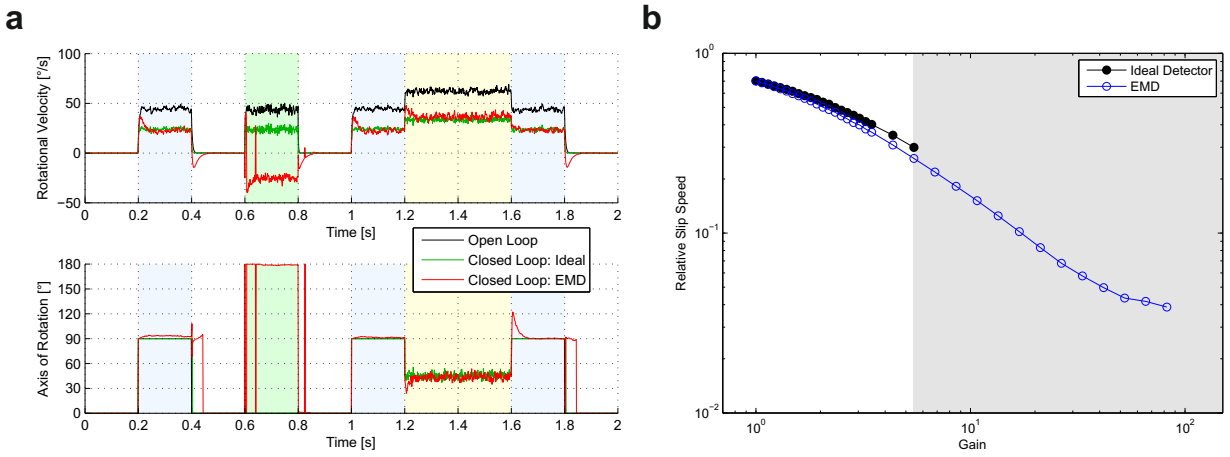

Figure 5.7: Gain and residual slip speed analysis for unitary step disturbance with added noise. (**a**) Disturbance combination as in Figure 5.4 with gain $g = 2.0$, but with superimposed noise torque added on top of disturbance torques. (**b**) Residual slip speed analysis revealing permissible gains with the same simulation parameters as shown in Figure 5.6 with added noise torque on top of disturbance torques.

5.2.3 Influence of Translational Superposition

The analysis thus far only considers a stationary fly with superimposed rotational torques. This, however, is not a typical flight situation of a fly. A fly is capable of intricate maneuvers including not only rotation but also translation along all its body axes [199]. As to analyze this kind of situation also translational motion is considered in the following.

Albeit possessing a rich repertoire of flight maneuvers the most classic of its flight situations is a direct forward flight with possible disturbance torques such as imposed upon by wind gusts or drafts. Moreover, as indicated in Eq. 5.19 and Eq. 5.20 as long as the lift translation along the z axis remains small, i.e. $t_B^z \approx 0$, the translatory influences can be filtered out using the correct templates for global wide field integration. The receptive fields of the VS cells employed here are examples of such rotational templates and should therefore help filtering out these unwanted translational components of motion. In order to corroborate this assumption, simulations are carried out similar to the ones exemplified in Figure 5.4, with added continuous translation throughout the simulation. This translation is implemented as a behaviorally relevant translation towards the front of the virtual fly along its longitudinal axis. Note, translation being restricted to motion along the longitudinal body axis does not restrict motion only to the equatorial plane. Similar to a real fly, through roll and pitch motion more complicated flight patterns can arise, including the typical *banked turn* [199] that is ubiquitous in flies or technical systems such as airplanes and helicopters.

In Figure 5.8 the influence of a translation of $0.4\,\mathrm{m\,s^{-1}}$ is shown, which is close to the reported average forward velocity of the blowfly *Calliphora* [199]. As can be seen in the resulting upper figure, with added forward translation (green trace) the system's rotational velocity remains remarkably close to the system's stationary response without any translation (red trace). In fact, in this case the difference in rotational velocity between the system with and without $0.4\,\mathrm{m\,s^{-1}}$ forward translation amounts to on average $1.88\,^\circ\,\mathrm{s^{-1}}$. Keeping in mind that for the virtual fly a forward velocity of $0.4\,\mathrm{m\,s^{-1}}$ equates to about 33

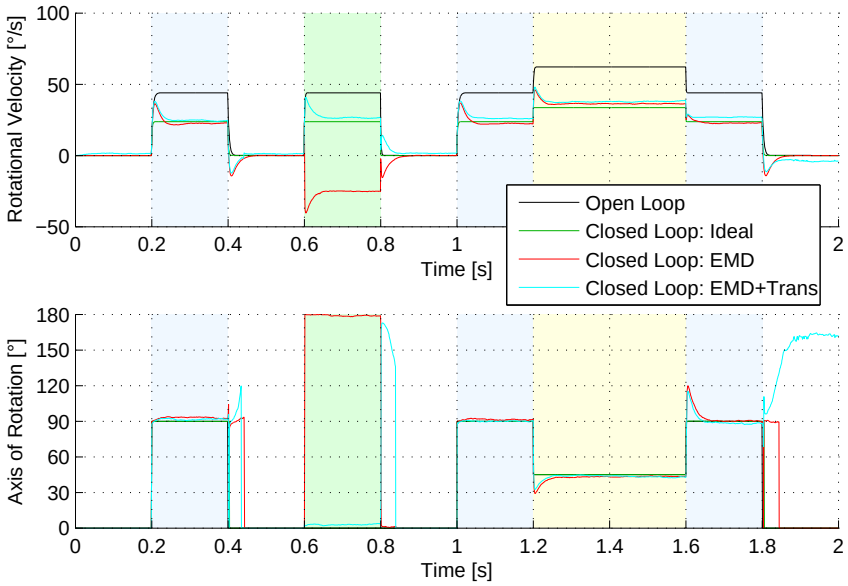

Figure 5.8: Closed loop trial with a combination of disturbances at gain $g = 2$.

body lengths per second and given that the visual test environment shown here is highly rotationally asymmetric (see Figure 4.10f) this performance is remarkable.

5.2.4 Influence of Delays

As a consequence of the *Drosophila* phototransduction cascade the internal delay until a Ca^{2+} signal is produced after photon absorption, i.e. quantum bump latency, lies roughly between 12 ms and 41 ms [213, 214], depending on the adaptation state of the animal. This means that in the fly visual system there is an inherent internal delay, which consequently presents a considerable destabilizing effect on the closed loop visuomotor system.

Then again, a fly is capable of correcting perturbations in its flight with high precision and high speed, thus indicating a high feedback gain in its sensorimotor loop. This, however, paired with the existence of sizable delays within the loop would render the system vulnerable to instability. Yet, the exact opposite is commonly observed as flies navigate with great robustness and stability. This suggests a high resilience against temporal delays already in the early stages of the fly motion detection system.

To see whether this holds true also for the dynamic model system investigated here a freely adjustable delay block is added to the sensor model. By now varying this delay time the system's response can be assessed in terms of its temporal disturbance rejection and stability. For the following simulations the same exemplary torque disturbance trajectory is used as previously described, while at the same time introducing a fixed sensor delay for each trial. The delay range is chosen as to be in the biologically relevant range for the implemented virtual fly.

In Figure 5.9 the system's responses are illustrated when facing delays in the range from 5 ms to 30 ms for using either the ideal linear or the EMD-based sensor. The disturbance rejection of the EMD-based sensor can be identified as generally being smoother, albeit at very low delay values presenting more overshoot and higher settling time. However, as delays become larger than 5 ms the ideal sensor continually presents more overshoot

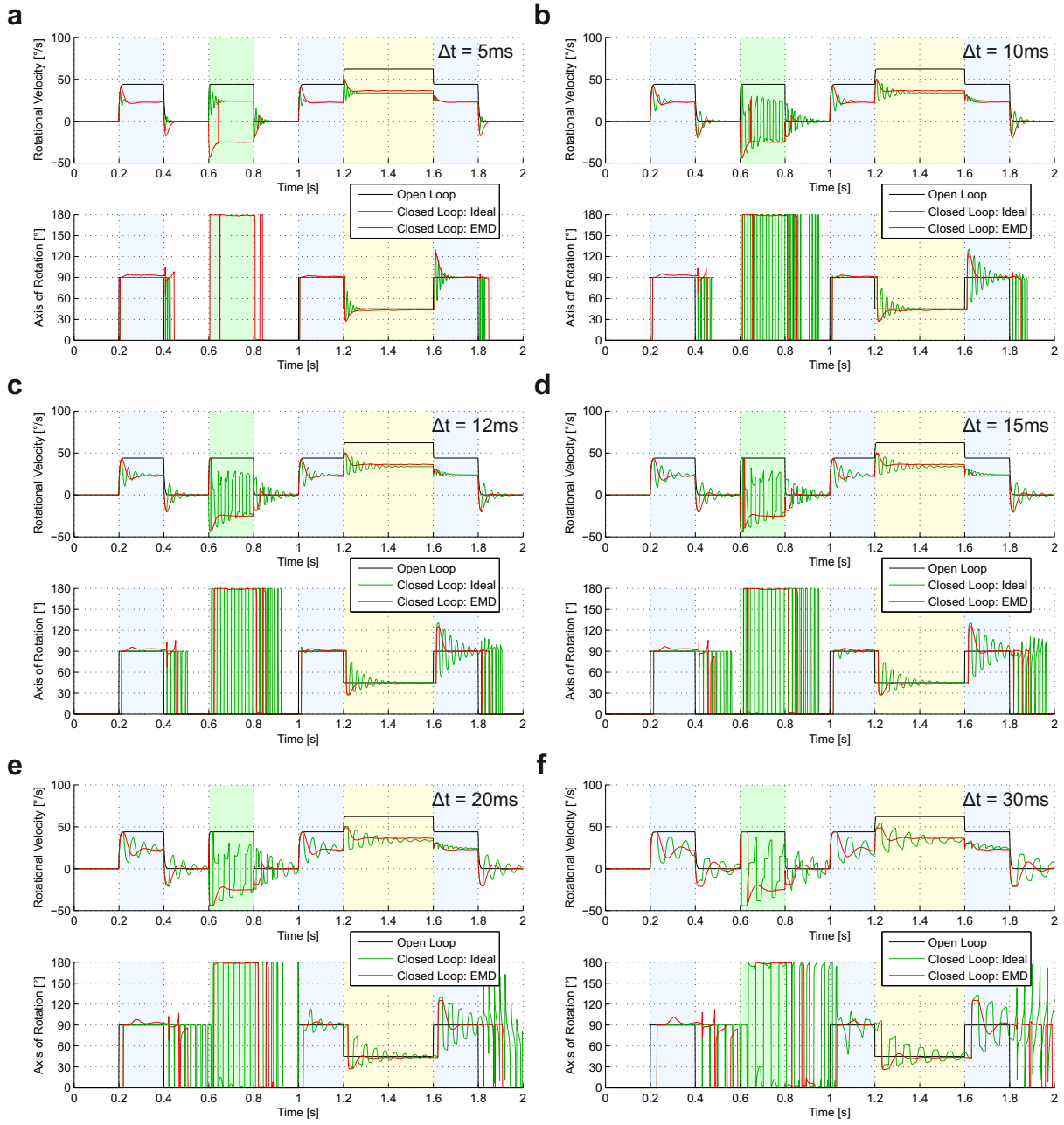

Figure 5.9: System responses with delays ranging from 5 ms to 30 ms at gain $g = 2.0$ while using either type of sensor.

and oscillations, thus increasing the system's settling time. At the same time, while using the EMD-based sensor the system only marginally increases its settling time and remains virtually oscillation free. Only when facing very large delay times, such as 20 ms and 30 ms onward, oscillations arise. Nevertheless, these are notably less than for the ideal sensor.

When analyzing the smoothness of the system's response in terms of pose and angular velocities it is important to note that with this being a biological system a minimum jerk trajectory is desirable [215]. For both real fly and implemented virtual fly the effective variable for actuation and change of pose and trajectory is the motor torque generated by the wing muscles. Consequently, a smooth torque trajectory is favored [216]. In fact, as

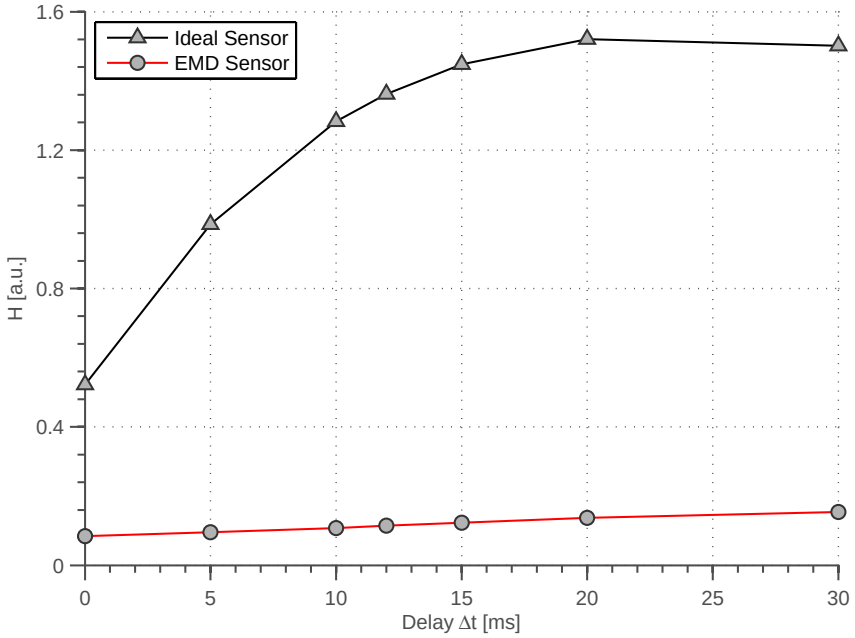

Figure 5.10: Minimum torque change cost function H over a range of delays for the system using either type of sensor. Data is taken from simulations presented in Figure 5.4 and Figure 5.9.

opposed to the minimum jerk criterion the minimum torque change criterion is directly applicable when external forces act upon the system, which is the case when considering external wind gusts and drafts [216,217]. Hence, the minimum torque change criterion can be defined as a cost function indicating performance as

$$H = \frac{1}{2}\int_{t_1}^{t_2}\left(\left(\frac{\mathrm{d}\tau_\theta}{\mathrm{d}t}\right)^2 + \left(\frac{\mathrm{d}\tau_\phi}{\mathrm{d}t}\right)^2 + \left(\frac{\mathrm{d}\tau_\psi}{\mathrm{d}t}\right)^2\right)\mathrm{d}t, \tag{5.57}$$

where τ_θ, τ_ϕ and τ_ψ denote roll, pitch and yaw torques, while t_1 and t_2 indicate the start and end time points of the trajectory, respectively. For this application, a lower torque cost function H indicates better performance.

A comparison between the ideal linear sensor and the EMD-based sensor in terms of the torque cost function H is presented in Figure 5.10. For this analysis the same experimental procedures are used as for the data plotted in Figure 5.9. Exemplarily, the region of interest $t_1 \ldots t_2$ is set to the time frame from 200 ms to 400 ms, i.e. facing a pitch torque disturbance. As can be readily seen, the EMD-based sensor outperforms the ideal linear sensor at all delay values. This is the case even when facing very small or no delays at all, which is due to the fact that the EMD explicitly filters out these high frequency components and, thus, produces a smoother response than the ideal sensor.

At very high delay times the torque cost function H of the system with the ideal sensor reaches a plateau and even decreases slightly—which, strikingly, would indicate better performance. However, while yielding a marginally smoother performance the system becomes prone to instabilities. This happens especially when operating at higher gains.

To assess the regions of stability, a gain response analysis of the system using the ideal sensor is conducted for different delay conditions. The results are shown in Figure 5.11.

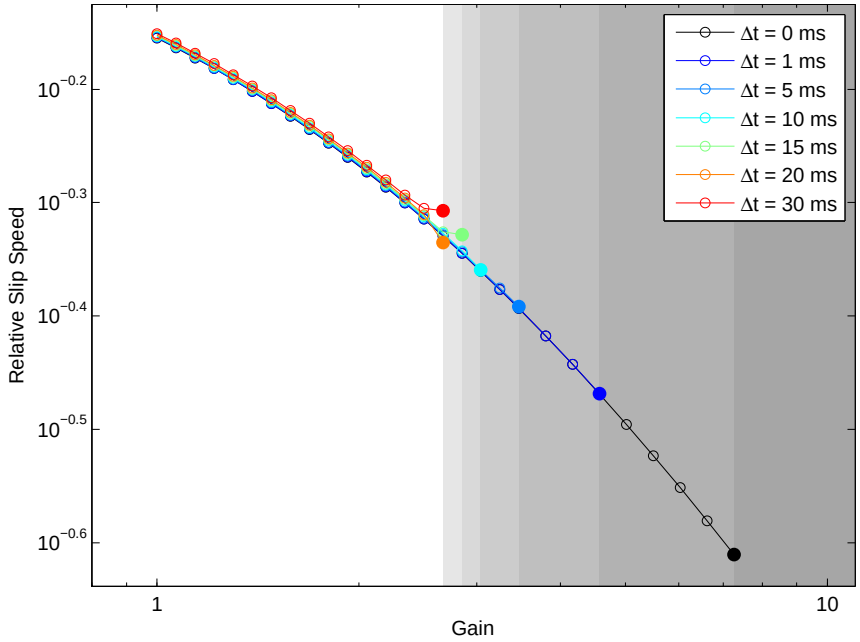

Figure 5.11: Residual slip speed under closed loop conditions for ideal sensor. Open circles denote data points whereas closed circles represent maximum stable gain for each delay scenario. Increasingly shaded areas indicate unstable regions for decreasing delay values.

Here, the attainable relative slip speeds are plotted as a function of the system gain g for several delay values in the range from 0 ms to 30 ms. Note, that the higher the delay value is, the earlier the system becomes unstable. The respective regions of instability are shown in increasingly grey shaded areas for decreasing delays. On the other hand, when using the EMD-based sensor the system does not get unstable. Instead, it remains stable for any combination of gain and delay throughout all ranges used in this study.

From the simulations presented thus far in this chapter it is conclusive that an EMD-based sensor bears several advantages over an ideal linear angular velocity sensor for an air-borne system such as a fly. Hence, using an EMD-based sensor such a system is far less prone to instabilities when using high gains. A direct consequence of this is the possibility of reducing slip speeds via higher gain settings, thus outperforming a system using an ideal linear sensor. Also, when using an EMD-based solution the system is less susceptible to noise, whether that be noise in the visual input or noise in disturbance torques. Moreover, the angular velocity trajectories generated using this fly-inspired rotation sensing scheme tend to be smoother than those generated with ideal sensors. This mainly results in less toque fluctuations and thereby less associated stress on the actuators, whether that be flight muscles in flies or motors in technical applications.

However, it is important to point out the susceptibility of this type of sensor to vertical lift translations. Even though being mainly tuned to visual input arising from rotations around particular body axes, fly LPTCs tend to be highly susceptible also to translation along the vertical axis. This can be mostly attributed to the non-linear wide-field integration scheme of LPTCs, which presents a high degree of saturation [218]. Despite this scheme not being employed in this study, even with linear integration these neurons show considerable dependency on vertical translation (see Eq. 5.16 and Eq. 5.17). Nevertheless, as flies tend to fly in straight paths using *banked turns* and similar moves involving rota-

tions for navigating [199], it is possible to avoid lift components and exclude them from this analysis without losing much validity.

5.3 Real Time Experimental Evaluation

The analysis presented so far in this chapter has been restricted to analytical assessment and *in silico* simulations. The sensing strategies presented here, however, are intended primarily for real-world application and deployment. It is therefore important to assess the closed loop sensing characteristics of this system also in real-world trials on-board a full scale MAV. The approach and results of this analysis are detailed in the following.

5.3.1 Closed Loop Rotation Analysis

In order evaluate the proposed sensing strategy in closed loop in a real-world setting, the sensor system described in Chapter 4 is mounted on-board an AscTec Pelican MAV (Ascending Technologies, Krailling, Germany) as depicted in Figure 5.12a. Anlyzing the quadrocopter's operational principles and motion characteristics the yaw angle is chosen as the degree of freedom to be controlled. Therefore the camera is mounted vertically pointing downwards as to have the desired axis of rotation near the center of the field of view of the camera (see Figure 5.12b). For integrating the camera system into the quadrocopter the camera PCB described in Chapter 4 is installed into the quadrocopter's rack mount and interfaced via USART with the quadrocopter control board, via WLAN with a monitoring PC and finally via a ZigBee module with the ground control station PC.

For tracking the quadrocopter in flight and providing ground truth flight data a *Visualeyez II* VZ4000 tracking system (Phoenix Technologies Inc.) is used in conjunction with four active infra-red LED markers attached to the four corners of the quadrocopter protection frame. By sequential activation of the markers the relative 3D pose of the quadrocopter can be determined by triangulation using the tracking system's three overhead cameras. In Figure 5.12d an outline of the complete setup can be seen, including the tracking system and quadrocopter with its on-board equipment. A view of the quadrocopter hovering in position over the flight arena tiled with high contrast visual patterns is shown in Figure 5.12c.

With the sensor system in place a 1 DOF on-board control loop is implemented as to control the angular velocity around the yaw axis. To achieve this the quadrocopter is to be stabilized in a hovering state using the tracking system, i.e. all pitch, roll and lift commands are controlled by the external tracking system. This leaves only yaw to be controlled by the on-board control system. The PID parameters for the external control loops are roughly identified applying the Ziegler-Nichols method [219] and manually fine-tuned. However, small oscillations along and around all three body axes still remain, which can significantly affect sensor performance—especially when thusly introducing translatory components along the implemented VS cells' main direction [218]. This prompts for the implementation of an additional filter to cope with these unwanted disturbances. In related works filters with fixed time constants have been proposed for this purpose [196]. These large time constants of 750 ms, however, introduce sizable delays and a skewed response signals. Therefore, here an infinite impulse response (IIR) filter with variable time constants is proposed instead. For filtering the rotation velocity estimates this filter makes use

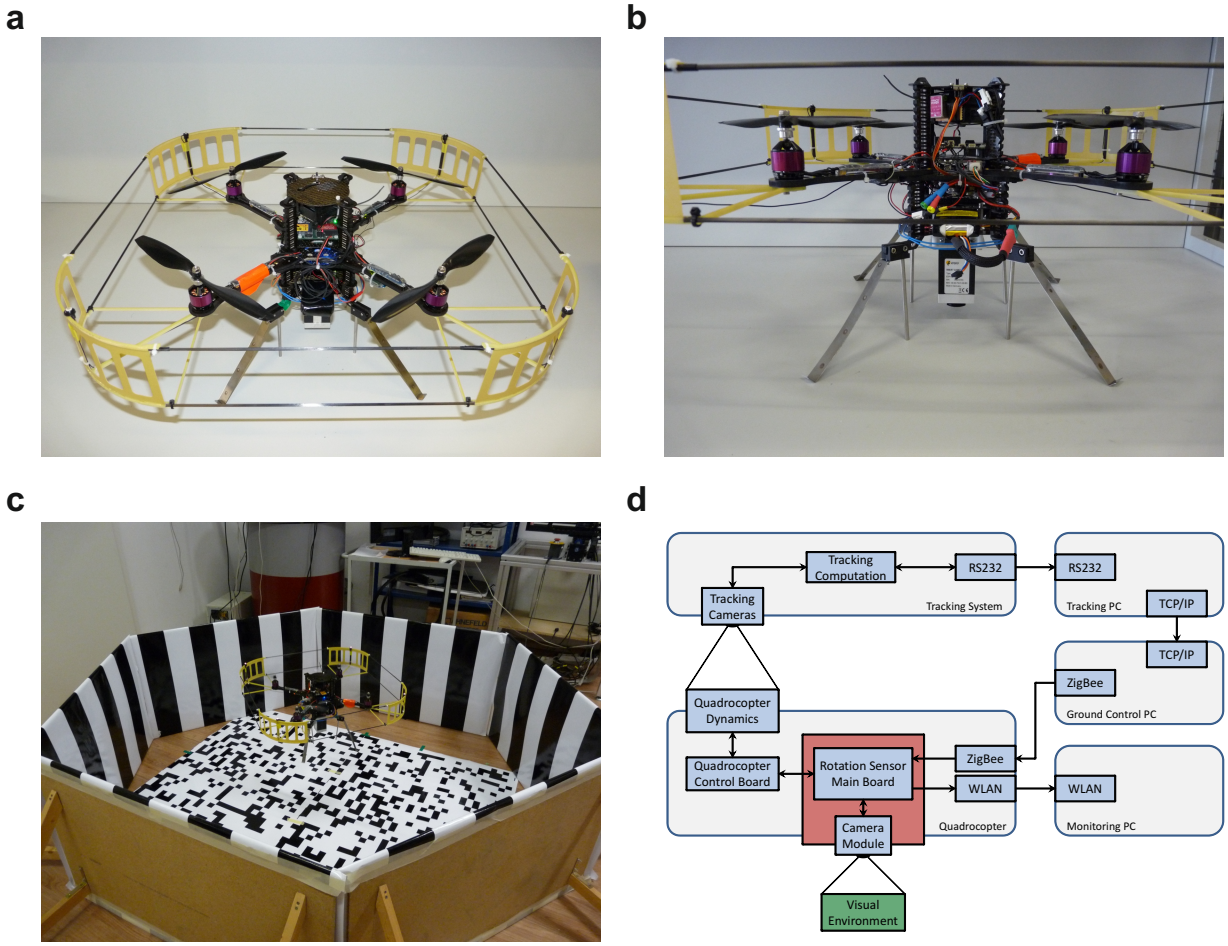

Figure 5.12: Experimental AscTec Pelican quadrocopter with attached downward facing camera and active LED tracking markers.

of the concurrent computation of the rotation angle. Depending on the estimated angle the time constant is accordingly modified, thereby effectively eliminating both high frequency noise as well as low frequency tilting oscillations.

Tethered Flight

Once the parameters for the external stabilizing control are determined a first set of experiments is conducted, in which the quadrocopter is operated while being tethered as to avoid lift translations and potential damage in the case of becoming unstable. A zero-control law is implemented for the yaw rotational velocity using a PI controller. For assessing system performance a step perturbation is superimposed. In one set of experiments the EMD-based rotation sensor is used in the yaw control loop, while for comparison the on-board IMU is used in a second set of trials. Here, the IMU data is used as ground truth.

In Figure 5.13 the quadrocopter response is depicted for step disturbance sizes of $50\,^\circ\,\mathrm{s}^{-1}$ and $100\,^\circ\,\mathrm{s}^{-1}$. For each step disturbance size the ground truth rotational velocity data is shown for the case of using the EMD-based sensor (red traces) and the case of using the IMU itself (green traces) for the control loop. As can be seen, both sensing modalities stabilize the system after either step disturbance within reasonable time frames. In both

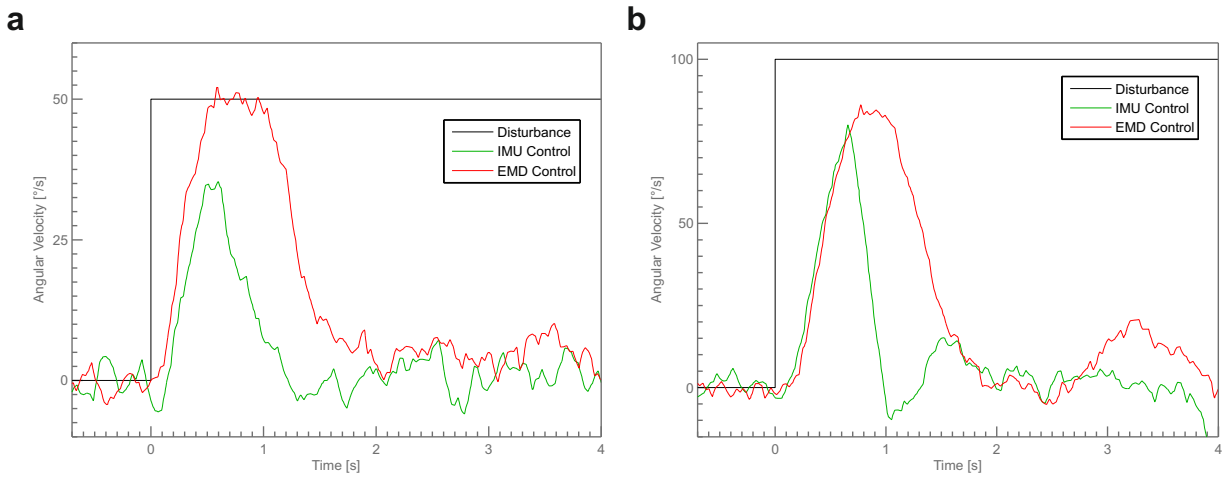

Figure 5.13: Quadrocopter closed loop performance in a tethered state for step disturbances of (**a**) $50\,^\circ\,\mathrm{s}^{-1}$ and (**b**) $100\,^\circ\,\mathrm{s}^{-1}$.

cases, however, the IMU-based control loop is faster in stabilizing the system, i.e. around 1 s response time for the IMU as opposed to about 1.5 s for the EMD-based control. Also, the system's transitory peak response is higher for the EMD-based control loop. Nevertheless, both sensing schemes effectively balance out even large disturbances, leading the system back to a stable state around the zero base line. Note the influence of the integral term of the PI controller largely eliminating residual velocity, as opposed to the purely proportional controllers used in the previously described simulation studies, which yield residual slip speeds.

Free Flight

The same experimental procedures are carried out with the quadrocopter in a non-tethered free flying state. Again, the control of roll, pitch and lift are exerted by the external tracking system and the associated control PC, whereas yaw is controlled on-board the MAV. As shown in Figure 5.14a both IMU and EMD-based controllers effectively counter-balance the disturbances, leaving the system to settle around the base line. In this free flight scenario, however, the EMD-based control takes approximately 1 s longer than the IMU-based control. This is about 0.5 s slower than for the tethered case and is mainly due to the lower performance of the external position control, thereby introducing translatory movements that perturb the EMD-based sensor.

The EMD-based sensor depends strongly on the contrast of the visual environment. The performance of the visual sensor is therefore also assessed using different visual environments. The system's response when facing high contrast random dot pattern, as used in the previous experiments, is compared to the performance with a naturalistic low contrast visual environment. From the results depicted in Figure 5.14b it can be inferred that for both scenarios the performance is similar and the step disturbance is compensated in about 2 s. The conclusion can be drawn, that the EMD-based sensor can be applied in both artificially structured as well as naturalistic visual environments without considerable degradation of performance. Nevertheless, it is important to note that the PI controller parameters need to be slightly adjusted to yield optimal performance depending on the visual

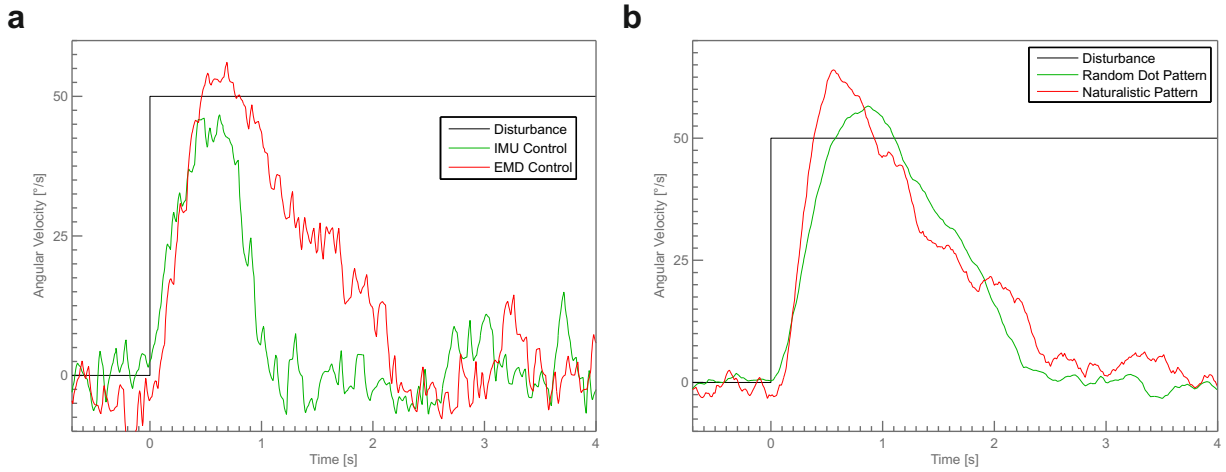

Figure 5.14: Quadrocopter closed loop performance in free flight. (**a**) Comparison of control performance when using EMD or IMU rotation sensors. (**b**) Comparison of EMD-based control performance for two different visual environments.

environment. This can be implemented complementarily using dedicated gain-adjusting algorithms such as recently proposed [197].

5.3.2 Influence of Delays

In the previous sections of this chapter it is shown by numerical simulations that, as opposed to an ideal linear rotation sensor, an EMD-based sensor is capable of coping with large delays without becoming unstable. In order to see if this also applies to real-world environments and operating conditions a FIFO memory delay block is implemented on-board the quadrocopter control system as to introduce precisely timed delays into the control loop and analyze the quadrocopter control performance for a range of delays. This is done for both IMU and EMD as input sensor of the control loop. The IMU is used here as a close approximation of an ideal linear sensor. Two experimental conditions of the quadrocopter are assessed, first while being tethered and then in a free flight situation. Accounting for the difference in scale between the virtual fly used in the numerical simulations and the quadrocopter used for experimental validation the range of relevant delays for the latter situation is found to lie approximately between 0 ms and 1000 ms.

The results of the IMU-based control loop with delays are displayed in Figure 5.15. As can be seen, in both experimental conditions the control performance when facing no delay is stable and fast, reaching base line after a step disturbance in about 1 s without much overshoot or oscillations (red traces). However, this changes considerably when introducing delays. For the situation of a 200 ms delay the response time remains similar to the situation without delay, but the quadrocopter rotation responses show large overshoot and oscillations (green traces). For the case of a 400 ms delay the system displays permanent oscillations, remaining but critically stable (blue traces). Delay values larger than 400 ms render the system unstable.

A different picture presents itself when assessing the EMD-based sensor with delays. As can be seen in Figure 5.16 for all experimental conditions and delay values the system remains stable. A delay of 200 ms for the tethered scenario (green trace of Figure 5.16a)

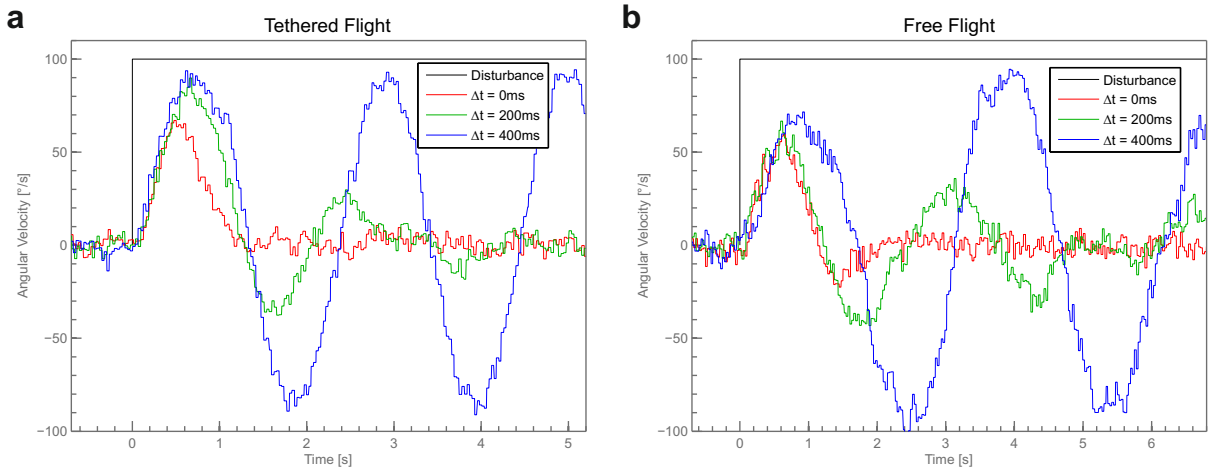

Figure 5.15: IMU-based control performance when facing a range of fixed delays Δt for the quadrocopter in (**a**) a tethered state and (**b**) in free flight. Maximum delay for stable performance is $\Delta t = 400\,\text{ms}$ for both flight scenarios.

increases the response time from about 1.5 s to approximately 1.8 s when compared to the situation without delay (red trace of Figure 5.16a). A delay of 400 ms further produces overshoot (blue trace of Figure 5.16a). Added overshoot and an increase in response time can also be observed for 600 ms and 800 ms delays (red and green traces of Figure 5.16b, respectively). Finally, a 1000 ms delay introduces damped oscillations while remaining stable. Due to the more complex nature of the free flight situation no large oscillations can be observed for any delay values (see Figure 5.16c and Figure 5.16d). This stands in contrast to the oscillations reported in [220] and is probably a result of the much increased complexity of the 6 DOF system used in the present work. However, increasing delay values induce increasing response times until the system reaches base level.

5.4 Discussion

As the algorithmic core underlying fly motion vision the correlation-type Elementary Motion Detector is a formidable tool for gauging motion—and ego-motion in particular. Provided with several beneficial attributes due to its intrinsic properties, such as high resilience to noise [4, 5] or dynamic adaptation to prevailing stimulus statistics [6]. Much is known about its open loop characteristics. Also, the way rotations are sensed using Elementary Motion Detectors is currently being unraveled. However, little is known about the primary goal of this type of motion detection scheme: closed loop control of an aerial system.

In this chapter the EMD-based rotation estimation paradigm is systematically investigated. The approach taken here is threefold. First the system is analytically assessed as to its separability into translational and rotatory components. Then, model simulations are conducted establishing this sensor system and assessing its advantages over ideal linear sensors. Finally, this sensing scheme and its advantages are experimentally validated in a real-world environment. As a potential drawback, the correlation-type EMD is not a linear sensor and as such does not report actual rotational velocities. However, this fact is exploited in closed loop to improve stability. The main focus of the investigation is on closed loop system performance in terms of stability and tolerance of delays. An improve-

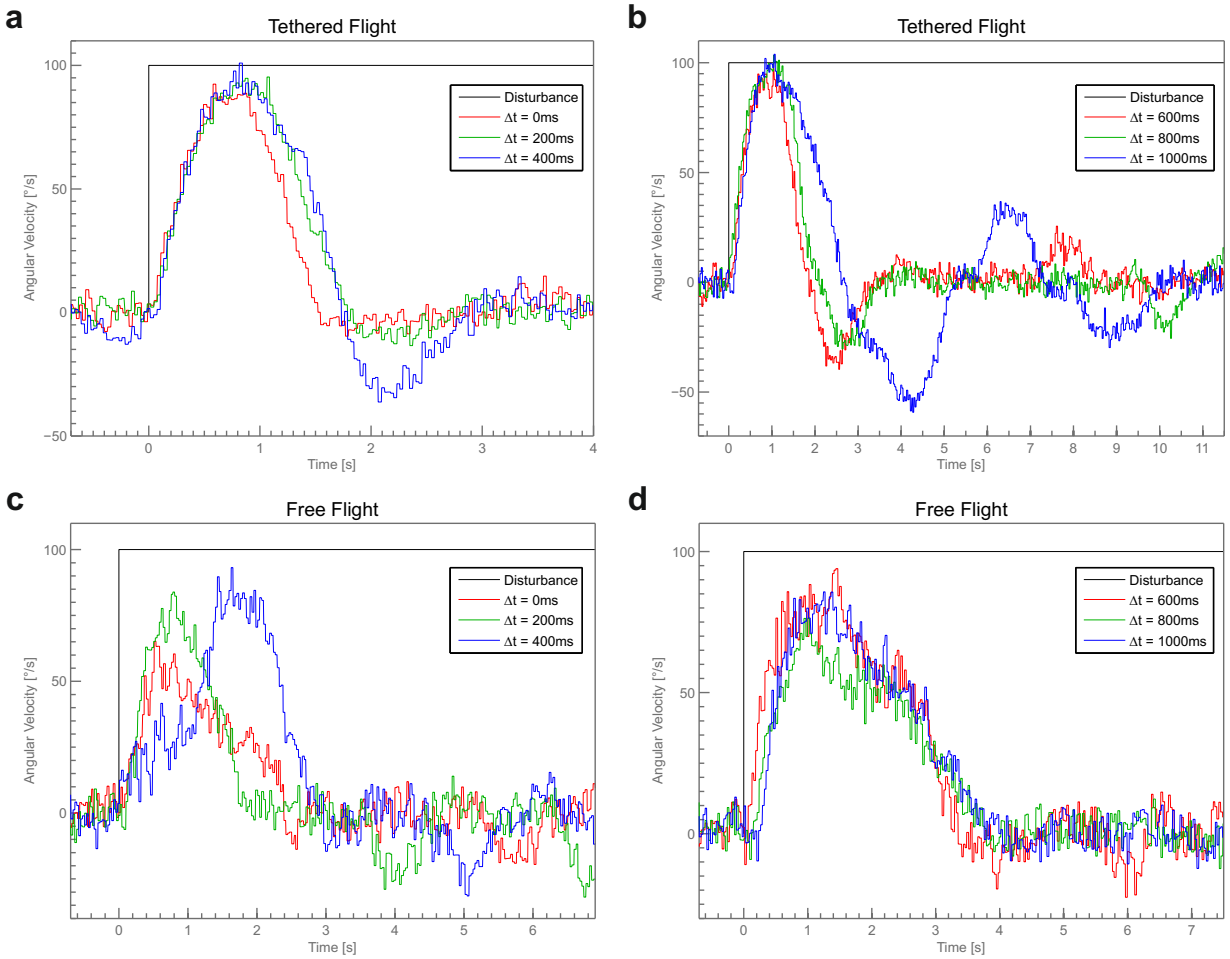

Figure 5.16: EMD-based control performance when facing a range of fixed delays Δt for the quadrocopter in (**a,b**) a tethered state and (**c,d**) in free flight. For all delay conditions and flight scenarios the system remains stable.

ment over ideal linear sensors is achieved. Also, high immunity against concurrent thrust and sideslip translations is observed. However, one drawback of this fly LPTC-inspired rotation sensing scheme is its sensitivity to lift translations [218]. While in practice simple to correct for by appropriate choice of trajectories as is often done by flies themselves [199], a more general solution will be subject to future research.

The contribution of this chapter establishes the EMD-based rotation estimation scheme as a superior alternative to conventional rotation sensing algorithms in terms of stability and resilience against delays when operating in a feedback control loop. On one hand, these findings lay the groundwork for further closed-loop analysis of the EMD in the context of its benefits over other possible motion detection schemes in animals and why it has proven optimal through evolution, while on the other hand these results pave the way for investigation of practical technical applications of this biological principle.

6 Conclusions and Future Directions

6.1 Concluding Remarks

The work presented in this thesis concentrates on systematical analysis of the algorithmic core underpinning the fly motion vision system and its application to flight control. In order to do so, the fly visual system is assessed in a multidisciplinary framework ranging from biological aspects such as electrophysiology, two-photon imaging and behavioral assays, to more engineering approaches such as control theoretic analysis, simulation studies, technical implementation and experimental validation. The fly visual system has been the focus of intense research for many decades and much is known about its biological properties. However, an aspect that only recently has begun to emerge is its application to technical systems. The present work therefore sets out to establish this type of visual processing as a promising alternative to conventional techniques by demonstrating its advantages and possible application scenarios. The main contributions of this work are manifold. Among these figure i) a new type of visual stimulation device allowing for a manifold of biological studies on insects previously not feasible, ii) substantial advances in insight into how motion vision is computed in the fly brain, iii) a novel type of visual rotation estimation based on purely biological principles, iv) establishing the fly-inspired rotation estimation scheme as a superior approach in a control loop when compared to conventional techniques. The main approaches along with the major findings are summarized in the following.

Much is known about how flies process visual information, particularly motion vision. Most of this knowledge is derived from behavioral and anatomical studies on large fly species such as a the blowfly *Calliphora vicina* or the common housefly *Musca domestica*, which lend themselves well for neurobiological research due to their relatively large size. But in order to gain further insight these techniques do not suffice and more refined approaches such as specifically targeted genetic tools are required. However, these genetic tools for fly research currently exist only for the much smaller fruitfly *Drosophila melanogster*. Yet, the prevailing stimulation and recording techniques in existence for large flies can not be applied to *Drosophila* due its much reduced size. In Chapter 3 new methods for visual stimulation and recording are proposed and implemented. Employing these novel techniques a series of key aspects of fly motion vision are investigated. As such, first conclusive evidence is provided for the functional equivalence of the LPTC cell system—roughly the fly equivalent of an airplane cockpit—between *Calliphora* and *Drosophila*. Using two-photon excitation microscopy a separation of visual input in the fly visual system into two separate pathways processing light-increments and light-decrements is found, which has a deep impact on the internal processing stages of fly elementary motion detection. Finally, the role of the descending neurons from these LPTC cells is assessed. As the main conveyors of information between the cockpit-like LPTC neurons and the motor-neurons that directly act upon the flight muscles these cells are of particular interest in the sen-

sorimotor loop of the fly. Using the novel techniques presented here these neurons are found to increase signal robustness and immunity to noise. These results contribute to the understanding of how motion vision is processed in biological systems. Moreover, the novel techniques and stimulation systems established here open up new research directions and directly impact current research.

Vision is a prime source of information about motion and ego-motion such as ego-rotations in particular. However, there currently exist only few technical applications for sensing ego-rotation using visual input cues. Moreover, these typically suffer from shortcomings such as poor performance under low SNR conditions or unstructured visual environments. The fly motion vision system on the other hand is capable of high performance under these conditions. Therefore, in Chapter 4 a sensor is developed that remains algorithmically as close as possible to the fly visual system in order to benefit from its advantageous features, therefore overcoming the drawbacks of most conventional techniques. Apart from very fast and accurate performance the system is designed to have a low footprint in terms of size, weight and power requirements, as to be easily mounted and interfaced with common UAVs or MAVs. The resulting sensor system is thoroughly assessed in multiple environments and conditions. This novel sensor contributes to the toolbox of rotation sensors by providing improved performance in terms of speed and accuracy even under adverse operating conditions.

The correlation-based elementary motion detectors underlying fly motion vision are not linear velocity sensors and, thus, do not report actual angular or linear velocities. Although much is known about its static open loop sensing characteristics, little is known about the performance of the algorithmic fly elementary motion detector under closed loop conditions. Yet, since motion vision is a pivotal part of such an agile and dynamic system as the fly it is axiomatic that it must operate well in closed loop. Therefore, in Chapter 5 the algorithmic fly motion vision system and its rotation sensing system in particular are assessed while operating in a closed feedback loop. First, the separability of translations and rotations is analytically evaluated, thereby establishing necessary conditions. Then, in extensive simulations the system performance is gauged in terms of stability, as well as delay and disturbance rejection. This performance is then compared to ideal linear sensors. Finally, the fly-inspired sensing scheme is experimentally assessed in real-life conditions on-board an MAV and compared to inertial measurement units. The contribution of this novel sensing scheme is much improved closed loop stability, especially when facing delays.

Taken together, the techniques, systems, algorithms and approaches developed in this work on one hand significantly advance the current state of knowledge in neurobiology in the field of motion vision and information processing. On the other hand, from an engineering point of view they significantly advance the state of art in vision based control and motion sensing. In this thesis the two very different fields of as biology and engineering are brought together, considerably furthering insight into either one of them and, even more, capitalizing on the synergies between them and thereby creating novel approaches and solutions.

6.2 Outlook

Biological vision systems are highly diverse and adapted to numerous different environmental conditions. Examples of this range from the dark adapted eyes of night predators that can see clearly in extremely dim lighting conditions to the exceedingly fast visual systems of flying insects, such as the fly. Current and future advances in biology continue to provide further insight into how these feats are achieved. As a natural consequence these advances in knowledge can be applied in technical solutions. In fact, biologically inspired solutions often turn out to be astoundingly effective as a result of a long process of evolution and the resulting optimization and selection. Particularly the fly motion vision system analyzed in this thesis is a prime example due to its low computational cost and multitude of operational advantages. Although several of these advantages have been investigated in the present work there is a number of open questions and research directions directly emerging from this thesis, some of which are detailed in the following.

- *Neurobiological advances* - As the exact neuronal implementation of elementary fly motion detection remains elusive further steps need to be undertaken before knowing the exact computations necessary. A promising approach as presented here is examining the neurons constituting the separate pathways computing light increments and decrements. Future research will focus on finding their connectome.

- *Saturation effects in wide-field integration* - The interneurons of the fly that compute wide-field integration of local motion estimates exhibit a non-linear saturation behavior. This results in an augmented sensitivity for small objects, albeit also introducing an increase in sensitivity for lift translation. This phenomenon needs to be addressed, thereby elucidating its benefits and how separability of translation and rotation can be maintained.

- *Full six degree of motion motion estimation* - This thesis focuses on assessing the fly-inspired rotation estimation scheme in one and two degree of freedom operational spaces. As with the biological original, this can be extended to a full six degree of freedom motion estimation scheme, thereby eliminating the need for external sensors and control loops. In order to do so, different motion detection templates and wide-field integration schemes of local motion estimates will need to be addressed.

- *Multimodal sensor fusion* - Flies use multimodal integration for motion estimation and course control. Apart from visual input, they also integrate inertial information using modified hind-wings called *halteres*. It can be generally stated that both sensing modalities occupy distinct regions in frequency space. Whereas *halteres* are used mainly for detecting for high frequency accelerations the visual systems tends to be used for lower frequency ranges. This approach can also extended to the technical sensor implementation. In this way more robust motion estimation could arise.

Research on motion vision and course control is starting to become increasingly multidisciplinary. As flight systems become more and more complex the solutions for sensing and control need to be adapted. In order to cope with this rising complexity in engineering tasks biology can serve as a prime model of optimal solutions to very complex problems. Integration of these diverse research areas can lead to superior solutions in the fields of robotics, transportation and other related areas.

A Procedures for Drosophila VS Cell Analysis

For obtaining the fly data in section 3.2 the following procedures and materials were used.

Flies

Flies were raised on standard cornmeal-agar medium at a 12 h light / 12 h dark cycle, 25 °C and 60% humidity. Female experimental flies were used, one day post-eclosion. The DB331-Gal4 line (kindly provided by R. Stocker, Fribourg, Switzerland) was used to express Gal4 mostly in tangential cells and a few unidentified columnar neurons. UAS-YC3.3 was used in Fig. 3.9b to highlight entire cells by cytosolic expression of the reporter molecule. In all other experiments UAS-mCD8-TN-XL-8aa was used to predominantly stain cell bodies.

Preparation

Flies were anesthetized on ice and waxed on a Plexiglas holder using bee wax. The head was bent down to expose the caudal backside of the head (Fig. 3.9a) and the extended proboscis was fixed. Occasionally wax was put on the thorax and parts of the contra lateral eye to stabilize the preparation. Aluminum foil with a hole of about 1 mm to 2 mm sustained by a ring shaped metal holder was placed on top of the fly such that thorax and head tightly fitted into the hole. The aluminum foil separated the upper wet part (covered with ringer solution [16]) of the preparation from the lower dry part. The foil was aligned to the most dorsal ommatidia located in the dorsal rim area. Water immersion optics were used from above and visual patterns (see below) were presented to dry and intact facet eyes. A small window was cut into the backside of the head and during mild protease treatment (protease XIV, E.C.3.4.24.31, Sigma, Steinheim, Germany; 1 mg / ml, max 3 min) the neurolemma was partially digested and main tracheal branches and fat body were removed. The protease was rinsed off carefully and replaced by ringer solution. A ringer-filled cleaning electrode (tip around 4 µm) was used to remove the extracellular matrix and to expose the VS cell somata for recording.

UAS-mCD8-TN-XL-8aa

The low-affinity calcium indicator TN-XL [44] was fused on its N terminus to the transmembrane domain mCD8; on its C terminus a short Glycin-linker was used to connect TN-XL to six amino acids known to bind to the PDZ domain of mint. The idea for this construct came from an article by [221] where the authors describe the targeting of N-type voltage-gated calcium channels in hippocampal neurons. The authors describe a binding motif of only six amino acids (DQDHWC) located at the C terminus of the α1B subunit. In their account, this motif was sufficient to cause specific targeting of a mCD4-GFP construct to axons and presynaptic terminals of hippocampal neurons in culture. This idea was used in the present work to clone a synaptically targeted version of TN-XL. However,

axonal targeting was not retained in transgenic flies and the calcium sensitivity of the reporter was essentially lost. Instead, at low to medium expression levels, mCD8-TN-XL-8aa highlights somata efficiently when expressed in neurons of transgenic flies. The protein seems to be trapped in the endoplasmatic reticulum. Although initially unintended, here this expression pattern was used because somata were much brighter compared with an UAS-GFP-nls construct. In the experiments described here, a chromosomal insertion on the third chromosome was used. These flies were crossed to the DB331-Gal4 driver. Even flies homozygous for the driver line and the UAS-construct were behaving normally and no obvious differences could be observed compared to wild-type flies.

Visually Guided Whole Cell Recording

Genetically labeled green fluorescent VS cell somata covered by ringer solution [16] were approached with a patch electrode filled with a red fluorescent dye (intracellular solution as in [222]; containing additional 5 mM Spermine and 30 µM Alexa-Fluor-568-hydrazide-Na, Molecular Probes, adjusted to pH = 7.3). Recordings were established under visual control using a 40X water immersion objective (LumplanF, Olympus), a Zeiss Microscope (Axiotech vario 100, Zeiss, Oberkochen, Germany), fluorescence excitation (100 W fluorescence lamp, heat filter, neutral density filter OD 0.3; all from Zeiss, Germany) and a dual band filter-set (EGFP / DsRed, Chroma Technology, Rockingham, USA). During recordings the fluorescence excitation was shut off to prevent blinding of the fly. 5 MΩ to 7 MΩ patch-electrodes (thin wall, filament, 1.5 mm, WPI, Florida, USA) were pulled on a Sutter-P97 (Sutter Instrument Company, CA, USA). A reference electrode (Ag-AgCl) was immerged in the extra cellular saline (pH 7.3, 1.5 mM $CaCl_2$, no sucrose). Signals were recorded on an NPI BA-1S Bridge Amplifier (NPI Electronics GmbH, Tamm, Germany), low-pass filtered at 3 kHz and digitized at 10 kHz via a digital-to-analog converter (PCI-DAS6025, Measurement Computing, Norton, MA, USA) using MATLAB (Vers. 7.3.0.267, MathWorks Inc.). After recording, several images of each Alexa-filled LPTC were taken at different depths along the z axis (HQ-filter-set Alexa 568, Chroma Technology, Rockingham, USA) using a CCD camera (Spot Pursuit 1.4 Megapixel, Visitron Systems GmbH, Puchheim, Germany). These images allowed anatomical identification of the recorded cell based on their characteristic branching patterns. Additionally, cells were digitized by confocal fluorescence microscopy (see next section). The precise position of the fly's head was controlled using the deep pseudo-pupil technique [223]. Deviations of more than 5° were corrected during data analysis.

Confocal Microscopy

Serial optical sections were taken from recorded VS cells in the intact preparation using a Leica confocal microscope (TCSNT, Leica) and a 40X water-immersion objective (LUM-PlanF, Olympus). Images were taken at 1 µm intervals and 1024 × 1024 pixel resolution. Size, contrast and brightness of the resulting image stacks were adjusted using ImageJ (http://rsb.info.nih.gov/ij).

Neurobiotin Coupling

VS cells were targeted and perfused using patch electrodes as described above. 3% Neurobiotin (Vector Labs, Burlingame) was added to the intracellular solution. Neurobiotin

and Alexa Fluor 568 were co-injected using ±0.5 nA current pulses for up to 10 min. For initial identification the perfused individual VS cell was imaged using the fluorescence microscope and CCD-camera described above. For Streptavidin staining, brains were fixed in 4% PFA (40 min), washed in PBT (45 min to 60 min; PBT: PBS, including 1% Triton X-100, pH 7.2) and incubated in PBT including 2% normal goat serum (Sigma Aldrich, St. Louis, MO; G9023). Streptavidin Alexa Fluor 568 conjugate (Invitrogen) was added at 1:100 overnight (4 °C). Streptavidin was removed by several washing steps (5 x 20 min in PBT) and followed by final washing steps in PBS (5 x 20 min). The stained brains were mounted in Vectashield (Vector Laboratories, Burlingame, CA) and analyzed by confocal microscopy. Perfusion of a single VS-cell never resulted in more than one Alexa-568 filled cell. Only after labeling of Neurobiotin using Streptavidin-Alexa-568 conjugate other cells lighted up. The second red label was used to prevent spectral overlap with the green fluorescence of genetically labeled neurons.

Data Analysis

Data were acquired and analyzed using the data acquisition and analysis toolboxes of MATLAB (Vers. 7.3.0.267, MathWorks Inc.). Receptive fields were calculated by binning responses of single VS cells to vertical stimulation (roughly 5° elevation and 6° azimuth) and subtracting the mean response during null direction from the mean response during preferred direction motion. The data of each individually identified cell was normalized to the maximum response. The projection of the receptive field on the azimuth was calculated for each VS cell individually by averaging the binned responses at different elevations at each position along the azimuth. Contrast was calculated as $(I_{\max} - I_{\min})/(I_{\max} + I_{\min})$ with an absolute $I_{\min}$ and $I_{\max}$ of 0 and 80 cd m^2, respectively.

B Materials and Methods for 2-Photon Imaging

In order to carry out the experiments in Section 3.3 the following procedures and flies were used.

Flies and 2PLSM

The Gal4/UAS system, 21D-Gal4 [104], UAS-ort7 [104] and UAS-TN-XXL42 were used to target all expression to L2 lamina monopolar cells. In the imaged area in the optic lobes, 21D-Gal4driven expression was fairly specific for L2. Female flies were exclusively used in all experiments. Flies were dissected as described previously [76] with two differences: no protease was used and 3 mM Ca^{2+} was used instead of 1.5 mM Ca^{2+} in the ringer solution. L2 terminals in the medulla were imaged using a previously described custom-built two-photon microscope (design provided by W. Denk, MPI Heidelberg) which allows for wide-field or two-photon imaging through the same objective (63, 0.90 NA, water immersion, IR Achroplan; Zeiss). Two-photon fluorescence was excited by a mode-locked Ti:Sapphire laser ($<$ 100 fs, 80 MHz, 700 nm to 1000 nm, pumped by a 10 W Millenia laser; both Tsunami, Spectraphysics). Laser intensity was held constant at typically 5 mW and maximally 10 mW at the specimen. CFP of TN-XXL was selectively excited at 825 nm and CFP and YFP emission were recorded simultaneously (64×64 pixels;, 128 ms per image) with two separate photomultipliers. Visual stimuli were programmed in MATLAB (version 7.3.0.267, MathWorks Inc.) and presented to the eye of the fly using the custom built LED arena (see Section 3.1) operating at four intensity levels.

Interlaced Visual Stimulation

As detailed in Section 3.1, a TTL signal generated at the beginning of each line-scan of the horizontal scanning mirror was used to trigger the individual panels of the LED arena. Stimuli were exclusively presented during 330 of the 400 µs fly-back period of the horizontal scanning mirror after the mirror having reached its final position (1.6 ms scanning per line). Image sequences of 10 cd m^{-2} mean brightness (corresponding to 60 cd m^{-2} during light-ON) were generated. Temporal switching between fluorescence recording and stimulus presentation was performed at a frequency of 500 Hz, which is well above the flicker-fusion frequency of the *Drosophila* eye [131].

Imaging and Data Analysis

In all calcium-imaging experiments, 4 to 6 neighboring terminals were recorded per image sequence (64×64 pixels, 128 ms). Individual image sequences of about 20 s were taken every 2 min, the sequences were separated by complete darkness. Thus, the eye was always fully dark adapted before onset of each recording trial. For calculation of fluorescence change, background fluorescence was subtracted in each recorded channel and a ratio movie was generated (R = (YFP background) / (CFP background)). The expression pattern and

anatomy of TN-XXL-expressing neurons was analyzed by recording image stacks (512×512 pixels per image) with $\Delta z = 1\,\mu m$. Four images were taken and averaged at each z position. Data was analyzed using MBF-ImageJ (US National Institutes of Health) and Origin 7.5 (Additive). Figures were prepared using Adobe Photoshop 8.0 (Adobe Systems).

C Experimental Procedures for DNOVS Analysis

Electrophysiology

Female blowflies (*Calliphora vicina*, 2 to 10 days old, laboratory stock) were prepared as previously described [149] and mounted on a heavy recording table facing the LED arena (Fig. 3.28c). DNOVS1 and VS cells were recorded intracellularly with sharp glass electrodes (Flaming/Brown micropipette puller, P-97; Sutter Instrument, Novato, CA) using glass capillaries with an outer diameter of 1 mm (GC100F-10; Science Products, Hofheim, Germany). Electrodes had resistances between 25 MΩ to 50 MΩ. Tip solutions contained either 10 mM Alexa 488 or 10 mM Alexa 594 (both Invitrogen, Carlsbad, CA), allowing for identification of more than one cell at a time. The electrode shaft was filled with 2 M potassium acetate plus 0.5 M potassium chloride. For data analysis, the output signals of the amplifiers were fed to a PC via an A/D converter (PCI-DAS6025, Measurement Computing, Massachusetts, USA) with a sampling rate of 10 kHz for intracellular recordings. For recordings from DNOVS1, a VS cell was filled with Alexa and visualized under fluorescence light. The VS cell then served as a landmark for finding the DNOVS1 neuron (see [146]). DNOVS1 was recorded in the dendrite and VS cells in their axon. For the experiments shown in Fig. 3.34 VS cells were also recorded in their dendrite. After recording, several images of each Alexa-filled VS cell were taken by a CCD camera (Leica DC 320, Bensheim, Germany). These images allowed anatomical identification of the recorded cell on the basis of their characteristic branching patterns and the relative position of their ventral dendrite within the lobula plate. The V2 cell was recorded intra- and extracellularly from its axonal arborization and could be identified due to its invariant anatomy [191] and its sensitivity to vertical motion along the azimuth [149].

Standard extracellular tungsten electrodes with an impedance of about 1 MΩ were used to record activity of V2 or DNOVS2 cells. Extracellular signals were amplified, band-pass filtered and subsequently processed by a threshold device delivering a 100 mV pulse of 1.1 ms duration as each spike was detected. The resulting signal was recorded at a sampling rate of 1 kHz. To record from DNOVS2, electrodes were positioned in the connective near the thoracic ganglion. To stabilize the recordings, the connective was lifted up by a hook. DNOVS2 was identified based on the position of the tungsten electrode within the connective together with the cell's strong response to downward motion and the specific sensitivity profile along the azimuth [149].

Visual Stimulation Protocols

In order to measure the global motion responses of a cell, a virtual room was programmed (Fig. 3.28b) in which a virtual fly was translated and rotated along the x, y and z axes. In addition the fly was rotated around 36 axes lying on the horizontal plane. At every point in time, the environment was projected onto the virtual fly's eye and the resulting movies subsequently were used as stimuli displayed to a real fly in the LED arena while recording

from the cells (Fig. 3.28c). The virtual room was 2 m in length, 1 m wide and 2 m in height. The lower left corner in the front was defined as origin with coordinates [0 0 0] and the top right corner in the back was analogously defined as endpoint with coordinates [2 1 1] (see Fig. 3.28b). To generate the translational movies, the virtual fly was moved for 1 s as follows: from [1 0.5 0.14] to [1 0.5 0.74] for upward lift, from [1 0.14 0.5] to [1 0.74 0.5] for rightward sideslip and from [0.5 0.5 0.5] to [1.33 0.5 0.5] for forward thrust. For the opposite movements the fly was moved mirror inversely e.g. from [1 0.5 0.86] to [1 0.5 0.26] for downward lift. This resulted in velocities of $0.6\,\mathrm{m\,s^{-1}}$ for lift and sideslip and $0.83\,\mathrm{m\,s^{-1}}$ for thrust. For rotations the virtual fly was positioned at [1 0.5 0.5] and rotated around the x, y and z axes at an angular velocity of $300\,^\circ\,\mathrm{s^{-1}}$.

For the first set of experiments (Fig. 3.28, Fig. 3.29 and Fig. 3.30) the virtual room was tiled with a checkerboard pattern consisting of squares of 0.2 m side length. In the following this stimulus is referred to as the "checkerboard room". All stimulus movies were presented for one second at a frame rate of 300 fps. The preferred ego-motion is defined as the movement eliciting maximal response in the investigated cell. For measuring preferred motion along or around the x, y or z axis the movies were presented in the following sequence: up- and downward lift, right- and leftward sideslip, for- and backward thrust, left- and rightward yaw, down- and upward pitch and finally clock- and counterclockwise roll (color coded as black and red in Fig. 3.29a and Fig. 3.30a).

As the spatial frequency content and local velocities differ for translational and rotational movements, the movies of the checkerboard room were quantified by feeding them into an array of elementary motion detectors of the Reichardt type [224]. The array consisted of a pair of detectors at each location in space, one being oriented along the azimuth and the other along elevation. Each detector consisted of two mirror-symmetrical subunits, where within each subunit, the luminance value derived from one image pixel was low-pass filtered and subsequently multiplied with the high-pass filtered luminance value of the neighboring pixel. The first order low- and high-pass filters used in this study possessed time constants of 20 ms and 50 ms, respectively [6, 225]. The final output signal of each detector was obtained by subtracting the results of the multipliers from each subunit. These signals were then treated as x and y components of the local motion vector. The spatial resolution of the input image amounted to 2°, as was the sampling base of the Reichardt Detectors. Temporal resolution was set to 2 ms. Motion strength was defined as the spatio-temporal average of the vector length of motion detector output. For the velocities used to determine preferred ego-motion (Fig. 3.29 and Fig. 3.30), motion strength for translation was about 1.3 times higher than for rotations. Thus, despite different local velocities and spatial frequency distributions, overall stimulus strength was found to lie in the same range for both kinds of motion. This allowed for comparison of responses of a cell to rotation with responses to translation.

To measure the preferred axis of rotation 18 movies were generated in the "checkerboard room" showing rotations around 18 different axes lying on the horizontal plane. These axes were regularly spaced 10° apart and played for- and backwards yielding 36 counterclockwise rotations. In the following, a rotation around an axis at 0° represents a counterclockwise rotation around the fly's longitudinal axis, i.e. a roll movement. Nose-down pitch corresponds to 90° and nose-up pitch to −90°.

For investigating pattern dependences of cell responses, the virtual room was fitted with two further patterns. The first pattern consisted of checkerboard ceiling and floor, striped side walls and a plaid as front wall. This room was called "artificial room" (Fig.

3.34b). The second pattern consisted of a more naturalistic scene ("natural room") with images of trees on the walls (Fig. 3.34i) taken from a natural image collection (see http://hlab.phys.rug.nl/imlib/index.html and [226]). Both rooms possess rather irregular texture and inhomogeneous contrast distributions. To generate the movies, the virtual fly was rotated around approximately the preferred axis of DNOVS1 (Fig. 3.34) as well as pitch and roll axes (Fig. 3.35). The resulting movies were then displayed on the LED arena while recording from VS cells in both dendrite and axon as well as from DNOVS1 in its dendrite. Movies were displayed for- and backwards for 2 s at 150 fps with 1 s of rest in between.

In order to quantify the differences between movies showing roll rotations in the "artificial room" and movies showing roll rotations in the "checkerboard room" luminance and motion variances were analyzed. Luminance variance was calculated from the mean gray value in a 5° by 5° patch as a function of time. Thus, in the "artificial room" and the "checkerboard room" luminance variance in arbitrary units amounted to 5.6 and 6.1, respectively. To calculate motion variance, both movies were fed into a two-dimensional array of Reichardt type local motion detectors (see details above) [224]. Motion variance was then calculated as the responses of local motion detectors oriented along the elevation axis and integrated within a stripe of 20° in azimuth and 100° in elevation as a function of time. Resulting values for motion variance were, again in arbitrary units, 127 for the "artificial room" and 34 for the "checkerboard room". Thus, while both rooms produce similar local luminance variances, the "artificial room" yields approximately four times higher motion variance than the "checkerboard room".

Data Analysis

Graded neural responses were calculated by taking an average of the membrane potential from 100 ms after stimulus onset minus the mean membrane potential within 200 ms before stimulus onset. Spiking responses of DNOVS2 and V2 were calculated by counting the average number of spikes minus resting firing frequency for the same time intervals as indicated above. The exact axis of rotation was determined by fitting a sine function to the cell responses to different axes of rotation (Fig. 3.31b, see also [151]). Fits were based on the free parameters phase shift, amplitude and offset. Preferred axes of rotation were obtained from the fits by determining the azimuth position at which the fitted tuning curve displayed its maximum. In addition, the tuning curve width was defined as its width at half-maximum fit height. For DNOVS2 a truncated sine function was fitted to the responses to account for the fact that the cell's firing frequency cannot become negative.

For stimulus dependency analysis of DNOVS1, VS dendrite and VS axon responses the average membrane potential distributions were calculated. Membrane potentials of three to five trials per recording site were averaged as to avoid intrinsic noise fluctuations. Membrane potential distributions were determined for 1800 ms starting 200 ms after stimulus onset, normalized by the number of events, i.e. 18000 for a sample rate of 10 kHz. Normalized membrane potential distribution during rest was calculated for 1200 ms (400 ms before movie was played forwards and 800 ms for backwards playback). To quantify the responses the Fano factor of each cell was determined by first averaging trials and then calculating the variance of the average beginning 100 ms after stimulus onset for 1900 ms and subsequently normalizing by the mean value of the average.

Bibliography

[1] B. Hassenstein and W. Reichardt, "Systemtheoretische Analyse der Zeit-, Reihenfolgen- und Vorzeichenauswertung bei der Bewegungsperzeption des Rüsselkäfers *Chlorophanus*," *Zeitschrift für Naturforschung B*, vol. 11b, pp. 513–524, 1956.

[2] J. Harrison, "Macro portrait of the fleshfly (*Sarcophagidae*)," 2009.

[3] **J. Plett**, A. Bahl, M. Buss, K. Kühnlenz, and A. Borst, "Bio-inspired visual ego-rotation sensor for MAVs," *Biological Cybernetics*, vol. 106, pp. 51–63, 2012.

[4] M. Potters and W. Bialek, "Statistical mechanics and visual signal processing," *Journal de Physique I*, vol. 4, pp. 1755–1775, 1994.

[5] J. Haag, W. Denk, and A. Borst, "Fly motion vision is based on Reichardt detectors regardless of the signal-to-noise ratio," *Proceedings of the National Academy of Sciences*, vol. 101, pp. 16333–16338, 2004.

[6] A. Borst, V. L. Flanagin, and H. Sompolinsky, "Adaptation without parameter change: Dynamic gain control in motion detection," *Proceedings of the National Academy of Sciences*, vol. 102, pp. 6172–6176, 2005.

[7] S. Exner, *Die Physiologie der facettirten Augen von Krebsen und Insecten: Eine Studie*. Leipzig : Franz Deuticke, 1891.

[8] A. Mallock, "Insect sight and the defining power of composite eyes," *Proceedings of the Royal Society of London*, vol. 55, pp. 85–90, 1894.

[9] S. Ramón y Cajal, "Nota sobre la estructura de la retina de la mosca *M. vomitoria*," *Trabajo del Laboratorio de Investigación biológica*, vol. VII, 1908.

[10] S. Ramón y Cajal, *Recuerdos de mi vida*. Madrid Imprenta y Librería de N. Moya, 1917.

[11] G. Seitz, "Der Strahlengang im Appositionsauge von *Calliphora erythrocephala* (Meig.)," *J. Comp. Physiol. A*, vol. 59, pp. 205–231, 1968.

[12] K. G. Götz, "Optomotorische Untersuchung des visuellen Systems einiger Augenmutanten der Fruchtfliege *Drosophila*," *Kybernetik*, vol. 2, pp. 77–92, 1964.

[13] E. Buchner, "Elementary movement detectors in an insect visual system," *Biological Cybernetics*, vol. 24, pp. 85–101, 1976.

[14] E. Buchner, K. G. Götz, and C. Straub, "Elementary detectors for vertical movement in the visual system of *Drosophila*," *Biological Cybernetics*, vol. 31, pp. 235–242, 1978.

[15] M. Heisenberg, R. Wonneberger, and R. Wolf, "optomotor-blindH31 - a *Drosophila* mutant of the lobula plate giant neurons," *Journal of Comparative Physiology A*, vol. 124, pp. 287–296, 1978.

[16] R. I. Wilson, G. C. Turner, and G. Laurent, "Transformation of olfactory representations in the *Drosophila* antennal lobe," *Science*, vol. 303, pp. 366–370, 2004.

[17] B. Schnell, M. Joesch, F. Forstner, S. V. Raghu, H. Otsuna, K. Ito, A. Borst, and D. F. Reiff, "Processing of horizontal optic flow in three visual interneurons of the *Drosophila* brain," *Journal of Neurophysiology*, vol. 103, pp. 1646 –1657, 2010.

[18] H. Eichner, M. Joesch, B. Schnell, D. F. Reiff, and A. Borst, "Internal structure of the fly elementary motion detector," *Neuron*, vol. 70, pp. 1155–1164, 2011.

[19] M. V. Srinivasan, J. S. Chahl, K. Weber, S. Venkatesh, M. G. Nagle, and S. W. Zhang, "Robot navigation inspired by principles of insect vision," *Robotics and Autonomous Systems*, vol. 26, pp. 203–216, 1999.

[20] M. Srinivasan, S. Thurrowgood, and D. Soccol, "Competent vision and navigation systems," *IEEE Robotics and Automation Magazine*, vol. 16, pp. 59–71, 2009.

[21] R. Moeckel and S.-C. Liu, "Motion detection chips for robotic platforms," in *Flying Insects and Robots* (D. Floreano, J.-C. Zufferey, M. V. Srinivasan, and C. Ellington, eds.), pp. 101–114, Springer Berlin Heidelberg, 2009.

[22] S. Ramón y Cajal and D. Sánchez, *Contribución al cocimiento de los centros nerviosos de los insectos*. Madrid Imprenta de Hijos de N. Moya, 1917.

[23] K.-F. Fischbach and C. R. Götz, "Das Experiment: ein Blick ins Fliegengehirn: Golgi-gefärbte Nervenzellen bei *Drosophila*," *Biologie in unserer Zeit*, vol. 11, p. 183187, 1981.

[24] N. J. Strausfeld, *Atlas of an insect brain*. Springer-Verlag, 1976.

[25] K. F. Fischbach and A. P. M. Dittrich, "The optic lobe of *Drosophila melanogaster*. I. A Golgi analysis of wild-type structure," *Cell and Tissue Research*, vol. 258, pp. 441–475, 1989.

[26] I. A. Meinertzhagen and S. D. O'Neil, "Synaptic organization of columnar elements in the lamina of the wild type in *Drosophila melanogaster*," *The Journal of Comparative Neurology*, vol. 305, pp. 232–263, 1991.

[27] S.-Y. Takemura, Z. Lu, and I. A. Meinerzhagen., "Synaptic circuits of the *Drosophila* optic lobe: the input terminals to the medulla," *The Journal of Comparative Neurology*, vol. 509, pp. 493–513, 2008.

[28] F. Gabbiani and P. W. Jones, "A genetic push to understand motion detection," *Neuron*, vol. 70, pp. 1023–1025, 2011.

[29] B. Bausenwein and K. F. Fischbach, "Activity labeling patterns in the medulla of *Drosophila melanogaster* caused by motion stimuli," *Cell and Tissue Research*, vol. 270, pp. 25–35, 1992.

[30] G. Geiger and D. R. Nässel, "Visual orientation behaviour of flies after selective laser beam ablation of interneurones," *Nature*, vol. 293, pp. 398–399, 1981.

[31] A. Borst and J. Haag, "Neural networks in the cockpit of the fly," *Journal of Comparative Physiology A*, vol. 188, pp. 419–437, 2002.

[32] A. Borst, J. Haag, and D. F. Reiff, "Fly motion vision," *Annual Review of Neuroscience*, vol. 33, pp. 49–70, 2010.

[33] K. Hausen and C. Wehrhahn, "Microsurgical lesion of horizontal cells changes optomotor yaw responses in the blowfly *Calliphora erythrocephala*," *Proceedings of the Royal Society of London B*, vol. 219, pp. 211–216, 1983.

[34] R. Hengstenberg, "Spike responses of non-spiking visual interneurone," *Nature*, vol. 270, pp. 338–340, 1977.

[35] J. Haag and A. Borst, "Encoding of visual motion information and reliability in spiking and graded potential neurons," *The Journal of Neuroscience*, vol. 17, pp. 4809–4819, 1997.

[36] H. G. Krapp, B. Hengstenberg, and R. Hengstenberg, "Dendritic structure and receptive-field organization of optic flow processing interneurons in the fly," *Journal of Neurophysiology*, vol. 79, pp. 1902–1917, 1998.

[37] M. O. Franz and H. G. Krapp, "Wide-field, motion-sensitive neurons and matched filters for optic flow fields," *Biological Cybernetics*, vol. 83, pp. 185–197, 2000.

[38] R. Hengstenberg, K. Hausen, and B. Hengstenberg, "The number and structure of giant vertical cells (VS) in the lobula plate of the blowfly *Calliphora erythrocephala*," *Journal of Comparative Physiology A*, vol. 149, pp. 163–177, 1982.

[39] J. Haag and A. Borst, "Neural mechanism underlying complex receptive field properties of motion-sensitive interneurons," *Nature Neuroscience*, vol. 7, pp. 628–634, 2004.

[40] K. Farrow, A. Borst, and J. Haag, "Sharing receptive fields with your neighbors: Tuning the vertical system cells to wide field motion," *The Journal of Neuroscience*, vol. 25, pp. 3985–3993, 2005.

[41] A. Borst, "Fly motion vision: from optic flow to visual course control," *e-Neuroforum*, vol. 3, pp. 59–66, 2012.

[42] A. Borst and J. Haag, "Optic flow processing in the cockpit of the fly," *Cold Spring Harbor Monograph Series*, vol. 49, pp. 101–122, 2007.

[43] O. Shimomura, F. H. Johnson, and Y. Saiga, "Extraction, purification and properties of aequorin, a bioluminescent protein from the luminous hydromedusan, *Aequorea*," *Journal of Cellular and Comparative Physiology*, vol. 59, pp. 223–239, 1962.

[44] M. Mank, D. F. Reiff, N. Heim, M. W. Friedrich, A. Borst, and O. Griesbeck, "A FRET-Based calcium biosensor with fast signal kinetics and high fluorescence change," *Biophysical Journal*, vol. 90, pp. 1790–1796, 2006.

[45] W. Denk, J. H. Strickler, and W. W. Webb, "Two-photon laser scanning fluorescence microscopy," *Science*, vol. 248, pp. 73–76, 1990.

[46] A. H. Brand and N. Perrimon, "Targeted gene expression as a means of altering cell fates and generating dominant phenotypes," *Development*, vol. 118, pp. 401–415, 1993.

[47] N. A. Campbell and J. B. Reece, *Biology*. Pearson - Benjamin Cummings, 6th ed., 2001.

[48] M. H. Dickinson and J. R. Lighton, "Muscle efficiency and elastic storage in the flight motor of *Drosophila*," *Science*, vol. 268, pp. 87–90, 1995.

[49] R. Strauss, S. Schuster, and K. G. Götz, "Processing of artificial visual feedback in the walking fruit fly *Drosophila melanogaster*.," *Journal of Experimental Biology*, vol. 200, pp. 1281–1296, 1997.

[50] J. Lindemann, R. Kern, C. Michaelis, P. Meyer, J. van Hateren, and M. Egelhaaf, "FliMax, a novel stimulus device for panoramic and highspeed presentation of behaviourally generated optic flow," *Vision Research*, vol. 43, pp. 779–791, 2003.

[51] M. Reiser, "Panels Page." http://www.dickinson.caltech.edu/PanelsPage, 2006.

[52] M. B. Reiser and M. H. Dickinson, "A modular display system for insect behavioral neuroscience," *Journal of Neuroscience Methods*, vol. 167, pp. 127–139, 2008.

[53] F. Iida, "Biologically inspired visual odometer for navigation of a flying robot," *Robotics and Autonomous Systems*, vol. 44, pp. 201–208, 2003.

[54] S. Bermudez i Badia, P. Pyk, and P. F. M. Verschure, "A fly-locust based neuronal control system applied to an unmanned aerial vehicle: the invertebrate neuronal principles for course stabilization, altitude control and collision avoidance," *International Journal of Robotics Research*, vol. 26, pp. 759–772, 2007.

[55] J. Conroy, G. Gremillion, B. Ranganathan, and J. S. Humbert, "Implementation of wide-field integration of optic flow for autonomous quadrotor navigation," *Autonomous Robots*, vol. 27, pp. 189–198, 2009.

[56] S. Han, A. D. Straw, M. H. Dickinson, and R. M. Murray, "A real-time helicopter testbed for insect-inspired visual flight control," in *Proceedings of the IEEE International Conference on Robotics and Automation*, pp. 3055–3060, 2009.

[57] F. Ruffier, S. Viollet, S. Amic, and N. Franceschini, "Bio-inspired optical flow circuits for the visual guidance of micro air vehicles," in *Proceedings of the IEEE International Symposium on Circuits and Systems*, vol. 3, pp. 846–849, 2003.

[58] S.-C. Liu, "A neuromorphic aVLSI model of global motion processing in the fly," *IEEE Transactions on Circuits and Systems II: Analog and Digital Signal Processing*, vol. 47, pp. 1458–1467, 2000.

[59] C. Higgins and S. Shams, "A biologically inspired modular VLSI system for visual measurement of self-motion," *IEEE Sensors Journal*, vol. 2, pp. 508–528, 2002.

[60] E. Nakamura, S. Asami, T. Takahashi, and K. Sawada, "Real time parameter optimization for elementary motion detectors," in *IEEE International Conference on Image Processing*, pp. 1065–1068, 2006.

[61] F. Aubepart, M. El Farji, and N. Franceschini, "FPGA implementation of elementary motion detectors for the visual guidance of micro-air-vehicles," in *Proceedings of the IEEE International Symposium on Industrial Electronics*, vol. 1, pp. 71– 76, 2004.

[62] T. Köhler, F. Röchter, J. P. Lindemann, and R. Möller, "Bio-inspired motion detection in an FPGA-based smart camera module," *Bioinspiration and Biomimetics*, vol. 4, p. 015008(10pp), 2009.

[63] T. Zhang, H. Wu, A. Borst, K. Kühnlenz, and M. Buss, "An FPGA implementation of insect-inspired motion detector for high-speed vision systems," in *Proceedings of the IEEE International Conference on Robotics and Automation*, pp. 335–340, 2008.

[64] T. Poggio and W. Reichardt, "Visual control of orientation behaviour in the fly. Part II. Towards the underlying neural interactions," *Quarterly Reviews of Biophysics*, vol. 9, pp. 377–438, 1976.

[65] R. C. Miall, "The flicker fusion frequencies of six laboratory insects, and the response of the compound eye to mains fluorescent ripple," *Physiological Entomology*, vol. 3, pp. 99–106, 1978.

[66] H. Autrum, "Über zeitliches Auflösungsvermögen und Primärvorgänge im Insektenauge," *Die Naturwissenschaften*, vol. 39, pp. 290–297, 1952.

[67] B. Tatler, D. C. O'Carroll, and S. B. Laughlin, "Temperature and the temporal resolving power of fly photoreceptors," *Journal of Comparative Physiology A*, vol. 186, pp. 399–407, 2000.

[68] M. F. Land, "Visual acuity in insects," *Annual Review of Entomology*, vol. 42, pp. 147–177, 1997.

[69] M. F. Land and H. Eckert, "Maps of the acute zones of fly eyes," *Journal of Comparative Physiology A*, vol. 156, pp. 525–538, 1985.

[70] M. Mank, A. F. Santos, S. Direnberger, T. D. Mrsic-Flögel, S. B. Hofer, V. Stein, T. Hendel, D. F. Reiff, C. Levelt, A. Borst, T. Bonhoeffer, M. Hübener, and O. Griesbeck, "A genetically encoded calcium indicator for chronic in vivo two-photon imaging," *Nature Methods*, vol. 5, pp. 805–811, 2008.

[71] D. F. Reiff, **J. Plett**, M. Mank, O. Griesbeck, and A. Borst, "Visualizing retinotopic half-wave rectified input to the motion detection circuitry of *Drosophila*," *Nature Neuroscience*, vol. 13, pp. 973–978, 2010.

[72] E. K. Scott, T. Raabe, and L. Luo, "Structure of the vertical and horizontal system neurons of the lobula plate in *Drosophila*," *The Journal of Comparative Neurology*, vol. 454, pp. 470–481, 2002.

[73] S. V. Raghu, M. Joesch, A. Borst, and D. F. Reiff, "Synaptic organization of lobula plate tangential cells in *Drosophila*: γ-Aminobutyric acid receptors and chemical release sites," *The Journal of Comparative Neurology*, vol. 502, p. 598610, 2007.

[74] W. Reichardt, "Autocorrelation, a principle for the evaluation of sensory information by the central nervous system," in *Principles of Sensory Communications* (W. Rosenblith, ed.), pp. 303–317, John Wiley, NY: MIT Press, 1961.

[75] A. Borst and M. Egelhaaf, "Principles of visual motion detection," *Trends in Neurosciences*, vol. 12, pp. 297–306, 1989.

[76] M. Joesch, **J. Plett**, A. Borst, and D. F. Reiff, "Response properties of motion-sensitive visual interneurons in the lobula plate of *Drosophila melanogaster*," *Current Biology*, vol. 18, pp. 368–374, 2008.

[77] H. Cuntz, J. Haag, F. Forstner, I. Segev, and A. Borst, "Robust coding of flow-field parameters by axo-axonal gap junctions between fly visual interneurons," *Proceedings of the National Academy of Sciences*, vol. 104, pp. 10229–10233, 2007.

[78] K. Hausen, "Motion sensitive interneurons in the optomotor system of the fly," *Biological Cybernetics*, vol. 45, pp. 143–156, 1982.

[79] M. Egelhaaf, A. Borst, and W. Reichardt, "Computational structure of a biological motion-detection system as revealed by local detector analysis in the fly's nervous system," *Journal of the Optical Society of America A*, vol. 6, pp. 1070–1087, 1989.

[80] S. Single and A. Borst, "Dendritic integration and its role in computing image velocity," *Science*, vol. 281, pp. 1848 –1850, 1998.

[81] E. Buchner, S. Buchner, and I. Bülthoff, "Deoxyglucose mapping of nervous activity induced in *Drosophila* brain by visual movement," *Journal of Comparative Physiology A*, vol. 155, pp. 471–483, 1984.

[82] J. Haag, A. Wertz, and A. Borst, "Integration of lobula plate output signals by DNOVS1, an identified premotor descending neuron," *The Journal of Neuroscience*, vol. 27, pp. 1992–2000, 2007.

[83] F. Weber, H. Eichner, H. Cuntz, and A. Borst, "Eigenanalysis of a neural network for optic flow processing," *New Journal of Physics*, vol. 10, p. 015013, 2008.

[84] J. Haag and A. Borst, "Dye-coupling visualizes networks of large-field motion-sensitive neurons in the fly," *Journal of Comparative Physiology A*, vol. 191, pp. 445–454, 2005.

[85] P. Kunze, "Untersuchung des Bewegungssehens fixiert fliegender Bienen," *Zeitschrift für Vergleichende Physiologie*, vol. 44, pp. 656–684, 1961.

[86] G. Fermi and W. Reichardt, "Optomotorische Reaktionen der Fliege *Musca domestica*," *Kybernetik*, vol. 2, pp. 15–28, 1963.

[87] H. Eckert, "Optomotorische Untersuchungen am visuellen System der Stubenfliege *Musca domestica* L," *Kybernetik*, vol. 14, pp. 1–23, 1973.

[88] M. Heisenberg, "Comparative behavioral studies on two visual mutants of *Drosophila*," *Journal of Comparative Physiology A*, vol. 80, pp. 119–136, 1972.

[89] H. Eckert, "Functional properties of the H1-neurone in the third optic ganglion of the blowfly, *Phaenicia*," *Journal of Comparative Physiology A*, vol. 135, pp. 29–39, 1980.

[90] M. Egelhaaf and A. Borst, "Transient and steady-state response properties of movement detectors," *Journal of the Optical Society of America A*, vol. 6, pp. 116–127, 1989.

[91] C. Reisenman, J. Haag, and A. Borst, "Adaptation of response transients in fly motion vision. I: Experiments," *Vision Research*, vol. 43, pp. 1293–1309, 2003.

[92] A. Borst, C. Reisenman, and J. Haag, "Adaptation of response transients in fly motion vision. II: Model studies," *Vision Research*, vol. 43, pp. 1311–1324, 2003.

[93] R. A. Harris, D. C. O'Carroll, and S. B. Laughlin, "Contrast gain reduction in fly motion adaptation," *Neuron*, vol. 28, pp. 595–606, 2000.

[94] A. Borst and M. Egelhaaf, "Direction selectivity of blowfly motion-sensitive neurons is computed in a two-stage process.," *Proceedings of the National Academy of Sciences*, vol. 87, pp. 9363–9367, 1990.

[95] C. Gilbert, "Membrane conductance changes associated with the response of motion sensitive insect visual neurons.," *Zeitschrift für Naturforschung C*, vol. 45, pp. 1222–1224, 1990.

[96] M. Egelhaaf, A. Borst, and B. Pilz, "The role of GABA in detecting visual motion," *Brain Research*, vol. 509, pp. 156–160, 1990.

[97] A. S. Thum, S. Knapek, J. Rister, E. Dierichs-Schmitt, M. Heisenberg, and H. Tanimoto, "Differential potencies of effector genes in adult *Drosophila*," *The Journal of Comparative Neurology*, vol. 498, pp. 194–203, 2006.

[98] G. Miesenböck and I. G. Kevrekidis, "Optical imaging and control of genetically designated neurons in functioning circuits," *Annual Review of Neuroscience*, vol. 28, pp. 533–563, 2005.

[99] L. F. Tammero and M. H. Dickinson, "The influence of visual landscape on the free flight behavior of the fruit fly *Drosophila melanogaster*," *Journal of Experimental Biology*, vol. 205, pp. 327–343, 2002.

[100] M. Heisenberg and R. Wolf, "On the fine structure of yaw torque in visual flight orientation of *Drosophila melanogaster*," *Journal of Comparative Physiology A: Neuroethology, Sensory, Neural, and Behavioral Physiology*, vol. 130, pp. 113–130, 1979.

[101] L. F. Tammero and M. H. Dickinson, "Collision-avoidance and landing responses are mediated by separate pathways in the fruit fly, *Drosophila melanogaster*," *Journal of Experimental Biology*, vol. 205, pp. 2785–2798, 2002.

[102] M. Mronz and F.-O. Lehmann, "The free-flight response of *Drosophila* to motion of the visual environment," *Journal of Experimental Biology*, vol. 211, pp. 2026–2045, 2008.

[103] C. Clifford and M. Ibbotson, "Fundamental mechanisms of visual motion detection: models, cells and functions," *Progress in Neurobiology*, vol. 68, pp. 409–437, 2002.

[104] J. Rister, D. Pauls, B. Schnell, C.-Y. Ting, C.-H. Lee, I. Sinakevitch, J. Morante, N. J. Strausfeld, K. Ito, and M. Heisenberg, "Dissection of the peripheral motion channel in the visual system of *Drosophila melanogaster*," *Neuron*, vol. 56, pp. 155–170, 2007.

[105] P. E. Coombe and M. Heisenberg, "The structural brain mutant vacuolar medulla of *Drosophila melanogaster* with specific behavioral defects and cell degeneration in the adult," *Journal of neurogenetics*, vol. 3, pp. 135–158, 1986.

[106] Y. Zhu, A. Nern, S. L. Zipursky, and M. A. Frye, "Peripheral visual circuits functionally segregate motion and phototaxis behaviors in the fly," *Current Biology*, vol. 19, pp. 613–619, 2009.

[107] A. Y. Katsov and T. R. Clandinin, "Motion processing streams in *Drosophila* are behaviorally specialized," *Neuron*, vol. 59, pp. 322–335, 2008.

[108] B. Hassenstein and W. Reichardt, "Systemtheoretische Analyse einer Verhaltensweise (der Wechsel-Folgen-Reaktion des Rüsselkäfers *Chlorophanus viridis*)," *Verhandlungen der Deutschen Zoologischen Gesellschaft*, pp. 96–102, 1952.

[109] A. J. van Doorn and J. J. Koenderink, "Temporal properties of the visual detectability of moving spatial white noise," *Experimental Brain Research*, vol. 45, pp. 179–188, 1982.

[110] H. B. Barlow and W. R. Levick, "The mechanism of directionally selective units in rabbit's retina.," *The Journal of Physiology*, vol. 178, pp. 477–504, 1965.

[111] J. P. van Santen and G. Sperling, "Temporal covariance model of human motion perception," *Journal of the Optical Society of America A*, vol. 1, pp. 451–473, 1984.

[112] E. H. Adelson and J. R. Bergen, "Spatiotemporal energy models for the perception of motion," *Journal of the Optical Society of America A*, pp. 284–299, 1985.

[113] N. A. Franceschini N, Riehle A, "Directionally selective motion detection by insect neurons," in *Facets of vision* (D. Stavenga and R. Hardie, eds.), ch. 17, pp. 360–390, Berlin: Springer, 1989.

[114] A. Riehle and N. Franceschini, "Motion detection in flies: parametric control over ON-OFF pathways," *Experimental Brain Research*, vol. 54, pp. 390–394, 1984.

[115] M. Egelhaaf and A. Borst, "Are there separate ON and OFF channels in fly motion vision?," *Visual Neuroscience*, vol. 8, pp. 151–164, 1992.

[116] S. Ullman, *The Interpretation of Visual Motion*. Cambridge, Massachussetts: MIT Press, 1979.

[117] S. M. Anstis and B. J. Rogers, "Illusory reversal of visual depth and movement during changes of contrast," *Vision Research*, vol. 15, pp. 957–IN6, 1975.

[118] C. Gengs, H.-T. Leung, D. R. Skingsley, M. I. Iovchev, Z. Yin, E. P. Semenov, M. G. Burg, R. C. Hardie, and W. L. Pak, "The target of *Drosophila* photoreceptor synaptic transmission is a histamine-gated chloride channel encoded by ort (hclA)," *The Journal of Biological Chemistry*, vol. 277, pp. 42113–42120, 2002.

[119] R. C. Hardie, "A histamine-activated chloride channel involved in neurotransmission at a photoreceptor synapse," *Nature*, vol. 339, pp. 704–706, 1989.

[120] D. R. Skingsley, S. B. Laughlin, and R. C. Hardie, "Properties of histamine-activated chloride channels in the large monopolar cells of the dipteran compound eye: a comparative study," *Journal of Comparative Physiology A*, vol. 176, pp. 611–623, 1995.

[121] S. B. Laughlin and D. Osorio, "Mechanisms for neural signal enhancement in the blowfly compound eye," *Journal of Experimental Biology*, vol. 144, pp. 113–146, 1989.

[122] M. Järvilehto and F. Zettler, "Electrophysiological-histological studies on some functional properties of visual cells and second order neurons of an insect retina," *Cell and Tissue Research*, vol. 136, pp. 291–306, 1973.

[123] F. Zettler and M. Järvilehto, "Lateral inhibition in an insect eye," *Journal of Comparative Physiology A*, vol. 76, pp. 233–244, 1972.

[124] F. Zettler and M. Järvilehto, "Active and passive axonal propagation of non-spike signals in the retina of *Calliphora*," *Journal of Comparative Physiology A*, vol. 85, pp. 89–104, 1973.

[125] F. Zettler and H. Straka, "Synaptic chloride channels generating hyperpolarizing on-responses in monopolar neurones of the flowfly visual system," *Journal of Experimental Biology*, vol. 131, pp. 435–438, 1987.

[126] L. Zheng, G. G. de Polavieja, V. Wolfram, M. H. Asyali, R. C. Hardie, and M. Juusola, "Feedback network controls photoreceptor output at the layer of first visual synapses in *Drosophila*," *The Journal of General Physiology*, vol. 127, pp. 495–510, 2006.

[127] J. K. Douglass and N. J. Strausfeld, "Visual motion detection circuits in flies: peripheral motion computation by identified small-field retinotopic neurons," *The Journal of Neuroscience*, vol. 15, pp. 5596–5611, 1995.

[128] J. K. Douglass and N. J. Strausfeld, "Visual motion-detection circuits in flies: Parallel direction- and non-direction-sensitive pathways between the medulla and lobula plate," *The Journal of Neuroscience*, vol. 16, pp. 4551–4562, 1996.

[129] E. K. Buschbeck and N. J. Strausfeld, "Visual motion-detection circuits in flies: small-field retinotopic elements responding to motion are evolutionarily conserved across taxa," *The Journal of neuroscience: the official journal of the Society for Neuroscience*, vol. 16, pp. 4563–4578, 1996.

[130] T. Euler, P. B. Detwiler, and W. Denk, "Directionally selective calcium signals in dendrites of starburst amacrine cells," *Nature*, vol. 418, pp. 845–852, 2002.

[131] C. Wu and F. Wong, "Frequency characteristics in the visual system of *Drosophila*. genetic dissection of electroretinogram components," *The Journal of General Physiology*, vol. 69, pp. 705–724, 1977.

[132] P. E. Coombe, "The large monopolar cells L1 and L2 are responsible for ERG transients in *Drosophila*," *Journal of Comparative Physiology A*, vol. 159, pp. 655–665, 1986.

[133] H. Wässle, "Parallel processing in the mammalian retina," *Nature reviews. Neuroscience*, vol. 5, pp. 747–757, 2004.

[134] A. Molnar, H.-A. Hsueh, B. Roska, and F. S. Werblin, "Crossover inhibition in the retina: circuitry that compensates for nonlinear rectifying synaptic transmission," *Journal of Computational Neuroscience*, vol. 27, pp. 569–590, 2009.

[135] R. C. Rentera, N. Tian, J. Cang, S. Nakanishi, M. P. Stryker, and D. R. Copenhagen, "Intrinsic ON responses of the retinal OFF pathway are suppressed by the ON pathway," *The Journal of Neuroscience*, vol. 26, pp. 11857–11869, 2006.

[136] S. H. Chalasani, N. Chronis, M. Tsunozaki, J. M. Gray, D. Ramot, M. B. Goodman, and C. I. Bargmann, "Dissecting a circuit for olfactory behaviour in *Caenorhabditis elegans*," *Nature*, vol. 450, pp. 63–70, 2007.

[137] J. J. Gibson, *The perception of the visual world*, vol. xii. Oxford, England: Houghton Mifflin, 1950.

[138] W. H. Warren, B. A. Kay, W. D. Zosh, A. P. Duchon, and S. Sahuc, "Optic flow is used to control human walking," *Nature Neuroscience*, vol. 4, pp. 213–216, 2001.

[139] M. N. O. Davies and P. R. Green, "Optic flow-field variables trigger landing in hawk but not in pigeons," *Naturwissenschaften*, vol. 77, pp. 142–144, 1990.

[140] M. Collett, T. S. Collett, and M. V. Srinivasan, "Insect navigation: Measuring travel distance across ground and through air," *Current Biology*, vol. 16, pp. R887–R890, 2006.

[141] H. G. Krapp and R. Hengstenberg, "Estimation of self-motion by optic flow processing in single visual interneurons," *Nature*, vol. 384, pp. 463–466, 1996.

[142] K. Nordström, P. D. Barnett, I. M. Moyer de Miguel, R. S. Brinkworth, and D. C. O'Carroll, "Sexual dimorphism in the hoverfly motion vision pathway," *Current Biology*, vol. 18, pp. 661–667, 2008.

[143] R. Pierantoni, "A look into the cock-pit of the fly. The architecture of the lobular plate," *Cell and Tissue Research*, vol. 171, pp. 101–122, 1976.

[144] J. Haag, M. Egelhaaf, and A. Borst, "Dendritic integration of motion information in visual interneurons of the blowfly," *Neuroscience Letters*, vol. 140, pp. 173–176, 1992.

[145] J. Haag and A. Borst, "Orientation tuning of motion-sensitive neurons shaped by vertical-horizontal network interactions," *Journal of Comparative Physiology A*, vol. 189, pp. 363–370, 2003.

[146] J. Haag and A. Borst, "Reciprocal inhibitory connections within a neural network for rotational optic-flow processing," *Frontiers in Neuroscience*, vol. 1, pp. 111–121, 2007.

[147] Y. M. Elyada, J. Haag, and A. Borst, "Different receptive fields in axons and dendrites underlie robust coding in motion-sensitive neurons," *Nature Neuroscience*, vol. 12, pp. 327–332, 2009.

[148] N. Strausfeld and U. Bassemir, "Lobula plate and ocellar interneurons converge onto a cluster of descending neurons leading to neck and leg motor neuropil in *Calliphora erythrocephala*," *Cell and Tissue Research*, vol. 240, pp. 617–640, 1985.

[149] A. Wertz, A. Borst, and J. Haag, "Nonlinear integration of binocular optic flow by DNOVS2, a descending neuron of the fly," *The Journal of Neuroscience*, vol. 28, pp. 3131–3140, 2008.

[150] A. Wertz, B. Gaub, **J. Plett**, J. Haag, and A. Borst, "Robust coding of ego-motion in descending neurons of the fly," *The Journal of Neuroscience*, vol. 29, pp. 14993–15000, 2009.

[151] K. Karmeier, H. G. Krapp, and M. Egelhaaf, "Population coding of self-motion: Applying bayesian analysis to a population of visual interneurons in the fly," *Journal of Neurophysiology*, vol. 94, pp. 2182–2194, 2005.

[152] H. G. Krapp, "Ocelli," *Current Biology*, vol. 19, pp. R435–R437, 2009.

[153] J. van Kleef, R. Berry, and G. Stange, "Directional selectivity in the simple eye of an insect," *The Journal of Neuroscience*, vol. 28, pp. 2845–2855, 2008.

[154] G. Stange, "The ocellar component of flight equilibrium control in dragonflies," *Journal of Comparative Physiology A*, vol. 141, pp. 335–347, 1981.

[155] C. P. Taylor, "Contribution of compound eyes and ocelli to steering of locusts in flight: I. Behavioural analysis," *Journal of Experimental Biology*, vol. 93, pp. 1–18, 1981.

[156] M. M. Parsons, H. G. Krapp, and S. B. Laughlin, "A motion-sensitive neurone responds to signals from the two visual systems of the blowfly, the compound eyes and ocelli," *Journal of Experimental Biology*, vol. 209, pp. 4464–4474, 2006.

[157] W. Gronenberg, J. J. Milde, and N. J. Strausfeld, "Oculomotor control in calliphorid flies: Organization of descending neurons to neck motor neurons responding to visual stimuli," *The Journal of Comparative Neurology*, vol. 361, p. 267284, 1995.

[158] N. J. Strausfeld, H. S. Seyan, and J. J. Milde, "The neck motor system of the fly *Calliphora erythrocephala*," *Journal of Comparative Physiology A*, vol. 160, pp. 205–224, 1987.

[159] J. J. Milde, H. S. Seyan, and N. J. Strausfeld, "The neck motor system of the fly *Calliphora erythrocephala*," *Journal of Comparative Physiology A*, vol. 160, pp. 225–238, 1987.

[160] S. J. Huston and H. G. Krapp, "Visuomotor transformation in the fly gaze stabilization system," *PLoS Biology*, vol. 6, p. e173, 2008.

[161] K. Karmeier, J. H. van Hateren, R. Kern, and M. Egelhaaf, "Encoding of naturalistic optic flow by a population of blowfly motion-sensitive neurons," *Journal of Neurophysiology*, vol. 96, pp. 1602–1614, 2006.

[162] N. J. Strausfeld and U. K. Bassemir, "The organization of giant horizontal-motion-sensitive neurons and their synaptic relationships in the lateral deutocerebrum of *Calliphora erythrocephala* and *Musca domestica*," *Cell and Tissue Research*, vol. 242, pp. 531–550, 1985.

[163] A. Borst and S. Bahde, "Spatio-temporal integration of motion," *Naturwissenschaften*, vol. 75, pp. 265–267, 1988.

[164] A. Borst and S. Bahde, "Visual information processing in the fly's landing system," *Journal of Comparative Physiology A*, vol. 163, pp. 167–173, 1988.

[165] M. A. Frye and M. H. Dickinson, "Fly flight: A model for the neural control of complex behavior," *Neuron*, vol. 32, pp. 385–388, 2001.

[166] M. V. Srinivasan and S. Zhang, "Visual motor computations in insects," *Annual Review of Neuroscience*, vol. 27, pp. 679–696, 2004.

[167] C. Schilstra and J. H. v. Hateren, "Stabilizing gaze in flying blowflies," *Nature*, vol. 395, pp. 654–654, 1998.

[168] J. H. van Hateren and C. Schilstra, "Blowfly flight and optic flow. II. Head movements during flight," *Journal of Experimental Biology*, vol. 202, pp. 1491–1500, 1999.

[169] N. Franceschini, J. M. Pichon, C. Blanes, and J. M. Brady, "From insect vision to robot vision," *Philosophical Transactions of the Royal Society B*, vol. 337, pp. 283–294, 1992.

[170] F. Kendoul, I. Fantoni, and K. Nonami, "Optic flow-based vision system for autonomous 3D localization and control of small aerial vehicles," *Robot. Auton. Syst.*, vol. 57, pp. 591–602, 2009.

[171] R. R. Harrison, "A biologically inspired analog IC for visual collision detection," *IEEE Transactions on Circuits and Systems I: Regular Papers*, vol. 52, pp. 2308–2318, 2005.

[172] J.-C. Zufferey and D. Floreano, "Fly-inspired visual steering of an ultralight indoor aircraft," *IEEE Transactions on Robotics*, vol. 22, pp. 137–146, 2006.

[173] A. Beyeler, J.-C. Zufferey, and D. Floreano, "Vision-based control of near-obstacle flight," *Autonomous Robots*, vol. 27, pp. 201–219, 2009.

[174] A. Hyslop, H. G. Krapp, and J. S. Humbert, "Control theoretic interpretation of directional motion preferences in optic flow processing interneurons," *Biological Cybernetics*, vol. 103, pp. 353–364, 2010.

[175] T. Netter and N. Franceschini, "A robotic aircraft that follows terrain using a neuromorphic eye," in *Proceedings of the Conference on Intelligent Robots and Systems*, vol. 1, pp. 129–134, 2002.

[176] F. Valette, F. Ruffier, S. Viollet, and T. Seidl, "Biomimetic optic flow sensing applied to a lunar landing scenario," in *Proceedings of the IEEE International Conference on Robotics and Automation*, pp. 2253–2260, 2010.

[177] D. C. O'Carroll, P. A. Shoemaker, and R. S. A. Brinkworth, "Bio-inspired optical rotation sensor," in *Proceedings of the SPIE Symposium on Smart Structures, Devices, and Systems IIIst. III*, vol. 641418, pp. 1–12, 2006.

[178] A. Borst, "Correlation versus gradient type motion detectors: the pros and cons," *Philosophical Transactions of the Royal Society B*, vol. 362, pp. 369–374, 2007.

[179] W. Reichardt and M. Egelhaaf, "Properties of individual movement detectors as derived from behavioural experiments on the visual system of the fly," *Biological Cybernetics*, vol. 58, pp. 287–294, 1988.

[180] P. Stumpf, "Über die Abhängigkeit der visuellen Bewegungsrichtung und negativen Nachbildes von den Reizvorgängen auf der Netzhaut," *Zeitschrift für Psychologie*, vol. 59, pp. 321–330, 1911.

[181] **J. Plett**, K. Kühnlenz, and A. Borst, "Bio-Inspired visual ego-motion sensor for unmanned aerial vehicles," in *Proceedings of the ESF-EMBO International Conference of Functional Neurobiology*, pp. 59–60, 2010.

[182] R. Petrowitz, H. Dahmen, M. Egelhaaf, and H. G. Krapp, "Arrangement of optical axes and spatial resolution in the compound eye of the female blowfly *Calliphora*," *Journal of Comparative Physiology A*, vol. 186, pp. 737–746, 2000.

[183] R. C. Gonzalez and R. E. Woods, *Digital Image Processing*. Upper Saddle River, NJ: Prentice Hall, 3 ed., 2007.

[184] XILINX, *XAPP134: Virtex synthesizable high performance SDRAM controller*. XILINX, 1999.

[185] XILINX, *XAPP394: Interfacing to mobile SDRAM with CoolRunner-II CPLDs*. XILINX, 2003.

[186] K. G. Götz and H. Wenking, "Visual control of locomotion in the walking fruitfly *Drosophila*," *Journal of Comparative Physiology A*, vol. 85, pp. 235–266, 1973.

[187] M. E. Chiappe, J. D. Seelig, M. B. Reiser, and V. Jayaraman, "Walking modulates speed sensitivity in *Drosophila* motion vision," *Current Biology*, vol. 20, pp. 1470–1475, 2010.

[188] B. J. Duistermars, D. M. Chow, M. Condro, and M. A. Frye, "The spatial, temporal and contrast properties of expansion and rotation flight optomotor responses in *Drosophila*," *Journal of Experimental Biology*, vol. 210, pp. 3218–3227, 2007.

[189] S. N. Fry, N. Rohrseitz, A. D. Straw, and M. H. Dickinson, "Visual control of flight speed in *Drosophila melanogaster*," *Journal of Experimental Biology*, vol. 212, pp. 1120–1130, 2009.

[190] A. Borst and S. Bahde, "Comparison between the movement detection systems underlying the optomotor and the landing response in the housefly," *Biological Cybernetics*, vol. 56, pp. 217–224, 1987.

[191] K. Hausen and C. Wehrhahn, "Neural circuits mediating visual flight control in flies. I. Quantitative comparison of neural and behavioral response characteristics," *The Journal of Neuroscience*, vol. 9, pp. 3828–3836, 1989.

[192] S. N. Jung, A. Borst, and J. Haag, "Flight activity alters velocity tuning of fly motion-sensitive neurons," *The Journal of Neuroscience*, vol. 31, pp. 9231–9237, 2011.

[193] F. Weber, C. K. Machens, and A. Borst, "Spatiotemporal response properties of optic-flow processing neurons," *Neuron*, vol. 67, pp. 629–642, 2010.

[194] M. Goslin and M. R. Mine, "The Panda3D graphics engine," *Computer*, vol. 37, pp. 112–114, 2004.

[195] N. Greene, "Environment mapping and other applications of world projections," *IEEE Computer Graphics and Applications*, vol. 6, pp. 21–29, 1986.

[196] A.-K. Warzecha and M. Egelhaaf, "Intrinsic properties of biological motion detectors prevent the optomotor control system from getting unstable," *Philosophical Transactions of the Royal Society B*, vol. 351, pp. 1579–1591, 1996.

[197] H. Wu, K. Zou, T. Zhang, A. Borst, and K. Kühnlenz, "Insect-inspired high-speed motion vision system for robot control," *Biological Cybernetics*, vol. 106, pp. 453–463, 2012.

[198] N. Franceschini, "Visual guidance based on optic flow: a biorobotic approach," *Journal of Physiology - Paris*, vol. 98, pp. 281–292, 2004.

[199] C. Schilstra and J. H. van Hateren, "Blowfly flight and optic flow. I. Thorax kinematics and flight dynamics," *Journal of Experimental Biology*, vol. 202, pp. 1481–1490, 1999.

[200] H. G. Krapp and M. Lappe, "Neuronal matched filters for optic flow processing in flying insects," in *Neuronal Processing of Optic Flow*, vol. Volume 44, pp. 93–120, Academic Press, 1999.

[201] A. Borst and F. Weber, "Neural action fields for optic flow based navigation: A simulation study of the fly lobula plate network," *PLoS ONE*, vol. 6, p. e16303, 2011.

[202] J. J. Koenderink and A. J. van Doorn, "Facts on optic flow," *Biological Cybernetics*, vol. 56, pp. 247–254, 1987.

[203] M. Chasles, "Note sur les propriétés générales du système de deux corps semblables entr'eux et placés d'une manière quelconque dans l'espace; et sur le déplacement ni ou inniment petit d'un corps solide libre," *Bulletin des Sciences Mathematiques, Astronomiques, Physiques et Chimiques*, vol. 14, pp. 321–326, 1830.

[204] T. Zhang, *Control and Bio-Inspired Motion Estimation of a Vision-Guided Quadrotor*. PhD thesis, Technische Universität München, München, 2010.

[205] R. W. Beard, "Quadrotor dynamics and control," tech. rep., Brigham Young University, 2008.

[206] A. R. Ennos, "The kinematics and aerodynamics of the free flight of some diptera," *Journal of Experimental Biology*, vol. 142, pp. 49–85, 1989.

[207] T. Hesselberg and F.-O. Lehmann, "Turning behaviour depends on frictional damping in the fruit fly *Drosophila*," *Journal of Experimental Biology*, vol. 210, pp. 4319–4334, 2007.

[208] S. N. Fry, R. Sayaman, and M. H. Dickinson, "The aerodynamics of hovering flight in *Drosophila*," *Journal of Experimental Biology*, vol. 208, pp. 2303–2318, 2005.

[209] S. N. Fry, R. Sayaman, and M. H. Dickinson, "The aerodynamics of free-flight maneuvers in *Drosophila*," *Science*, vol. 300, pp. 495–498, 2003.

[210] R. Ramamurti and W. Sandberg, "Computational study of 3-d flapping foil flows," in *Proc. 39th Aerospace Sciences Meeting and Exhibit*, (Reno, NV), 2001.

[211] R. Zbikowski, "Fly like a fly," *IEEE Spectrum*, vol. 42, pp. 46–51, 2005.

[212] J. A. Fleming, *Magnets and electric currents*. E. & F.N. Spon, 2nd ed., 1902.

[213] J. Howard, A. Dubs, and R. Payne, "The dynamics of phototransduction in insects," *Journal of Comparative Physiology A*, vol. 154, pp. 707–718, 1984.

[214] R. C. Hardie and P. Raghu, "Visual transduction in *Drosophila*," *Nature*, vol. 413, pp. 186–193, 2001.

[215] T. Flash and N. Hogan, "The coordination of arm movements: an experimentally confirmed mathematical model," *The Journal of Neuroscience*, vol. 5, pp. 1688–1703, 1985.

[216] Y. Uno, M. Kawato, and R. Suzuki, "Formation and control of optimal trajectory in human multijoint arm movement," *Biological Cybernetics*, vol. 61, pp. 89–101, 1989.

[217] Y. Wada, Y. Kaneko, E. Nakano, R. Osu, and M. Kawato, "Quantitative examinations for multi joint arm trajectory planning-using a robust calculation algorithm of the minimum commanded torque change trajectory," *Neural Networks*, vol. 14, pp. 381–393, 2001.

[218] K. Karmeier, H. G. Krapp, and M. Egelhaaf, "Robustness of the tuning of fly visual interneurons to rotatory optic flow," *Journal of Neurophysiology*, vol. 90, pp. 1626–1634, 2003.

[219] R. C. Dorf and R. H. Bishop, *Modern Control Systems*. Prentice Hall, 11th ed., 2008.

[220] H. Wu, *Aspects of High-Speed Visual Servo Control*. PhD thesis, Technische Universität München, München, 2012.

[221] A. Maximov and I. Bezprozvanny, "Synaptic targeting of n-type calcium channels in hippocampal neurons," *The Journal of Neuroscience*, vol. 22, pp. 6939–6952, 2002.

[222] R. I. Wilson and G. Laurent, "Role of GABAergic inhibition in shaping odor-evoked spatiotemporal patterns in the *Drosophila* antennal lobe," *The Journal of Neuroscience*, vol. 25, pp. 9069–9079, 2005.

[223] N. Franceschini and K. Kirschfeld, "Les phénomènes de pseudopupille dans l'œil composé de *Drosophila*," *Kybernetik*, vol. 9, pp. 159–182, 1971.

[224] W. Reichardt, "Evaluation of optical motion information by movement detectors," *Journal of Comparative Physiology A*, vol. 161, pp. 533–547, 1987.

[225] J. Haag, A. Vermeulen, and A. Borst, "The intrinsic electrophysiological characteristics of fly lobula plate tangential cells: III. Visual response properties," *Journal of Computational Neuroscience*, vol. 7, pp. 213–234, 1999.

[226] J. H. van Hateren and A. van der Schaaf, "Independent component filters of natural images compared with simple cells in primary visual cortex," *Proceedings of the Royal Society of London B*, vol. 265, pp. 359–366, 1998.